UNIVERSIDAD COMPLUTENSE DE MADRID
FACULTAD DE FÍSICAS
Departamento de Física Atómica, Molecular y Nuclear

TESIS DOCTORAL

Hydrogenic and impurity retention studies on liquid lithium and tungsten as materials for a nuclear fusion reactor by glow discharge and laser techniques

MEMORIA PARA OPTAR AL GRADO DE DOCTOR

PRESENTADA POR

Alfonso de Castro Calles

Director

Francisco Luis Tabarés Vázquez

Madrid, 2018

UNIVERSIDAD COMPLUTENSE DE MADRID

FACULTAD DE CIENCIAS FÍSICAS

DEPARTAMENTO DE FÍSICA ATÓMICA, MOLECULAR Y NUCLEAR

Hydrogenic and impurity retention studies on liquid lithium and tungsten as materials for a nuclear fusion reactor by glow discharge and laser techniques

---

Estudios de retención hidrogénica e impurezas en litio líquido y tungsteno
como materiales para un reactor de fusión mediante técnicas
glow discharge y láser

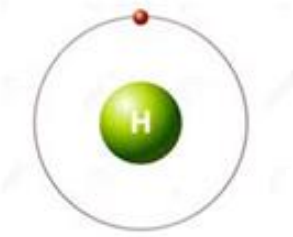

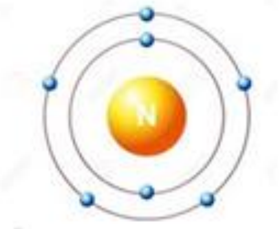

Memoria presentada para optar al título
de doctor en Física por:

Alfonso de Castro Calles

Director:
Francisco Luis Tabarés Vázquez
Madrid, 2017

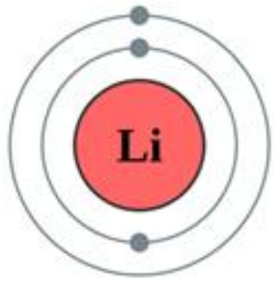

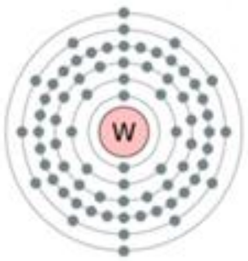

GOBIERNO
DE ESPAÑA

MINISTERIO
DE ECONOMÍA, INDUSTRIA
Y COMPETITIVIDAD

Laboratorio Nacional
de Fusión
Ciemat

Infraestructuras
Científicas y Técnicas
Singulares

A mi hermano Lorenzo

TABLE OF CONTENTS

AGRADECIMIENTOS

Sirvan estas líneas para agradecer a todas aquellas personas que me han ayudado en mi trabajo experimental durante estos cuatro años, sin su ayuda la realización de esta tesis doctoral hubiera sido imposible.

Agradecer en primer lugar a mi director de tesis, Francisco Tabarés, del que he aprendido prácticamente todo durante mi doctorado, por su apoyo y motivación constantes y por darme la oportunidad de realizar esta tesis e introducirme en el mundo de la investigación en fusión nuclear.

A mis compañeros del grupo de interacción plasma-pared: Daniel Alegre, Ana Belén Martín, Eider Oyarzábal y David Tafalla, por toda su ayuda en las tareas experimentales y por los buenos ratos pasados en el laboratorio. Gracias también a Pranay Valson y Arvydas Sepetys, compañeros que realizaron su tesis de máster en colaboración directa conmigo y nuestro grupo. Su ayuda durante la puesta a punto de las técnicas glow-discharge y láser ha sido inestimable. A los doctores Pawel Gasior (IFPiLM Varsovia) y Jesús González (centro de láseres de la UCM) por sus enseñanzas e indicaciones indispensables para la puesta a punto de la técnica LIDS. A la doctora María González (CIEMAT) por su colaboración en la realización de los análisis SIMS realizados durante la última parte de la tesis.

Al conjunto de técnicos del Laboratorio Nacional de Fusión, en especial a Miguel, Luis Alfonso, Régulo, Andrés, Fernando de Aragón, Félix†, Raúl, Lolo, Julián, Javiloncho Gregorio, Justo, Javi y al resto de empleados del taller general del Laboratorio Nacional de Fusión por su ayuda técnica y su colaboración en los montajes y reparaciones relacionadas con los dispositivos experimentales utilizados en esta tesis. A los compañeros de NBI: Fernando, José Antonio, Beatriz, Macarena y Emilio por prestarme algunos materiales y equipos necesarios durante mi experimentación. A mi compañero de penurias pre-doctorales Ulises Losada por tantos momentos compartidos en el CIEMAT y en JET.

Por último quisiera agradecer encarecidamente a mi novia y a mis padres su apoyo constante e incondicional durante todo el período de doctorado, plagado de buenos y no tan buenos momentos, siempre os estaré agradecido.

RESUMEN

La energía de fusión es un proceso perfectamente viable desde el punto de vista científico. El Sol y las demás estrellas del universo actúan como “reactores de fusión” que funcionan adecuadamente día tras día. Un ejemplo de ello lo tenemos en nuestro Sol cuya superficie emite una enorme cantidad de radiación ($\sim 4.5\cdot 10^{20}$ W), consumiendo para ello unas 5 toneladas de hidrógeno cada segundo. Sin embargo la reproducción de este proceso en nuestro planeta a través de dispositivos controlados de fusión magnética que puedan producir electricidad resulta extremadamente complicada debido a desafíos tecnológicos muy importantes. Entre ellos, la selección de materiales en contacto con el plasma, capaces de extraer la potencia generada y resistir bajo las extremas condiciones esperadas en el interior de estos reactores, es uno de los asuntos más críticos a resolver. El tungsteno y el litio líquido están entre los candidatos mejor considerados para conseguir este objetivo. Esta tesis explora la utilización de estos elementos para conformar estos componentes, enfatizando en dos importantes problemas derivados de su uso: la formación de amoníaco (tritiado) durante las descargas con “seeding” de N_2 y la potencial absorción hidrogénica (tritio) en capas híbridas litio líquido-tungsteno.

La problemática relacionada con la formación de amoníaco ha sido abordada simulando el ambiente del divertor de un reactor de fusión con plasmas tipo glow discharge. El amoníaco producido ha sido principalmente investigado en paredes de tungsteno, aunque la investigación se extendió a otros materiales relevantes para ITER como aluminio (proxy del berilio) y acero inoxidable. Distintos plasmas mixtos fueron estudiados: N_2-H_2, N_2-D_2 y N_2-H_2-He, explorando la formación de amoníaco en función de la concentración de nitrógeno y helio en el plasma y variando además las características de la descarga (voltaje y corriente). La influencia de la temperatura superficial y del contenido de nitrógeno plasmático en los rendimientos de formación de amoníaco ha sido determinada, además de los cambios inducidos por un distinto tiempo de residencia para la molécula de nitrógeno en el reactor y la presencia de helio en el plasma. Se estudió asimismo la química de plasma-superficie en experimentos específicos con plasmas glow discharge encaminados a entender el rol del contenido de nitrógeno en las paredes y la recombinación superficial en el proceso global. Finalmente la retención de amoníaco debido a su absorción superficial fue investigada en experimentos con exposición de gas. En todos estos experimentos, la detección y cuantificación del amoníaco generado fue realizada con espectrometría de masas cuadrupolar mientras que otros diagnósticos como la sonda de Langmuir simple y la espectroscopía de emisión óptica se usaron para caracterizar el plasma.

Los resultados presentados muestran que la problemática relacionada con la formación de amoníaco en dispositivos futuros como ITER es difícilmente evitable si el nitrógeno es usado como seeding gas para el enfriamiento radiativo del divertor. Las condiciones experimentales como una creciente temperatura para los materiales de pared, un bajo contenido en nitrógeno del plasma y la presencia de helio están lejos de ser una solución, pudiendo incluso agravar el problema. La retención por absorción superficial en líneas de bombeo y crio-bombas sería asimismo un importante problema que sin duda limitaría el ciclo operacional de la máquina.

La investigación asociada a la retención hidrógenica en superficies híbridas de tungsteno-litio se centró en comprender el rol que en este proceso tiene la presencia de litio implantado y co-depositado en tungsteno. Plasmas tipo glow discharge fueron de nuevo utilizados para irradiar tungsteno (a una temperatura aproximada de unos 100ºC) con plasmas de hidrógeno e hidrógeno-litio, tratando de estudiar las diferencias en retención del litio depositado e implantado. Las medidas de retención de hidrógeno se llevaron a cabo usando espectroscopía de desorción térmica asistida por espectrometría de masas, mientras que la espectroscopía de emisión óptica ayudó a caracterizar los plasmas. Para investigar el fenómeno de co-deposición, varias muestras de tungsteno fueron preparadas mediante su exposición a diferentes ambientes con litio y deuterio gaseoso. Un diagnóstico de desorción inducida por láser fue desarrollado y puesto a punto para medir la retención hidrogénica, estudiando además la influencia de la temperatura superficial en el proceso y empleando varias técnicas post-mortem (espectrometría de masas de iones secundarios, perfilometría y espectroscopía de emisión atómica asistida por llama) para la caracterización completa de las películas de litio-tungsteno.

Los resultados más destacables incluyen una retención menor (en factor 3-4) en superficies de tungsteno con litio implantado comparado con las superficies que contenían litio simplemente depositado. La co-deposición simultánea de litio y deuterio en tungsteno mostró una retención despreciable (por debajo del límite de detección de la técnica) en la capa híbrida a 225ºC de temperatura. Por el contrario, muestras pre-litiadas y expuestas a una presión mayor de deuterio, sí presentaron una retención medible a distintas temperaturas superficiales (200ºC, 300ºC y 400ºC). Se encontró, una drástica y no lineal reducción en la retención a temperaturas más altas en la película híbrida, con ratios atómicos deuterio-litio menores de 10^{-4} a 400ºC. Basándonos en los resultados obtenidos se ha realizado una extrapolación de la retención de deuterio por co-deposición sobre las capas de la primera pared de tungsteno-litio esperadas en reactores con un diseño consistente en una primera pared de tungsteno sólido y un divertor de litio líquido. Dicha extrapolación ha demostrado que la retención de tritio asociada a la co-deposición de litio en una primera pared de tungsteno caliente puede ser compatible con las limitaciones requeridas por las condiciones de seguridad nuclear y de riesgo radiactivo.

RESUMEN

ABSTRACT

Fusion energy is a perfectly feasible process from the scientific point of view. The Sun and the rest of stars act as "fusion reactors" that work properly day by day. A clear example can be found in the Sun, whose surface emits a huge radiation power ($\sim 4.5 \cdot 10^{20}$ W), employing for this purpose a hydrogen amount of 5 tons per second approximately. However, the reproduction of this process in our planet by means of magnetic controlled fusion devices that could produce electric power results extremely complicated due to very important technological challenges. Among them, the selection of the materials in contact with the plasma, able to extract the generated power and resist under the extreme conditions expected in such reactors, is one of the most critical issues to solve. Tungsten and liquid lithium are among the candidates better considered to develop this purpose. This thesis explores the utilization of these elements to conform the “plasma facing components”, emphasizing in two important problems derived of their use: the formation of (tritiated) ammonia during N_2 seeded discharges and the potential hydrogenic (tritium) uptake in tungsten-liquid lithium mixed layers.

The problematic of ammonia formation has been approached by simulating the environment of a fusion reactor divertor with glow discharge plasmas. The produced ammonia has been mainly investigated on tungsten walls, although the research was extended to other ITER-relevant materials as aluminium (proxy of beryllium) and stainless steel. Different mixed plasmas were studied: N_2-H_2, N_2-D_2 and N_2-H_2-He, scanning in the nitrogen and helium concentrations and also varying the discharge characteristics (voltage and current). The influence of the wall temperature and the nitrogen plasma concentration in the ammonia formation yields has been determined, as well as the changes induced in the process due to different residence times for nitrogen in the reactor and the presence of helium in the plasma. The basic plasma-surface chemistry was studied in specific experiments with glow discharge plasmas aimed to understand the role of the nitrogen walls legacy and surface recombination in the global process. Finally, the retention of ammonia by means of sticking on the surface was investigated with gas exposure experiments. In all these experiments, the ammonia detection and quantification was performed by using quadrupole mass spectrometry while other diagnostics as single

Langmuir probe and optical emission spectroscopy were implemented to characterize the plasma.

The presented results show that the problematic of ammonia generation in future devices as ITER is difficulty avoidable if nitrogen is used as seeding gas for divertor radiative cooling. Experimental conditions as increasing temperature for the wall materials, low nitrogen plasma content and the helium plasma presence are far from being a solution, and could even worsen the problem. Retention by sticking in pumping lines and cryo-pumps will be also important as this process will limit the operational cycle of the machine.

The research associated to the hydrogenic retention in tungsten-lithium hybrid layers was centred in the understanding of the role of lithium implantation and co-deposition on tungsten in the process. Glow discharge plasmas were again utilized to irradiate tungsten (at T~100ºC) with hydrogen and lithium-seeded plasmas to study the differences in terms of associated retention of deposited and implanted lithium. The hydrogen retention measurements were carried out by using thermal desorption spectroscopy assisted by mass spectrometry, while optical emission spectroscopy helped to characterize the plasmas. To investigate the co-deposition, several tungsten samples were prepared by their exposition to different lithium-deuterium (gaseous) environments. A laser induced desorption diagnostic was developed and tuned up to measure the hydrogenic retention, also studying the influence of the surface temperature in the process and employing several post-mortem techniques (secondary ion mass spectrometry, profilemetry and flame atomic emission spectroscopy) for the complete characterization of the tungsten-lithium films.

The remarkable results include a lower retention (factor 3-4) in tungsten surfaces with implanted lithium compared to surfaces that contained simply deposited lithium. Simultaneous co-deposition of lithium and deuterium in tungsten showed a negligible uptake (below the limit of detection of the technique) in the hybrid layer at 225ºC. On the contrary, pre-lithiated samples presented a measurable retention at different superficial temperatures (200ºC, 300ºC and 400ºC). A non-linear drastic reduction in the retention was found for increasing temperatures on the hybrid films that determined deuterium-lithium atomic ratios lower than 10^{-4} at 400ºC. Based on the obtained results, an extrapolation of the deuterium uptake by co-deposition on the tungsten-lithium first wall layers expected in such reactor designs with a solid tungsten first wall and a liquid lithium divertor is performed. It has showed that this associated fuel (tritium) retention in a hot tungsten first wall may be compatible with the tritium inventory limitations associated with radioactive risk and nuclear safety.

1. GENERAL MOTIVATION AND INTRODUCTION

The projections and estimations for the worldwide energy needs in the next decades establish a 60% higher global energy consumption as a result of the energetic demands and population increase projections [1, 2]. At the present time, the majority of the primary energy consumed in the planet (around 80%, [2]) comes from the non-renewable fossil fuels. These energetic resources are not distributed homogeneously over the world and their availability depends strongly on the economic and political international situation. The technologically advanced consumer society is exploiting the existent deposits at fast rates, thus threatening to phase out the fossil fuel reserves in an unknown time period. In this sense, the general consensus between industry leaders and analysts establishes that world oil production will peak between 2010 and 2030 (for a more extensive discussion about the timing of peak oil see the references [3] and [4]). The problematic related with the excessive consumption of another raw materials (i.e. strategic minerals, metals and compounds) is completely equivalent. The global worldwide economy is based on a continuous growing that in pure logical terms is undoubtedly unsustainable in the medium-long term[1]. The direct consequence for the fossil fuels exploitation is that the exhaustion of the conventional reserves will determine a higher cost for the extraction of alternative ones as franking oil prospections. Furthermore, the generation of electricity with fossil fuels entails the massive generation of CO_2 leading to the concerning problematic effects of the global warming and associated climate change. Among the alternative (and CO_2 free) solutions to satisfy the growing energy demand, the green (renewable) energy sources (solar, hydroelectric, wind power, biomass and waste…) seems to offer an interesting and reliable option but nowadays their exploitation is significantly more expensive. Additionally, they are non-homogeneously time and geo-localized over the world, supposing another important limitation for the implantation of these sources at global scale as baseline energy

---

[1] The continuous growing necessary in advanced capitalist economies is based on overconsumption of energy and the overexploitation of the nature. This *modus operandi* does not seem the most reasonable strategy in a planet with finite resources. Opposed ideas and theories as de-growth and post-growth have emerged. They rightly claim that this capitalist system is the root of long term environmental issues and social inequalities. Moreover, they argue, from the logical point of view, that this economical growing could produce the collapse of the global system, when conventional resources run out. To go deeper into these subjects, authors as Serge Latouche and Carlos Taibo are especially recommendable.

solution. On the other hand, the nuclear fission energy presents high conversion efficiency without producing greenhouse gases. Its use, however, generates high activity radiological wastes that will remain dangerous during time periods over thousands of years. Furthermore, the great risk associated to the possibility of nuclear accidents, as happened in Chernobyl (Ukraine, 1986) or most recently in Fukushima (Japan, 2011), poses serious doubts about the applicability of the fission energy as suitable solution. In this scenario, the development of the nuclear fusion energy is seen as a hopeful option. It can potentially produce huge amounts of energy using raw materials inexhaustible in the human time scale, being the power generation theoretically free of nuclear wastes[2] and inherently safe, with no danger of runaway reaction or explosions unlike fission energy.

---

[2] Fusion energy that, in principle, would employ the deuterium-tritium reaction needs to solve the problem of tritium (radioactive hydrogen isotope) accumulation in the reactor. This drawback constitutes a main challenge studied as an important Plasma-Surface Interaction topic.

1.1. FUSION ENERGY GENERALITIES

The nuclear fusion of hydrogen isotopes is a process in which light atomic nuclei are combined to create a heavier one. It is the stellar energy source, as well as the origin of all the energetic resources of the Earth (that directly or indirectly comes from the Sun energy input), excepting the radioactive isotopes whose origin lays in the supernovae explosions, the geothermal energy (gravitational and radioactive origin) and the tidal energy that comes from the gravitational effects of the Earth-Moon system induced in the oceans. Additionally, the nuclear fusion process carried out in the stars is the responsible to produce the whole set of the chemistry elements (excluding hydrogen, helium and some lithium that were created in the early universe after the Big-Bang, as well as the transuranic artificial elements) present in the observable universe. The nuclear fusion reactions generate tremendous amounts of energy as a part of the mass of the precursor constituents is transformed directly into energy accordingly to the famous Einstein's mass-energy equivalence equation. According to the conservation law, this fact implies that the original mass of the individual protons and neutrons is bigger compared to the mass of the formed nucleus, being this difference related with the binding energy that holds the nucleus together. For the fusion of the nuclei, it is necessary that they collide with sufficient kinetic energy to overcome the electrostatic repulsion of the positively charged nuclei. At these energetic levels, the matter is in plasma state that is basically a gaseous mixture of negatively charged electrons and positively charged ions. It constitutes the fourth state of matter that supposes the 99% of the observable particles (visible matter) in the universe. In a laboratory, the most favourable fusion reaction scheme (whose interaction cross section presents the highest value at the current feasible energy levels that available technology supplies, figure 1.1) is the deuterium-tritium (D-T) reaction represented as:

$$ {}_{1}^{2}D + {}_{1}^{3}T \rightarrow {}_{2}^{4}He + \mathrm{n} + 17.6\ \mathrm{MeV}. \quad (1.1) $$

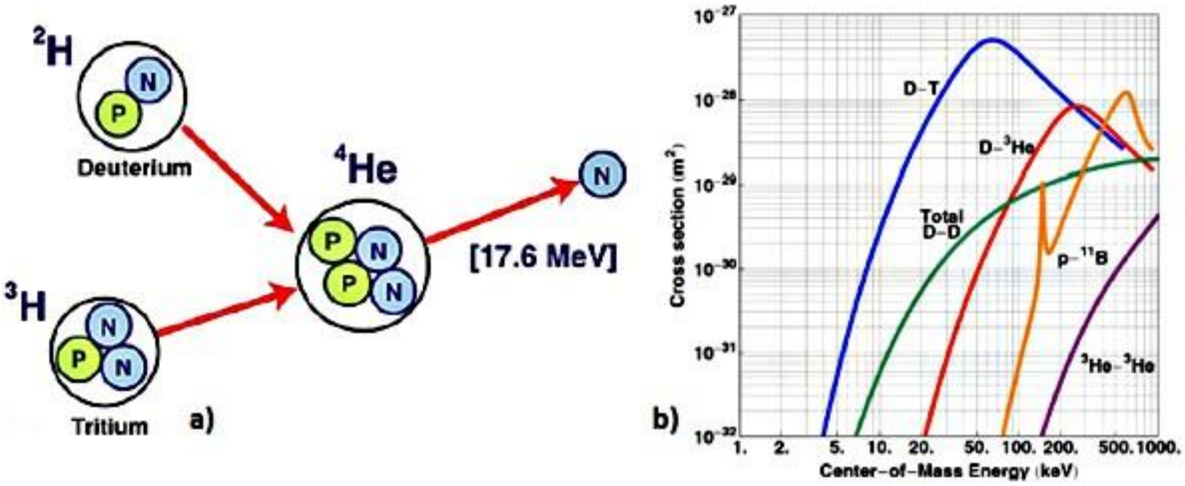

Figure 1.1. a) Scheme of the D-T reaction, b) Collision cross sections (σ) for fusion reactions depending on the energy of the particles

The products of this reaction are a helium nucleus (fast α particle) and a neutron. As a result, the energy output is 17.6 MeV per D-T pair, being the 80% of this energy transported by the neutrons and the rest by the helium ashes. The necessary deuterium can be extracted from the ocean water (1 L of water contains approximately 30 mg of deuterium) and tritium can be generated *in situ* through lithium bombardment with the previous fusion neutron in the so-called in-vessel breeder blanket elements:

$${}^{6}_{3}Li + n \rightarrow {}^{4}_{2}He\,(2.05\text{ MeV}) + {}^{3}_{1}T\ (2.73\text{ MeV}). \quad (1.2)$$

$${}^{7}_{3}Li + n \rightarrow {}^{4}_{2}He\ (2.05\text{ MeV}) + {}^{3}_{1}T\ (2.73\text{ MeV}) + \text{n}\ (-2.47\text{ MeV}). \quad (1.3)$$

It is estimated that the reserves of these element are abundant enough to produce fusion energy to the current world population (assuming energy consumption equals to the existing one) during 35 million of years [5]. About the availability of enough suitable materials (as structural and special superconducting components for the magnets) to develop the construction of fusion reactors as a large scale power source during numerous millennia, the related limitations does not seem to be important [6]. To reproduce this process in our planet in a controlled device, this burning D-T plasma must be confined and heated at temperatures around 200 million of Celsius degrees (~20 keV)[3]. In general a

---

[3] In plasma physics, temperatures are expressed generally in electron volts (eV). 1 eV corresponds approximately to 11600 K.

broader requirement is necessary to produce efficiently these fusion reactions. They are included in the so-called Lawson triple product criterion that takes into account the temperature (T_i), density (n_i) and energy confinement time (τ_E) of the D-T ionic species in the plasma:

$$n_i \cdot T_i \cdot \tau_E > 5 \cdot 10^{21} \ (\mathrm{keV \cdot s \cdot m^{-3}}). \quad (3.4)$$

This expression means that the D-T nuclei must be confined during enough time at a density and temperature level that assure the ignition plasma conditions simplified in the triple product result. It implies temperatures around 20 keV, densities in the range of 10^{20} m^{-3} and confinement times of few seconds. Moreover to obtain a net power gain, the energy produced by the thermonuclear fusion reactions must be higher compared to the necessary energy to heat the plasma until its ignition. This is frequently represented using the Q factor ($Q=P_{fusion}/P_{heating}$) that needs to be higher than the unity to maintain the fusion process extracting net power from it. To reproduce these experimental conditions that lead to achieve the nuclear fusion in a controlled device the plasma needs a confinement method. The gravity force is providing this requirement inside the stars as the Sun by using their enormous gravitational effect that is converted into kinetic pressure thus compressing the hydrogen nuclei until they are fused. However, on Earth laboratories this effect cannot be reproduced. Although another confinement methods are being investigated (inertial confinement that uses enormous laser irradiation onto a D-T small capsules to induce its compression and thermonuclear ignition) the most promising (and wider studied) system is the magnetic confinement that utilizes strong magnetic fields to direct the charged particles along the closed field lines of a toroidal geometry magnetic trap according to the Lorentz law.

1.2. MAGNETICALLY CONFINED FUSION DEVICES: TOKAMAK AND STELLARATOR

To create the magnetic structure where the plasma must be confined, a set of toroidal coils are used producing the primary toroidal magnetic field that would force the particles to follow the circular resultant field lines. However, this simple structure is not enough to confine efficiently the particles as this configuration is not stable due to magnetic drift effects that tend to separate the charged particles (this separation is different for ions and electrons as they have different charge and mass that determine the opposite direction and velocity of the drift) from the field lines trajectories, thus destroying the confinement. To solve this problem the magnetically generated structure must avoid the magnetic drift effects by twisting the field lines helicoidally, thus forcing to the charged particles to follow the closed field lines around the generated torus, forming nested flux surfaces. There are three ways to twist the magnetic field [7] and generate the *rotational transform* that assure the stability of the magnetic configuration with the particles turning in both poloidal and toroidal directions. This parameter ($\iota=n/m$) is defined as the number of poloidal transits (n) per single toroidal transit (m) of a field line. The inverse parameter, denominated the safety factor ($q=1/\iota$) is more frequently used in Tokamaks while the rotational transform is utilized in the Stellarator literature. These methods define the two main types of magnetic fusion devices (Tokamak and Stellarator) and their geometrical (and concomitant physics) differences. Briefly they consist on:

- Driving a toroidal current in the plasma (induced by a transformer placed in the toroidal center of the machine). This net current creates a poloidal magnetic field that compensates the magnetic drift. This method is used in Tokamaks
- Elongating the flux surfaces and making them rotate poloidally as one moves around the torus. Stellarators employ this strategy where all the necessary magnetic fields are created by means of external coils
- Making the magnetic axis non planar (eight shaped). This method was only used by the first prototypes of stellarators that were built in Princeton

The first method is the simplest one and was conceptually developed in the USRR by I.E. Tamm and A.D. Sakharov [8] in the 1950s. It implies axisymmetric devices with a two dimensional (2D) plasma structure that makes it easier to build, although the necessary current drive determines an impossible steady state operation. The second method was firstly proposed in the USA by L. Spitzer (1951) [9]. This kind of devices does not need the presence of the plasma itself to configure a closed magnetic surface structure. Indeed, they have rotational transform and thus magnetic surfaces even in vacuum, when the magnetic fields are generated by the external coils prior to the gas injection in the beginning of the discharge. Stellarators do not own axisymmetry as their plasmas have a more complicated three dimensional (3D) structure, but the non-existence of (large) toroidal plasma current leads to great advantages in terms of stability making these devices able to operate in steady state. In addition, Stellarators are free from disruptions. These dramatic events collapse the plasma due to the accumulation of magnetohydrodynamic (MHD) instabilities related with the high toroidal current present in tokamaks. Other advantages of stellarators are: macroscopic stability and possible higher density operation (as it is not limited by the Greenwald density limit). As key disadvantages it is important to mention that the higher neoclassical particle transport in stellarators produces significant confinement degradation. Nonetheless, the main handicap of stellarators is the technical complexity of their design and construction, especially for the necessary (and very complex) set of coils that create the magnetic 3D structure. An illustration of both devices, showing the trajectories of charged particles along the field lines, the magnetic surface geometry and their plasma shape is shown in figure 1.2.

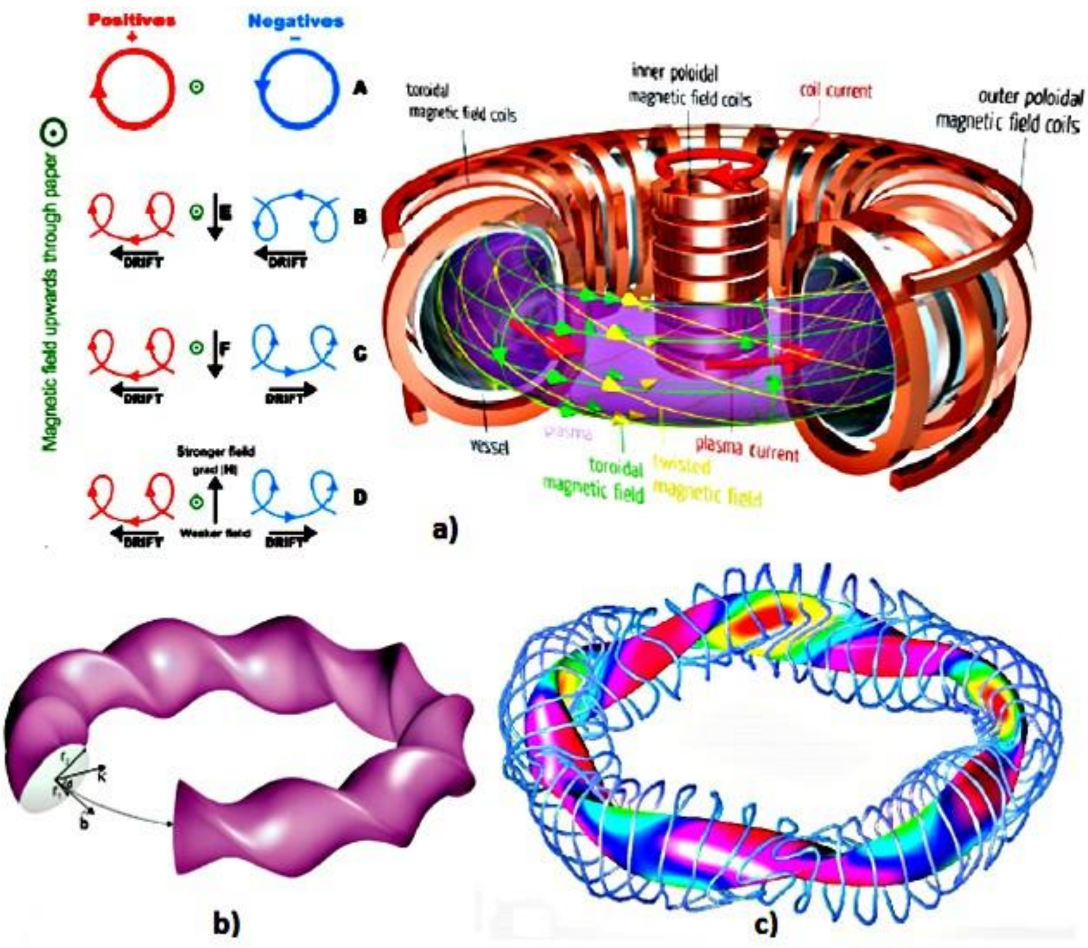

Figure 1.2. Schematic view of tokamak and stellarator: a) Magnetic structure, particle motion and geometry in a tokamak, b) Flux surface geometry of LHD stellarator (Japan), c) Coil (modular) design and plasma geometry of W7-X stellarator (Germany)

Currently, tokamaks are the most studied and developed machines due to the simplicity of its construction, being the chosen option for ITER (International Thermonuclear Experimental Reactor). This device (at present under construction in Cadarache, France) is an international project whose associated partners are the UE, USA, Japan, Russia, China, South Korea and India. The ITER operation is projected to start in 2025 and it will be devoted to demonstrate that the fusion energy process is viable with D-T equimolar fueling, producing power with high Q gain (factor 5-10) at plasma ignition conditions during pulses of around 400 seconds of duration. The cost of the project is estimated around 15 billion €. The preliminary designs for the first demonstration fusion power plant

(DEMO) projected by 2035 are also based in the tokamak concept. At this point it is important to note that due to the further tokamak research, the stellarator plasma physics is less well understood. Despite this situation, the flexibility and intrinsic stability of stellarators converts them a serious candidate for future magnetic fusion reactors. Moreover, the more recent advances in the last years in terms of MHD stability and neoclassical confinement as well as the promising results in reducing turbulence (improving the confinement) makes the stellarator option even more attractive.

1.3 PLASMA SURFACE INTERACTION IN MAGNETIC FUSION DEVICES. PLASMA FACING MATERIALS AND COMPONENTS

The plasma physics is a wide scientific discipline that includes the study of a different variety of plasmas e.g., astrophysical, technological, fusion-like plasmas among others. Respect to the fusion energy, its main task is to deepen in the understanding and characterization of magnetically confined high temperature plasmas, being its study the basis for the developing of thermonuclear fusion as future energy source. However, in addition to plasma behavior, the successful operation of a fusion device strongly depends on the unavoidable interaction of the hot plasma with the materials that compose the vacuum vessel that contains it. This matter denominated as Plasma Surface Interaction (PSI) is essential for the reactor performance. The power produced in the fusion reactions must be extracted out of the reactor to feed the associated steam electric power station. As the fusion neutrons do not follow the magnetic field lines, they will be expected to overpass the plasma region, reaching the lithium breeding blanket panels and being used for the *in situ* generation of the tritium fuel. Hence, their energy would be absorbed by these elements. However, the hot alpha particles (helium ashes) generated in the process, are positively charged and due to the imperfect confinement they escape from the plasma impacting on the surrounding materials (Plasma Facing Materials, PFMs). In equilibrium (steady state) the energy flow from the plasma to the surrounding material surfaces is equal to the heating from α particles and the additional heating (necessary to produce the plasma ignition). In ITER this energy flow will be in the order of 200 MW while for DEMO these requirements will be at least a factor 5-10 higher. This power dissipation must be managed by the reactor components that face the plasma directly. These constituents, chosen to build the elements that constitute the first barrier against the burning plasma (being known as Plasma Facing Components, PFCs), must carry out the predominant role on the heat and particle exhaust (helium ashes, D-T extinguished fuel particles and impurities) removal, being this action completely mandatory for a continuous operation of a fusion reactor. Hence the PSI constitutes a key field for the development of nuclear fusion energy and technologically feasible power plants. The main functions [10] of the plasma facing components are: 1) to shape the plasma edge, 2) to absorb particle and heat fluxes from the plasma and thus protect the other components from it and 3) to allow for the neutralization of plasma ions by impact on the material surface so that the recycled neutral particle can be pumped out of the machine (helium ash and impurity exhaust). Consequently, the plasma facing components have to absorb the large heat fluxes from incident plasma particles and radiation, as well as a little fraction of the neutron energy that causes volumetric heating. This required heat exhaust is more difficult to achieve because its radial extension is only in the order of centimeters around the plasma edge, thus generating higher heat load densities on rather small areas on the target plates compared to the total area of the inner surface of the vacuum vessel. Nevertheless, the heat load density on plasma wetted areas can be reduced by up to a factor 6 by geometrical considerations in targets, even then, in ITER the area for the heat exchange (6-8 m^2) [11] is only a very small fraction compared to the total vacuum vessel area. In addition to the power exhaust handling, the unavoidable material damage (due to erosion with plasma particles via sputtering mechanisms and excessive heat loads that produces melting or sublimation on the PFCs) and the hydrogen isotope retention (tritium inventory) constitutes the most challenging issues from the PSI research area to be solved for the development of magnetic fusion energy.

1.3.1. Plasma Facing Materials as sinks for confined plasma. Limiter and Divertor configurations

The PFCs are the first surface that the plasma reaches after escaping from the magnetic field confinement. For this reason these materials are also essential to handle the plasma shape, acting as sinks for the exhaust plasma. An excessive interaction of the plasma with the limiting surfaces is translated in impurity production and accumulation that will cool down the plasma, thus deteriorating its performance. To control this interaction and establish a suitable plasma-surface interface, specific targets need to assume the role of intersecting the most of the charged particles escaping the plasma. In this way, a net transport of charged particles is established from the plasma (source) and these target surfaces (sinks). When this transport regime is achieved, an intermediate layer between the confined plasma and the surface is formed, that receives the name of Scrape Off Layer (SOL). It contains the most of the exhaust charged particles and a concomitant neutral fraction generated via surface neutralization/recombination of the ions transported from the main plasma. Normally this layer has a thickness in the order of few millimeters. Inside the confined plasma, two main different parts can be differenced: the plasma core where the magnetic field lines are closed and almost all the particles are very hot and ionized and the plasma edge where the magnetic field lines are intercepted by the surrounding surfaces, creating a much colder and weakly ionized plasma with the presence of an important proportion of neutrals and simple hydrogenic molecules. The SOL can be considered as the last part of the plasma edge, being the interphase between it and the limiting surface sinks. The targets that are used as plasma sinks must carry out the heat and particle exhaust task as well as minimizing the impurity generation that leads to contaminate the plasma. Hence its selection and design is of paramount importance in any fusion reactor scheme. Two different main configurations have been developed to carry out this action:

- **Limiter configuration:** in consist on a PFC block situated close to the main vessel wall that is in direct contact (conforming in this way a sacrifice element that concentrates the PSI on it) with the plasma magnetic surface called as the last closed flux surface (LCFS also known as separatrix). Beyond this region the SOL is extended where the particles reaches the limiter surface and are neutralized. To produce a good plasma operation the limiter surface must assure a suitable power loading and its impurity generation has to be compatible with an appropriated plasma performance. The most used limiter elements are configured in the toroidal direction placed as a surrounding belt around the toroidal vacuum vessel. Consequently the interaction of the limiter with the plasma is sufficiently large to define the limits of the plasma and avoid the volumetric interaction of the plasma with the vessel walls. This strong localized interaction can suppose at the same time an important drawback as it could lead to excessive heat flux to the limiter target, thus producing material melting, cracking or disintegration with the deleterious effect associated to the plasma impurity contamination and the degradation of the confinement and performance. A scheme of the limiter configuration is illustrated in figure 1.3.

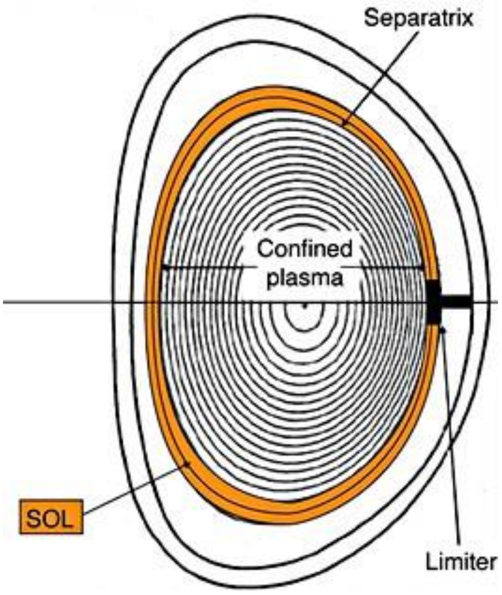

Figure 1.3. Limiter configuration in a toroidal device

- **Divertor configuration:** this concept arose as a technological solution to minimize the problem of limiters to handle power loads to surfaces by direct contact with the plasma. Divertors are directly located intersecting the plasma in the separatrix, immediately below the X point (where the poloidal magnetic field tends to zero) position (see figure 1.4 for illustrative details). The divertor SOL is characterized by open magnetic field lines towards the surface. The charged particles escaping the plasma core are directed to this zone where recombination takes place, thus producing the increase in the neutral particle density. With this configuration, the pressure at the divertor chamber can be high enough to allow reducing the energy of the incoming plasma particles by means of screening thus decreasing the induced damage to the plasma facing component. The divertor is also the zone where the most of the power and particle exhaust fluxes are directed and concentrated to be removed. The first wall (FW) constitutes the rest of the vacuum vessel area that contains the plasma. Regarding to heat exhaust, its function is to absorb most of the radiation from the plasma. Since the first wall is usually located at some distance from the last closed magnetic flux surface, the power fluxes to this component are rather small compared to the divertor, with typical values of the order of 0.1 to 1 MW/m^2 for the case of ITER while the divertor region concentrates a much higher nominal power load in the order of 10 MW/m^2. In Tokamaks, this divertor configuration is achieved by using an extra set of coils concentric with the plasma current that are placed on the toroidal base of the machine, while in Stellarators present a so-called divertor magnetic island structure produced by the magnetic configuration itself. Nowadays, the most important and advanced tokamaks (ASDEX Upgrade, JET, NSTX…) and stellarators (LHD, W-7X) use this configuration to achieve higher confinement regimes (H-Mode) and more relevant conditions closer to future ITER or reactor operation. For ITER, tungsten will be used to construct the divertor tiles PFCs, being this element the basis of the preliminary designs for the DEMO divertor.

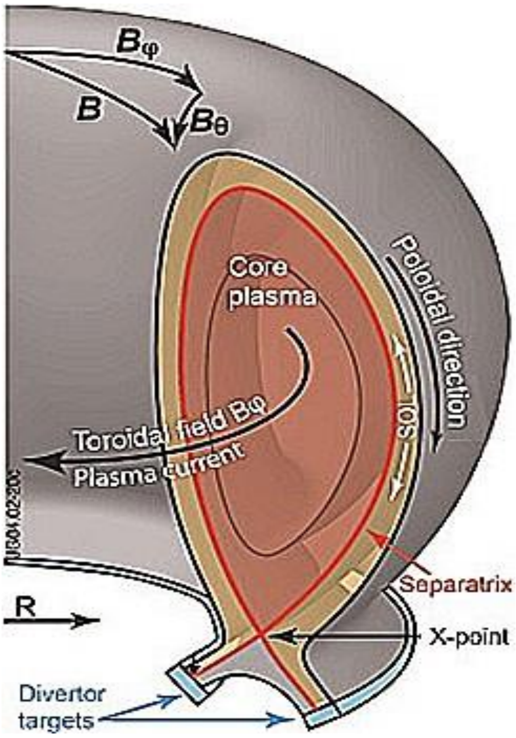

Figure 1.4. Section of toroidal plasma, showing the divertor location and the magnetic structure related elements

1.4. POWER EXHAUST IN FUSION DEVICES. PLASMA DETACHMENT AND ELM MITIGATION FOR PFM PROTECTION

In fusion devices the nominal power loading from plasma to the PFCs must be evacuated for the reactor vessel for an efficient operation. As was inferred previously, this task will be mostly carried out by the divertor elements. The continuous impact of energetic plasma particles escaping from confinement to the PFMs will produce material damage on them. Hence the erosion of surface material has to be limited to ensure a sufficient lifetime on the PFCs. For ITER, the maximum nominal heat load is considered to be around 10 MWm^{-2} [12]. For DEMO like devices the longer pulsed operation and the associated higher neutron fluence needs to be taken into account. These particularities will constrain the power loading limits [13]. Assuming a DEMO reactor prototype with tungsten as PFM for the divertor, with a maximum allowed erosion thickness of 5 mm in two operational years [14], the erosion thickness rate would correspond to 0.08 nm/s and the concomitant net erosion rate would be around $5 \cdot 10^{18}$ $m^{-2}s^{-1}$. To operate the fusion device below these erosion limits the divertor temperature in front of the tungsten targets should be below 5 eV with maximum heat flux of 5 MWm^{-2} in order to maintain the material damage below the tolerable levels. During ITER operation, high levels of divertor radiation will be mandatory to achieve the volumetric power dissipation without thermal overload on the PFMs. This high radiation levels are obtained in a plasma configuration with respect to the limiting PFC surface that is known as *plasma detachment.*

1.4.1. Plasma detachment

It is defined as “a plasma state with large parallel gradients in total plasma pressure that leads to a concomitant reduction in the plasma power and ion fluxes to the surrounding surfaces” [15]. To induce the plasma divertor detachment for ITER and present day tokamaks (ASDEX Upgrade, JET) the injection of nitrogen in the plasma edge-divertor region is frequently used due to the radiative characteristics of the nitrogen molecule, although the injection of neon is also considered. For DEMO, other noble gases (argon and krypton) are considered for the divertor detachment and/or simultaneous improvement in the core radiation. The primary factor to evaluate the power reaching the

PFCs surface is the parallel heat flux across the separatrix (q_{sep}). This parameter can be approximated to follow this expression:

$$q_{sep} \sim P_{sep}/(R \cdot \lambda_q \cdot B_p/B_t), \quad (3.5)$$

where P_{sep} is the total power in the separatrix, R is the major radius of the machine, B_p and B_t are the poloidal and toroidal magnetic fields and λ_q is the power decay length in the SOL. This parameter is crucial for the estimation of the peak heat load deposited on the divertor target. It measures the exponential decay of the parallel heat flux along the plasma edge. This exponential profile is also affected by a perpendicular heat transport that diffuses the power load along the edge region. To take into account this particularity, a Gaussian width parameter (S) is introduced. This parameter represents the competition between parallel and perpendicular heat transport in the divertor volume. The deconvolution of the exponential profile (λ_q) with the Gaussian width S leads to the definition of the integral power decay width λ_{int}, a parameter frequently used to relate the peak heat load on the divertor target to power deposited on the materials [16]. This resulting parameter can be considered as the combination of an exponential profile for the parallel heat flux with its radial diffusion into the SOL from the X point. The relation between exponential and integral decay lengths is found to be linear [17]:

$$\lambda_{int} = \lambda_q + 1.64S, \quad (3.6)$$

being S the broadening parameter that describes the Gaussian shaped power spreading. Predictions or estimations of this parameter are essential to evaluate their effects and implications for the design of future fusion devices (i.e. ITER and DEMO). Recent analyzes have concluded that the λ_q parameter does not scale with machine size (R), having this conclusion a big impact in future machines as the expected power exhaust will be significantly increased. For plasma conditions with no detachment, the extrapolations and models predict a λ_q value around 1 mm for ITER that would imply a value for λ_{int} of 2.6 mm approximately [16]. Predictions from ITER experts group assessed values of λ_q=5 mm for an acceptable plasma performance with tolerable material damage and suitable power dissipation [18]. To get higher values for these parameters, thus reducing the peak heat loads to the PFMs, the achievement of plasma detachment seems essential.

The reduction of global and transient heat loads to the PFCs is of paramount importance for the successful development of the magnetic fusion energy. In DEMO like reactor devices, it is estimated that a high fraction (75-95%) of the power (f_{rad}) must be dissipated volumetrically by divertor and core radiation, protecting in this way the material elements from direct thermal loads. Moreover, large transient loads need to be suppressed, using methods to develop mitigation that will be tested in ITER to be applied in DEMO. Advanced divertor configurations with alternative geometries (as Super-X [19] and Snowflake [20] concepts) together with innovative liquid metal PFCs [21] and vapor box divertor [22-24] emergent technological solutions can also help in this challenging task. The main method to achieve this global radiation level is inducing the divertor detachment and the protection of the first wall heat fluxes by means of plasma core radiation (induced by high Z noble gas seeding, Ar, Kr…). As was introduced previously, the main extrapolations for the parallel heat flux values for DEMO are based on the consideration of traditional scaling: $q_{sep} \propto P_{sep}/R$, (alternative divertor scaling based on the Greenwald density limit has been recently proposed and can be found in the following reference [25]). Furthermore the power at the separatrix scales faster than $\propto R$, and the power decay length does not follow the P_{sep}/R scaling [13] being found as independent with the power and machine size. These factors would determine a more problematic power exhaust handling in the DEMO divertor. On the other hand the plasma core power exhaust in future larger devices, that will be dissipated through the first wall surfaces, seems less difficult as the radiated power (P_{rad}) scales with R^{-2}. Recent experiments suggest that the use of argon to radiate the core power is more suitable than krypton for the case of DEMO operation with its specific requirements [14]. Hence the biggest problem related with the heat removal is clearly located on the divertor. To avoid the destruction of these elements the ITER and DEMO divertors will operate under at least partial detachment (PD) conditions. This divertor regime is defined as a significant reduction of heat flux and pressure along the magnetic lines between the divertor surfaces for a width in the order of few power decay lengths in the SOL [26]. It is characterized by an increase in the divertor (X-point) and core radiation that decreases the parallel heat flux through the separatrix and the pressure (about a factor 3 lower). The plasma boundary structure in high confined regimes presents enhanced profiles for density, pressure and temperature in a narrow edge plasma region known as *pedestal*. Its confinement and stability is strongly affected by the plasma detachment. During partial detachment the inner divertor area presents a more prominent detachment compared to the outer divertor that is considered as the critical location in terms of parallel heat flux. The transition regime towards full detachment is called pronounced detachment and supposes a pedestal and core density rise (20-40%) implying a confinement degradation (around 20% lower), an enhanced radiation (in zones adjacent to the divertor X point), the reduction of the periodic transient heat loads size and the increase in their frequency. In the full detachment window both the inner and outer divertor targets are completely detached and the divertor radiation enters widely in the X-point, even reaching the confined plasma region. These high radiation zones can induce an edge plasma phenomenon known as MARFE [27] (Multifaceted Asymmetric Radiation From the Edge). It is characterized by a greatly increased radiation, density fluctuations, and decreased temperature in a relatively small volume at the inner major radius edge of the plasma. The MARFE formation can drive a transition in the global plasma confinement of the device from high confinement modes (H-mode) to low confinement modes (L-mode) with the subsequent deleterious effect in the reactor performance, even producing sudden destabilization with abrupt collapse of the plasma (disruptions). Consequently the plasma detachment must be limited to the regions exposed to the highest power flux (inner divertor, strike points and baffles) while the remainder SOL and outer divertor should be maintained attached. The evolution of the divertor radiated power (bolometric measurements) and its displacement into the X-point and plasma edge region can be visualized in the figure 1.5 for the cases of initial partial detachment and pronounced (transition to full) detachment in an ASDEX Upgrade discharge. Excellent reviews about these experiments with partial and complete detachment can be found in [26, 28].

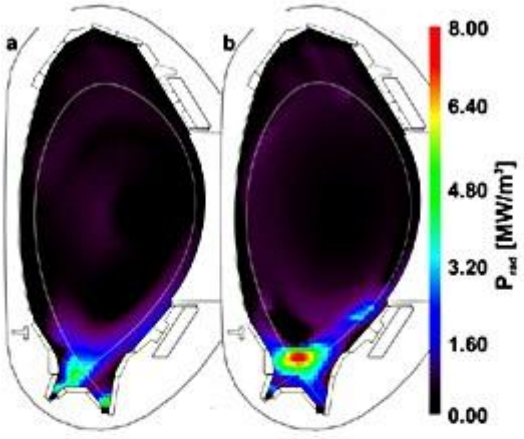

Figure 1.5. Radiated power distribution (bolometric estimations) in the AUG divertor (adapted from [27]). a) partial detachment, b) transition to full detachment

The divertor detachment in H-mode discharges can be mainly produced in three ways:

- Low Z impurity seeding in the divertor region. The most utilized seeding specie is molecular nitrogen (N_2) although noble gases, as neon (Ne), are also studied. In addition to enhance the divertor radiation, the nitrogen seeding also causes an improvement of the confinement [29]. This injection has made possible to re-establish the confinement level in the JET ITER like wall experiment (JET-ILW operating with tungsten divertor and beryllium first wall) [30] achieved in the previous JET-C (with carbon walls) operation that was favored by the intrinsic radiation of the carbon impurities on the divertor.
- Increase of the divertor neutral pressure due to deuterium puffing. This method produces a higher radiation in the region with more pronounced confinement degradation (unlike N_2 seeding). It allows achieving partial (low) detachment but it is insufficient to obtain complete detached conditions.
- Reducing the separatrix power flux (P_{sep}) by core radiator impurity (Ar, Kr) seeding. It supports the detachment state by radiation causing less confinement degradation. However the excessive high Z impurity accumulation in the plasma core can produce fuel dilution that will reduce the fusion reaction rates and consequently the generated power. To avoid this issue the concentration of such impurities must be carefully controlled, thus maintaining it below maximum limits approximately considered as [12]: n_{Ar}/n_e=0.3 and n_{Kr}/n_e=0.1.

The best plasma performance is experimentally obtained by combining a high neutral deuterium divertor pressure together with low Z (N_2) impurity seeding. The stationary control of divertor detachment is complicated as it depends on global parameters changes on the core and divertor at the same time, being its configuration reversible. In general, nitrogen seeding is used for divertor radiation enhancement and confinement improvement associated with the presence of nitrogen. The involving mechanism that determines this confinement recovery is not fully understood but among the factors that could explain it, the following ones have been postulated [29]:

- Possible enhancement of plasma core temperature gradients. Up to date, it has not been observed in JET-C or JET-ILW
- Ion dilution in the pedestal region. This mechanism would also need hollow edge impurity profiles (with strong peaking of Z_{eff}, parameter that measures the effective charge of the impurities). This assumption is not confirmed by experimental observations in AUG or JET
- The effect of nitrogen seeding and deuterium fueling in the pedestal structure and pressure due to changes in its width and gradient. Although both gas injections have shown to widen the pressure pedestal, only the nitrogen seeding is traduced in a confinement improvement. The D_2 fueling also produces a strongly reduced pressure gradient at the same time as the pedestal widens, hence not resulting in a net confinement benefit

The detachment caused by an increase of the deuterium divertor neutral pressure is associated with considerable confinement degradation and the core radiation by Ar or Kr seeding uses to reduce the stored plasma energy by a 10% factor. The combination of these three mechanisms presents a flexible scenario with a wide operational detachment window for DEMO. Further future research will determine the optimum operational characteristics of divertor detachment for fusion reactors.

1.4.2. Transient heat and particle loads. Edge Localized Modes (ELMs)

In addition to the heat loads during normal plasma operation (steady state), the plasma facing components (PFCs) can be subjected to short episodes with very high power deposition during off-normal operation events (up to tens of GW/m^2) and transients (around 1 GW/m^2) of the plasma. Among them, the plasma disruptions deposit the thermal energy content stored in the plasma into the PFCs in a short time around 0.1 to few milliseconds. The deposited energy in ITER can be up to 20 MJ/m^2 and for DEMO more severe disruptions are expected. Eventually, the electrons can be accelerated to high energies (up to 300 MeV), impacting powerfully on the PFCs. These runaway electrons can also cause extremely high local energy deposition (100 MJ/m^2). Finally another transient phenomena know as vertical displacement events (VDE) can deposit a large fraction of the plasma energy in relatively small wall areas after the sudden destabilization of the plasma position in the vertical direction, leading to energy loads around 50-60 MJ/m^2 in time scales in the order of milliseconds.

Furthermore, local and periodic events in the plasma boundary are produced by disruptive MHD instabilities during the relaxation of transport barriers placed on the SOL in regimes with enhanced global energy confinement thus producing transient loads of energy and particles impinging the PFCs. Due to the extremely high energetic level (~GW/m^2) of these relaxation periodic processes events and their periodic frequency, they would originate important damage on the wall components. These periodic events named as Edge Localized Modes, (ELMs) imply rapid removal of energy and particles in the plasma edge, reducing its temperature and density. They are produced in the so-called H mode (high confinement) [31], regime that has been achieved in diverted Tokamaks and Stellarators. It is characterized by an increase in the particle confinement -factor 2- that results in improved density and temperature in the plasma core. Furthermore in this regime, the formation of transport barriers in the plasma boundary leads to a global confinement enhancement that supposes a desirable option for the plasma operation in future fusion reactors, hence the H-mode plasma operation constitutes the baseline scenario to produce net fusion power in future magnetic devices. The origin of the ELMs is found in the MHD stability of the plasma edge in the H-mode, specifically on the instability of “peeling” (current driven) and “ballooning” (pressure driven) modes with high toroidal mode number (n) at the edge [32], being the development of the “peeling-ballooning” model essential to explain a suitable mechanism for ELMs. The ELMs studied for the ITER operation in H-mode can be classified in two main groups depending on their frequency and stored energy:

- Type I ELMs: They present a low frequency (0.5-2 Hz), but large stored energy (extrapolation to ITER gives values around 8-20 MJ), resulting in power densities ~1GW/m^2 that will be deposited onto the materials in a timescale of milliseconds. This power load is high enough to ablate solid metallic surfaces even for the case of the elements with the best physical and thermo-mechanical properties (tungsten, molybdenum…). Their management (with mandatory mitigation or their ideal suppression) is therefore an important issue among the global manipulation of power exhaust for ITER and DEMO. The material erosion limitations imply that no type I ELMS will be, in principle, allowed for the DEMO operation.

- Type III ELMs: They appear in regimes with dissipated heat flux (via impurity radiation in the plasma edge). Their levels of stored energy are much lower (0.3 MJ expected in ITER) with frequencies in the range of 0.1-2 kHz. Hence, the expected heat loads are not as worrying as in the case of type I ELM's, but the associated impurity levels during these transients can produce confinement losses that would affect the operation of the device.

For next step fusion devices operation, the ELMs loading control is essential to have plasma operation with acceptable PFMs degradation that assures long enough lifetime for the components compatible with an economically viable operation. Plasma detachment has an important effect on ELMs normally increasing their frequency, thus reducing the size and the stored energy that they liberate. The nitrogen seeding on the divertor and Ar/Kr core seeding change the nature of the ELMs. The main effect is the increasing of the frequency to more benign conditions. For type III ELMs, effective detachment can increase the frequency from 0.1 kHz to 2 kHz. Moreover, operation of fusion devices in high confinement modes with suppression of ELMs, has been achieved by using lithium coatings on the plasma facing components. The phenomenon was observed in NSTX spherical tokamak [33]. The lithium wall coatings applied onto the PFCs suppressed the ELMs with additional positive effects as an increase in the energy confinement time (50% higher), enhanced radiated power and lower Dα emission related with reduced deuterium recycling from the walls. Ionic (T_i) and electron (T_e) temperature profiles were significantly increased without important changes in the pedestal density profile. These changes are also associated with lower recycling and core fueling from the lithium wall coatings. ELM free operation modes have been also achieved in several devices. These regimes include the so-called I confinement mode [34] that combines an energy H mode confinement with a particle L mode (without ELMs) edge confinement and the ELM free H mode [35] among others. Additionally the ELM size and their energy load can be managed by using ELM pacing or triggering techniques that consist basically in the injection of small granules or pellets in the plasma edge thus cooling down and relaxing the external edge and SOL turbulent structures that determines the ELM ejection. Injection of deuterium and lithium pellets has been used for this purpose in several devices [36, 37].

1.5. MATERIAL DAMAGE AND EROSION INDUCED IN PFCS

Burning plasmas at ignition conditions will be extremely hot with temperatures even higher than the Sun core. In ITER the core temperature for the confined particles is expected to reach 150 million Celsius degrees. This thermal energy is transported into the plasma and finally needs to be handled by the plasma facing materials. The momentum transfer between plasma projectiles and wall materials determines the damage induced on the PFC, thus producing its gradual deterioration. Hence, the enormous and continuous energetic loads damage irreversibly the components inducing erosion, evaporation, melting and/or sublimation of the materials, limiting the lifetime of the walls and threating their destruction [38]. Furthermore, the eroded materials will be deposited along the inner vessel wall. Although this co-deposition can reduce the net erosion, on the other hand it will lead to the creation of mixed layers with different nature compared to the original material. Additionally, the deposition of this layer together with fuel wastes (D-T ashes) produces co-deposited zones that can potentially retain large amounts of tritium with the subsequent problems related with radioactivity inventory limitations and radioactive safety. Dust formation during these erosion events and its accumulation inside the vacuum chamber is also a serious concern, as they can produce explosive episodes. Estimations for ITER based on extrapolations from present devices and modeling indicate that the number of pulses before reaching maximum allowed erosion in the components could be unacceptably low for an economically viable operation. This erosion rate will obviously depend on the chosen material. Several types of mechanisms are involved in t is process, thus determining different erosion and damage in fusion devices components that are described below.

1.5.1. Physical sputtering

The basic phenomenon that causes physical sputtering is based on the momentum transference of incoming projectiles from plasma (energetic ions or neutrals) to the surface atoms of the PFM via collisions. Consequently, the surface atoms can be detached if the energy transfer is larger than the surface binding energy of the material target. At first, the momentum transfer direction would determine the implantation or backscattering of the projectile and the surface atom movement into deeper positions, but subsequent collisions during its penetration on the material layer activate the “collision cascade regime” that leads to opposite momentum transfer, thus directing the surface atoms out of the PFM. The basic process is represented in figure 1.6.

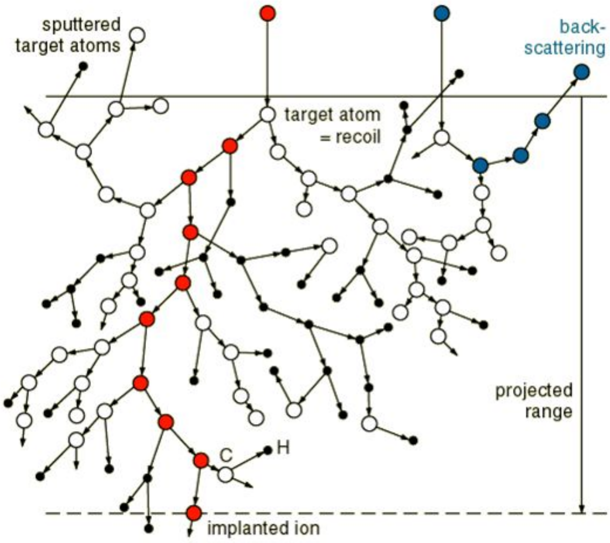

Figure 1.6. Physical sputtering mechanism with collision cascade

Due to the nature of the process, there is a threshold energy level for the incoming particles to produce physical sputtering. If the energy of the projectile is low enough compared to the binding energy of the surface, thus the particle can be simply stuck on the surface, especially in the case of polar molecules where dipole electrostatic forces between them and the surface are established. Sticking of impurities is important in the case of water residual molecules and other harmful compounds that can be generated in the plasma surface processes as for example ammonia molecules during the N_2 seeding used for heat load mitigation into the PFCs and confinement restoring. This specific problem will be approached in the chapter 2.4. The net erosion by physical sputtering is characterized with a yield that represents the erosion probability and is defined as:

$$Y_{Phys,Sput} = \Gamma_{ero} / \Gamma_{in}, \quad (1.7)$$

where Γ_{ero} represents the flux (number) of eroded particles form the substrate and Γ_{in} the total flux of incident particles. This yield depends on the impact energy of the projectiles, the angular properties of the collision and the atomic mass relation between projectile and target materials. Solid materials has not a significant dependence with temperature for physical sputtering, but on the contrary, liquid surfaces can be strongly dependent on it, showing enhanced yields for increasing temperatures.

The physics of the process determines that for projectile energies below the threshold, the sputtering yield will be zero. Threshold energies are specific for each material and also depend on the nature (mass) of the projectile. Normally this energy is higher for high Z materials (Z is the atomic number) compared to low Z elements. For impact energies above the threshold, the yields increase until reaching a maximum value for a given energy. Beyond this maximum, a further increase in the energy leads to a decrease in the physical sputtering yield as a result of the deeper penetration and implantation of the projectiles into the target, resulting in a lower transference of energy to the surface atoms that consequently cannot be sputtered. In fusion confined plasmas the energy of the projectiles depends on the charge (q) of the specie, the electron (T_e) and the ion (T_i) temperature, following this approximated relationship:

$$E_{projectile} \sim 3q \cdot T_e + 2 \cdot T_i \ . \ (1.8)$$

Additionally, the relationship between the masses of the projectile and the target atoms also affect to the process. The momentum transfer (and hence the yield) are maximum when both species are identical (self-sputtering). This is the case of facing materials that are bombarded by previously eroded atoms of its surface, that come back to the target with high energetic content after being accelerated in the plasma sheath. Furthermore, in the case of mixed materials (co-deposited areas, steel or other alloy components) the different elements of the hybrid surface will be differentially sputtered as a result of their different atomic masses. This process is known as preferential sputtering, a phenomenon which can be important as it leads to macroscopic changes in the surface composition thus altering the original properties of the material and the response to the plasma-surface interplay. The angle of incidence (α, defined as the velocity vector angle respect to the normal surface vector) affect to the sputtering, producing primary yields for normal incidence (α=0º) that are higher when this angle is increased, until reaching a maximum yield. After overpassing this maximum the yields strongly decreases, as the angle is approximated to grazing incidence (α=90º). The angular distribution of sputtered particles for normal incidence shows an approximate cosine distribution.

1.5.2. Chemical sputtering

It involves thermal particles (with much lower energy content) that interacts with the surface atoms producing chemical reactions thus producing different (frequently volatile) compounds that later can be easily eroded. The process is limited to specific combinations of impinging and target atoms. The traditional cases are the erosion of carbon and beryllium by hydrogen isotopes bombardment. Chemical erosion of carbon has been widely studied as it causes strong hydrogenic retention in the form of hydrocarbon co-deposits eroded from such carbon based components. In fact, this enhanced retention has motivated the rejection of carbon based materials for the divertor PFCs in ITER. The process is mainly influenced by the bombardment energy and surface temperature of the substrate. It implies a complex chemistry that leads to changes on the carbon surface bonds thus producing hydrocarbon molecules (C_xH_y) that are eroded from the surface and finally deposited in other zones of the inner vessel. The energy threshold for the process (~2 eV) is much lower compared to physical sputtering (in the order of few tens of eV). The effect of the surface temperature is the same compared to any chemical reaction thus increasing the yields as the temperature becomes higher, although normally, it presents a maximum. Beyond a certain temperature the erosion reactions are less favored as a result of the competition with another chemical processes or the formation of passivating layers on the surface. Additionally, very high ionic fluxes to the material have a positive effect as they decreased the chemical erosion yields as has been shown in experiments with large fluxes in linear plasma devices. In lithium based materials, its low vapor pressure causes its evaporation and deposition in adjacent components. The process is favored when lithium is used in liquid state and the temperature of the surrounding surfaces is below the melting point of lithium. Under these conditions, the potential interaction of such layers with fuel species (tritium) can suppose a serious drawback.

1.5.3. Other erosion mechanisms

Among them, the most important are related with sudden melting, sublimation or evaporation due to heat loads, and deformations induced by trapping of gaseous species on the surfaces that lead to blister formation. The high power exhaust fluxes and more frequently the transients can induce these thermal processes that will result in the net erosion of the affected zone. Type I ELMs and dramatic events as disruptions are the most problematic phenomena related with this damage. The problem is more accentuated for lighter materials (carbon) or light metals (beryllium, lithium) compared to refractory ones as molybdenum or tungsten that have much higher melting and evaporation points. The induced melting can produce liquid layers on the surface. If they are too big it could lead to material or droplet ejection. In the case of metallic elements, the fast movement of this surface can interact with the machine magnetic field thus producing net Lorentz forces that could result in improved ejection. For the case of blistering, these material aggregates are formed by the retention of light particles as hydrogen or helium on metal surfaces as tungsten. It can lead to enhanced erosion due to grain ejection or sudden decompression that produces evaporation or splashing of such structures into the plasma. The effect of alpha particles (He ashes) present in a reactor environment is especially important in this case as the formation of blisters and other "fuzzy tungsten" microstructures has been experimentally observed in helium containing energetic plasmas.

1.5.4. Neutron irradiation induced effects

In a fusion reactor, very energetic (14 MeV) neutrons will be produced in the D-T reactions. The neutron flux to the wall of ITER will be of the order of $5{\cdot}10^{17}$ $m^{-2}s^{-1}$ [40], being the fluxes and the accumulated fluence at least one order of magnitude higher for DEMO. This problematic implies reactor materials with low activation for neutrons. The energy of the neutrons is supposed to be transformed in the blanket modules in thermal energy for the power cycle and tritium for the reactor fueling. However, as the neutrons do not follow the magnetic field lines they will be released from the plasma core and can reach the in-vessel surfaces without an oriented direction. It will produce the volumetric heating by radiation damage and the chemical modification of the components, thus leading to the change and deterioration of the material properties.

The principal effects of the neutron loading are the structural induced damage and nuclear transmutation, being these processes directly inter-related. Nuclear transmutation depends on the material nature and the present impurities. High Z materials present a higher transmutation rate compared to lighter ones (although light elements such as beryllium and boron also exhibit intense interaction with neutrons) . The structural damage consists on the displacement of the atoms that forms the surface, thus originating volumetric damage (dislocations, vacancies…). It is measured in displacement per atoms (dpa) units. Deep changes in the volume configuration of the substrate will induce dramatic changes in the thermo-physical properties of the material. Probably the most concerning problem is related with ductile-brittle transition. If the microstructure of the component is sufficiently altered, the surface layer can be transformed to brittle even at relatively low temperatures. It would determine enhanced net erosions due to physical sputtering and thermal loading that can suppose finally the destruction of the component.

Up to date the experimental research in neutron irradiation effects at fusion reactor scale is very limited as relevant neutron sources with energetic content close to the neutrons produced in D-T reactions are not available. In this sense, the International Fusion Materials Irradiation Facility (IFMIF-EVEDA project), is an accelerator-based neutron source that will use Li reactions to generate a flux of neutrons with a broad peak energy of 14 MeV equivalent to the conditions of the D-T reactions in a fusion power plant. The project (jointly developed by the EU and Japan) will proportionate a suitable facility to study this critical issue.

1.6. RADIOACTIVITY ISSUES RELATED WITH TRITIUM ACCUMULATION. HYDROGENIC RETENTION IN PFM

The operation with D-T fuel in a fusion reactor will irreparably conduct to radioactivity issues as the efficiency for the thermonuclear reactions is not complete (burn efficiency of a few percent is estimated) and consequently an important part of tritium can be retained in the PFCs. Hence, the management of tritium inventory is a central issue for the development of magnetic fusion energy. In this sense, the choice of suitable materials is a key factor for the in-vessel tritium retention. The allowable tritium inventory in a fusion reactor is limited for three reasons [41]. Firstly, tritium is a source of direct radioactivity. This hydrogen isotope is characterized by an unstable nucleus with two neutrons and one proton. The nucleus decay by means of low energy beta (electron, β^-) emission with a Half-life of $t_{1/2}$=12.32 years:

$$ {}^{3}_{1}T\ (\beta^-)\rightarrow {}^{3}_{2}He + 18.59\ \text{keV}\ . \quad (1.9)$$

The activity of 1 g of tritium is approximately 9652 Ci ($3.571\cdot10^{14}$ Bq). Consequently, the administrative limits for the in-vessel tritium accumulation have been recently determined as 700 g of total moveable inventory. If this level is overcome, the clean-up of the vessel must be performed to reduce the radioactivity. Hence, the tritium inventory must be controlled to ensure that any tritium released in the case of potential accidents is below the risk levels that would determine the evacuation of the inhabited vicinities. Second, tritium is a very expensive element that does not exist in appreciable and useful amounts in the nature. Its optimal utilization is mandatory for an economical operation. Finally, the breeding of tritium by transmutation of lithium in the blanket modules is affected by a low supply margin that limits the total tritium that can be lost from the fuel cycle to approximately the 0.1 % of the fuelled tritium. It supposes that the amount of tritium circulating through the plasma is more than an order of magnitude higher compared to the tritium burnt in the nuclear reactions. Experience with tritium operation was gained during D-T campaigns in TFTR (acronym of Tokamak Fusion Test Reactor, a device placed in Princeton and whose total dismantling was completed in 2002) and JET tokamaks that produced fusion power. TFTR produced peaks of 10 MW of fusion power with Q factor values ~0.5 while JET developed maximum power of 16 MW with slightly higher Q~0.6-

0.7, being both machines below the breakeven critical conditions (Q=1). For the D-T JET experiment (1998) the primary retention of global fuelled tritium was around 40% of the injected amount (35 g). This amount was decreased by means of cleaning discharges up to 17%. This retention was mainly produced in carbon co-deposits with average H/C atomic ratios in the range of 0.7-1 in the areas located at the inner divertor corner. In TFTR, after cleaning procedures, the long term tritium retention after campaigns was around the 16% of the supplied fuel, mostly concentrated in the plasma facing component gaps. These tritium experiments revealed the importance of this radioactive issue and showed that tritium retention in PFMs is mainly placed and defined in two different locations associated with different uptake mechanisms. The first one implies the direct implantation of ions and neutrals on the surfaces and its diffusion into the bulk material. The second one is produced by the formation of co-deposits of hydrogen with eroded wall materials. As tritium is extremely expensive, and its management requires a very strict safety procedure, the experimental work to investigate this issue is performed with hydrogen and deuterium isotopes, being these results extrapolated to the case of tritium.

1.6.1. Implantation and bulk retention

The continuous bombardment of energetic hydrogen isotope ions from the plasma to the machine walls can lead to the direct implantation of tritium particles on the surface. Diffusion and recombination characteristics of the PFM respect to these isotopes, as well as the characteristics and concentration of trapping sites in the material layers will determine the tritium storage by this mechanism. When the material is bombarded, a dynamic retention regime is achieved, in a depth of few nm that saturates with time and fluency. A key factor to measure the evolution of the retention is the *recycling coefficient* that measures the ratio of hydrogenic particles coming back from surfaces after its bombardment. For refractory materials (for example W) this coefficient is generally quite high (0.9 or larger), thus implying a low fraction of associated retention (generally below 0.1 atomic %). However other materials (especially lithium) with strong chemical affinity with hydrogen can bond these atoms producing much lower levels of global recycling that supposes a net higher retention (theoretically up to 1/1 atomic ratio for lithium with hydride formation although this extreme limit has never been observed in any fusion device experiment). The second step in this process is the diffusion of trapped hydrogen isotopes to the material bulk depending on the affinity and kinetic parameters (diffusivity) of the process for the different materials, being trapped as solute or at the material defects (boundary irregular grains, defects, dislocations…). This subsequent process can increase the retention on W up to the 10% atomic fraction for example in a depth range of few nanometers. Moreover, on this element, the depth range of diffused hydrogen is in the order of several microns. It affects to the potential removal of tritium that will be much more complicated in deeper zones of the solid W PFCs.

1.6.2. Co-deposition

The chemical interaction of hydrogen isotopes with materials as carbon or beryllium leads to the production of mixed material layers that are called co-deposits. Atomic ratio of such co-deposits is frequently up to 0.5 or even higher for the case of carbon based components. The involved mechanism to produce these compounds is different for carbon and beryllium. In the case of carbon, the low energy bombardment with hydrogen isotopes leads to the chemical erosion of the surfaces, producing volatile hydrocarbons that interact with the plasma edge, being transported to other vessel areas (material migration). These molecules are finally absorbed on a PFCs surfaces (sticking). These co-deposits are affected by erosion with the plasma particles and re-deposition. If re-deposition rate is higher than erosion, the created film grows up forming amorphous layers known as a:C-H co-deposits. The potential massive formation of such films and their high associated fuel retention has motivated that finally carbon will not be used in any PFC of the ITER vessel. However for beryllium the mechanism to produce co-deposits does not produce the direct reaction between hydrogen and Be atoms. It has been observed for example in JET that beryllium first wall tiles are eroded by plasma. After this, the eroded Be particles are transported until the W divertor being deposited there. On this zone the hydrogenic flux is much bigger thus leading to the formation of mixed H/Be-W layers. It is expected that tritium retention will be dominated in ITER by the formation of such co-deposits. The hydrogenic content of such layers is expected to decrease with wall temperature (~250ºC-300ºC) in ITER active operation, but even in this case global contents around up to 0.1 H/Be ratio are expected. Additionally, they present a challenging removal as has been experimentally found. Beryllium co-deposits will need very long thermal outgassing methods to release significant amounts of tritium at low temperatures (300ºC-400ºC). For efficient and fast enough thermal desorption, much higher temperatures (even 800ºC) will be necessary. Other methods as laser localized heating will require the partial or total melting of beryllium (melting point is 1287ºC) to remove efficiently the hydrogenic content. Co-deposition of hydrogen isotopes mixed with Li layers can also occur if lithium is used as PFC. The low melting point of lithium can determine migration of such atoms around the in-vessel surfaces thus producing its deposition together with hydrogenic atoms. This topic is widely approached in the chapter 3.3 of the thesis.

1.6.3. Effect of impurities in the hydrogenic retention in PFMs

The presence of active residual (oxygen) and seeded (N_2) impurities in the reactor environment have a strong influence in the concomitant retention of the material surfaces. For beryllium, low oxygen contents lead to oxidation of its surface that could increase significantly the associated hydrogenic retention. In the case of tungsten the frequently necessary operation with nitrogen impurity seeding on the divertor lead to N implantation and formation of tungsten nitrides. The formation of these compounds has a positive effect in terms of reduced erosion but also leads to an increase in the deuterium uptake. Furthermore, interaction of nitrogen and hydrogen isotopes on the metallic tungsten walls of the divertor leads to the formation of ammonia molecules as the W surface acts as a catalyst for the reaction. This process has been observed in N_2 seeded discharges in relevant tokamaks (JET, ASDEX Upgrade). The formation of tritiated ammonia could represent additional problems due to the chemical characteristics of this compound that present corrosive behavior in contact with metals. This problematic can also suppose a challenge for the cryompumps used for the efficient removal of gas exhaust and for the subsequent steel pumping lines of the gas processing plant as the ammonia molecules are polar and can be highly stuck at room temperatures on the metallic surfaces. This topic is widely treated in the following chapter of this thesis as the study of potential ammonia formation on ITER relevant PFCs supposes an important part of this research work. For lithium, when it is mixed with carbon in the PFM surfaces, the contamination of their surfaces with oxygen leads to increased fuel retention. It has been hypothesized that the formation of Li-O-D complexes on the exposed surfaces could be the key mechanism that determines his enhanced retention. On the contrary, the presence of oxygen in these Li-D layers decreases the thermal requirements to induce the hydrogenic outgassing.

1.6.4. Hydrogenic cleaning and recovery strategies

An extensive variety of techniques have been developed aiming to reduce the tritium inventory up to acceptable values. In brief, they can be classified in three main groups depending on the used treatment: gas chemistry methods, thermal bulk heating procedures (long term baking and thermal desorption spectroscopy, TDS) and surface localized photonic cleaning (laser desorption and ablation). There are other special techniques that involve the use of glow discharge conditioning discharges, controlled disruptions, divertor manipulation (strike point sweeping and displacements) and gamma irradiation based methods, however, the objectives and techniques used in the experimental research of this thesis are not related with them. In this work laser techniques and TDS have been studied for hydrogenic removal and measurements in W, Li and their hybrid combinations. These methods together with the previously developed gas methods for carbon components are briefly described:

- **Gas chemistry methods:** developed mostly to hydrogenic removal in carbon co-deposits, via inhibition of the hydrocarbon formation during its chemical erosion. They include the injection of scavenger compounds (nitrogen, ammonia, NO_2) that preclude the formation of such hydrocarbon layers due to the formation of very stable HCN based compounds and molecules. These methods have shown a very good efficiency and potential application for the tritium inventory control and cleaning in carbon based materials.
- **Thermal desorption spectroscopy:** It is based on the thermal release of volatile compounds (hydrogen isotopes) when a bulk material is progressively heated up. When the temperature reaches the level where the trapping hydrogen sites are unstable, the release of hydrogenic molecules takes place. There are different kind of trapping sites for hydrogen depending on the chemical state of the trapped hydrogen, its energetic characteristics and the surface material that retains the hydrogenic atoms. If the temperature of the substrate is increased beyond the limits for stability of all these hydrogen trappings, thus the total release of the hydrogenic uptake is, in principle possible, implying only a carefully controlled heating of the PFC. The necessary temperature to achieve total desorption in the PFMs depends on the nature of the support element and their combinations with hydrogen. For W it is assumed that for bulk hydrogen retention, a temperature increase higher than

1000ºC that probably implies the annealing of the bulk material will be necessary for total hydrogenic desorption, thus presenting this application as especially challenging and difficult. Recent experiments have shown that for Be, thick co-deposits will need very long (several weeks) thermal treatments at moderate temperature (300ºC-400ºC). For faster and realistic hydrogenic removal in these layers, thermal treatments with heating temperatures around 800ºC, or even higher, with a duration that could be extended up to hours, would be necessary (treatment that appears expensive and unfeasible). In contrast, for lithium, although its potential hydrogen uptake in liquid state at low temperatures (200ºC-300ºC) is considerably higher compared to Be and W, beyond 400ºC the retention drops significantly and several laboratory experiments have demonstrated the total desorption of hydrogen isotopes below 600ºC without showing problems related with lithium hydride stability.

- **Laser based removal methods:** these techniques are localized in the region of interest, thus avoiding potential deleterious effect in the whole elements of the PFC. They suppose an interesting alternative for the cleaning of thick localized co-deposits, however the complexity of operation is much larger compared to the previous methods and they require the use of technological/engineering devices and tools (lasers, robotic arms remotely controlled to move the laser irradiation around the in-vessel areas, etc) and have limitations in their applicability as they need to be generally applied during reactor shutdowns. These techniques can be classified depending on the energy density that they use and the concomitant effects on the surface that they induce. Laser Induced Desorption Spectroscopy (LIDS) uses a moderate power density (~150 kW/cm^2) to induce thermal desorption avoiding the sudden ejection of the PFM. Laser Induced Ablation Spectroscopy (LIAS) produces the disintegration of the co-deposit by means of an ablation mechanism that implies the ejection of the particles in time scales around milliseconds. It utilizes a higher power density (around a few GW/cm^2) laser able to remove the hydrogenic layers without damage the substrate PFC.

1.7. PLASMA FACING MATERIALS FOR THE FIRST WALL AND DIVERTOR COMPONENTS

Once explained the power/particle exhaust, the erosion and tritium retention needs for PFCs, we approach the selection of materials that are investigated for the processing of such components. To fabricate these components, a different variety of elements have been studied. In general the critical requirements for the plasma facing materials can be summarized in the following ones:

- Compatibility with plasma operation, in other words, the capability of the material to reduce plasma contamination, guaranteeing plasma discharges with low impurity levels (water, oxygen and other gaseous residual molecules present in the vacuum chamber). The chemical affinity of the elements with oxygen and water play an important role in this issue as it defines the capability of the material to get these deleterious particles. Their transport along the SOL can induce undesirable effects in the plasma performance and generate dust clusters or aggregates that will be accumulated in the reactor. The transient burst of dust particles can also cause disruptive problems in the plasma.
- Resistance against physical and chemical sputtering. This issue is directly related with the net erosion rate allowed for solid components as they will be progressively damaged and disintegrated during the plasma operation. The lifetime of the PFCs will depend strongly on their capabilities to minimize this problematic.
- Good thermo-physical properties and thermal shock resistance. These characteristics are essential to develop an acceptable management of the extremely high power loads expected in a fusion reactor.
- Acceptable retention of hydrogen isotopes (potential tritium accumulation in the reactor) to avoid radioactive issues and potential safety limitations. Real possibilities of tritium removal from such materials in an integrated processing plant are also mandatory.
- Low activation by neutron bombardment with small transmutation yields for the chosen materials is desirable. In addition, resistant materials to volumetric

displacement damage are needed to ensure a reasonable lifetime for the components.

Unfortunately, a suitable material that gathers all these requirements is not available, having the studied materials advantages in certain characteristics and drawbacks in other ones. They can be classified in two main groups depending on their atomic number (Z):

- **High Z materials:** mainly tungsten (W), molybdenum and different varieties of stainless steel among others. They are employed for their excellent mechanical (very low sputtering yields) and thermal properties (highly elevated melting points), very important to limit and control the thermal damage and material erosion. Respect to their behavior against the particle exhaust issues, they present low impurity (hydrogenic and helium) retention values, although its removal can represent an important issue related with radioactive safety protocols (tritium storage and management). Furthermore, its degradation (erosion mechanisms) leads to heavy impurity influx to the plasma whose concentration cools down the plasma by successive ionizations. This accumulative problematic can destabilize the plasma until its disruption. For this reason, very low high Z impurity fractions ($\sim 10^{-5}$ in the case of W) are allowed in the plasma core.
- **Low Z materials:** The most investigated elements are carbon, beryllium and lithium. They present low charged, moderate impurity production (from sputtering and evaporation) under plasma erosion. Naturally, compared with high Z impurities, fusion plasmas can tolerate larger amounts of low Z impurities as they radiate a considerable lower amount of stored energy to be fully ionized. Its employment is translated into a significant plasma performance in those devices (JET, NSTX, TJ-II…) where they have been used as plasma facing materials due to the benefit of light impurity presence compared to heavy ones. Resistance to erosion and fuel retention characteristics are generally the weaknesses of these materials.

1.7.1. Tungsten

Tungsten has been selected as the material for the ITER divertor and up to date the DEMO designs are based on it. It has an extremely high (the biggest one among all chemical elements) melting point and good thermal conductivity. It makes that from the thermo-physical point of view tungsten is the most attractive candidate to manage heat fluxes. Additionally as a refractory metal it presents very low sputtering and global erosion yields under plasma bombardment. However, together with the negative aspects that are common to other high Z materials, its ductile-brittle transition temperature (DBTT), when it is bombarded by neutrons (from 0.1 dpa neutron load values), is located around 700ºC-800ºC. This particularity represents a potential drawback as during plasma operation in D-T reactors, the overheating of W can induce important damage in the components. Finally this element presents a strong tendency to recrystallize at high temperatures high below the melting point and compared to other low Z material candidates it is significantly activated during neutron irradiation [39].

1.7.2. Carbon

It was during several years an important candidate to be used in ITER. Its thermo-physical capabilities are excellent with thermal conductivities equal or even better compared to copper. Moreover the intrinsic divertor radiation of carbon PFCs during plasma operation showed effects in the plasma confinement as this mechanism contributed to dissipate part of the exhaust power load to the materials, thus reducing the contamination of the plasma that is much more important when high Z materials are used in these high heat flux regions. However its chemical erosion rate due to the associated chemical sputtering with hydrogen isotopes leads to excessive co-deposition of mixed and amorphous hydrogenated carbon (a-C:H) co-deposits in the chamber walls. This process has a strong implication in the associated tritium inventory for a hypothetic fusion reactor with carbon walls. After decades of intense investigation the use of carbon based components has been rejected for this reason.

1.7.3. Beryllium

It is the elected material for the ITER first wall. Due to its affinity with oxygen, it is an excellent getter for this molecule, thus allowing plasma operation with low impurity levels. It also exhibits better erosion resistance compared to carbon and hence a concomitant reduced material transport during plasma operation. As the heat fluxes to the first wall are not so critical, the use of refractory metals is not mandatory, thus making its election for this area preferred due to its very low associated plasma contamination. Its main drawback is the very toxic and carcinogenic nature, (especially in the form of dust), that result in a highly strict and rigorous handling. Only a small number of laboratories worldwide have the adequate and safe installations to work with beryllium.

1.7.4. Lithium and other liquid metals

Lithium is the lightest element suitable to be used as PFM. It is also a good oxygen and nitrogen getter and its interaction with hydrogen isotopes leads to a reduced fuel recycling to the SOL, producing associated and spectacular benefits to the plasma performance. This fact has potentiated its use as wall conditioning element with the purpose of improving the quality of the discharges in a wide number of fusion devices worldwide [42]. Additionally, it also presents very good thermal properties. Among their applications, the use of liquid lithium elements deserves attention as liquid surfaces can be in principle renewable, thus free of irreversible degradation due to erosion mechanisms or neutron irradiation. This potential application results very attractive as it could enlarge the lifetime of such components. In this way, the associated cost of PFCs replacement in a reactor would be diminished, thus enabling its economy viability. Lithium is a connatural element for fusion as its use inside the vacuum vessel (breeder blanket modules) is mandatory to produce the tritium for the reactor fueling. The main disadvantage of lithium is related with its high reactive chemical nature that leads to a strong hydrogenic (potentially tritium) retention, as well as, potential hazards associated with the use and manage of lithium whose chemical characteristics could produce explosive episodes and deflagrations during its accidental contact with water or atmospheric gases. For the case of the liquid metal components option, other candidates have been studied as tin and gallium. In the case of tin, its low hydrogenic retention and low vapor pressure levels make it a very promising option, especially in the form of Sn-Li alloy. It can be considered as a hybrid high-low Z material that combines the good properties of both elements (low fuel retention of tin and good compatibility and improved plasma performance of lithium PFCs). However, its hybrid nature could represent a problem as preferential sputtering (more favored to lithium erosion) would alter the bulk properties of such elements, precluding the benefits of lithium content and thus needing Li surface replenishment to restore the Li-Sn proportion on the exposed layers. Investigations with pure tin elements are currently underway and also show good perspectives for its potential future use in fusion reactors. For the case of gallium, its problems with the material compatibility and corrosion issues when it is mixed with other materials have precluded its potential use.

1.7.5. Comparative scheme among the different elements considered as PFM options

Table 1.1 shows a comparison among the previously examined materials with their main advantages and drawbacks associated with the main PFM challenges related with fusion reactors.

Element	Atomic number, Z	Main advantages	Important drawbacks
Tungsten	74	-Highest melting point -Very good mechanical and refractory properties -Low sputtering yields and good behavior against net erosion -Reduced hydrogenic retention	-Very limited plasma core concentration (10^{-5}) -Potential surface melting and concomitant enhanced deterioration of PFCs -Blistering under He bombardment and neutron activation -High ductile to brittle transition -Complicated thermal tritium removal for long term (in bulk) fuel uptake
Carbon	6	-Good thermal and mechanical properties -Beneficial intrinsic radiation of eroded carbon particles for the confinement and core contamination -Low activation with neutrons of carbon based materials -Wide experience in its use and employment as PFM	-High chemical sputtering (erosion) with H isotopes -Co-deposition with hydrogen isotopes determines an excessive fuel retention -Neutron loading leads to important deterioration of mechanical, thermal and electrical properties -Large dust production as a result of its high net erosion

Beryllium	4	-Very light impurities compatible with great plasma performance -Oxygen getter that determines low plasma contamination levels -Moderated hydrogenic retention -Potential formation of protective re-deposited layers -Low activation with neutrons	-Melting point is relatively low, thus its melting can produce potential deleterious effects -Physical sputtering yields are important with concomitant limited lifetime of the PFCs due to net erosion -Co-deposition with H and W. Slow and difficult (very high temperature) thermal removal of H,D,T -High toxicity and hazardous handling
Lithium	3	-Extremely good thermal properties. Able to manage heat loads up to 50 MW/m^2 -Lightest element and lowest Z impurities -Exceptional compatibility with fusion plasmas -Excellent impurity (N_2, O_2…) getter -Formation of vapor clouds and ionic non coronal radiation in the plasma edge protects the PFCs surfaces against thermal loads and transients -Hydrogen retention highly reduced for T>400ºC -Total hydrogenic desorption at T<600ºC -Liquid state avoid the problems with disintegration and material permanent damage	-High hydrogen isotope retention up to 1:1 atomic ratio (hydride) at moderate temperatures -Excessive evaporation at high temperatures (>550ºC). Problems with limited core accumulation -MHD instabilities could lead to splashing of liquid surfaces by thermoelectric driven forces -Compatibility and corrosion issues with another elements (steels) at high temperatures -Very reactive element. Fire and deflagration risks with potential leaks and water/oxygen interaction -Liquid surface components needs the development of appropriated technology not available at present

Tin-Lithium alloy	50-3	-It also presents the good benefits of lithium element as the lithium atoms are segregated into surface -Very low hydrogenic retention associated to tin	-Preferential sputtering could destroy the benefits of the lithium presence in the superficial layer -The concomitant exposition of tin can lead to plasma contamination incompatible with commercial reactor operation

Table 1.1. Comparative scheme among the different Plasma Facing Materials

1.8. OBJECTIVES OF THIS THESIS RESPECT THE PFM SELECTION FOR FUSION REACTORS

The main goal of this thesis is to study the potential application of tungsten and liquid lithium as PFMs that can solve the challenging operation of a fusion reactor emphasizing the potential problems related with the tritiated ammonia generation associated with N_2 seeding plasma operation (developed to achieve divertor detachment for PFCs power loading protection) and the hydrogenic (tritium) retention of tungsten-liquid lithium mixed components.

Related to the ammonia formation in chapter 2, the parametric influence of surface temperature and the nitrogen content in the plasma, the basic plasma-surface chemistry and the influence of the reactor residence time and helium presence in the plasma has been studied by approximating the tokamak divertor environment with Glow Discharge plasmas. Additionally, the sticking of the ammonia molecules on stainless steel surfaces has also been quantified, focusing in the influence of the surface temperature in the process.

In chapter 3, the lithium research has been oriented to approach the effects of W-Li mixing processes (implantation and co-deposition) in the hydrogenic retention with especial emphasis in the temperature dependence of such co-deposition. Moreover the PFM solution for a future reactor combining liquid lithium components in the highest power load zones (divertor) and W in the first wall is proposed. Its viability (in terms of associated fuel co-deposition) is widely investigated showing that potential operation with hot (>400ºC) first W wall and liquid lithium divertor is feasible from the point of view of adequate tritium retention in the first wall compared to official inventory limitations.

Finally, chapter 4 contains a summary with the main conclusions extracted from the experimental works. The corresponding projections and considerations for fusion reactors are also addressed.

2. AMMONIA FORMATION AND RETENTION ON PLASMA FACING MATERIALS

The use of carbon based materials as a suitable election in fusion devices has been ruled out due to the associated enhanced hydrogen retention and co-deposition [43]. Consequently, the PFM design for ITER was modified, finally employing tungsten (W) elements on the divertor tiles and beryllium (Be) ones on the first wall. This change in the PFMs has reduced the long term hydrogen retention by one order of magnitude [44] on the ILW JET operation in comparison with the previous operation (JET-C) based on carbon PFCs. On the contrary the intrinsic radiation of carbon impurities in the divertor region has been suppressed. Recent experiments in magnetic fusion devices, as ASDEX Upgrade with full tungsten wall, and the ILW-JET, with beryllium first wall and tungsten divertor, have shown problems related with plasma core contamination due to sputtering of W atoms, thus claiming for strict divertor electron temperature control under high Z PFC scenarios [44]. This temperature should be low enough to keep ion energies below the sputtering threshold [45]. Hence, methods to control the divertor temperature, reducing the heat load to the PFM and the concomitant erosion and plasma contamination are necessary. Among them, radiative cooling by gas impurity seeding is the most commonly used, being nowadays essential to achieve good plasma performance. Several impurities have been tested so far (N_2 argon, neon…), being nitrogen the impurity that presents the most favourable effects, as its injection induces the plasma divertor detachment with an additional confinement improvement [14, 26, 27, 46]. Its extended use in the JET-ILW operation has re-established the confinement level achieved in JET-C operation [30]. For this reason nitrogen is commonly considered as the best candidate for radiator in the future ITER impurity seeded plasma operation (although as we will see in this chapter, for its application in ITER, it is absolutely indispensable to solve the problems related with the ammonia formation). Nevertheless, its use with tungsten and beryllium as PFMs and the interaction between hydrogen isotopes and nitrogen on these metallic surfaces leads to a significant ammonia production in relevant nuclear fusion devices. [47-50]. The associated tritium retention in ITER, the strong affinity of ammonia with water and the sticking of ammonia on the vacuum system ducts represent an important issues whose study has been given priority for the future ITER operation [51, 52]. The presence of tritiated ammonia would be quite problematic as it would increase the tritium inventory and its reactivity. Moreover, the deleterious effects of ammonia corrosion on the vacuum system, cryopump panels and pumping lines would limit the ITER operational cycle due to the more frequent necessary regeneration of the cryopump modules that collect the exhaust gas from the discharges and the safety issues related with the tritium inventory. Formation of partially deuterated ammonia has already been reported in ASDEX Upgrade tokamak (AUG) [47, 50] (showing that approximately an eight percent of the injected N_2 was converted into ammonia) and evidence of similar ammonia production has also been obtained in ILW-JET operation [48-50]. The last studies and observations show that with a 5% conversion of nitrogen gas into ammonia, 0.2 grams of associated tritium could be trapped per pulse in the future ITER D-T operation [51].

The formation of ammonia takes place on the surface of the metallic wall materials that surround the plasma in a heterogeneous catalysis process. The general chemistry utilized in the industrial ammonia production is well known since the beginning of the 20th century. In 1913 the Haber-Bosch process was developed in the BASF chemical company. It is the basis for the industrial production of ammonia whose main utility is to be a very important raw material for the fertilizers industry. The use of such fertilizers has enabled the improvement in the agricultural production that has been essential to cover the needs of the growing human population during the 20th century[4]. The Haber-Bosch process is based on the gas-phase reaction between N_2 and H_2 under high pressure (≥200 atm) and high temperature conditions (500ºC). The thermodynamic establishes that the equilibrium is favored to the ammonia formation at high pressures and as the reaction is exothermic, an increasing temperature will produce the opposite effect, displacing the equilibrium to the decomposition of ammonia to nitrogen and hydrogen. However the process at low temperatures is very slow and for this reason the industrial production is carried out at 500ºC with a net conversion degree to ammonia around 50%. The global process can be schematically represented with this chemical equation:

$$N_2\,(g) + 3H_2\,(g) \leftrightarrow 2NH_3\,(g). \quad (2.1)$$

Even though the process is exothermic (ΔH^o=-45.8 kJ/mol) and thermodynamically spontaneous ($\Delta G^o<0$), the natural reaction is extremely slow. Nitrogen is a very stable molecule with a strong triple N-N bond that determines a high value for the activation energy of the global process. To

---

[4] The Haber-Bosch process is considered as the scientific finding that has contributed to save more human lives in the history (see http://www.scienceheroes.com/ for further details). It is calculated that the feeding of a half of the human population depends on the fertilizer production derived from this chemical process. Thanks to the discovery, both German scientists (Fritz Haber and Carl Bosch) were awarded with the Nobel Prize in Chemistry. More information about the worldwide importance of this invention can be found in: *Nature Geoscience 1, 636 - 639 (2008)*

speed up the reaction a mixture of iron, potassium and aluminum oxides ($Fe_2O_3/K_2O/Al_2O_3$) is used as solid catalyst. The global chemical mechanism involves the dissociation of both molecules and a set of complicated intermediate steps, being the cracking of the nitrogen bond (dissociation) and the adsorption of the N atoms on the catalyst surface the limiting steps. The active centers of the catalyst are able to induce a faster adsorption and dissociation of the nitrogen and hydrogen molecules. The nitrogen atoms adsorbed on the catalyst surface recombine with H atoms in consecutive steps (N-H recombination), thus producing the ammonia molecules that are finally desorbed from the catalyst. Under high pressure conditions, collisions between hot dissociated species coming from the catalyst surface can be suitable to propitiate that a part of the N-H recombination reactions take place in the gas phase. However in diverted fusion plasmas or cold laboratory plasmas (as our glow discharge utilized in the experiments), the number of collisions between the gaseous atoms and radicals is small compared to the case of an industrial high pressure reactor, hence the role of the gas-phase N-H recombination reactions in the ammonia formation can be considered as negligible. Thus, in such system the N-H recombination into ammonia molecules must occur on the surface of the PFM that surrounds the plasma (heterogeneous catalysis). In the case of plasma-solid heterogeneous reactions, the process is known as plasma-activated heterogeneous catalysis. In such plasmas, the dissociation of nitrogen and hydrogen is also produced by means of electron impact processes, in this way the surface is bombarded with a (at least partially) dissociated reactant flow. The posterior adsorption of the species is necessary to continue with the process. In theory, the N-H recombination reactions on surface can be produced following two different mechanisms:

- Langmuir-Hinshelwood (L-H) mechanism: In this mechanism, two adsorbed molecules placed on neighbour surface sites recombine undergo a bimolecular reaction. In the case of nitrogen and hydrogen recombination the process can be represented in this way:

$$N(ads) + H(ads) \leftrightarrow NH\ (ads). \quad (2.2)$$

- Eley-Rideal (E-R) mechanism: in this case only one of the molecules is adsorbed, the other one reacts with it directly from the gas (plasma) phase, without adsorbing. For our ammonia formation, in principle, these two cases could be possible:

$$N\ (ads) + H\ (g) \leftrightarrow NH. \quad (2.3)$$

$$\text{H (ads)} + \text{N (g)} \leftrightarrow \text{NH}. \quad (2.4)$$

Both processes are represented in figure 2.1. After the production of the NH radical the successive recombination of it with H atoms produces the NH_3 molecules with the intermediate formation of the NH_2 radical.

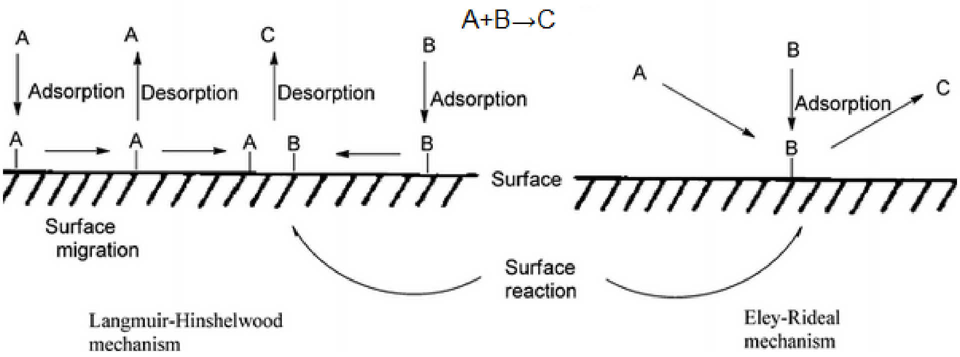

Figure 2.1. Langmuir-Hinshelwood and Eley-Rideal reaction schemes

On a tokamak environment, both processes, L-H and E-R recombination, can lead to the ammonia formation as the nitrogen/hydrogen molecules are dissociated by the plasma itself. Consequently, this ammonia formation is considered to be produced by means of both Eley-Rideal and Langmuir-Hinshelwood recombination reactions.

In this thesis the problematic of ammonia formation and retention in PFMs, as a consequence of the use of nitrogen as seeding gas in the divertor region has been approached by using glow discharge and gas exposure experiments. An important part of these results has been presented in international conferences (PSI 2014, PFMC 2015 and PSI 2016) and published in several papers [53-55]. The different experiments were performed in the plasma wall interaction laboratory sited in the Fusion National Laboratory (CIEMAT). They are included in this chapter divided in five sections.

The chapter 2.1 presents the experimental studies devoted to estimate the ammonia formation in ITER-relevant PFMs. In these studies, glow discharge plasmas were employed to approach the phenomenology of the process, trying to simulate diverted plasma conditions. This alternative technique represents an approximation to the relatively cold (with electronic temperature around a few eV) plasma conditions expected in the plasma surface boundary of fusion devices.

Although their fluxes and fluencies are approximately lower by three order of magnitude compared to normal divertor tokamak conditions, discharges with long duration (hours) can approximate the total fluency present in a tokamak discharge (with a pulse duration of few seconds). The aim of this first work was to study the effects of surface temperature and N_2 concentration on the yield of ammonia formation in N_2/H_2 direct-current glow discharge (DC-GD) plasmas. The formation process has been studied under relevant PFM's for ITER: tungsten (W), stainless steel (SS) and aluminium (Al) as a proxy of beryllium (Be), trying to detect conditions that minimize the produced ammonia and estimate the amounts that could be produced in fusion devices, as ITER.

The basic surface chemistry (N-H recombination processes) was also studied by using N_2-D_2 glow discharge plasmas, being these results presented in chapter 2.2. In particular, the importance of the nitrogen presence on the surface to produce ammonia and the role of nitrogen/hydrogen depth implantation on the two different possible recombination reactions was study by means of alternative (D_2 or N_2) GD plasmas performed on a tungsten wall previously saturated with N_2 or D_2 GD plasmas in order to analyse the reaction products when the tungsten wall only contains nitrogen or deuterium and is bombarded with the opposite ammonia constituent (deuterium or nitrogen)

In chapter 2.3 the influence of reactor relevant parameters in the ammonia formation on W was studied by using the glow discharge technique. If nitrogen is finally chosen in the active phase of ITER as impurity seeding gas necessary for the radiative divertor power load spreading (induction of divertor detachment), the particular effects of this reactor environment must be taken into account in order to assess their influence in the expected ammonia generation. In particular, in ITER a longer residence time, compared to our previous experiments, for the seeded species is expected. Additionally, the presence of helium (He) as an intrinsic plasma impurity generated in the D-T nuclear reactions will be unavoidable. Up to date, the influence of such factors on the plasma-surface processes behind the ammonia formation is uncertain. Hence, the comprehension of these effects induced by the reactor conditions is clearly necessary in order to estimate and try to mitigate its generation. In this study, several experiments were performed to measure the ammonia formation in N_2-H_2 direct-current Glow Discharge (DC-GD) plasmas on a W wall device, at different and increasing residence times for the active species. Additional experiments with N_2-H_2-He DC GD plasmas were performed, trying to measure the possible modification in the net formation of ammonia induced by the presence of helium in the plasma. The next analysis was focused on the understanding of the effects induced by the helium presence in the underlying plasma-surface processes that determine the changes in the ammonia generation.

The quantification of the ammonia sticking on stainless steel surfaces is approached in chapter 2.4. During the hypothetic ITER D-T N_2 seeded operation, the transportation of these produced molecules through the pumping system, situated beyond the cryopump modules, will transfer the tritiated ammonia to the tritium processing plant. This processing unit will be designed to separate the tritium present in the exhaust gas, to be re-injected as reactor fuel. The formation of considerable amounts of tritiated ammonia will affect to the performance of this tritium processing plant. Generally, this unit would process the generated ammonia to induce its thermal decomposition into N_2 and hydrogen isotopes, or its oxidation into N_2 and water molecules. Ammonia is a polar molecule that presents a lone pair of electrons in its electronic configuration. This peculiarity leads to an electrostatic interaction of these molecules with metallic surfaces that own empty electronic orbitals (type d). As a result of this interaction the ammonia molecules can be adsorbed (sticking) on the surfaces of the metallic pumping lines, thus causing net tritium retention on these zones. The polarity of the molecule also leads to a strong interaction between ammonia molecules (hydrogen bonds) that can be adsorbed (physisorbed) on the previous stuck layer placed directly on the metallic surface, thus leading to a multilayer adsorption. The problem is aggravated due to the high solubility of ammonia into residual water [56, 57] (whose separation can be extremely complicated as the phase diagram of ammonia-water system present many eutectics) that can induce enhanced condensation and corrosion. Furthermore, ammonia presents a relative high decomposition temperature [58]. Additionally, the associated corrosion effects on the pumping conductions can be extremely problematic as ammonia can induce mechanical stress and cracking in several steel or copper elements [51, 52], that are frequently used for pumping or cooling lines. Although strong evidences of this sticking process have been observed [47, 49] the total amount of ammonia that could be retained by sticking in these parts of a fusion device is still uncertain [51, 59]. For all these reasons, the potential sticking of the ammonia molecules in pumping lines of the vacuum system was investigated, being the purpose of this work to quantify the amounts of ammonia retained by sticking on AISI 304 L stainless steel surfaces (material frequently used in vacuum components and lines) at different temperatures in gas exposure experiments to have an approximate estimation of this problematic and to minimize it as much as possible. Finally, in chapter 2.5, a brief comment about the participation in the JET tokamak experiments dedicated to quantify the ammonia formation in N_2 seeded H-mode discharges is introduced as this participation was important for the academic training of the student.

2.1. AMMONIA FORMATION IN N_2-H_2 GLOW DISCHARGE PLASMAS. PARAMETRICAL CHARACTERIZATION OF THE PROCESS. SURFACE TEMPERATURE AND N_2 PLASMA CONTENT EFFECTS

2.1.1. Experimental procedure

2.1.1.1. Glow Discharge Plasmas

This kind of plasma is formed by providing a voltage between two electrodes (anode and cathode). The anode is a copper disk fed with a voltage provided by a bipolar direct current three phase power supply. The cathode is the wall of the plasma chamber (that also acts as the ground of the electrical circuit) where the gas for the discharge is introduced. When the voltage is applied to the anode, the presence of free electrons (primary electrons) produces a collision cascade between them and the gas atoms or molecules that generates more electrons (and the consequent ions) thus ionizing the gas and producing a current between the anode and the cathode. If the potential provided to the anode is fed continuously, the ion and electron population is maintained, and thus the global plasma, remains. A glow discharge plasma contains free charges (electrons and ions) being the net plasma charge neutral as the ionic and electron densities are approximately equal. The primary electrons are present in the gas randomly due to collisions with gamma (cosmic) ray radiation or intentionally injected in the gas bulk by means of an electron gun (in our case a rolled tungsten filament fed with a small DC current). If the pressure of the discharge is sufficiently high, the collisions with cosmic rays produce a suitable amount of primary electrons that is able to initiate the glow discharge. However, for low pressure discharges (around some Pa, as the case of our experiments) the injection of electrons by an electron gun is necessary to start the plasma. These plasmas are characterized by a light emission that depends on the gas of the discharge. There are several kinds of particles that are present in glow discharge plasmas: electrons, ions and metastable atoms or molecules. Different collision processes can happen among these species [60]:

- Electron impact collisions. A neutral specie collides with an electron, thus producing the ionization of the neutral or if the energy of the collision is not enough to produce the ionization, the neutral only increases its energy up to a excited or metastable state:
  Ionization: $A^0 + e \rightarrow A^+ + 2e$
  Excitation: $A^0 + e \rightarrow A^* + e$

Metastable formation: $A^0 + e \rightarrow A^m + e$

- Penning ionization. A collision between a metastable atom and a neutral is produced. The neutral specie is ionized or excited and the metastable is neutralized:
  $A^0 + B^m \rightarrow A^+ + e + B^0$
  $A^0 + B^m \rightarrow A^* + B^0$
- Asymmetric charge transference. A neutral transfers an electron to an ion. Hence the neutral is ionized (remaining normally in a excited ionic state) and the ion neutralized:
  $A^+ + B^0 \rightarrow B^{+*} + A^0$

In glow discharge plasmas the ionization degree is low (around 1%). However the amount of excited species and radicals is significantly higher. The interphase between the plasma and the surrounding chamber walls is a thin layer positively charged known as the plasma sheath. It is created due to the different velocity of the electrons respect to the ions (being the velocity of electrons higher due to their much lower mass). Consequently, the electrons arrive to the wall surface before the ions, thus charging negatively the wall respect the plasma bulk. This negative charge leads to the repulsion of the electrons and the attraction of the ions. Consequently a potential gradient is established in the plasma that touches the wall surface. The thickness of this positive sheath depends on the plasma characteristics (electron temperature and density) being in the order of a few Debye lengths (see more details about this parameter in subchapter 2.1.2.5). Typical electron densities of glow discharges are in the order of 10^{10} cm^{-3}, being the electron temperature, in the range of 1-10 eV. With these values, a sheath thickness of few tenths of microns is expected.

2.1.1.2. Experimental setup

The experimental apparatus, similar to one used previously in our group [61], is shown in figure 2.2. It consists on a cylindrical stainless steel (V=5.4 L) vacuum vessel, which acts as the grounded cathode, pumped out with a turbomolecular pump and backed by a rotary pump (base pressure of 10^{-5} Pa). High purity (>99.999%) gases (H_2, N_2, Ar) are introduced into the chamber by electronic flowmeters. Inside this primary vessel, a concentric liner is placed. It consists of a thin SS sheet whose inner wall (A=0.14 m^2) eventually covered by high purity cold rolled tungsten or commercial aluminium sheetsly. The annular space between the liner and the main plasma chamber walls is isolated with boron nitride elements to avoid plasma exposition and the concomitant ammonia formation on these surfaces, thus limiting the plasma processes to the liner inner wall (SS, W or Al) that is the object of study. A thermocoax wire is rolled in the external wall of the liner, to heat it. The wall temperature is measured with a thermocouple inserted in the external wall of the liner and controlled by a power supply.

The plasma chamber is connected with the analysis chamber through a small collimator, where a differential pumped residual gas analyser (Pfeiffer Vacuum Prisma QMS 200) is placed. This chamber is pumped down with another turbomolecular-rotary pump set at a base pressure lower than 10^{-7} Pa. The vacuum residual pressure in both chambers is measured with ionization gauges, and a capacitance manometer (0.1-100 Pa) is used to measure the total pressure of the discharge. A value of 2 Pa was used in all instances. Different experiments were carried out with the three wall materials. For each one, different plasmas were performed by changing the nitrogen concentration of the plasma (from 1.5% to 15%) to study the dependence of nitrogen plasma content in the ammonia formation. The measured discharge characteristics are: discharge voltage (300-600V) and plasma current (50-400 mA). The plasma parameters as electronic density (n_e) and temperature (T_e) were measured in these experiments by using a single Langmuir probe (see further details in the corresponding subchapter 2.1.2.5).

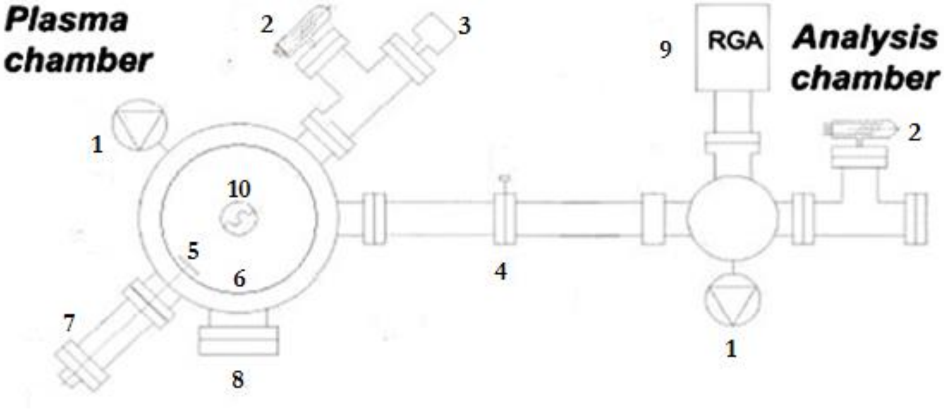

Figure 2.2. Schematic view of the experimental setup: 1. Pumping system, 2. Manometer (Bayard Alpert), 3. Capacitance manometer, 4. Diaphragm (Differential pumping), 5.Anode, 6. Concentric SS liner, 7. Gas inlet, 8. Optical window, 9. Mass spectrometer, 10. Electron gun

The produced ammonia was measured by differential pumped mass spectrometry (see subchapter 2.1.1.3 for details). All the experiments were carried out after a wall conditioning that assures the reproducibility of the experiments. It consists on pure DC-GD Ar plasma for 30 minutes followed by 1 hour of wall baking at 200ºC. A water-free environment is assured in this way (avoiding the effects of water contamination in the mass spectrometry ammonia measures due to their strong affinity [61]). Then the DC-GD plasmas at several N_2/H_2 mixtures are performed in two phases: a first part at constant plasma current of 1-1.5 hours of duration, until the steady state was reached in the system. This steady state is characterized by a thermal equilibrium in the chamber and constant plasma parameters as: $n_{e,}$ T_e, ion and neutral fluxes, etc. Later, a second phase with scans in plasma current is performed. Two different wall temperature regimes were used:

- Plasma heated (PH regime) liner experiments from 25ºC (RT) until ~100ºC at steady state with no external temperature control.
- Experiments at constant wall temperature controlled by the heating power supply (from 200ºC to 350ºC).

2.1.1.3. Mass spectrometry measurements

The detection and quantification of the produced ammonia (NH_3) was carried out by using a Prisma Pfeiffer Vacuum mass spectrometer (residual gas analyser, RGA) operating in high vacuum conditions through the differential pumping system. The mass spectrometer was used in the MID mode (temporal scanning of several amu/e signals). Generally a mass spectrometer consists of two different parts, the quadrupole probe whose sensor is placed inside the vacuum chamber, directly coupled to it with a conflat (CF) port, and the electronic control unit mounted directly on the probe external connection. This electronic control unit is fed with a 24 DC volts power supply. The probe consists in three main parts (figure 2.3): the ionizer, the quadrupole mass filter and the ion detector.

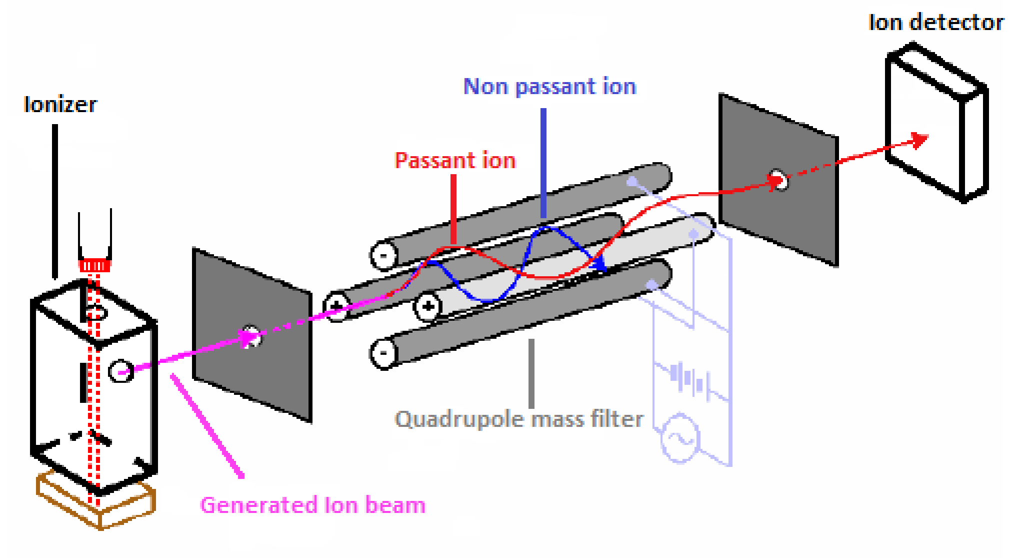

Figure 2.3. Schematic view of the RGA internal parts

Ion currents from the gas environment are detected in the ion detector by using a Faraday cup detector (direct detection) or by an optional electron multiplier (normally employed for higher sensitivity measurements). The residual gas molecules are previously ionized (into positive ions) by electron impact ionization processes in the ionizer. It creates an electron current (by means of a heated filament) that is accelerated and directed to the gas molecules. Owing to this impact, any produced ion presents a characteristic mass to charge (m/q) ratio that depends on the molecular mass of the precursor molecule and the ionization state of the ion. Finally, the quadrupole mass filter separates the different ions that reach the detector. Four cylindrical poles (reason why the device is frequently named simply as quadrupole) are placed in this part of the sensor to separate the different ions depending on the different mass to charge ratio. This separation is produced by a combination of RF and DC voltages that determines different ion trajectories inside the RF and DC created fields. These trajectories depend on the mass to charge characteristic ratio of the ionic specie. The magnitude and frequency of the RF field determine the specific mass to charge ratio of the particle that can pass through the filter, while the RF/DC ratio determines the filter selectivity. The ions that pass the filter (passant ions) are directed to the detector and the collected current is measured. As a result, different ion currents associated to each mass to charge value are detected as the measured signals, being these current signals proportional to the flux of the precursor gaseous species present in the vacuum chamber. Normally mass to charge ratio signals are measured in atomic mass unit (amu) over electron charge (e^-) units, being 1 amu equivalent to $1.66 \cdot 10^{-27}$ Kg. A positive monovalent ion will present an electronic charge, q=+1. In general the electronic charge of the ion is equal to the absolute value of the ionization state. It is important to note that mass spectrometry does not measure the molecular mass of the compound directly, the mass to charge ratio measurement only agrees with the molecular mass in the case of monovalent ions (singly charged). With the calibration work (explained, in the next subchapter) the main signals associated to nitrogen and ammonia (28 amu/e for N_2 and 17 amu/e for NH_3) can be absolutely quantified.

2.1.1.4. Absolute calibration work for N_2 and NH_3

The method used for the calibration of the RGA signals is based on the injection of gaseous flows and its correlation against the resultant mass to charge RGA signals measured by the mass spectrometer and their pressures (measured with the capacitance manometer). This calibration work was performed individually for nitrogen and ammonia that are the species involved in the calculations. The gases were injected into the chamber by using flowmeters (previously adjusted for the gaseous specie). As the RGA is sensitive to the flux, their signals in the analysis chamber are proportional to the injected amounts of each gas in the plasma chamber. Furthermore, the measured pressure (p) in the plasma chamber is related with the flux (Γ) through the individual pumping speed (S) for the gas specie: ($\Gamma_x = p_x \cdot S_x$). The slope obtained from the linear fit of a Γ (sccm) vs p (mTorr) plot gives us the pumping speed. If m (sccm/mTorr) is the slope of this fit, the pumping speed (S in L/s) is obtained with this expression:

$$S(L/s) = \frac{m \cdot N_A \cdot \frac{750.2 mTorr}{mbar} \cdot \frac{1 \min}{60 s}}{\frac{1000 cm^3}{L} \cdot \frac{22.4 L}{mol} \cdot n_0} = 12.5 \cdot m(sccm/mTorr). \quad (2.5)$$

In this expression, N_A is the Avogadro's number ($6.022 \cdot 10^{23}$ particle/mol), and n_0 the Loschmidt number ($2.69 \cdot 10^{19}$ particle/mbar·L). The corresponding fit in a RGA signal against p plot gives the calibration RGA constant (K) that relates the RGA signal with partial pressures (K_{N_2} and $K_{NH}3$). With these parameters the measured RGA signals can be converted into pressures (dividing by the calibration constant) and fluxes (multiplying the previously obtained partial pressure by the pumping speed). Nitrogen pressure and flow was correlated to 28 amu/e and ammonia to 17 amu/e. Due to the low water content propitiated by the good residual vacuum of the system, the values of 17 amu/e RGA signal were around 100 times lower before performing plasma, so the contribution of water to this signal can be considered as negligible and the amount of ammonia can be related directly to this signal. In most of the experiments the residual water levels were low enough to ignore the contribution of residual water molecules to 17 amu/e. Anyway these levels were checked, in order to subtract these contributions in the few cases when they were not negligible. Additionally the possible contribution of CO molecules to 28 amu/e signal can be considered as negligible due to the its very low residual level. The ultra-high vacuum experimental conditions and the absence of significant carbon content on the utilized wall materials assure that this contribution is absolutely negligible in comparison with the N_2 gas puffing injected in the experiments. With the RGA calibration constant, the nitrogen partial pressure in the gas mixture introduced to create the plasma can be calculated, converting the value of 28 amu/e to the partial pressure and dividing it by the total pressure (2 Pa). The nitrogen plasma concentration can be considered approximately equal to this nitrogen concentration in the gas mixture introduced previously to the plasma build up. To calculate the ammonia formation yields, the pumping speed and calibration constant obtained previously are also essential. Two different formation yields are calculated. The first one is the $NH_3/N_2^{\text{injected}}$ yield calculated as the number of produced ammonia molecules divided by the number of injected ammonia atoms. By definition, this yield is a-dimensional and can reach values between 0 and 2. The second one is the $NH_3/2\Delta N_2$ yield that represents the number of ammonia molecules formed in the process normalized to the number of nitrogen atoms that disappear in the plasma. The divisor of this second yield is the "depleted nitrogen" in the plasma. It is calculated as the difference between the number of nitrogen atoms injected in the system (calculated from the value of 28 amu/e without plasma after transforming it to atom flows with K_{N_2} and S_{N_2}) and the corresponding nitrogen atoms when the plasma is active and ammonia is produced. The factor 2 for the normalization of this yield appears because one molecule of nitrogen can produce 2 molecules of ammonia. Hence, this yield is also a-dimensional and can present values from 0 to 1. In the same way, for calculations of the nitrogen retention on the PFM walls, the RGA signals are converted to partial pressures (with the calibration constants) and then to particle fluxes with the pumping speed. The corresponding plots for the determination of S and K for nitrogen and ammonia are shown in figures 2.4 and 2.5. The calculated values are shown in table 2.1.

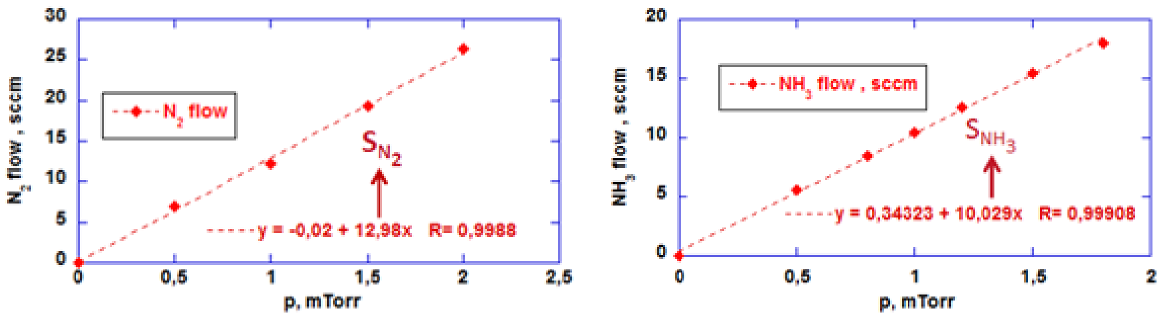

Figure 2.4. Determination of the pumping speed for nitrogen and ammonia

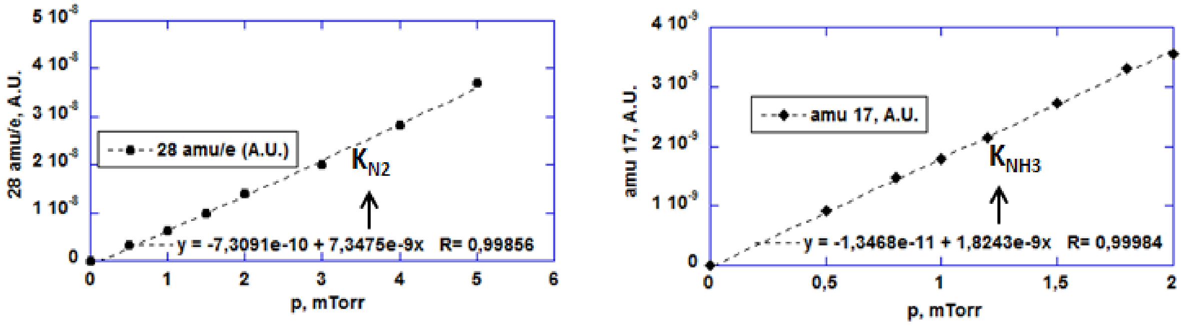

Figure 2.5. Determination of the RGA calibration constant for nitrogen and ammonia

Gas	Pumping Speed, S (L/S)	Calibration constant, K ($mTorr^{-1}$)
Nitrogen	162	$7.35 \cdot 10^{-9}$
Ammonia	125	$1.82 \cdot 10^{-9}$

Table 2.1. Values obtained from the calibration for nitrogen and ammonia

2.1.1.5. Plasma characterization by using single Langmuir probe measurements

This sensor constitutes one of the simplest and most used plasma diagnostics. It receives the name of Langmuir probe (LP) in honor of Irving Langmuir, the American chemist and physicist that was one of the first scientists to use these electric probes for the direct plasma fluxes measurements and the associated plasma (n_e, T_e) characterization [62]. The diagnostic is suitable for good estimations in low temperature plasmas (1 eV<T_e<100 eV) for a wide range of electron densities (10^6 cm^{-3} <n_e<10^{14} cm^{-3}), where the inserted probe (that directly senses the plasma particle fluxes) can survive. Particularly, they are used in SOL/divertor edge regions of fusion devices. They are generally quite robust and cheap and can be embedded into limiters and divertor tiles. A wide variety of electrostatic probes are used in different geometrical (cylindrical and spherical metallic collectors are the most used) and electrical (single, double or triple) configurations depending on the number of utilized and biased collectors. In this work the single Langmuir probe configuration was used, so we limit the required explanations to only this one. A single Langmuir probe consists on a metallic (normally made of stainless steel, tungsten or molybdenum) bare wire, which is inserted into a plasma and electrically biased respect to a reference electrode (in our case the anode that starts the glow discharge) to collect electron and/or positive ion currents. The dimensions of the probe collector (length, L and diameter, Ø) electrode needs to be suitable compared to the Debye length (L and Ø>>λ_D) to do not produce perturbative effects (charge screening) and associated unacceptable errors on the measured local parameters. At dimensions around the Debye length, charge screening and effective separation effects can happen. This parameter is given by the following expression:

$$\lambda_{Debye} = \sqrt{\frac{\varepsilon_0 \cdot k_B \cdot T_e}{n_e \cdot e^2}} \text{, (2.6)}$$

where ε_0 corresponds with the permittivity of free space, k_B is the Boltzmann constant, T_e, n_e the electron temperature and density and e the electron charge. Perturbing effects of charges tend to penetrate into the plasma a distance only in the order of the Debye length. For laboratory plasmas the Debye length is generally in the order of tens of microns, while typical probe dimensions (length and diameter) are in the order of millimeters. The potential of the plasma at the location of the probe is known as the plasma potential (V_p). The potential of the probe respect to the electrode is the floating potential (V_f) that is generally not the same as the plasma potential [63]. By definition, a probe that is electrically floating collects no net current from the plasma. In typical plasmas, the electrons because of their smaller mass have significantly higher thermal speeds than the positive ions, even if the electrons and ions are at the same temperature. Usually the electrons have a higher temperature than the positive ions. Although plasmas are electrically neutral, and the electron and ion densities are nearly equal, a floating probe will tend initially to draw a higher electron current because the electrons reach the probe faster than the more massive ions. Because the net current to the floating probe must be zero, the probe floats to a negative potential relative to the plasma so that further collection of electrons is retarded and ion collection is enhanced. Thus, the floating potential is lower than the plasma potential. The plasma potential is the potential of the plasma with respect to the walls of the device at a given location. It is generally a few volts positive with respect to the walls, again because the swifter electrons tend to escape to the walls first, leaving the plasma with a slight excess of positive space charge. The bulk of the plasma, however, is “quasineutral” (electron density ≈ ion density), and the potential difference between the bulk of the plasma and the wall is concentrated in a thin layer or sheath near the wall. The method developed by Langmuir allows finding the difference between V_f and V_p and determine the plasma density and the electron temperature. Langmuir’s method consists on the measurement of the current-voltage (I-V) characteristic curve of the probe by swiping the applied bias voltage (V_{bias}) from negative to positive potential. The difficulty to understand the I-V characteristics stems from the fact that the electrons and ions are not mono-energetic and often have very different temperatures. As a result, the probe sometimes collects only ion current, sometimes only electron current, and sometimes both. It is easier to understand and analyze the full I-V characteristic if the ion and electron current contributions are separated. Hence, the calculation of individual electron and ion currents and then the construction of an ideal I-V probe characteristic are essential for accurate estimations of n_e and T_e. In our experiments, the LP measurements were performed by inserting the device in the plasma bulk (a few centimeters inside the plasma to avoid systematic errors in the measurements related with the interaction of the probe with plasma sheath) through the optical window represented in figure 2.2. The biasing voltage was provided to the probe pin by using a bipolar (4 quadrants) power supply able to feed a voltage between -50 V to 50 V. The pin voltage (V_{LP}) and current (I_{LP}) were measured by using a voltmeter and an ampere-meter respectively. The pin was biased respect to the GD anode that initiates the plasma. A sketch showing the electrical configuration is shown in figure 2.6.

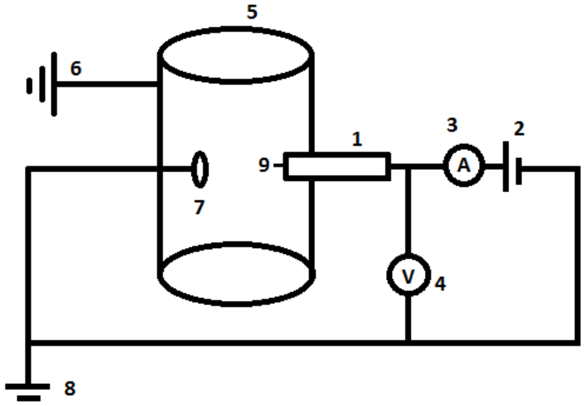

Figure 2.6. Scheme of the single LP installation and electrical connections: 1. LP installed on the chamber, 2. DC bipolar power supply, 3. Ampere meter, 4. Voltmeter, 5. Plasma chamber, 6. Ground connection for the GD (vacuum chamber walls), 7. Anode, 8. Three phase DC power supply for the GD, 9. Biased LP pin

The measurements were performed with tungsten walls on the plasma chamber and aluminum walls after replacing the tungsten sheet rolled in the liner placed inside the chamber by an aluminum one. For each material, different measurements were performed with different H_2- N_2 plasmas (with N_2 plasma concentration of 5 and 15% approximately). Several I-V scans on the probe were carried out for the plasmas at different discharge current (I_p, from 100 to 400 mA). An example of a LP I-V characteristic curve is shown in figure 2.7.

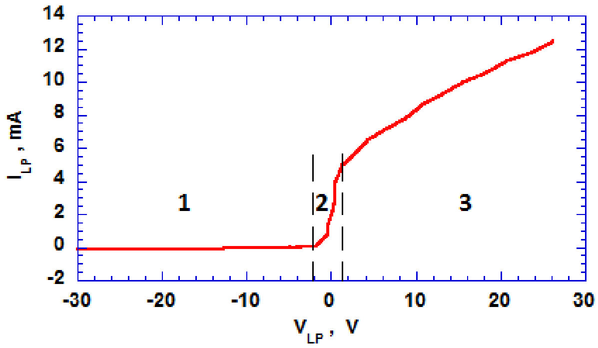

Figure 2.7. I-V characteristics (W wall, Ip=200 mA)

In this figure, three regions clearly separated are visible (numbered from 1 to 3). On the left (from -30 to -2 volts) in the region 1, the collected probe current exhibits a plane evolution with voltage. When the applied bias is sufficiently negative respect to the plasma potential (situated around 0 as the probe pin is biased respect the anode that provide this plasma potential) the probe collets the called *ion saturation current* (I_{is}). It can be easily obtained from the asymptote of the I-V curve when $V_{LP} \rightarrow -\infty$. Positive ions are collected by the probe until the bias voltage reaches V_P, at which point ions begin to be repelled by the probe. For $V_{LP} > V_P$, all positive ions are repelled, and the ion current to the probe is null. For a Maxwellian ion distribution at the temperature T_e, the value of ion saturation current can be calculated with this expression:

$$I_{is} = \frac{1}{4} e \cdot A_{LP} \cdot n_e \cdot v_{i,th} \cdot \quad (2.7)$$

In this equation, A_{LP} is the area of the biased pin exposed to the plasma (a cylindrical pin with L=10 mm and Ø=0.4 mm gives an exposed area of $1.3 \cdot 10^{-5}$ m^2), n_e is the electron density, e the electron charge and $v_{i,\ th}$ is the thermal speed of the ions:

$$v_{i,th} = \sqrt{\frac{8k_b \cdot T_i}{\pi \cdot m_i}}, \quad (2.8)$$

where m_i is the mass of the ions and T_i the ionic temperature. The point at the I-V characteristic with $I_{LP} = 0$ defines the floating potential and the start of the second region of the curve (displayed from -2 to 2 V approximately in the figure 2.7). It is characterized for a drastic inflexion in the curve slope. Beyond this region the curve exhibits another change of slope with a characteristic "knee" and an approximated linear dependence between V_{LP} and I_{LP} from this point. The value of V_{LP} at the knee point is considered the plasma potential (V_p) and its corresponding I_{LP} value is the electron saturation current (I_{es}). To determine the knee point with a better accuracy, the I-V curve regions two and three are fitted linearly. The intersection of these two fit lines defines the knee point whose abscissa is V_p and the corresponding ordinate gives the I_{es} value. The third region of I-V characteristic is defined from this "knee" points. It is known as the electronic part of the curve because for these values of biased voltage, the probe collects only electrons. The dependence of the current collected by the probe in the region 2 of the curve with the corresponding biased voltage can be expressed in this way:

$$I_{LP} = I_{is} \cdot \exp\left(- \frac{e}{k_b \cdot T_e} \cdot V_{LP} \right) + I_{is} \quad . (2.9)$$

Hence, taking logarithms and representing ln (I_{LP}-I_{is}) vs V_{LP} for the values contained in the region 2 of the I-V curve, the electron temperature (in eV) can be extracted directly from the inverse of the slope. An example of this semi-logarithmic plot is presented in figure 2.8.

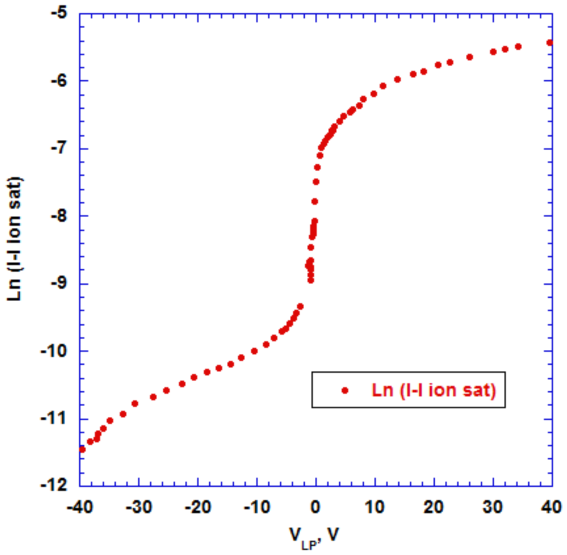

Figure 2.8. Example of semi-logarithmic I-V plot for T_e determination

Previously, for this determination, the ion saturation current (I_{is}) needs to be obtained graphically from the region 1 of I-V curve. The electron saturation current is given by an expression equivalent to the equation 2.3:

$$I_{es} = \frac{1}{4} e \cdot A_{LP} \cdot n_e \cdot v_{e,th} \ , \quad (2.10)$$

where n_e is the electron density and $v_{e,th}$ is the thermal velocity of electrons that can be calculated using the equation 4 previously changing T_i for T_e and m_i for m_e (electron mass). Hence, obtaining the electron temperature from the slope of the semi-logarithmic I_{LP}-V_{LP} plot and the I_{es} value graphically from the I-V plot (knee point), the electron density can be easily calculated with the equation 2.10.

2.1.2. Results and discussion

2.1.2.1. Electron temperature and density measurements

The results of the Langmuir probe measurements are presented in table 2.2. It shows the values obtained from the measurements implemented in N_2-H_2 plasmas scanning the plasma current (I_p) from 100 to 400 mA in plasmas with an approximated N_2 content (f_{N_2}) of 5% and 15%. The determinations were carried out with two different PFMs: tungsten and aluminium.

PFM	**f_{N_2}, %**	**I_p , mA**	**T_e , eV**	**n_e , cm^{-3}**	**λ_D , mm**	**Ø/λ_D**
W	**15**	**100**	2.2	5.9E+09	0.14	2.8
		200	1.1	2.0E+10	0.05	7.5
		300	1.1	1.2E+10	0.07	5.6
		400	1.1	2.7E+10	0.05	8.5
	5	**100**	1.4	9.1E+09	0.09	4.3
		200	1.1	1.7E+10	0.06	6.7
		300	1.1	2.0E+10	0.05	7.3
		400	1.8	1.2E+11	0.03	13.9
Al	**15**	**200**	1.0	1.1E+10	0.07	5.6
		300	1.2	1.3E+10	0.07	5.5
		400	1.2	1.5E+10	0.07	5.9
	5	**200**	1.1	5.0E+09	0.11	3.6
		300	0.9	1.0E+10	0.07	5.7
		400	0.9	7.8E+09	0.08	5.0

Table 2.2. Plasma parameters obtained with the Langmuir probe

Observing the electron temperature results, the obtained values are between 1-2 eV, on the lower limit (~1 eV) for determination with reasonably accuracy with single Langmuir probes. Additionally, there is not a general trend for the T_e dependence with I_p and f_{N_2}. Using the results for both materials and all plasma conditions a mean value of $T_e = 1.2 \pm 0.3$ eV is obtained. In the case of n_e, the values oscillate mostly between $1\text{-}3 \cdot 10^{10}$ cm^{-3} and the general trend gives an increasing density with the plasma current. The deduced values for the Debye length (λ_D) oscillates from 0.03 to 0.14 mm, values that are smaller compared to the diameter of the probe biased pin in a factor 3-10. The condition to obtain T_e and n_e values not affected by the induced probe perturbations in the plasma as charge screening that can produce associated errors in the collected current, establishes $Ø >> \lambda_D$. The obtained values show that in some cases Ø is similar to the values of the Debye length, thus suggesting that the accuracy of the obtained parameters may be limited. Furthermore, according to the T_e dependence of the electron impact dissociation and ionization processes for nitrogen [64], a value higher than 2 eV is necessary for a sufficient cracking of the nitrogen molecule that allows the formation of the ammonia on the surfaces.

However, the obtained T_e values are below this threshold. Although the existence of a supra-thermal electron tail population in the electron distribution function of the plasma could provide the necessary amount of hot electrons to induce the cracking of the nitrogen molecule and the concomitant ammonia formation, in principle this result suggests that the parameters obtained with the Langmuir probe (specially T_e) may be underestimated. In fact, the T_e values deduced from the measurements are very close to the detection limit of the probe. Consequently, the screening effects related with the interaction of the pin at the Debye length scale could be producing an erroneous current collection by the probe, thus resulting in a deficient measurement that would determine the inaccurate estimation of the plasma parameters.

2.1.2.2. T_{wall} and N_2 plasma content dependence in NH_3 formation

In figure 2.9, an example of the N retention on W and the time evolution of ammonia formation yield, estimated as the produced NH_3 flux normalized to the net amount of disappeared N atoms ($2\Delta N_2$) are shown. An increasing ammonia formation takes place during the first moments, reaching a constant value after a few minutes. Therefore, during these moments the clean wall retains nitrogen via ions and neutrals up to surface saturation with possible formation of the nitride. This stabilization does not mean that the steady state was reached in the whole system in this moment, is just an indication of the wall saturation that takes place. The nitrogen wall saturation is the first step in ammonia production. After this step the N/H and N/N recombination surface reactions determine the amount of produced ammonia, released from the wall [65].

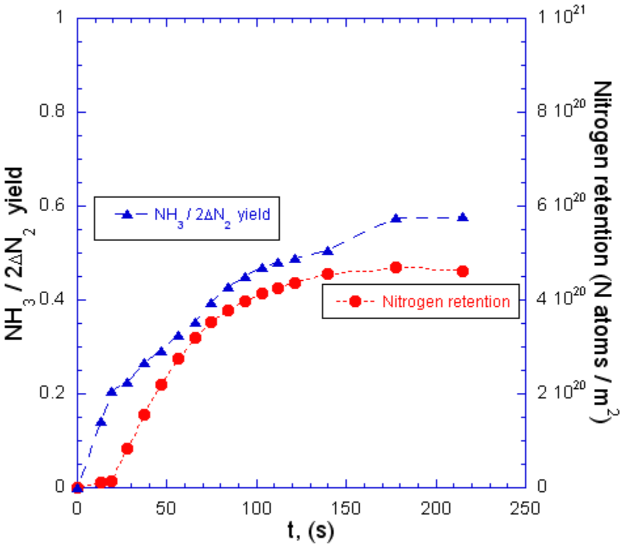

Figure 2.9. Example of time evolution in ammonia formation and W wall saturation

In figure 2.10 the dependence of the produced ammonia normalized to injected nitrogen ($NH_3/N_2^{injected}$ yield) with the nitrogen cracking efficiency at steady state is shown, at constant wall temperature for each material (comparable data due to the little effect of temperature up to 300ºC) is shown. The cracking efficiency of nitrogen is an experimental parameter defined as the ratio between the net amount of N_2 molecules that disappear in the plasma (as produced ammonia, wall retention, sticking…) calculated by RGA measurements, divided by the injected nitrogen ($\Delta N_2/N_2^{injected}$). It is calculated by using the measured 28 amu/e signal before starting the plasma and when the plasma is active. This parameter increases with higher plasma currents (I_p) and low N_2 plasma content (measured as N_2 concentration in the gas mixture). The yields are in agreement with previous results [66], a linear dependence with the cracking efficiency is observed, being the $NH_3/N_2^{injected}$ yields higher for lower N_2 concentration and high plasma currents that result in an increased N-H recombination on the walls. Furthermore, the ratio of injected N_2 converted into NH_3 in steady state is usually between 0.05-0.35, except at very low N_2 concentration (1.5%) on SS where values close to 0.6 are achieved.

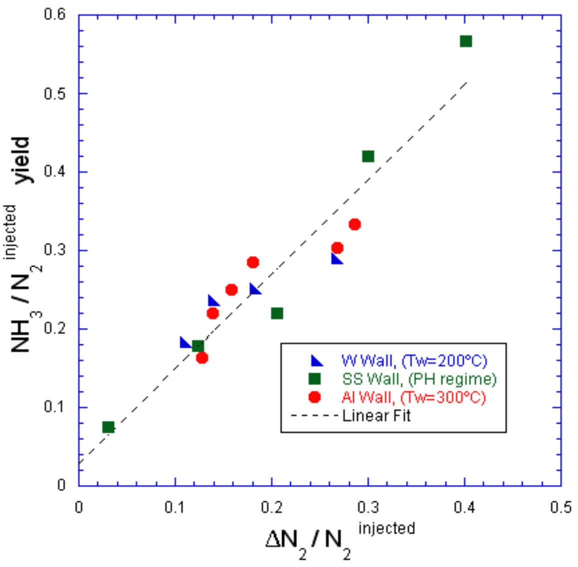

Figure 2.10. $NH_3/N_2^{injected}$ yield dependence with N_2 cracking efficiency for W, SS and Al

The influence of T_{wall} in the $NH_3/2\Delta N_2$ yield at steady state is displayed in Figure 2.11 for all metals. The ammonia production increases weakly with wall temperature up to 300ºC. At 350ºC almost 100% of the cracked nitrogen is converted into NH_3 on Al wall. The T_{wall} can change the kinetic of N/N and N/H recombination processes, resulting in higher $NH_3/2\Delta N_2$ yields.

Moreover, different wall temperatures and materials could produce very small variations on plasma parameters (n_e, T_e). It could also contribute to weak changes in the ammonia yields.

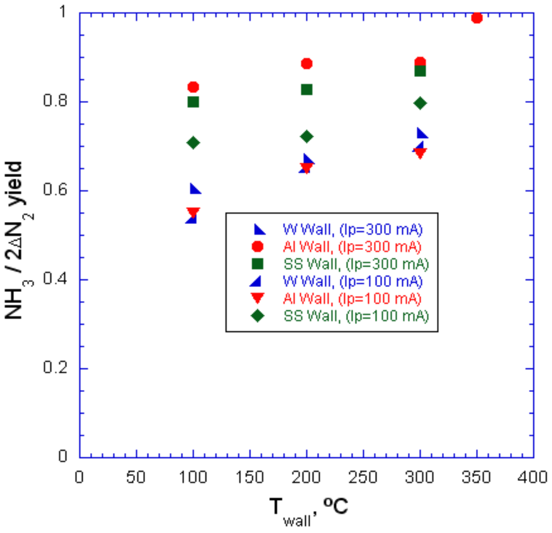

Figure 2.11. $NH_3/2\Delta N_2$ dependence with T_{wall} for W, SS and Al walls

The error associated to both ammonia formation yields has been evaluated taking into account the statistical bias related with the determination (linear fitting) of the pumping speeds (S) and calibration constants (K) (for N_2 and NH_3) and the experimental errors produced during the mass spectrometry measurements. For the measured mass to charge signals, the time average value for each plasma parameters (voltage and current) was calculated previously to obtain the ammonia yields, being the maximum standard deviation around 2-3%. On the other hand, the least square error associated to the calculations of S and K (for ammonia and nitrogen) has been evaluated, resulting in an estimated error of ~2%. The calculation of the linear propagation of errors taking into account all these contributions gives a maximum global error associated to the calculated yields around 10-15%. Comparing these values at different plasma currents, a difference is shown for Al and SS compared to W, as their ammonia yield increases with plasma current. There are no big differences with I_p for the case of W wall. These results could be explained for the different sputtering yields on the wall materials. A higher I_p (that implies higher discharge voltage and energy for the ions) would enhance the sputtering yield for nitrogen bombardment on Al and SS walls compared with W, thus renewing the active centres of the surface that catalyse the ammonia formation. To check it, calculations following the Bohdansky model for physical sputtering were performed. Three different cases were considered to study the surface bombardment with N impinging ions (N^+) in three different substrates (tungsten, aluminium and iron that is the majority component of stainless steel). Although in our plasmas the proportion of N^+ ions is very low (N_2^+ molecular ions are the predominant, [67]) it can be considered that the energy supplied to the ions through the plasma sheath acceleration (that depends on the discharge voltage) is equally divided between the two N atoms of the molecular ion. In any case these comparative calculations will show the differences in terms of sputtered surface at same impinging energy for the three different materials. If we assume normal incidence for the nitrogen projectiles on the surface, the sputtering yield dependence with the projectile energy (E_0) is given by this expression [68]:

$$Y_{sputtering} = Q \cdot s_n(\varepsilon) \cdot \left(1 - \left[\frac{E_{th}}{E_0}\right]^{2/3}\right)\left(1 - \frac{E_{th}}{E_0}\right)^2 . \quad (2.11)$$

This semi-empirical formula contains an energy threshold term (E_{th}) that is characteristic for physical sputtering and depends on the material substrate (M_2) and the projectile atomic mass (M_1), the ratio M_1/M_2, and the tabulated [69] surface binding energy of the substrate (E_s):

$$\begin{aligned} \frac{M_1}{M_2} < 0.2 &\rightarrow E_{th} = \frac{E_s}{\gamma(1-\gamma)} \\ \frac{M_1}{M_2} > 0.2 &\rightarrow E_{th} = 8E_s\left(\frac{M_1}{M_2}\right)^{2/5} \end{aligned} \quad . (2.12)$$

Being γ a non-dimensional parameter that depends on M_1 and M_2: $\gamma = \frac{4M_1M_2}{(M_1+M_2)^2}$. (2.13)

The parameter Q is usually obtained from the fitting of experimental data and is also tabulated depending on the substrate and projectile elements [69]. s_n is the nuclear stopping cross section that depends on the reduced energy, ε. This parameter can be calculated by using this expression:

$$\varepsilon = E_0 \frac{M_2}{M_1 + M_2} \frac{a_L}{Z_1 Z_2 e^2} \quad , (2.14)$$

where M_1 and M_2 are the masses of the projectile and the substrate atom, Z_1 and Z_2 the atomic numbers and e, the electron elemental charge. The parameter a_L is the Linhard screening length given by:

$$a_L = 0.4685 \cdot \left(Z_1^{2/3} + Z_2^{2/3}\right) \text{ (in Å units)}, \quad (2.15)$$

The values of s_n (ε) can be obtained from empirical plots [69] calculating previously the reduced energy for each projectile impinging energy (E_0). Moreover the values of Q are also tabulated for each projectile-target atom pair. All this formulation allows to the calculation of sputtering yields (for normal incidence) of N^+ ions in the target materials (W, Al, Fe) depending of the energy of the projectiles (E_0). The results of these calculations are shown in figure 2.12.

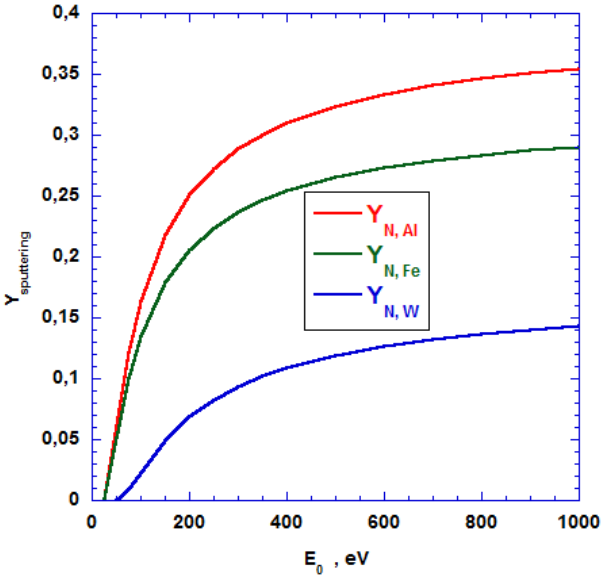

Figure 2.12. Calculated sputtering yields of N ions on Al, Fe and W surfaces

These results reveal higher sputtering yields on aluminium surfaces compared to tungsten and iron, being a factor 3 higher comparing the values for aluminium to the case of tungsten. These calculations following the Bohdansky model for physical sputtering could explain the previous result as the nitrogen ions could release metallic nitride aggregates and passive dust particles from the wall, renewing in this way the surface and producing new active surface centres that would increase the recombination area and the ammonia production in these conditions.

2.1.2.3. Nitrogen retention on ITER-relevant PFMs

The evolution of NH_3 and N_2 signals monitored by RGA allows us to estimate the N retention on the clean tungsten surface during the first minutes of the plasma operation. With a simple N particle balance calculation, taking into account the calibration constants and pumping speeds for each specie, the amount of N atoms retained on W surface is estimated at a given time. Time integration up to the saturation time (3-4 minutes) leads to an estimate of the N areal density retained on W. The set of necessary equations is:

$$\Delta 28\ \text{amu/e} = 28\ \text{amu/e}^{\text{gas}} - 28\ \text{amu/e}^{\text{plasma}}\ , \quad (2.16)$$

where 28 amu/e^{gas} and at 28 amu/e^{plasma} are the signals related with nitrogen before and during the plasma. These values are translated to fluxes by using the parameters obtained in the calibration work (K_{N_2} and S_{N_2}). The same procedure is applied to ammonia to get their flux values. Then, the number of retained nitrogen atoms can be calculated performing a gas (particle) balance between the depleted nitrogen and the produced ammonia molecules:

$$N_{\text{ret}} = \frac{n_0}{A} \cdot I\,, \quad \text{(Nitrogen atoms/m}^2\text{)}, \quad (2.17)$$

where n_0 the Loschmitd's number, and A the wall surface. The term I represents the integral of the nitrogen atoms balance over the saturation time t_s:

$$I = \int_0^{t_s} \left(\frac{2 \cdot S_{N_2} \cdot \Delta 28 \text{ amu/e}}{K_{N_2}} - \frac{S_{NH_3} \cdot 17 \text{ amu/e}}{K_{NH_3}} \right) dt. \quad (2.18)$$

Nitrogen implantation and retention on tungsten is produced by the impinging plasma ions. Using a [70] Monte Carlo code (SRIM), simulations of the interaction with the tungsten surface of the nitrogen dominant ions (NH_4^+ and N_2H^+ [67]) have been performed. During the W wall saturation phase, typical values in plasma potential are ~ 400 V, so assuming no ion-neutral collisions in the sheath at 2 Pa, the N ions energies are ~ 311 eV/N for NH_4^+ and ~ 193 eV/N for N_2H^+ (momentum transfer proportional to the atomic mass of each atom) respectively. The ion distribution in our plasmas with ~10-15% in N_2 on the steady state can be considered approximately: 50% NH_4^+, 20% N_2H^+ and 30% H_3^+ [67]. An implantation depth of 3 nm for NH_4^+ and 2.5 nm for N_2H^+ is obtained and no diffusion into the W bulk at the temperatures of these works is expected [71]. Together with the retained N areal density calculated by particle balance, this value allows us to obtain the N/W atomic rates at the implantation region, presented in table 2.3.

T_{wall} (ºC)	f_{N2}(%)	N atoms/m^2	N/W	N/Al
50	16.1	$4.7 \cdot 10^{20}$	2.5	-
50	14.1	$3.3 \cdot 10^{20}$	-	0.37
200	15.1	$4.3 \cdot 10^{20}$	2.3	-
200	16.5	$2.5 \cdot 10^{20}$	-	0.28
200	5.8	$2.6 \cdot 10^{20}$	-	0.29
300	15.2	$5.0 \cdot 10^{20}$	2.6	-

Table 2.3. Nitrogen retention values (during the plasma) and atomic ratios on Al and W walls depending on the surface temperature and nitrogen plasma content

Interstingly, no significant differences on the resulting implanted fluences is seen when the wall temperature is raised from room temperature to 300ºC. The N/W implantation ratios are close to 2.5, higher than the stoichometric relation corresponding with WN nitride or the more stable W_2N nitride probably due to dynamic retention. The N retained areal density during the plasma (dynamic and long term) is around $5 \cdot 10^{20}$ N/m^2, in good agreement with previous reports [72].

2.1.2.4. Ammonia formation and N retention on Al, as a proxy of beryllium

In ITER, beryllium will be the PFM for the first wall. The use of N_2 impurity seeding may lead to the formation of important amounts of ammonia on the (dominant) Be surface, (even at the divertor due to the large codeposit formation coming from eroded beryllium that is expected [73]). Since direct experiments with beryllium are very restricted, (due to the toxicity) aluminium has been used as a proxy. Its use is motivated by the similarity in some physical and chemical properties as a result of the diagonal chemical relationship between it and Be. Several experiments with energetic nitrogen ions interaction on Be were performed at IPP [73] and studies comparing physical and chemical properties of Be-Al-Mg for ITER issues have been published [74]. The results here presented can be an indication of the likehood of both metals respect to their response to N-containing plasmas.

As can be seen in figure 2.10, a linear dependence in the $NH_3/N_2^{injected}$ yield with the nitrogen cracking efficiency has been reported. On the other hand, in figure 2.11, the T_{wall} effects appears very clear, above 300 °C, where almost all the cracked N_2 is converted into ammonia. These results point to a higher dependence of the recombination into ammonia on wall temperature in Al. According to previous results [73], the N implantation on Be takes place at $4 \cdot 10^{20}$ N/m^2 within an implantation depth of 10 nm, resulting in a N/Be atomic ratio of 0.68, very close to stoichiometric Be_3N_2 nitride detected above N areal densities of $3 \cdot 10^{20}$ N/m^2.

Estimations of N retention (also shown in table 2.3) on Al show a lower N retention, (around $2.5 \cdot 10^{20}$ N/m^2), considering a depth implantation around 1-2 nm, [70] an atomic N/Al ratio lower than the stoichiometric AlN nitride results. However this atomic ratio could be affected by high N sputtering yield on Al, decreasing the thickness of N-Al layer. For these reasons, the certainty in the similarity between Al and Be for their interaction with N_2/H_2 DC-GD plasmas cannot be confirmed.

2.1.2.5. Comparative $NH_3/2\Delta N_2$ yield calculations for W, SS and Al

In table 2.4, a comparison of the resulting $NH_3/2\Delta N_2$ yield for all the tested materials at different plasma currents and wall temperatures under steady state conditions is presented. It is important to note that for all the materials, there are amounts of cracked N_2 that are not converted into ammonia and not registered as other gaseous compounds (N_2H_4, N_2H_2 or NO_x) by the RGA measurements.

Ip=100mA				Ip=200 mA				Ip=300 mA			
T (ºC)	**Wall Material**			**T(ºC)**	**Wall Material**			**T (ºC)**	**Wall Material**		
	W	**SS**	**Al**		**W**	**SS**	**Al**		**W**	**SS**	**Al**
100	0.54	0.71	0.55	**100**	0.58	0.74	0.65	**100**	0.60	0.80	0.83
200	0.65	0.72	0.65	**200**	0.67	0.76	0.72	**200**	0.67	0.83	0.88
300	0.70	0.80	0.68	**300**	0.73	0.82	0.8	**300**	0.73	0.87	0.87
350	-	-	-	**350**	-	-	0.89	**350**	-	-	0.99

Table 2.4. Normalized NH_3 / $2\Delta N_2$ yield for W, SS and Al in steady state DC-GD N_2/H_2 plasmas at different plasma currents and wall temperatures

Some possible explanations for this experimental fact could be: formation of metal nitride dust on surface and/or nitrogenated compounds re-deposition in plasma shadowed areas(not observed in the setup up to date), the N intergranular diffusion into the bulk (precluded on W according to [71]) and non-registered ammonia sticking or losses in cold parts of the system. For Al and SS walls an intrinsic dependence of plasma current itself can be claimed according to the displayed data. On Al wall at high I_p and 350ºC the $NH_3/2\Delta N_2$ yield is approximately 1. This observation could be explained (together with T_{wall} effects) by the enhanced sputtering yield. It would avoid the formation of metallic nitride dusts or aggregates that could inhibit the NH_3 formation. However on W walls the sputtering yields are lower, and the amount of "missing nitrogen" increases. This possible surface renewal has been previously commented.

2.1.3. Conclusions and future works

- The original goal of these experiments was to investigate if a decrease in the ammonia formation yield is possible at high wall temperature on the exposed materials. The results show an effect opposed to that sought, i.e. the amount of produced ammonia on all the investigated materials increases moderately with the temperature, especially on Al wall, where almost 100% of the cracked N_2 is converted into ammonia at 350ºC.
- The influence of N_2 content is clear in W and SS, where low N_2 concentrations in the plasma results in a higher nitrogen cracking efficiency that deterines an enhanced ammonia formation yield. Consequently, both N/H recombination on the wall and the

ammonia yield increase. Only under SS and Al walls, an intrinsic dependence on plasma current, seems to exist. The cause of this behaviour could be in agreement with higher sputtering yields by nitrogen bombardment on Al and SS compared to W.

- The amount of retained N on W is in good agreement with previous reports and nitride formation seems evident. However, although N retention on Al is close to the case of Be, the use of Al as a proxy for Be in this kind of studies could be limited. Our experiments show that the wall saturation with impinging nitrogen from the plasma occurs in the first moments, being later the competition between N/H-N/N recombination on the wall the key process that determines the ammonia formation yield.
- The results here shown may represent a good approximation to the problematic of ammonia formation in plasma operation with nitrogen impurity seeding. Experiments to investigate ammonia formation in W at higher temperatures relevants for ITER divertor and studying the kinetic aspects of the recombination processes, could be important to understand this relevant plasma wall interaction phenomenon.

2.2. GLOW DISCHARGE STUDIES OF THE MECHANISM OF AMMONIA FORMATION IN N_2-D_2 GLOW DISCHARGE PLASMAS UNDER TUNGSTEN WALLS

2.2.1. Experimental setup and procedure

These experiments were carried out in the setup used in the previous experiments (widely explained in subchapter 2.1.1.2.) In these experiments the inner wall of the liner placed inside the plasma chamber was always covered by the cold-rolled tungsten sheet, in order to study the recombination reactions on the W surface. Two different experiments were carried out:

- The first one consisted on performing a pure D_2 plasma on the tungsten walls previously saturated with nitrogen after the exposure to a pure N_2 GD plasma. Prior the experiment a wall conditioning procedure is necessary to assure the reproducibility. It consists on a wall baking at 423 K during 2 hours followed by 30 minutes of Argon GD plasma. Then the first part of the experiment is carried out by producing the nitrogen saturation of the W wall with a pure N_2 GD plasma (p= 2Pa, total fluency of 10^{23} N/m^2, plasma current of 300 mA and discharge voltage of 400 V). After this saturation, the N-saturated surface is irradiated with pure D_2 GD plasma (p= 2 Pa, total D/N fluency of 10^{23} m-^{2}, plasma current of 350 mA and discharge voltage of 500 V). During this irradiation the gas exhaust composition was monitored with the mass spectrometer. The differential pumped system assures a low impurity (including water) content in the analysis chamber.
- The second one was a symmetric experiment carried out in the inverse order, producing the saturation of the W wall with pure D_2 GD plasma followed by irradiation with pure N_2 GD plasma. The characteristics of the glow discharge plasmas and the wall conditioning procedure were the same compared to the experiment previously commented.

For the both experiments, the following mass to charge ratio signals were monitored with the mass spectrometer: 2,3,and 4 amu/e (H_2, HD and D_2), 15-20 amu/e (contributions from water and ammonia molecules), 28 amu/e (mainly nitrogen) and 30 amu/e (NO). The presence of deuterated and hydrogenated ammonia and water overlapping species (NH_3, NH_2D, NHD_2, ND_3, H_2O, HDO and D_2O) makes the mass spectrometry analysis for the quantification quite complicated. To separate the contribution of the different species in the overlapping masses is necessary a deconvolution calculation of the signals, taking into account the experimentally found cracking patterns for NH_3 and H_2O species.

2.2.2. Experimental results

2.2.2.1. D_2 plasma on a W wall saturated with nitrogen

In figure 2.13, the evolution of the RGA signals during the experiment is represented. During the first part of the experiment (from 5940 s to approximately 6000 s) a D_2 gas puffing is introduced in the plasma chamber with the W wall previously saturated with N_2 GD plasma. No changes in the signal evolution were observed during this gas injection. In the subsequent plasma phase a decrease in the mass 4 (due to the cracking of the deuterium molecules) and a concomitant increase in the 17-20 mass signals are clearly visible.

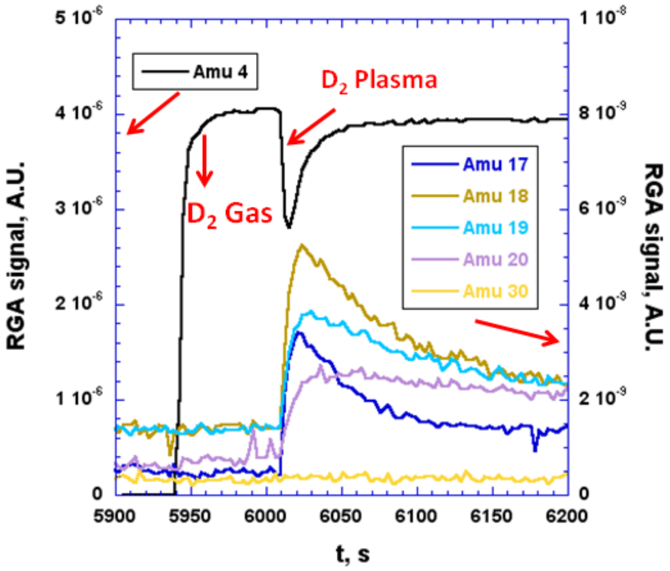

Figure 2.13. Pure D_2 GD plasma on a W wall previously saturated with a pure N_2 GD plasma

The increase in the RGA signals at 17-20 amu/e reveals the formation of different ammonia molecules. They are differenced in the molecular mass due to the different H/D content. In principle no hydrogen is injected in the system during the experiment, hence no hydrogen should be present in the ammonia molecules. However, the presence of water molecules or residual hydrogen from impurities in the chamber or on the tungsten wall is unavoidable, thus providing the necessary hydrogen atoms to produce hydrogenated ammonia molecules. Moreover from the experiments with N_2 seeded discharges in JET [49], it is well-known that deuterated ammonia is prone to an intense isotope exchange with hydrogen that determines a high degree of replacement of D atoms for H atoms during the transportation from the PFM surfaces to the mass spectrometer sensors through the pumping lines. These reasons explain the presence of important amounts of hydrogenated ammonia in our experiment. During the D_2 plasma performance the formation of ND radicals (that acts as precursors for the ammonia formation) must be initialized on the wall because there is no presence of nitrogen in the gas phase (nitrogenated W wall exposed to pure D_2 GD plasma). The recombination reactions can happen by means of L-H recombination between the previously adsorbed nitrogen and adsorbed deuterium atoms from the plasma, or by means of E-R recombination between adsorbed nitrogen and impinging deuterium from the plasma. In this way the chemical reactions related with the formation of ammonia take place on the tungsten surface. Hence, this experiment confirms the well-known conclusion that establishes the surface chemistry processes as determinant for the ammonia formation. The gas/plasma chemistry contribution in the ammonia formation cannot be totally rejected but at least in this experiment its role seems to be (as maximum) very limited compared to the surface processes.

For the quantification of the products in the range of 17-20 amu/e, a deconvolution calculation is necessary as water and ammonia molecules with different H/D content are isotopologues and overlap in the amu/e signals. In the case of ammonia these contributing molecules are NH_3, NH_2D, NHD_2, and ND_3, while for the case of water they are H_2O, HDO and D_2O. As a result of the interaction with the RGA ionization chamber during their detection, the different ammonia and water molecules are cracked in several partially dissociated fragments that contribute to the global values of the 15-20 amu/e signals detected by the mass spectrometer. These fragments are formed by depleting one or more hydrogenic atoms from the neutral molecule. The relative intensities of the resulting peaks registered by the RGA, directly related with the expected proportion of these partially dissociated species in the measurement, are known as cracking patterns. In table 2.5, the relative contributions of these species to the different amu/e signals for each molecule, (taking into account the experimental found cracking patterns for pure H_2O and $NH_{3,}$ -in red-) and the extrapolation of them to the deuterated molecules are presented.

Molecule	**M_m g/mol**	**20 amu/e**	**19 amu/e**	**18 amu/e**	**17 amu/e**	**16 amu/e**	**15 amu/e**
NH_3	**17**	**-**	**-**	**-**	**100/182** **NH_3^+**	**77.5/182** **NH_2^+**	**4.5/182** **NH^+**
NH_2D	18	-	-	100/182 NH_2D^+	51.7/182 NHD^+	27.3/182 NH_2^+ ND^+	3/182 NH^+
NHD_2	19	-	100 NHD_2^+	25.8/182 ND_2^+	51.7/182 NHD^+	3/182 ND^+	1.5/182 NH^+
ND_3	20	100 ND_3^+	-	77.5/182 ND_2^+	-	4.5/182 ND^+	-
H_2O	**18**	**-**	**-**	**100/128.7** **H_2O^+**	**25/128.7** **HO^+**	**3.7/128.7** **O^+**	-
HDO	19	-	100 HDO^+	12.5/128.7 DO^+	12.5/128.7 HO^+	3.7/128.7 O^+	-
D_2O	20	100/128.7 D_2O^+	-	25/128.7 DO^+	-	3.7/128.7 O^+	-

Table 2.5: Relative contribution of the overlapping ammonia and water species in the mass range between 15-20 amu/e

Hence if the mixture is assumed to contain seven molecules, but only 6 RGA signals related with them are available (from 15 to 20 amu/e) the system is not determined and cannot be solved. A possibility to solve the system is to reduce it, supposing that the more deuterated species (there is an empirical evidence that ND_3 production is quite small [59], hence all 20 amu/e signalcan be attributed to D_2O and considered as negligible, as rough approximation) are very unlikely to be detected by the RGA due to the high isotopic exchange to the hydrogenated molecules that have been experimentally observed [59]. In this way the species ND_3 and D_2O and their main RGA signals (20 amu/e) are eliminated and the system contains 5 equations (RGA signals from 15-19 amu/e) and 5 molecules. The equations that forms this determined algebraic system are the following ones:

$$\frac{4.5}{182}\cdot NH_3+\frac{3}{182}\cdot NH_2D+\frac{1.5}{182}\cdot NHD_2=\int(15amu/e)\cdot dt\,.(2.19)$$

$$\frac{77.5}{182}\cdot NH_3+\frac{27.3}{182}\cdot NH_2D+\frac{3}{182}\cdot NHD_2+\frac{3.7}{128.7}\cdot H_2O+\frac{3.7}{128.7}\cdot HDO=\int(16amu/e)dt\;(2.20)$$

$$\frac{100}{182}\cdot NH_3+\frac{51.7}{182}\cdot NH_2D+\frac{3}{182}\cdot NHD_2+\frac{100}{128.7}\cdot H_2O+\frac{12.5}{128.7}\cdot HDO=\int(17amu/e)dt.\;(2.21)$$

$$\frac{100}{182}\cdot NH_2D+\frac{25.8}{182}\cdot NHD_2+\frac{100}{128.7}\cdot H_2O+\frac{12.5}{128.7}\cdot HDO=\int(18amu/e)\cdot dt.\;(2.22)$$

$$\frac{100}{182}\cdot NHD_2+\frac{100}{128.7}\cdot HDO=\int(19amu/e)\cdot dt\,.\;(2.23)$$

This set of algebraic equations can be expressed in the more frequent algebraic-Cramer form (AX=B), where A is the coefficient matrix, X is the column vector of the variables and B the column vector of independent terms:

$$\begin{array}{ccccc} 4.5/182 & 3/182 & 1.5/182 & 0 & 0 \\ 77.5/182 & 27.3/182 & 3/182 & 3.7/128.7 & 3.7/128.7 \\ 100/182 & 51.7/182 & 3/182 & 100/128.7 & 12.5/128.7 \\ 0 & 100/182 & 25.8/182 & 100/128.7 & 12.5/128.7 \\ 0 & 0 & 100/182 & 0 & 12.5/128.7 \end{array} \bullet \begin{array}{c} NH_3 \\ NH_2D \\ NHD_2 \\ H_2O \\ HDO \end{array} = \begin{array}{l} \int(15amu/e)\cdot dt \\ \int(16amu/e)\cdot dt \\ \int(17amu/e)\cdot dt. \\ \int(18amu/e)\cdot dt. \\ \int(19amu/e)\cdot dt. \end{array}\quad(2.24)$$

In this expression, the values of the coefficient matrix are taken from the measured cracking patterns for the mixture molecules, the X vector contains the amount of produced ammonia and water molecules detected by the RGA and B is the column vector with the independent terms of the linear system that are calculated by integrating in time the measured values in the 15-19 amu/e range.

The composition of the mixture can be estimated in this way: 1) subtracting the background levels for each amu/e signal, 2) calculating the time integrated values for signals 15-19 amu/e during the ammonia formation experiment (approximately from t>6000 s in Figure 2.13), 3) solving this linear algebraic system. Unfortunately by applying this method the results obtained were not successful. The system needed negative solutions for the NH_3 contribution to be solved and this assumption has not physic sense. Probably the experimental data are not complete enough for the quantification due to the possible losses (sticking) and condensation of a part of the ammonia and water species in the system before reaching the RGA and be detected. To avoid this problem and have a better analysis, a solution is to use the cryo-trap assisted mass spectrometry technique (CTAMS, [76]) that uses a liquid nitrogen circuit for the condensation of all the ammonia and water molecules before they reach the RGA. This technique is also used in JET for mass spectrometry quantifications. It assures that all the molecules are trapped by the condensation and then finally evaporated and analysed in the RGA without any loss in cold parts of the system. Additionally, another estimation attempt was performed by supposing that the amount of NH_3 produced in the experiment is negligible. In this way we can eliminate this molecule and other equation and have a system with 4 equations (16-19 amu/e) and 4 molecules (NH_2D, NHD_2, H_2O, HDO). By solving this system and considering similar pumping speeds and calibration constants for water and ammonia (a gas calibration for water was not possible), a solution was obtained for the percentage mixture composition that is presented in table 2.6.

Molecule	**Percentage in the mixture**
NH_2D	44.0
NHD_2	33.2
H_2O	11.7
HDO	11.1

Table 2.6. Results of the RGA signal deconvolution simplified to only NH_2D, NHD_2, H_2O and HDO determination. NH_3 and D_2O are not included in the analysis

This assumption (and the concomitant result) does not seem very realistic due to presence of hydrogen, and water (H_2O) impurities on the tungsten surface environment and the isotope exchange process that leads to the production of hydrogenated ammonia instead the deuterated molecules as has been previously commented.

2.2.2.2. N_2 GD plasma on a W wall saturated with deuterium

The mass spectrum evolution over time for the experiment is shown if figure 2.14. As in the previous and symmetric experiment, the first part of the spectrum corresponds with a gas injection (in this case nitrogen). During this gas puffing a clear increase in the 18 amu/e and 19 amu/e signals can be observed, being the increase in the 20 amu/e smaller. No significant increase in 17 amu/e is detected. In the subsequent plasma phase these signals decrease until the background level before the injection of nitrogen and the 2 amu/e (H_2), 3 amu/e (HD) and the

30 amu/e (NO) RGA signals increase. No changes in the 17 and 20 amu/e signals are found during the plasma phase. This experimental observation can be interpreted in this way: during the N_2 gas puffing there is a decrease in the pumping speed of the system due to the increasing pressure (N_2 gas inlet) and the concomitant change in the pumping efficiency of the turbo-molecular pump, in this way the residual level of water molecules increases (mainly 18 and 19 amu/e signals). Due to the H/D isotope exchange reactions of this residual water on the deuterium saturated tungsten wall, amounts of partially (DHO) and totally (D_2O) deuterated water are produced. These molecules contribute also to the increase in the 19 and 20 amu/e signal that are visible in figure 2.14.

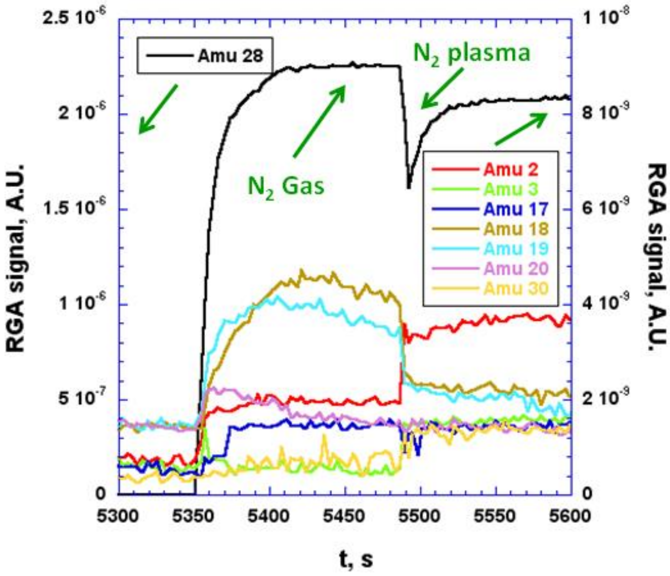

Figure 2.14. N_2 GD plasma on a W wall previously saturated with a D_2 GD plasma

During the plasma phase these molecules of water are decomposed, producing the depleted hydrogen and deuterium the H_2 and HD molecules that increase 2 and 3 amu/e traces in the RGA spectrum. The oxygen depleted from the water molecules produces NO molecules due to interaction with the nitrogen active atoms that are being trapped on the tungsten surface. This NO production can be seen as an increase in the 30 amu/e signal during the plasma phase. Although there is no a direct calibration of the involved species, the comparison of the time integrated values of 18 amu/e and 19 amu/e increase during the gas phase and the subsequent integrated values for the increase of the mass traces of HD and H_2 during the plasma phase shows a ratio around 0.9. This result also points to the water molecules cracking during the N_2

plasma and their conversion into HD and H_2. This calculation together with the formation of NO that happens in the system during the plasma phase seems to corroborate our assumption about the water contamination and shows qualitatively that no ammonia is significantly produced in this symmetric experiment. Hence, once again, it is demonstrated that the presence of dissociated nitrogen on the W surface is the first mandatory step necessary to trigger the ammonia formation process. The previously implanted deuterium atoms from the first plasma have a larger implantation range compared to the nitrogen ones. According to this premise, the nitrogen atoms depleted from the plasma could not interact with the deuterium atoms present (deeper) on the W surface, thus precluding the formation of ammonia.

2.2.3. Conclusions

- Despite the simplicity of the experiments and the impossibility of accurate determinations of the mass spectra that could proportionate the necessary data for the quantification of the produced species, these results are useful for a qualitative characterization of the involved processes.
- In the first experiment, the previous presence of nitrogen leads to the formation of ammonia when the wall is bombarded with D_2 plasma. On the contrary when nitrogen is not present on the wall previously, ammonia is not formed, thus confirming that the limiting steps in the reaction are the dissociation (in the plasma phase or on the wall) and the adsorption of N atoms (on the active sites of the wall).
- Although the nitrogen plasma of the second experiment produces the dissociation of nitrogen and thus, the N atoms can be adsorbed on the wall and react with the deuterium ones present on the wall through L-H recombination, this does not happen. For an L-H recombination the adsorption of N and H species must take place in determined catalytic active centres of the surface with sufficient energy to recombine. However it is well-known that the implantation range of deuterium on tungsten is significantly larger compared to nitrogen. Hence as a consequence of the experimental procedure the deuterium plasma loading will accumulate the D atoms in positions deeper compared to the posteriorly loaded nitrogen ones, thus precluding the mutual interaction of N and D and the formation of ammonia. Diffusion into the bulk of the previously loaded deuterium or the insufficient energetic content of the deuterium present on the wall can also preclude the effective N-D recombination. However the first experiment shows that

the saturation of the catalytic centres with nitrogen does not preclude the ammonia formation process. The subsequent impinging deuterium particles can react via E-R recombination or by means of L-H recombination as the impinging deuterium atoms can interact with the previously loaded nitrogen (implantation range of nitrogen smaller than deuterium).

- With the RGA measurements only the characterization of the global reaction products is possible, being impossible differentiate if both mechanisms are taking place on the W wall at the same time. To perform this investigation and study in a broader way the chemical mechanism of the ammonia formation, complementary techniques that involve the *in situ* diagnosis of the wall state with direct measurements that can detect the presence of adsorbed species and radicals would be necessary.

2.3. INFLUENCE OF RESIDENCE TIME AND HELIUM ADDITION IN THE AMMONIA FORMATION ON TUNGSTEN WALLS

2.3.1. Experimental setup

The used setup and the experimental procedure are exactly the same that were used in the previous experiments. Once again, the main used diagnostic was the differentially pumped mass spectrometry. In this case a different mass spectrometer (SRS 100 residual gas analyser) was utilized compared to the employed in the experiments detailed in chapter 2.1. In all instances, the inner wall ($A=0.14\ m^2$) of the SS liner placed inside the plasma chamber was totally covered with a cold-rolled tungsten sheet in order to study the experiments on this PFM. The surface temperature of the tungsten wall was kept constant at 200ºC and the total pressure of the discharge was 2 Pa in all instances. The discharge characteristics during the experiments were: N_2 plasma concentration around 3%, discharge voltage between 300-400 V, plasma current of 200-350 mA and hydrogen/nitrogen fluencies up to $10^{23}\ m^{-2}$ (calculated from the depleted gases integrated over the total time of the experiment (around 1.5-2 hours).

A complete wall conditioning, that assures a good reproducibility, was carried out before the experiments including: irradiation of the W wall with pure Argon DC-GD plasma and wall outgassing and baking up to 200ºC. Two different types of experiments were performed:

- Experiments with N_2-H_2 DC-GD plasmas with different residence times for the plasma species. The pumping efficiency of the system was decreased by changing (reducing) the vacuum conductance of the pumping duct (occluding it partially). Three different residence times for N_2 molecules (τ_{N_2}) were studied: 25, 50 and 100 ms.
- Experiments with N_2-H_2-He DC-GD plasmas using a $\tau_{N_2}=100$ ms, scanning the helium plasma content from 0 to 8%.

All the experiments were performed following the same strategy previously used and explained in chapter 2.1. Finally, absolute calibration works (equivalent to the explained in the subchapter 2.1.1.4.) were performed to correlate the single mass spectrometry signals (28, 2, 17 and 4 Amu/e) with the associated partial pressure and flux of N_2, H_2, NH_3 and He. In most of the experiments the residual water levels were low enough to ignore the contribution of residual water molecules to 17 Amu/e. Anyway these levels were checked, in order to subtract these contributions when they were not negligible. The possible contribution of CO molecules to 28 amu/e signal can be considered as negligible due to the its very low residual level. The ultra-high vacuum experimental conditions assure that this contribution is absolutely negligible in comparison with the N_2 gas puffing injected in the experiments. Additionally, Optical Emission Spectroscopy (OES) measurements were performed in order to estimate the electron temperature (T_e) and its changes during the helium addition to the plasmas, performing a 400-750 nm wavelength scan.

2.3.1.1. Optical Emission Spectroscopy

Emission spectroscopy is frequently used in plasma physics for qualitative and quantitative characterization of plasmas. In general this technique can be used for a wide variety of plasmas being a non-invasive, flexible and very useful diagnostic. The main application of such measurements is the detection of plasma species and impurities that are basic for the determination of the plasma composition, as well as the determination of important plasma parameters as electron temperature (T_e) and density (n_e). The measurements are performed for glow discharge plasmas, in which the collisions of plasma particle with electrons cause the excitation of the species to higher electronic levels (forming ions, excited neutrals or metastable species). The global emission of the plasma during the discharge can be considered as a mixture of all the individual spectral lines produced by the specific electronic transitions of the plasma constituents, including the impurities generated from the interaction of the plasma with the surrounding materials (in this case mostly tungsten). When these species are relaxed from excited to ground state levels, they emit light at their specific line radiation characterized by the wavelength. The wavelength of the spectral line gives the identity of the element while the intensity of the emitted light is proportional to the number of excited species of the element. The light coming from the plasma through the optical window is focused and concentrated before being directed to a diffraction grating (monochromator) that separates the different line radiation that compose the global plasma emission, depending of their wavelength. After this wavelength selection, the different lines are detected by the sensor, thus forming the emission spectra. For a better detection and quantification, normally the collected line signals are amplified to distinguish them from the background (noise) level. This action is carried out by the photomultiplier. It contains a photocathode that receives the photons from the monochromator. The photocathode material ejects electrons due to the photoelectric effect. These electrons are directed to the anode of the photomultiplier passing through specific electrodes (dynodes) that emit more electrons (secondary emission) when the primary electrons from photocathode collide with them. The dynodes are held with a sequential positive voltage that contributes to direct the generated electrons until the last dynode that acts as the anode of the photomultiplier. Generally a number of ten-twelve dynodes are used to generate the necessary amplification (normally in a factor 1000-10000) of the signal that is finally measured as a voltage with a voltmeter and visualized in a computer screen.

In these experiments, the OES diagnostic consists of a focusing lens that directs the plasma emitted light to the monochromator (Oriel 77250) in order to select the registered wavelength during the plasma operation. Then, a 400-750 nm wavelength scan in the visible region of the electromagnetic spectrum is performed with a resolution of 0.2 nm. The used photomultiplier, (Hamamatsu R3896) was chosen due to its high efficiency spectral response for the measured wavelength. The applied voltage to the photomultiplier was around 500-600 DC

Volts in order to optimize the signal intensity, minimizing the noise contribution. A schematic view of the diagnostic can be viewed in figure 2.15.

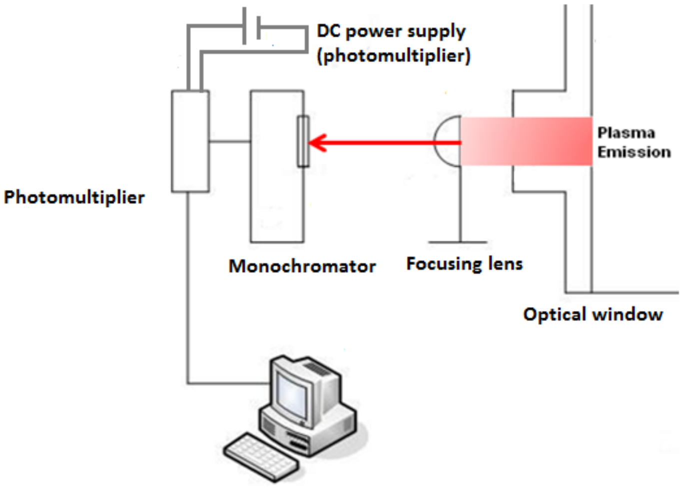

Figure 2.15. **Scheme of the Optical Emission Spectroscopy (OES) diagnostic**

2.3.2.2. Absolute calibration work for N_2 and NH_3 and He

In these experiments a different mass spectrometer (SRS 200) was used, compared to the previous first ammonia formation experiments (chapter 2.1.2). For this device, new calibration works were necessary to correlate the principal RGA measured signals (2, 4, 17 ad 28 amu/e) to the partial pressure and fluxes of hydrogen, helium, ammonia and nitrogen respectively. This calibration allows to the determination of the pumping speed and calibration (RGA) constant for the different species. The utilized method was exactly the same compared to the previously explained in the subchapter 2.1.1.4. Once these parameters are determined, the calculation of the ammonia formation yields, fluxes and partial pressures was performed following the explanations that can be found in the subchapter 2.1.2.4. The residence time for the nitrogen molecule in the plasma chamber was calculated as: $\tau_{N_2}=V/S_{N_2}$, where V is the volume of the plasma (5.4 L) defined by the liner shape and geometry (cylindrical) that confines it. For the experiments with different residence time for the nitrogen molecule, the calibration was performed for N_2 and NH_3. Additionally for the experiments with τ_{N_2}=100 ms the calibration work for helium was also necessary to estimate the helium concentration in the plasma (f_{He}). Extending the calculation explained in the subchapter 2.1.2.4, the partial pressure of helium was calculated, (using the 4 amu/e signal and its calibration constant) finally normalizing it to the total pressure (2 Pa):

$$f_{\mathrm{He}} = \frac{p_{He}}{p_T} = \frac{\dfrac{4amu/e}{K_{He}}}{\sum \dfrac{amu/e}{K_i}} \quad . \quad (2.25)$$

The different calibration parameters and residence times for N_2 used in the experiments are shown in table 2.7.

	Particle	**S, L/s**	**Calibration constant, K**
τ_{N2}=25 ms	N_2	210	1,95E-07
	NH_3	155	4,97E-08
τ_{N2}=50 ms	N_2	110	1,20E-07
	NH_3	69	3,54E-08
τ_{N2}=100 ms	N_2	55	1,16E-07
	NH_3	42	6,30E-08
	He	35	4,32E-08

Table 2.7. Results from the calibration work for N_2, NH_3 and He for the different experimental conditions

2.3.3. Experimental results and discussion

2.3.3.1. Influence of τ_{N_2} in the ammonia formation on W walls

In figure 2.16 the absolute ammonia formation yields deduced from the experiments for the different nitrogen residence time values (τ_{N_2} of 25, 50 and 100 ms), are shown depending on the N_2 cracking efficiency parameter (calculated as $\Delta N_2/N_2^{inj}$).

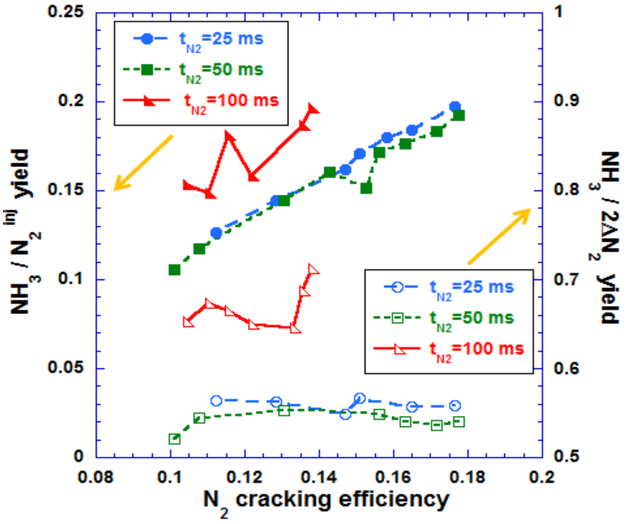

Figure 2.16. Deduced ammonia formation yields related to N_2 cracking efficiency for the different reactor conditions defined by τ_{N_2}

As can be seen, there are no significant differences between the ammonia formation yields for τ_{N_2} =25 ms and 50 ms. For all τ_{N_2} the yields normalized to the injected nitrogen present a linear dependence with nitrogen cracking efficiency while the $NH_3/2\Delta N_2$ yields are approximately constant and independent of this parameter. These yields are also very similar compared to findings shown in the previous subchapter obtained for an intermediate residence time (approximately 40 ms). On the other hand, both yields for a reactor configuration with τ_{N_2} =100 ms are a 25% larger than those of the other two reactor configurations, for similar values of $\Delta N_2/N_2^{inj}$. For the case of the NH_3/N_2^{inj} yield at this residence time of 100 ms, there is an experimental point (around 0.12 of cracking efficiency) that is deviated from the clear linear trend of the other two cases. This deviation is probably caused for the uncertainties associated with the experimental system. For the case of highest residence time (100 ms) the experimental plasma became more unstable compared to the cases of 25 and 50 ms. These instabilities produced that the plasma could touch a higher surface area inside the chamber (not only the W liner that confined it). In this way the recombination into ammonia (and the associated formation yield) would be increased. These experimental issues are probably the cause of this anomalous behaviour that gives a higher NH_3/N_2^{inj} yield for this experimental point compared to the expected from the linear trend.

From the gas phase balance at steady state for a given molecule (A) the dependence of its concentration (expressed as [A]) with the residence time can be deduced:

$$V\frac{d[A]}{dt} = [A]_0 \cdot S - K_{dis} \cdot n_e \cdot [A] \cdot V - [A] \cdot S = 0 \rightarrow [A] = \frac{[A]_0}{1+K_{dis} \cdot n_e \cdot \tau}. \quad (2.26)$$

In this expression V is the reactor volume, S the pumping speed for the gaseous specie, K_{dis} is the dissociation constant of the molecule in the plasma that depends on the electron temperature (T_e) [64], n_e the electron density of the plasma, and τ is the residence time in the reactor (calculated as V/S). Applying this balance to ammonia and nitrogen the general expression, (also applicable to different plasma devices), is obtained. It gives the dependence of the NH_3/N_2 ratio with the plasma parameters (T_e, n_e) and the reactor conditions (τ):

$$\frac{[NH_3]}{[N_2]} = \frac{[NH_3]_0}{[N_2]_0} \cdot \frac{1+K_{dis}^{NH_3} \cdot n_e \cdot \tau_{NH_3}}{1+K_{dis}^{N_2} \cdot n_e \cdot \tau_{N_2}}. \quad (2.27)$$

Unfortunately measurements of plasma parameters (T_e, n_e), for the different reactor conditions, that could enable a complete analysis of the residence time effect in the ammonia formation, are not available for these experiments. Previous estimations using a simple Langmuir probe gave electron temperatures around 1.5 eV and densities of $1\text{-}3 \cdot 10^{10}$ cm^{-3} for an intermediate residence time of 40 ms (chapter 2.1). However, it is important to note that the uncertainties of these measurements are high due to the significant error associated to the single probe measurements and the determination in plasmas with very low electron temperatures (~1-2 eV). These effects together with an exhaustive analysis of the electron temperature changes in the plasma (T_e estimations using helium line emission measurements) will be analysed in the following chapter about the ammonia formation in N_2-H_2-He DC-GD plasmas.

2.3.3.2. Ammonia formation in N_2-H_2-He plasmas

The presence of helium as an intrinsic impurity that will be produced from D-T nuclear reactions in the plasma core of a fusion reactor can also affect the ammonia formation in a hypothetic future ITER nitrogen-seeded plasma operation. The intense surface bombardment with energetic helium ions can modify the surface on the PFCs and the chemistry that determines the ammonia formation. Furthermore, important plasma parameters in the SOL region can be also affected, and the associated effect in the ammonia formation is difficult to predict. Several experiments involving N_2-H_2-He plasmas have been performed at different helium plasma contents (f_{He}) in order to study the modification of the ammonia formation induced by the presence of helium. The energetic content of helium ions is assumed to be determined by the discharge voltage. As this parameter is between 300-400 V, the energy of these particles was around 300-400 eV, that is a much higher value compared to the energy transferred to the impinging particles in the divertor region due to the acceleration in the plasma sheath (around some tens of eV). In figure 2.17 the ammonia formation yields (for a τ_{N_2} of 100 ms) is presented for the case of N_2-H_2 plasma and three different N_2-H_2-He plasmas ($f_{He} \approx$ 1.5, 3 and 8 %).

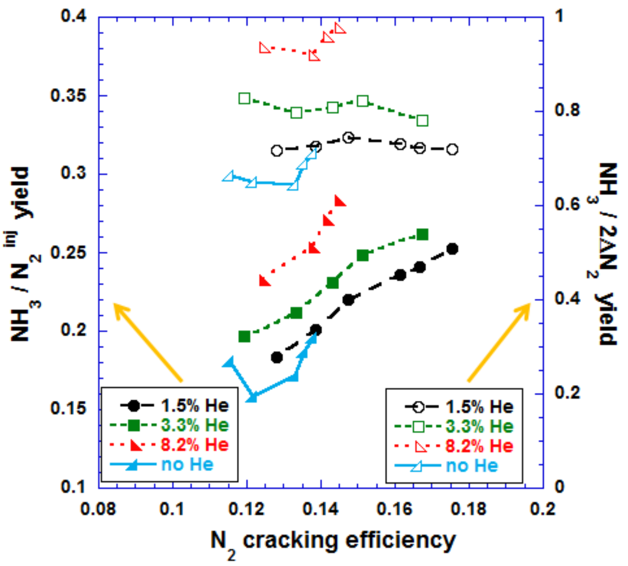

Figure 2.17. Ammonia formation yields related to N_2 cracking efficiency in N_2-H_2-He plasmas with different helium content at at τ_{N_2} of 100 ms

Both yields are increased up to a 45% factor for increasing helium plasma content by comparing values with similar nitrogen cracking efficiency. In principle, the improved ammonia formation could be affected by changes in the plasma parameters (T_e mainly) as well as modifications on the surface chemistry. Moreover, the helium addition in the plasma can change the pumping efficiency of the system, modifying the RGA detection of species and the calculated ammonia formation yields. This effect will be analysed in the next subsection.

2.3.3.2.1. Effects of helium addition in the RGA measurements

Helium is a small particle that can decrease the pumping efficiency of turbopumps when is injected in a gas mixture. This effect would decrease the effective pumping speed for the different species of the mixture, thus increasing the partial pressures and changing the signals obtained with the RGA. Although in ITER no change in the pumping speed is expected due to the presence of helium inside the vacuum vessel, this effect can be important and must be evaluated in our experiments. To calculate the ammonia formation yields we convert the measured RGA signals in the detection chamber, to absolute values in the plasma chamber using the calibration work that relates single RGA signals with partial pressures and fluxes. As the single pumping speed for the different molecules depends on the molecular mass, each molecule is affected in a different factor by the presence of helium, thus affecting the measured RGA signal ratio and the calculated ammonia formation yields. To evaluate the relative changes in signals of 17 amu/e and 28 amu/e, a gas test was performed. In this test, a NH_3-N_2-H_2 gas mixture at constant pressure (2 Pa), with different amounts of helium (keeping approximately constant the N_2 and NH_3 contents and decreasing the H_2 input at the same time that the He content is increased) was monitored, measuring the evolution of the signals 17 amu/e and 28 amu/e and calculating the ratio between them (previously subtracting the background level of both signals). The composition of the gas mixture was similar to the plasma experiments: N_2 fixed content around 3%, being NH_3 content approximately 7-8 times lower than N_2 content. The helium content in the gas mixture was varied from 0 to 8%. The results of this test showed that while the signal at 28 amu/e (directly related to nitrogen) is not changed by the helium injection, the signal at 17 amu/e (directly related to NH_3) is increased up to a 7% factor for the highest helium contents in the gas mixture, while the signal at 18 amu/e (water as it has a contribution to 17 amu/e) remains low, thus assuring that these changes are not caused by gas inlet contamination Consequently the 17/28 amu/e ratio is increased in the same factor compared to the 17 Amu/e signal. These changes are equivalent to a decrease (7%) in the pumping speed of ammonia while the residence time is increased in the same factor. As the signal related with nitrogen was not significantly modified by the presence of helium, the changes in pumping speed and residence time for nitrogen can be considered as negligible.

In figure 2.18 the evolution of the 17/28 Amu/e ratio (named as $F_{17/28}$ parameter that is represented in the left y-axis of the figure) normalized to the value with no helium content is presented.

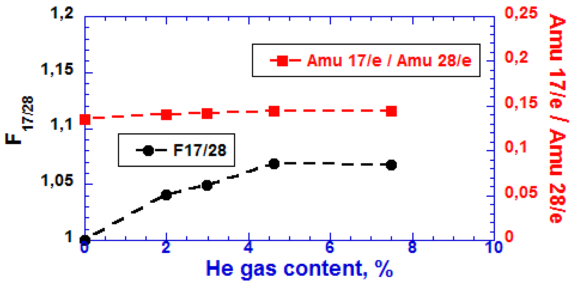

Figure 2.18. Evolution of the 17/28 amu/e ratio normalized to the value with no helium content ($F_{17/28}$) for the helium plasma content covered in the experiments

This parameter shows the normalized increase in the 17/28 amu/e ratio (represented on the right y-axis of the figure) due to the injection of helium and the concomitant change in the pumping speed of the system. The injection of helium increases the parameter $F_{17/28}$ up to 7% for helium concentrations in the gas mixture close to 8%, but the enhanced ammonia yields observed in the experiments cannot be totally explained by this effect.

2.3.3.2.2. The general plasma-surface chemistry in the ammonia formation and the influence of T_e in the process

The formation of ammonia takes place on metal walls that act as a heterogeneous catalyst. Surface recombination between nitrogen and hydrogen neutrals produces N-H radicals that are hydrogenated in consecutive steps until the formation of ammonia molecules that are finally desorbed from the walls [65]. Ions coming from the plasma can also be dissociated on actives sites of the walls providing active species for the formation process and NH_x radicals present in the gas phase may recombine on the surface producing ammonia. The desorbed ammonia molecules can be also destroyed in the plasma before leaving the plasma chamber (dissociation reactions that depends on T_e). The recombination reactions can happen following two mechanisms: Langmuir-Hinshelwood (L-H) reactions between two adsorbed species or Eley-Rideal (E-R) reactions between adsorbed species and impinging neutrals. Hence, in our plasmas the generation of ammonia is supposed to be produced by a mixture of L-H and E-R surface recombination reactions. These surface chemical processes are supposed to be independent on the electron temperature. Before these surface steps, the presence of the active species (neutrals, radicals and ions) on the W wall is necessary to start the process. These neutrals are generated in the plasma (ionization and dissociation) by means of electron impact processes.

Changes of the electron temperature can modify the ionization-dissociation of N_2 and H_2 molecules increasing or decreasing the content of the active species on the walls, and finally affecting the amount of produced ammonia. Moreover, these changes may affect to the dissociation of the produced ammonia molecules. Taking into account the rate coefficient expressions for the ionization/dissociation of nitrogen (source terms for ammonia formation) and for the dissociation of ammonia (sink terms) and their dependences with T_e [64], an estimation of the possible effect of the electron temperature in the global process, can be done. In figure 16 the ratio between the sum of ionization and dissociation rate coefficients for the N_2 molecule over the sum of the dissociation rate coefficients for the ammonia molecule is presented. This ratio gives an idea about the net effect of the electron temperature changes in the ammonia formation process and is defined as:

$$R = \frac{D_{N_2}+I_{N_2}}{D_{1_{NH_3}}+D_{2_{NH_3}}} . \quad (2.28)$$

In this expression D_{N_2} is the rate coefficient for the electron impact dissociation of nitrogen, $I_{N_2}$is the rate coefficient for the electron impact ionization of nitrogen to produce N_2^+ ions. The divider terms $D_{1_{NH_3}}$ and $D_{2_{NH_3}}$are the rate coefficients for the two possible routes for the electron impact dissociation of the ammonia molecules [64]. Only one electron impact ionization reaction (to produce molecular N_2H^+ ions that are the dominant in our plasmas [67]) for the N_2 molecule has been taken into account. The amount of N^+ ions is supposed to be very low in DC-GD plasmas, so this ionization process can be considered as negligible. Assuming that the wall chemistry parameters are not affected by changes in the electron temperature, then figure 2.19 shows that in the range of 2-12 eV an increasing electron temperature can enhance the ammonia formation because ionization/dissociation of nitrogen are more favoured than dissociation of ammonia molecules.

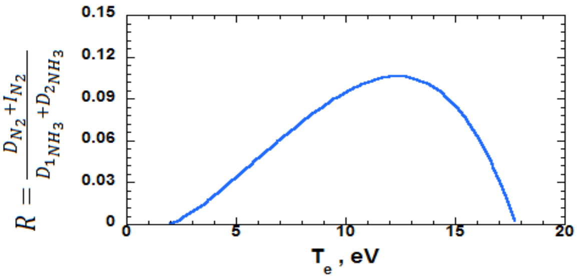

Figure 2.19. Electron temperature dependence of the ratio between the sum of dissociation and ionization rates coefficients for N_2 over the sum of the rate coefficients for NH_3 dissociation

The N_2 cracking efficiency parameter also gives a direct measure of the net depletion of nitrogen and the amount of nitrogen neutrals and radicals (precursors of the ammonia molecules) produced in the plasma. If the electron temperature of the plasma is increased (between 2-12 eV) due to the presence of helium, according to the previous result the nitrogen cracking efficiency measured in the experiment should show an increment with higher He plasma contents. To analyse this possible effect, the dependence of the N_2 cracking efficiency with the Helium plasma content for different plasma currents (250, 300 and 350 mA) is represented in figure 2.20. In all the cases the value of the discharge voltage was approximately constant (around 325-350 V) and consequently the experimental conditions (for different helium contents) are comparable.

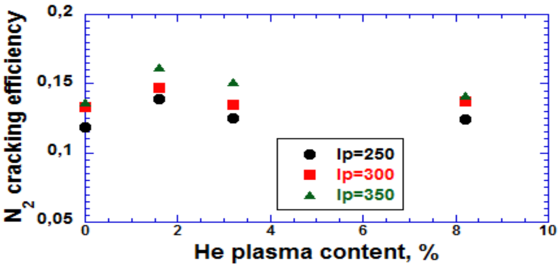

Figure 2.20. Evolution of the N_2 cracking efficiency with helium plasma content for several plasma currents

Although a light increase (≈10%) in the N_2 cracking efficiency is seen for the case of 1.6% of helium plasma content, for a higher content the values are very similar compared to the case of no helium. However the ammonia formation yields for the highest helium content are increased up to a 45% factor. This result would indicate that the plasma electron temperature (together with the concomitant dissociation/ionization of nitrogen) is not significantly affected by the presence of helium in the plasma. In any case in the next subchapter the electron temperature of the plasmas will be evaluated.

2.3.3.2.3. Evaluation of T_e in N_2-H_2-He plasmas using helium spectroscopy

To analyse if the enhanced ammonia yields obtained from the experiments can be attributed to changes in the electron temperature, estimations of this parameter have been performed by using helium optical emission spectroscopy. In order to estimate the electron temperature in our plasmas a theoretical calculation of several He lines ratios ($R_{728/667}$, $R_{706/667}$ and $R_{504/471}$) has been done taking into account the T_e dependence of the cross sections for the different He excited levels [77] in the case of a low density plasma ($n_e = 2{\cdot}10^{10}$ cm^{-3}, similar density compared to our plasmas). With these values the line ratio can be calculated by correcting the theoretical population levels with the corresponding atomic transition probabilities [78]. Finally comparing the experimental values with the theoretical ones, the electron temperature in our plasmas for the different helium contents can be estimated.

In figure 2.21a the theoretical dependence of the selected line ratios with the electron temperature is presented and in figure 2.21b the corresponding estimations of this parameter from the He line emission in the N_2-H_2-He DC-GD plasmas is shown. According to the experimental data, the electron temperature would be in the range of 2-5 eV depending on the used line ratio. He lines are weak when He content in the plasma is low and consequently the associated error in the T_e calculation increases. Hence, only at the highest He content the T_e estimation is reliable enough, being the evolution of this parameter with the helium addition uncertain. Moreover the analysis of the changes in the nitrogen cracking efficiency with helium content in the plasma, suggests that the electron temperature is not significantly modified by the presence of helium. As was explained previously, an increase in the electron temperature in this range would lead to a higher ammonia formation in our DC-GD plasmas, although is necessary to take into account that in ITER, the electron temperature along the divertor region, is not expected to be modified by the presence of helium. Nonetheless according with these estimations, the influence of this effect in the enhanced ammonia formation observed in the experiments with increasing helium plasma contents cannot be confirmed.

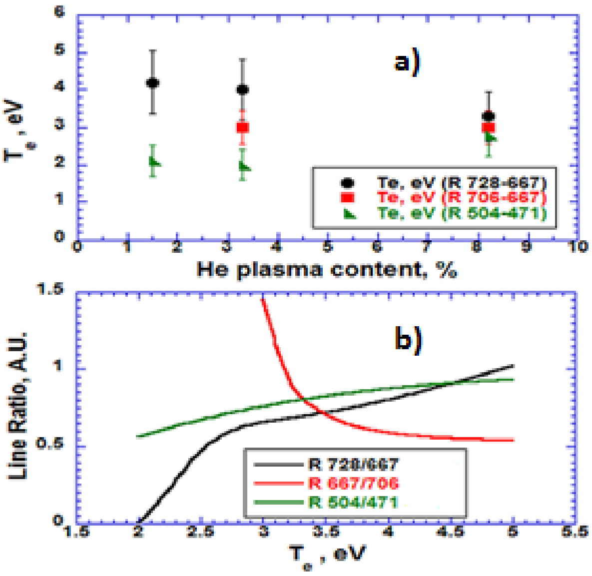

Figure 2.21. a): corresponding estimations of T_e for the He emission from N_2-H_2-He DC-GD plasmas with different helium content. b): theoretical dependence of selected He line ratios with T_e.

2.3.3.2.4. Possible modification of the surface chemistry induced by the helium bombardment

The wall bombardment with imping energetic helium ions or meta-stables from plasma can alter the chemistry between N and H on the W surfaces, then modifying the active surface centres where the L-H and E-R recombination reactions take place. Particle induced desorption and sputtering could also increase the surface roughness (and the effective recombination area) and the total number of free centres available for recombination. Moreover, the impact of chemically inert projectiles (He) can affect the activation of the surface free centres for N-H recombination (plasma activation). These effects might increase the rate coefficients for the recombination into ammonia. In table 2.8, the nitrogen (N_{ret}) and hydrogen retention (H_{ret}) on the W wall after reaching the steady state (calculated by particle balance, as in the calculations presented in subchapter 2.1.2.3) and the hydrogen flux (H_{imp}) calculated from the depleted hydrogen in the plasma are presented depending on the helium plasma content (f_{He}).

f_{He}, %	N_{ret}, m^{-2}	H_{ret}, m^{-2}	H_{imp}, $m^{-2}s^{-1}$
0	$1.5 \cdot 10^{21}$	$6.3 \cdot 10^{20}$	$1.1 \cdot 10^{19}$
1.6	$9.5 \cdot 10^{20}$	$4.2 \cdot 10^{20}$	$1.3 \cdot 10^{19}$
3.3	$1.2 \cdot 10^{21}$	$3.7 \cdot 10^{20}$	$1.2 \cdot 10^{19}$
8.2	$7.5 \cdot 10^{20}$	$3.1 \cdot 10^{20}$	$1.1 \cdot 10^{19}$

Table 2.8. Nitrogen and hydrogen retention on the W wall and impinging H flux (steady state) for the different helium plasma contents

Assuming that L-H recombination takes place between adsorbed N and H atoms and E-R recombination occurs between adsorbed N and impinging H atoms (according to the results of chapter 2.2 the symmetric E-R recombination can be ruled out), the normalized products $(N_{ret}*H_{ret})_{norm}$ and $(N_{ret}*H_{imp})_{norm}$ gives an idea about the amount of active species available to produce ammonia. These values are presented in figure 2.22.

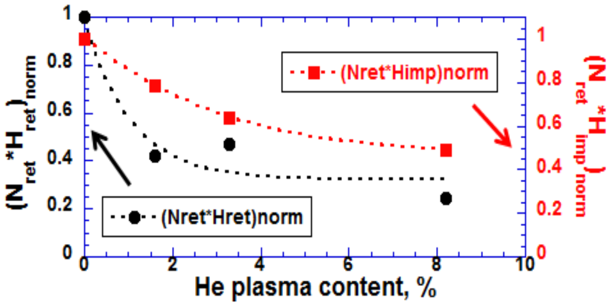

Figure 2.22. Normalized surface chemistry parameters for the different helium plasma contents. Dotted lines are just a guide for the eye

In general, both parameters decrease with increasing helium content. Hence, the quantity of the species present on the surface does not increase with the helium content, but the obtained ammonia formation yields are higher, pointing to enhanced N-H recombination induced by the helium bombardment as the key factor behind the higher ammonia formation. It is important to note that with these calculations is not possible to distinguish if the proportion of chemically active species (not implanted) is changing. In any case, to analyse the underlying chemistry in a more accurate way, experiments able to discern among these factors and with suitable diagnostics to analyse the ion/neutral composition of the plasma and to monitor the state of the surface are necessary.

2.3.4. Conclusions

- The effects of increasing residence time for nitrogen (τ_{N_2}) and the presence of helium in the ammonia formation in N_2-H_2-(He) DC-GD plasmas has been analysed. While a change of τ_{N_2} from 25 to 50 ms has no measurable effect on the ammonia formation yields, a value of 100 ms increases them up to a 25%.
- The presence of helium enhances the ammonia formation yields up to 45% factor for increasing helium content in the plasma. Three possible factors (induced by the presence of helium) have been analysed to explain this higher ammonia formation: 1) changes in the detection of ammonia by the RGA, 2) increasing electron temperature of the plasma and 3) modification of the surface chemistry induced by the helium bombardment.
- The changes in the ammonia detection by the RGA in helium containing plasmas cannot explain totally the enhanced ammonia formation. Increasing T_e (between 2-12 eV) can determine a more efficient ammonia production but our estimations do not assure that this parameter is increased with the helium addition.
- The surface modification induced by the helium bombardment seems to play a key role that modifies the net ammonia formation. Although the amounts of adsorbed and impinging species that determines L-H and E-R recombination reactions would not increase with the helium plasma content, other factors as the rate coefficients for these reactions, the effective W wall surface for the N-H recombination or the proportion of active/free surface centres could be enhanced by the energetic helium bombardment. This effect together with the changes in the mass spectrometry measurements might explain the enhanced ammonia yields obtained in the N_2-H_2-He DC-GD plasmas.
- To understand these effects, a further investigation (involving neutral/ion analysers and the in situ diagnosis [LIBS] or post-mortem characterization of the surface [XPS, ellipsometry, SIMS…] would be necessary in future works, being the employment of surface analysis techniques completely necessary for a better comprehension and quantification of the involved surface chemistry parameters. These results represent an approximation to the complex chemistry that determines the ammonia formation in a N_2-seeded plasma operation but is necessary to keep in mind that their extrapolation to the conditions of a hot and fully ionized plasma with much higher particle fluxes existing in the divertor of a fusion reactor may be not straight forward. In this sense, it is important

to note that another experiments performed in linear plasma devices and aimed to investigate the influence of helium in the ammonia formation process have obtained different results that show opposite effects of the helium in presence in the ammonia production [79, 80]. An important difference between our plasmas and linear device/divertor plasmas is that the energetic content of the helium ions bombarding the surface is higher, while the particle flux is quite lower. The magnitude of the involved particle fluxes and the energy content of the species seems crucial to compare among these experiments performed under very different experimental conditions.

2.4. STICKING OF AMMONIA ON AISI 304 L STAINLESS STEEL SURFACE TEMPERATURE DEPENDENCE

2.4.1. Experimental setup and procedure

The basic idea of the experiments in this section is to study the equilibrium that is reached in a gas-solid interface. In this case the equilibrium between ammonia gas molecules and the AISI 304 L stainless steel (SS) surface has been studied in several experiments by flowing ammonia gas (at constant temperature and pressure) and monitoring the time evolution of the 17 amu/e signal (directly related to ammonia) with a mass spectrometer (SRS 200) for different surface temperatures. The experimental setup is shown in figure 2.23.

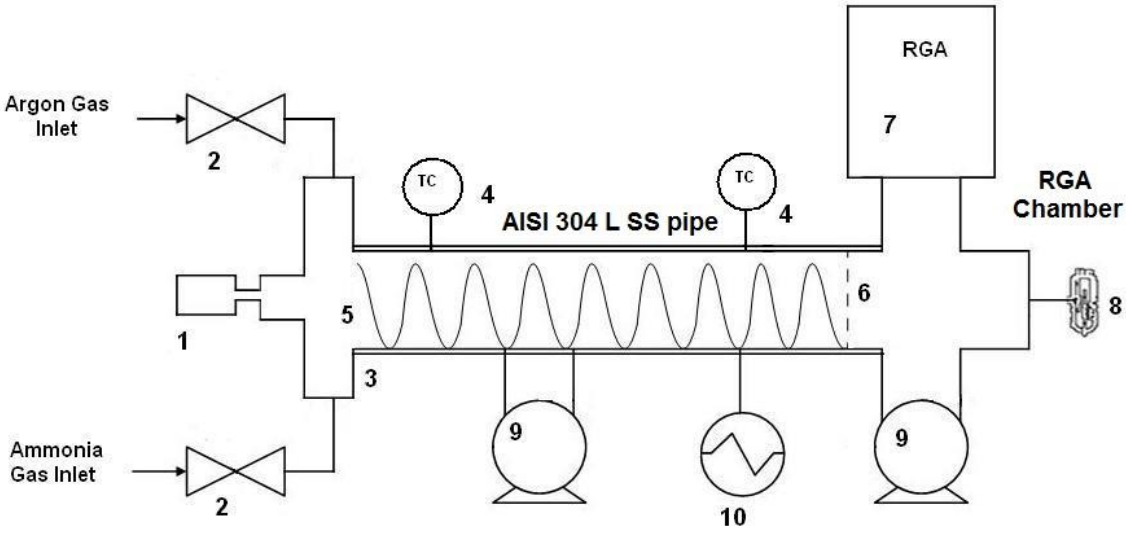

Figure 2.23. General view of the setup: 1. Capacitance manometer, 2. Mass-Flow controller (gas inlet), 3. Isolation elements, 4. Temperature sensor (thermocouple), 5. Heating element, 6.Teflon collimator (differential pumping), 7. Mass spectrometer, 8. Ionization Gauge (Bayard Alpert), 9. Pumping units, 10. Power supply (heating)

It consists on an AISI 304 L stainless steel (a material frequently used for vacuum technology components under magnetic fields) pipe pumped out by a turbomolecular-rotary pump set (base pressure of 10^{-4} Pa measured with an Ionization Gauge). At the beginning of the pipe, the high purity (99.999 %) gases (NH_3 for the experiments and argon for the blank test and cleaning procedure) are separately introduced into the pipe by using two different MKS mass flow controllers. At the end of this pipe, the mass spectrometer is connected to it (using a "T shaped"

AISI 304 L stainless steel connector named as the RGA chamber, with a total surface area of around 150 cm^2) to monitor the experiments following the evolution of the 17 amu/e (main signal for NH_3). The dimensions of the pipe with the total surface exposed to ammonia flow and the main composition of the experimental material are given in table 2.9.

<table>
<tr><th colspan="4">Dimensions of the AISI 304 L SS pipe exposed to NH_3 flow</th></tr>
<tr><th>$\varnothing_{in}$, mm</th><th>L, mm</th><th>S_{in} , cm^2</th><th>$\varnothing_{in}$ / L</th></tr>
<tr><td>35</td><td>400</td><td>440</td><td>0.09</td></tr>
<tr><th colspan="4">AISI 304 L SS composition</th></tr>
<tr><th>% Fe</th><th>% Cr</th><th>% Ni</th><th>ρ, g / cm^3</th></tr>
<tr><td>Balance</td><td>18-20</td><td>8-12</td><td>8.03</td></tr>
<tr><th>% Mn</th><th>% Si</th><th>% N</th><th>% C</th></tr>
<tr><td>2.00 max.</td><td>0.75 max.</td><td>0.10 max.</td><td>0.03 max.</td></tr>
</table>

Table 2.9. Dimensions of the pipe (including the total surface exposed to ammonia flow) and AISI 304 L SS main composition

The mass spectrometer is differentially pumped by another turbo-molecular and rotary pump set until a base pressure of 10^{-6} Pa. To restrict the flow and do not saturate the mass spectrometer, a Teflon disc with a 1 mm diameter hole is placed between the pipe and the RGA port connection. This disc acts as a collimator to provide a differential vacuum environment. With this configuration the ammonia pressure in the RGA chamber during the experiments is two orders of magnitude lower compared to the nominal pressure on the pipe and consequently the amount of adsorbed ammonia in this part of the setup can be considered as negligible. The collimator is made of Teflon (instead of usually used copper or stainless steel) to avoid changes in the conductance (and the concomitant RGA signal) related with possible thermal gradients between a metal collimator and the stainless steel walls of the setup. These changes in the RGA signals due to thermal gradients and conductance changes were observed in preliminary trials and have disturbed the mass spectrometry analysis. A Teflon collimator (due to its low thermal conductivity), prevents the temperature increase of a metal collimator that could change the conductance and the RGA signal measured by the mass spectrometer. The ammonia adsorption in the Teflon collimator and other parts of the system, as in the mass flow controller inlet, can be considered negligible compared to the adsorption on the rest of the setup due to their much smaller area (almost 2 orders of magnitude lower). Moreover the physical interaction between polymeric materials, as Teflon, and the ammonia molecules is supposed to be lighter compared to the case of ammonia on stainless steel [81]. With this strategy more accurate mass spectrometry measurements were also possible due to the presence of very low water (its contribution to 17 amu/e can be considered as negligible) and low impurity content in the RGA proximity.

All the equipment (included the RGA chamber) is heated homogeneously until its nominal experimental temperature (from 323 to 473 K) by using a thermal blanket fed by a power supply. The system is isolated with several layers of mineral wool and isolating blankets. The temperature is measured with two type K thermocouples at different and distant points of the system. The control of the temperature is carried out by a PID controller installed inside the power supply. It is of paramount importance to maintain the temperature homogeneous along the system to reduce ammonia condensation on cold parts in order to avoid systematic errors in the experiments.

To assure their reproducibility, the experiments were carried out after a conditioning procedure that consisted on the heating of the whole pipe until 473 K to desorb the ammonia residual content and water, reducing in this way its mutual and strong chemical interaction. Then a continuous and constant argon flow (p=0.75 Pa) is introduced into the pipe during 1 hour to clean it by dragging the possible rest of adsorbed ammonia and to assure the consistency in the RGA signal over the time. After this, the temperature is kept constant at this nominal value (from 323 to 473 K, depending on the experiment) and a constant flow (≈3.5 sccm) of ammonia gas is introduced. A total pressure of 0.75 Pa (measured with a capacitance manometer) was used in all instances. In principle, only the first monolayer adsorbed directly on the steel surface can be chemisorbed. The rest of monolayers will be adsorbed by means of physical adsorption (physisorption) interacting among themselves by means of electrostatic Van der Waals dipole forces. No significant ammonia decomposition into N_2-H_2 molecules was observed in the RGA spectra (no changes in the 28 amu/e and 2 amu/e signals) during the experiments. This observation seems logical as the first monolayer represents a tiny amount of chemisorbed ammonia molecules. The concomitant generation of hydrogen during this chemisorption would be too small to be detected by the RGA. The increase of the 17 amu/e signal with time is finally monitored by mass spectrometry until it reaches a constant value, i.e. the system is in equilibrium. At this moment the total amount of ammonia molecules that can be adsorbed on the walls is reached.

2.4.1.1. Calibration work for NH_3

An absolute calibration work that relates the single RGA peak (17 amu/e) with NH_3 total pressure and flow was carried out. The calibration was performed following the same procedure explained in the subchapter 2.1.2.4. From the slope of the Flow (sccm) vs p (mTorr) plot the pumping speed for ammonia is deduced using the equation 2.1. The slope of the 17 amu/e vs p (mTorr) gives directly the calibration constant for ammonia that relates the RGA signal with total pressure in the system. The corresponding plots and fits are shown in figure 2.24. A pumping speed of 22.5 L/s and a calibration constant with a value of 2.51e-6 $mTorr^{-1}$ are obtained. With this calibration work, and using a particle balance calculation, integrating the difference of 17 amu/e values between the start of the experiment and when the equilibrium at the 17 amu/e signal is reached, the total amount of retained ammonia by sticking can be obtained.

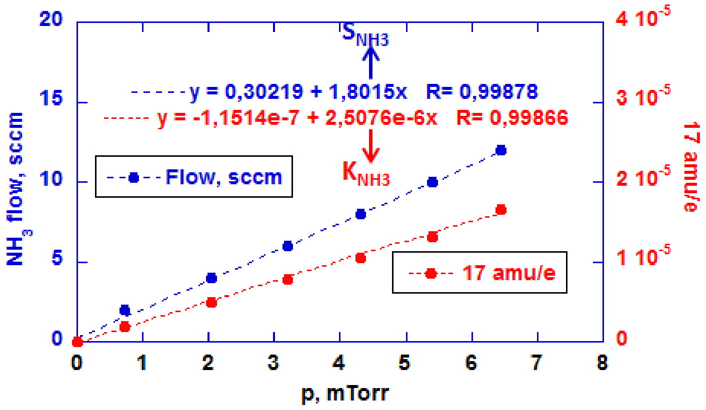

Figure 2.24. Calibration work for NH_3

2.4.2. Experimental results and discussion

In figure 2.25, the evolution of the normalized 17 amu/e signals for different surface temperatures, until its saturation, is represented. These normalized signals are calculated dividing the 17 amu/e values by its maximum value that is reached when the total saturation of the walls and the equilibrium in the system takes place. In this way the maximum value for the this parameter is 1 and the saturation is clearly visible in figure 2.25.

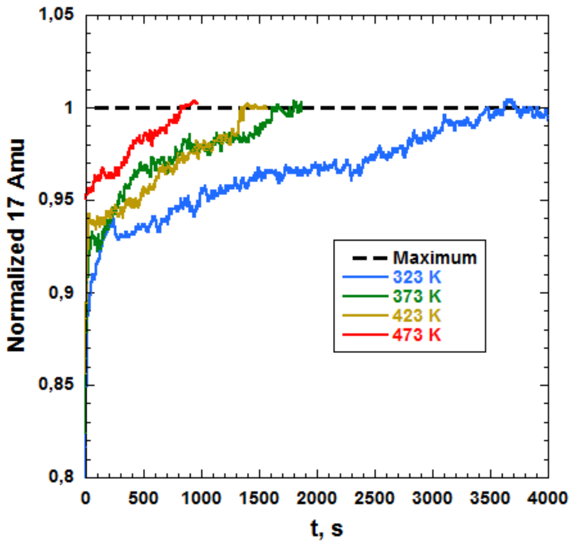

Figure 2.25. Evolution of the 17 amu/e signal for different surface temperatures

Performing an ammonia gas balance in the system, the evolution of the ammonia adsorption rate (n_{ads}) on the SS walls with time is expressed as a sink term:

$$\mathrm{n_{ads}}\,(\mathrm{t}) = \Gamma_{\mathrm{NH_3}} - \mathrm{P}\,(\mathrm{t}) \cdot \mathrm{S} - \mathrm{P}'(\mathrm{t}) \cdot \mathrm{S}', \quad (2.29)$$

where Γ_{NH_3} is the ammonia flow introduced in the system, expressed in molecules/s, P is the pressure in the stainless steel pipe, S the pumping speed of the first pumping unit (placed in the pipe), P' is the ammonia pressure in the RGA chamber and S' the pumping speed of the second pumping unit, placed in this part of the system (see figure 2.23). When equilibrium takes place in the system (at $t=t_{sat}$) the ammonia adsorption rate becomes zero and the total amount of ammonia molecules that can be adsorbed on the SS walls is reached. Unfortunately, direct measurements of the pressure evolution in the stainless steel pipe during the experiments were not possible because a sensor with enough accuracy in this pressure range was not available. Moreover, direct measurements of the pressure evolution in the RGA chamber were rejected due to the water outgassing induced by ionization gauge sensors that would affect the pressure measurements (and also the RGA measurements). Taking into account these experimental particularities, the use of differential pumped mass spectrometry measurements (without simultaneous measurement of the pressure evolution with ionization gauge sensor in the RGA chamber) was considered as the best solution to monitor the ammonia adsorption process in this range of pressure. By measuring the evolution of the 17 amu/e signal, we can relate it with the total ammonia pressure in the SS pipe (the performed calibration work shows a clear linear relationship between both parameters), thus the difference between the value of 17 amu/e when the equilibrium takes place and the value of this parameter in a given time allows calculating the adsorbed ammonia flux in the SS pipe walls. Converting this measurement using the parameters obtained in the calibration work, the absolute rate of stuck ammonia can be calculated:

$$\mathrm{n_{ads}}\,(\mathrm{t}) = [17\mathrm{amu/e(equilibrium)} - 17\mathrm{amu/e(t)}] \cdot \frac{\mathrm{S_{NH3} \cdot n_0}}{\mathrm{k_{NH3}}} \quad . (2.30)$$

In this expression S_{NH3} is the global pumping speed for ammonia in the stainless steel pipe obtained as the slope of the plot that represent flow vs pressure for ammonia, k_{NH3} is the calibration constant for 17 amu/e that relates this RGA signal with ammonia total pressure and n_0 is the Loschmidt number. Finally by integrating the previous expression over the time until t_{sat} and dividing over the surface area of the stainless steel pipe (440 cm^2) the total number of ammonia molecules per unit surface area that are retained on the SS walls for a given temperature is obtained (NH_3 ret). The accuracy of these measurements and calculations is around 10%-15% taking into account the errors associated with the RGA measurements and uncertainties in the estimation of S_{NH3} and k_{NH3}. The dependence of t_{sat} and the concomitant amount of total adsorbed ammonia, obtained by particle balance, with the surface temperature are presented in figure 2.26.

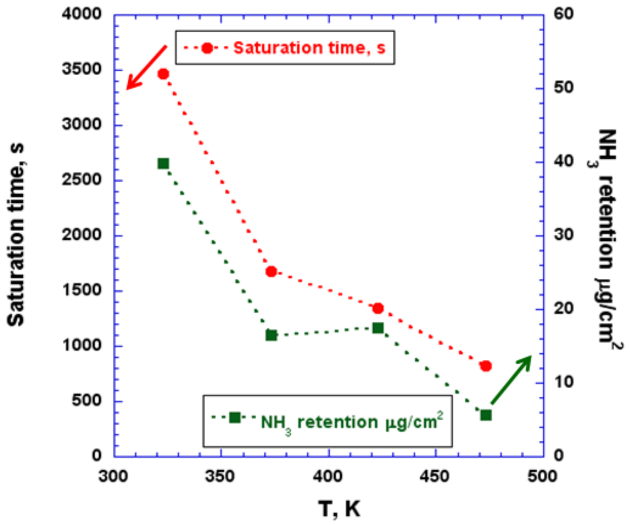

Figure 2.26. Wall temperature dependence of the saturation time and the total amount of retained ammonia. For higher surface temperatures both parameters decrease

A clear trend is visible: the characteristic time for the wall saturation with NH_3 molecules (t_{sat}) is lower for higher surface temperatures. The amount of stuck ammonia decreases clearly with surface temperature except in the range of 373-423 K. For these temperatures the estimated amount of retained ammonia is very similar (around 17 μg/cm^2). The anomalous trend observed in this temperature range is in agreement with previous experimental observations about the ammonia sticking evolution in variable surface temperature experiments [82] but it is necessary to take into account that the experimental uncertainties involved in the calculations and calibrations (10-15%) are higher compared to this small difference in terms of ammonia retention. The obtained results give total ammonia retention values on the SS surface among 5 and 40 μg/cm^2. The sticking coefficient is defined as:

$$Y_{\text{sticking}} = \frac{n_{\text{ads}}\ (t)}{n_{\text{tot}}\ (t)}\ . \quad (2.31)$$

Being n_{tot} the total number of incident ammonia molecules per second, and n_{ads} the adsorbed ammonia flux estimated as the difference between the value of 17 amu/e, when the equilibrium takes place, and the value of this parameter at a given time. The equation to calculate the evolution of the sticking coefficient for ammonia over time can be expressed in this form:

$$Y_{\text{sticking}} = \frac{17\text{amu/e(equilibrium)}\cdot\frac{S_{NH3}\cdot n_0}{k_{NH3}} - 17\text{amu/e(t)}\cdot\frac{S_{NH3}\cdot n_0}{k_{NH3}}}{17\text{amu/e(equilibrium)}\cdot\frac{S_{NH3}\cdot n_0}{k_{NH3}}} = 1 - \frac{17\text{amu/e(t)}}{17\text{amu/e(equilibrium)}}\ . \quad (2.32)$$

In figure 2.27 the time dependence of the sticking coefficient for the different surface temperatures and the subsequent exponential fit is shown.

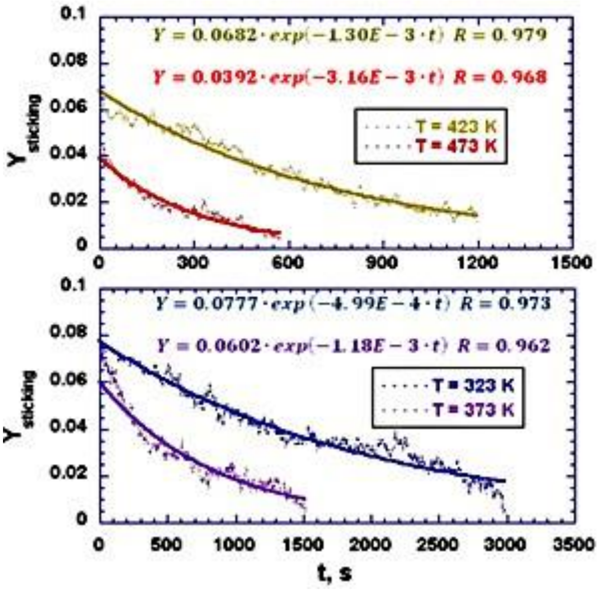

Figure 2.27. Time evolution of the sticking coefficient for the ammonia retention on SS for the studied surface temperatures

These plots show a sticking coefficient strongly dependent on time with maximum values between 0.04 and 0.08. The curves fit with reasonable accuracy to an exponential decay evolution that can be expressed in this form:

$$Y_{\mathrm{sticking}} = Y_0 \cdot e^{-\frac{t}{\tau}} \ . \quad (2.33)$$

From the exponential fit, the experimental parameter τ can be estimated. This value is the characteristic time for the sticking exponential decay observed in the experiments. Assuming that this parameter is inversely proportional to the kinetic constant for the physisorption of the ammonia molecules, and using an Arrhenius fit:

$$K_{\mathrm{ads}} = A \cdot e^{\frac{-E_a}{RT}}; \ \tau \propto \frac{1}{K_{\mathrm{ads}}} \rightarrow \tau = A' \cdot e^{\frac{E_a}{RT}} \ . \ (2.34)$$

An estimation of the activation energy for the process can be deduced as in figure 2.28, resulting in a value of: $E_{\mathrm{activation}}$ = 0.15 eV / molecule ≡ 14.3 kJ / mol.

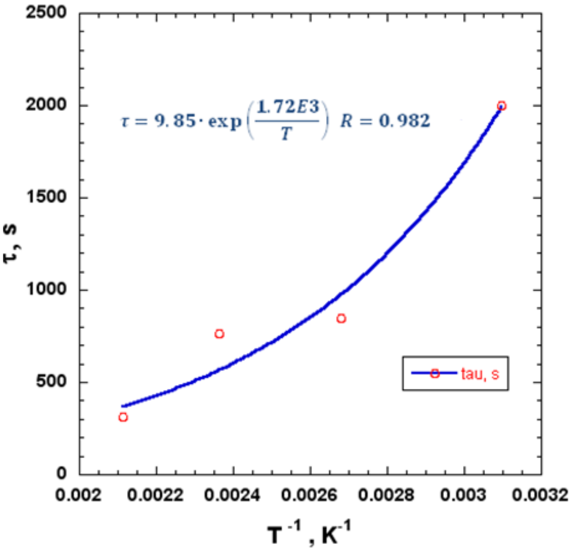

Figure 2.28. Arrhenius fit of the τ parameter for the estimation of the activation energy

Although the accuracy of the fitting seems limited, the experimental estimate gives a reasonable value that is lower compared to the latent heat of vaporization for pure ammonia (23.3 kJ / mol), being in agreement with the energy range for the physisorption of small molecules on metal walls [83]. On the other hand, using a nominal value for the number of ammonia molecules that are adsorbed in a monolayer (assuming one Langmuir ≡ 1.33^{-4} Pa·s ~ $6.2 \cdot 10^{14}$ molecules/cm^2 per monolayer [84]), the total number of ammonia monolayers adsorbed on the SS surface, can be calculated. A summary of the experimental results and calculated parameters including the number of monolayers and the associated hydrogen retention depending on the surface temperature can be found in the Table 2.10.

T, K	t_{sat} , s	τ , s	τ_{norm} , cm^{-2}	NH_3 ret , cm^{-2}	Monolayers	NH_3 ret, μg/cm^2	H ret, μg/cm^2
323	3,468	2,003	1.00E+21	1.41E+18	2200	39.9	7.04
373	1,678	851	4.26E+20	5.84E+17	940	16.5	2.91
423	1,347	767	3.84E+20	6.20E+17	1000	17.5	3.09
473	820	314	1.57E+20	2.00E+17	320	5.6	1.00

Table 2.10. Sticking experimental parameters and estimated NH_3 and hydrogen retention for the different surface temperatures

It is important to note that the experimental parameter τ gives an idea about the physisorption rate of ammonia on the AISI 304 L stainless steel surface for a given wall temperature, T. The extrapolation of the obtained τ (T) values for each wall temperature, to higher flux conditions can be an approximation for the saturation of the surface in pumping lines of relevant fusion devices. By multiplying this time by the nominal flux of ammonia (at steady state conditions) that was used in the experiments (ϕ_{NH_3} ~ $5 \cdot 10^{17}$ NH_3 molecules/$cm^2 \cdot s$) a normalized value of the τ parameter is obtained for each temperature, τ (T)$\cdot \phi_{NH_3}$. The nominal flux of ammonia is calculated by using this expression:

$$\phi_{NH_3} = p \cdot S_G \cdot n_0 / A_{pipe} \quad . \ (2.35)$$

In this expression p is the pressure value of the experiments (0.75 Pa), S_G is the global pumping speed of the system for the ammonia molecules obtained from the absolute calibration work (22.5 L/s), A_{pipe} is the cross sectional area of the pipe and n_0 the Loschmidt number ($2.69 \cdot 10^{19}$ molecules / mbar·L). Finally, this normalized parameter (τ (T)$\cdot$ ϕ_{NH_3}) can be extrapolated to devices with a higher particle flux as ITER, to estimate the necessary time to produce a total coverage of the surface with the NH_3 molecules at a given flux (ϕ_x) and surface temperature:

$$\tau_x = \tau\,(T) \cdot \frac{\phi_{NH_3}}{\phi_x} \quad . \ (2.36)$$

The characteristic regime of the ammonia flow can be defined by using the Knudsen number:

$$Kn = \frac{\lambda}{d} = \frac{\eta}{p \cdot d} \cdot \sqrt{\frac{\pi \cdot R \cdot T}{2 \cdot M_m}} \quad . \ (2.37)$$

This number determines the nature of the gas flow and takes into account the molecular mean free path (λ) and the characteristic dimension (diameter, d) of the pipe. Using our experimental parameters: p = 0.75 Pa, d = 35 mm, M_m = 17 g/mol and $\eta \approx 10^{-6}$ Pa·s (average value for all temperature estimated using the Chapman-Enskong equation [85]), a value of Kn = 0.02-0.025 is obtained depending on the different experimental temperatures, indicating a transitional regime flow for our experiments. For different Knudsen numbers and regime flows (molecular and continuum), additional experiments at different flow/pressure conditions would be necessary to extrapolate the results of this work. Another important parameter for the adsorption on the inner stainless steel surface is its roughness. Unfortunately the roughness of the used stainless steel pipe could not be measured. This roughness would increase the effective surface area of the pipe and hence the ammonia areal density would be lower. In our work the ammonia retention by physisorption is calculated considering that the effective area for the adsorption is equal to the geometric area of the pipe, (assuming in this way that the pipe is smooth and the roughness can be considered as negligible). Hence, these results give a maximum value for the ammonia physisorption on stainless steel depending on the surface temperature.

2.4.3. Conclusions and future works

- The quantification of the physisorption (sticking) of ammonia molecules on AISI 304 L stainless steel surface, under high vacuum conditions relevant for future fusion devices as ITER, has been carried out. The results show a total retention in the range of 5-40 $\mu g/cm^2$ that decrease clearly with the surface temperature, except at 373 and 423 K where the total amount of physisorbed ammonia was very similar (approximately 17 $\mu g/cm^2$).
- The sticking coefficient can be adjusted to an exponential decay with reasonably accuracy. The experimental parameter obtained from this fit (τ) allows the estimation of the activation energy for the multilayer adsorption. According to the experiments a value of 0.15 eV per molecule is obtained for the activation energy of the process.
- The normalization of the τ parameter to the incident molecular flow on the surface would give an applicable approximation for the sticking of ammonia molecules on stainless steel surfaces on the ITER vacuum lines with higher and more relevant particle fluxes.
- Experiments to investigate the sticking process on tungsten, at higher surface temperatures (beyond 473 K) and to study the thermal decomposition of the adsorbed ammonia on hot metal surfaces ($T_{surface}$>750 K) will be adequate to understand and mitigate the ammonia retention and the associated tritium inventory in a hypothetical ITER N_2-seeded operation.

2.5. AMMONIA FORMATION AND QUANTIFICATION IN JET N_2 SEEDED DISCHARGES

Related with the thesis topic of ammonia formation in N_2 containing plasmas, the pre-doctoral student has participated in the experimental campaign of the JET tokamak (Culham, UK) during thirty working days in 2016. These actions have been carried out within the framework of the EUROfusion Consortium. They consisted on the participation in several experiments devoted to study the ammonia formation during N_2 seeded discharges in a tokamak environment under similar wall conditions compared to the expected during the future ITER operation. The mass spectrometry was the main diagnostic involved in the measurements. The experiments were framed in the campaigns C36 (deuterium plasmas) and C37 (hydrogen plasmas) and were mostly carried out during January and October 2016.

The experiments performed during the C36 campaign were not specifically designed to study the ammonia formation, but their N_2 seeded discharges were utilized for the fine tuning of the mass spectrometry sensors and the data acquisition units as well as the familiarization with the code used for the mass spectra deconvolution [86]. The specific experiment performed during the C37 campaign (M15-29 experiment) was especially important. The scientific coordination of the experiment was carried out by the doctors Timo Dittmar and Aleksander Drenik. The goal of such experiment was try to quantify the ammonia formation and migration in N_2 seeded H-mode discharges. The experimental strategy was developed in order to relate the produced ammonia with the nitrogen content on the PFMs walls, trying to observe a saturation trend in the ammonia formation when the PFMs surfaces are saturated with nitrogen from the plasma. Other factors as the influence of the increasing surface temperature during the pulses, the spectroscopic detection (via ND radical) of the produced ammonia and the effect of disruptions in the ammonia outgassing from the PFMs and pumping ducts were also observed and studied during the tokamak pulses.

At the end of the experiment the regeneration of the liquid nitrogen cryopump system used for the condensation of molecules like water and ammonia from the exhaust gas was performed in order to quantify in an accurate way the produced ammonia, avoiding the possible losses of these molecules (sticking) in colder parts of the system. Detailed calibration works were additionally performed for the future absolute quantification of ammonia. Up to date, this global quantification has not been completed, requiring a more exhaustive data analysis. Although this collaboration and the involved experiments are out of the scope of this thesis, the student considers that his participation must be mentioned as this mission has proportionated to him several valuable skills and knowledge related with one of the main topics of the thesis. More details about the ammonia formation observed in JET and the specific work of this collaboration can be found in [49, 87].

3. HYDROGENIC RETENTION IN MIXED LITHIUM-TUNGSTEN PLASMA FACING MATERIALS

The research in the field of Plasma Facing Materials, able to survive in the extreme conditions expected in the boundary of burning D-T plasmas, is absolutely decisive for the development of nuclear fusion energy and the economic viability of commercial reactors. At present, after decades of intense investigation, the use of carbon based materials has been rejected due to the enhanced fuel retention in the a:C-H co-deposits and re-deposited mixed layers. Therefore, tungsten (W) has become the main candidate to be used in future reactors and it has been selected as the material for the ITER divertor [88-89]. Its selection is motivated by the excellent mechanical and thermal properties of W that probably offer the best performance (compared to another high Z solid metallic elements) against steady state and transient thermal loads, as the expected in magnetically confined fusion devices. Among the main problems related with the surrounding materials exposed to a burning D-T plasma during the operation of a future fusion reactor, the hydrogen isotope retention (tritium inventory), the unavoidable erosion from impinging plasma particles and the power exhaust handling are among the most challenging issues to be solved for the development of magnetic fusion energy. In ITER during short (~8 minutes) pulsed operation, the nominal heat loads expected in the divertor region will be in the range of 10-20 MW/m^2 while transient events as ELMs, disruptions, VDEs or runaways can increase the heat loads up to 1 GW/m^2 [90]. Moreover, the particle loading that also contributes to induce material erosion (sputtering) with important damage to the PFCs is also expected to be extremely severe ($\sim 10^{24}\ m^{-2}s^{-1}$).

It is evident that the longer pulsed mode operation and the increasing power and particle loads expected in a reactor as DEMO, will convert the removal of power/particle exhaust in an even more difficult issue. For an economically viable reactor design, the peak power must be reduced to tolerable levels in order to avoid the disintegration of the divertor elements, assuring a reasonable lifetime for this element. With the current design, the ITER divertor is supposed to manage the problem by operating in the partially detachment regime [4-5]. To avoid its disintegration, the limit for the nominal power load must is considered as $5MW/m^2$. In current fusion devices different primary actions are employed to reduce the power load to the PFCs [90] as the inclination of divertor tiles in the poloidal direction, the increase in the magnetic flux expansion and the concomitant enhanced perpendicular transport that supposes the broadening of the heat flux width and maximizes the area over which the power is deposited. In addition the optimization of the divertor geometry can increase its capability to radiate power [91-92]. These strategies also help to achieve the partially detachment regime [93-94]. This regime is considered as the reference for the ITER active phase. It is characterized by a high plasma edge and core radiation and a strong reduction of the power loading to the PFMs. Currently, modelling studies conclude that the total fraction of radiated power (f_{rad}) must be around 0.85-0.90 for ITER operation and for an hypothetic DEMO scenario the total radiation fraction must be increased up to 0.95 [95] to prevent the divertor damage. It means that 95% of the total power reaching the PFC surfaces must be dissipated by radiation. These high radiation levels would be induced by the injection of extrinsic impurities (molecular nitrogen or noble gases as neon, krypton and argon) in the well-known impurity seeding plasma operation [14].

Although these operational solutions are in principle possible, its development can be extremely challenging even for a pulsed device as ITER due to plasma dilution and contamination that degrade the confinement and preclude the ignition conditions, induced by the accumulation of the seeded impurities. Even, if this very high radiation fraction is feasible and the solid tungsten based PFC's can resist under the more drastic reactor conditions (40-60 MW/m^2 of unmitigated power load that pose significantly higher levels compared to ITER ones) expected in DEMO-like devices, the enhanced net erosion and the induced permanent degradation produced on PFCs will limit the lifetime of the divertor elements and the reactor operational cycle. At his point is important to emphasize again that even considering very optimistic conditions at the DEMO-like tungsten divertor as: a maximum electron temperature of 5 eV that results in significantly reduced erosion of tungsten and totally mitigated type I ELMs among others [14], the maximum operational life expected for the tungsten divertor elements does not exceed two years. Taking into account the enormous cost associated to the replacement of the divertor elements, this limited operational life will undoubtedly affect the viability of the project. Under this scenario the search of alternatives to this problematic is clearly necessary especially in the case of DEMO-relevant divertor prototypes. Liquid metal components (in particular lithium, Li) offer an innovative solution to this issue as the liquid surface is, in principle, free of irreversible degradation and damage. The use of lihium in several magnetic devices has shown unique advantages in terms of plasma confinement improvement and heat handling capabilities [42, 96], becoming an option that is currently studied in alternative divertor concepts [21]. Considering a future reactor (DEMO) scenario that combines a conservative hot solid tungsten first wall and liquid Li element at the divertor, where the power exhaust is concentrated and mitigated, as a viable solution in terms of technology and engineering development, several issues related with the material compatibility in terms of material migration, and mixing must be investigated. In particular, the mutual interaction of tungsten and lithium with hydrogen isotopes will lead to co-deposition, implantation and mixing processes that could increase the associated tritium retention and might represent a problem from the nuclear safety point of view. The hydrogenic retention in mixed tungsten-liquid lithium layers has been approached in this thesis chapter, being the main obtained exposed in international conferences and/or published in specialized papers [97-98]. This thesis chapter is structured in three sections.

The section 3.1 is dedicated to review briefly the state of art related with the properties of liquid lithium and another liquid metals as PFM and the different technologies studied for its implementation as PFC in nuclear fusion devices, emphasizing on the hydrogenic retention on liquid lithium and its possible removal by thermal techniques with moderate heating (ΔT~600ºC). The second section (chapter 3.2) describes the experiments performed at CIEMAT, designed to understand the behaviour in terms of hydrogen retention of tungsten exposed to Li containing plasmas that will cause implantation of lithium in the tungsten substrate. This implantation can happen in zones of the W first wall situated close to the liquid lithium divertor as important amounts of lithium can be evaporated from the divertor, ionized, transported around the SOL and finally implanted on the adjacent W surfaces. In fusion reactors based on a liquid lithium divertor target and a tungsten first wall this interaction of the wall material with plasmas of significant lithium content will be unavoidable. Under these conditions, the formation of mixed W-Li layers and the implantation of lithium in the solid structures will alter the behaviour of such solid elements against plasma surface interaction processes. The possible enhanced fuel retention of such hybrid layers could suppose a showstopper for the selection of a first wall material compatible with the presence of liquid lithium on the divertor. In this sense, several experiments investigating the interaction of W-Li hybrid layers with linear plasma have been performed. Neff et al [99] have studied the deuterium retention in W-Li coatings exposed to high fluency linear deuterium plasmas in Magnum PSI device. They reported the inhibition of Li-D-O complex formation (compound that is considered to have a key role in the enhanced hydrogenic retention in lithium layers, especially when it is mixed with carbon) and its associated enhanced fuel retention, when the deuterium linear plasma is seeded with helium. Other experiments involving lithiated tungsten samples exposed to Magnum PSI linear plasmas [100] have shown the possible saturation in the deuterium retention and the inhibition of blistering on the W surface due to the protective effect of the Li coating. However, the possible effects that a simultaneous irradiation with hydrogenic species and lithium on W substrates can have in key issues as global tritium retention are unknown. Hence, specific investigations in terms of fuel retention are clearly necessary. In this work, we address this topic for the first time at the laboratory level. Dedicated experiments and analysis oriented to quantify the H retention on several W-Li samples (at $T_{surface}$ ~100ºC) exposed to H_2 Direct Current (DC) Glow Discharge (GD) plasmas under different environments have been performed by using TDS in order to induce the *in situ* hydrogen desorption from the W-Li layers and mass spectrometry to quantify it. Global particle balance was also used for the determination of trapped H into the full W wall of the plasma chamber.

Finally the third section (chapter 3.3) approaches the problematic of Li and thermal D_2 co-deposition on tungsten and the influence of the surface temperature in the process. In a fusion reactor environment characterized by a liquid lithium divertor and a tungsten first wall, the interaction of such tungsten surface with neutral lithium atoms and neutral/molecular hydrogenic species also needs to be taken into account. These species will be present in the plasma edge region and its transportation along the SOL is expected, thus producing a mutual interaction between them and the W first wall that needs to be evaluated. The first expected effect is the growing of a Li film on the W surface. It can be beneficial from the point of view of thermal protection and erosion damage mitigation induced to the W surface as has been experimentally demonstrated [100, 101]. However, the affinity between lithium and the hydrogen isotopes can produce an increase in the associated fuel retention that could suppose a showstopper for the development of this PFC solution proposed for future fusion reactors if this hydrogenic uptake is sufficiently important compared to the tritium inventory requirements [102]. Furthermore, under this scenario the development of suitable techniques able to produce the efficient hydrogenic removal and the characterization of the fuel content present on such W-Li components will be clearly necessary. In this sense, the laser based methods offer an attractive option to perform this task, as they allow the *in situ* wall diagnosis without substitution or manipulation of the PFCs, avoiding in this way the disadvantages of post mortem analysis due the difficult access to the in vessel components [103]. In this pioneer investigation, the interaction of lithium and molecular deuterium with tungsten surfaces has been studied focusing the work in the parametrical dependence of the mixed co-deposition with the surface temperature of the W substrates. A Laser Induced Desorption Spectroscopy (LIDS) technique assisted by mass spectrometry has been developed to remove and quantify the deuterium uptake on W-Li-D layers after the deposition of evaporated Li and gaseous deuterium (D_2) on tungsten under differents exposure environments. The retention results were compared with Thermal Desorption Spectroscopy (TDS) measurements to corroborate the retention values. Thermal simulations certified that the temperature rise on the sample desorption volume is high enough to remove all the hydrogenic content. Several post mortem techniques (Secondary Ion Mass Spectrometry [SIMS], profilemetry and flame atomic emission spectrometry [FAES]) were performed to characterize the W-Li layers and quantify the absolute amount of lithium on samples.

This long and complex chapter is structured in several subchapters. Subchapter 3.3.1 explains the development and employment of the LIDS technique for the deuterium retention quantification in the W-Li-D layers as well as the necessary laser technology and its characteristics. The absolute calibration details for the mass spectrometry quantification during the LIDS pulses is introduced in subchapter 3.3.2. The heat transfer and temperature rise computer simulations performed to estimate the sample heating during the laser analyses are described in subchapter 3.3.3. Subchapter 3.3.4 introduces the experimental setups and works devoted to produce the W-Li-D samples, their laser irradiation and the post mortem analyses. The experimental LIDS results are presented in subchapter 3.3.5 while the rest of the experimental findings (TDS, SIMS, profilemetry and FAES) can be found in subchapter 3.3.6. In the subchapters 3.3.7 and 3.3.8 the experimental results in terms of deuterium retention and lithium film formation on the W samples are summarized. Finally subchapters 3.3.9 and 3.3.10 discuss the implication of the obtained results for the potential implementation of a hot W first wall together with a liquid lithium divertor as a PFCs solution for magnetic fusion reactors. The obtained results have been extrapolated to the case of a DEMO prototype with this PFCs combination, taking into account the operational and design parameters existent up to date. This extrapolation provides an estimation of the co-deposition of D in W-Li first wall areas, whose implication related the limited tritium inventory in DEMO prototypes designs is discussed. Other technical issues such as the stability of the co-deposited liquid thin films under intense magnetic fields in the reactor environment, the necessary limited core contamination and the recovery of the first wall deposited liquid lithium and hydrogen isotopes by the divertor are also addressed.

3.1 LIQUID LITHIUM PFM RESEARCH AND ASSOCIATED HYDROGENIC RETENTION ISSUES

Liquid metal surfaces can recover their original form after the modification induced by their exposure to burning plasma. In this way, it can be renovated and consequently avoid the irreversible degradation induced by particle, heat and neutron loading. The potential damage produced in these elements would not be as problematic compared to the traditional solid elements proposed as PFC. The liquid surface could (in principle) be regenerated and recirculated, thus contributing to the particle and power exhaust handling, increasing in this way the lifetime of the PFCs. The survival of these elements in the extreme conditions of a fusion reactor is crucial for the development of the magnetic fusion energy. Hence, the development of alternative solutions that allow the longer operation of such devices without the destruction and the mandatory replacement of the surrounding materials acquires a paramount importance. Liquid metal PFM solutions can enable the development of attractive, more durable and economically viable reactor designs. The most studied and promising element to be used as liquid metal PFM in fusion reactors is lithium, although the research in liquid metals has proposed another candidates [104] as gallium (Ga), tin (Sn) or lithium-tin alloys[5]. Lithium poses unique and exceptional characteristics for its use as the first component in contact with fusion plasmas. Due to its lowest atomic number (Z=3) among the elements capable to be used as PFC, it use offers very beneficial effects in terms of improved confinement, low impurity content and concomitant plasma performance, as the contamination induced by lithium impurities and the fuel recycling are significantly reduced compared to highest Z elements. Additionally, their thermo-physical properties (high thermal capacity and latent heat of melting and vaporization) make lithium attractive for heat removal issues on the divertor zones. Furthermore, its low ionization energy leads to high edge non coronal radiation that can dissipates an important fraction of the power load by radiative processes involving the ionization of the lithium atoms. This characteristic together with the vapour shielding effects of Li vapour clouds generated in such PFCs can be extremely helpful in the power exhaust handling, reducing the power loads to the surrounding walls. In table 3.1 the main physical and chemical properties of lithium together with the corresponding for Ga and Sn are presented.

---

[5] Even though the employment of lithium-tin alloy components is out of the scope of this thesis, it is important to mention that several investigations related with this hybrid material have been performed in the Fusion National Laboratory (CIEMAT) during the last years. In the publications section of this thesis an interesting paper that summarizes these experimental works can be found.

Property, symbol, [unit]	**Lithium**	**Gallium**	**Tin**
Atomic number, Z	3	31	50
Atomic mass, m_a, [amu]	6.94	69.72	118.7
Density, ρ, [kg/m^3]	535	610	699
Melting point, T_m, [ºC]	180.5	29.8	232
Latent heat of melting, ΔH_{melt}, [J/kg]	432	80.2	59.2
Boiling point, $T_{b,}$ [ºC]	1347	2403	2270
Latent heat of vaporization, ΔHvap, [kJ/g]	21.2	3.7	2.5
Dynamic viscosity (at T_m), η, [10^{-3} Pa·s]	0.25	0.95	1.85
Surface tension (at T_m), σ, [N/m]	0.4	0.69	0.55
Thermal conductivity, k, [W/m·K]	85.0	40.6	66.6
Heat capacity, C_p, [J/kg·K]	3582	370	228
Ionization energy, E_{ion}, [eV]	5.39	6.00	7.35

Table 3.1. Physical and chemical properties for Li, Ga and Sn

A fundamental problem derived of using liquid lithium metallic surfaces is their stability under MHD activity and electric J x B effects produced by the intense magnetic fields present in the reactor environment. They can induce Lorentz forces producing the splashing and ejections of liquid metal into the plasma. Consequently the first requirement for the application of these concepts is to assure the stability of the liquid metal surface under such conditions. A macroscopic static surface solution was proposed by the Russian teams that developed the so called Capillary Porous System (CPS) [105]. The liquid metal is sustained on a metallic (normally made of molybdenum stainless steel or tungsten) small size (with pores in the range of μm) mesh structure that acts as the substrate where the liquid is confined. In this system the capillary force compensates the induced electromagnetic effects in the liquid surface, being these static surface concepts widely tested on several magnetic devices with promising results [106-108]. Generally, the wetting characteristics of the liquid metal-substrate combination are determinant for a proper wetting of the liquid metal into the mesh. The presence of clean, free of oxides mesh surface is also essential. On the other hand, the use of elements with flowing liquid lithium surfaces has been also studied [109]. Ruzic and collaborators have developed a device that confines the liquid lithium on trenches [110]. It uses the thermal gradient present on the plasma boundary to induce magneto-thermoelectric effects that generates the movement of the liquid metal to remove in this way the heat from the PFCs. This concept (called LiMIT) has been tested in the Chinese tokamak HT-7. Other ingenious ideas that explore alternatives to confine and move the liquid metal with electric induced effects in PFCs can be found in the following reference [111]. Once the stability of liquid lithium in the plasma boundary seems achieved, the main drawback associated with the use of liquid lithium is probably its strong affinity with hydrogen isotopes as a result of its alkaline and very reactive chemical nature. As the level for total tritium inventory for the in vessel components is limited to 700 g [102], the potential tritium uptake of Li PFM could suppose a serious risk during D-T operation. At this point is important to note that the selection of plasma facing materials for ITER is in principle closed. The considered solution with beryllium (Be) at the first wall and W at the divertor was chosen to minimize the impact of potential fuel retention, especially in the higher particle loading zones (tungsten divertor). Under such scenario the long term fuel retention will be dominated by beryllium co-deposits [43]. The ITER like wall (ILW) operation in JET has shown a reduction in the long term hydrogenic retention by one order of magnitude [44] comparing to the previous JET-C operation with carbon walls.

In spite of this positive result, in the future ITER operation, the enhanced retention on beryllium co-deposits could also be problematic enough to limit and complicate the reactor performance in terms of safety and tritium inventory. Furthermore, the efficient removal of tritium from Be containing layers can be laborious. Several investigations have shown that laser based removal methods will require a temperature rise up to the melting point of beryllium (inducing the deformation of the first wall Be tiles) to desorb a significant fraction of trapped deuterium [112, 113]. In addition modelling of JET-ILW data and simulations predict slow outgassing in thick (50 μm) co-deposits implying long duration baking treatments (some weeks and even one month) at moderate temperatures (523-623 K) for the removal of significant hydrogenic fractions [114].

On the contrary, recent works have demonstrated the potential removal of the hydrogen isotopes from Li components by heating them up to 500ºC-550ºC [97, 115, 116, 117]. Additionally, the hypothetical formation of lithium hydride aggregates can be solved at moderated temperatures as the dissolution of LiH in Li and the concomitant hydrogen removal occurs below 600ºC (this desorption temperature depends on the external surrounding pressure) [116, 117] in high vacuum conditions. A suitable solution could consist on periodic baking at T≤600ºC or ultimately with the recirculation of liquid lithium present in the PFCs out of the vessel to be re-injected in the divertor components after its regeneration. In this regeneration the tritium and hydrogen isotopes can be extracted from Li and re-used in the fuel cycle. These close loop ideas has been described and proposed in several concepts that involve experimental and modelling works [118, 119]. In DEMO scenarios with hot solid tungsten first wall and liquid Li elements at the divertor; even though the fuel retention problems on the divertor can be solved with relative easy solutions, the lithium migration around the SOL and plasma edge produce the co-deposition and implantation of Li atoms on W surfaces thus creating mixed W-Li PFC surfaces. In principle such hybrid layers would protect the solid surface from heat loads due to vapour shielding effects and non-coronal radiation of Li ions in the plasma material interface [42]. However the potential increase in the hydrogenic retention could pose a serious issue as the thermal removal of tritium in remote parts and shadowed areas of the first wall can be complicated. With this problematic, the development of techniques for fuel removal and the quantification of the hydrogenic retention on the mixed W-Li surfaces acquire a paramount importance.

3.2. HYDROGEN RETENTION ON W-LI SURFACES EXPOSED TO GLOW DISCHARGE PLASMAS. ROLE OF IMPLANTED LITHIUM IN THE RETENTION

3.2.1. Experimental setup and procedure

The experiments were carried out in a full W wall device designed at CIEMAT and similar to the one previously used and described [61]. An overview of the setup can be visualized in figure 3.1.

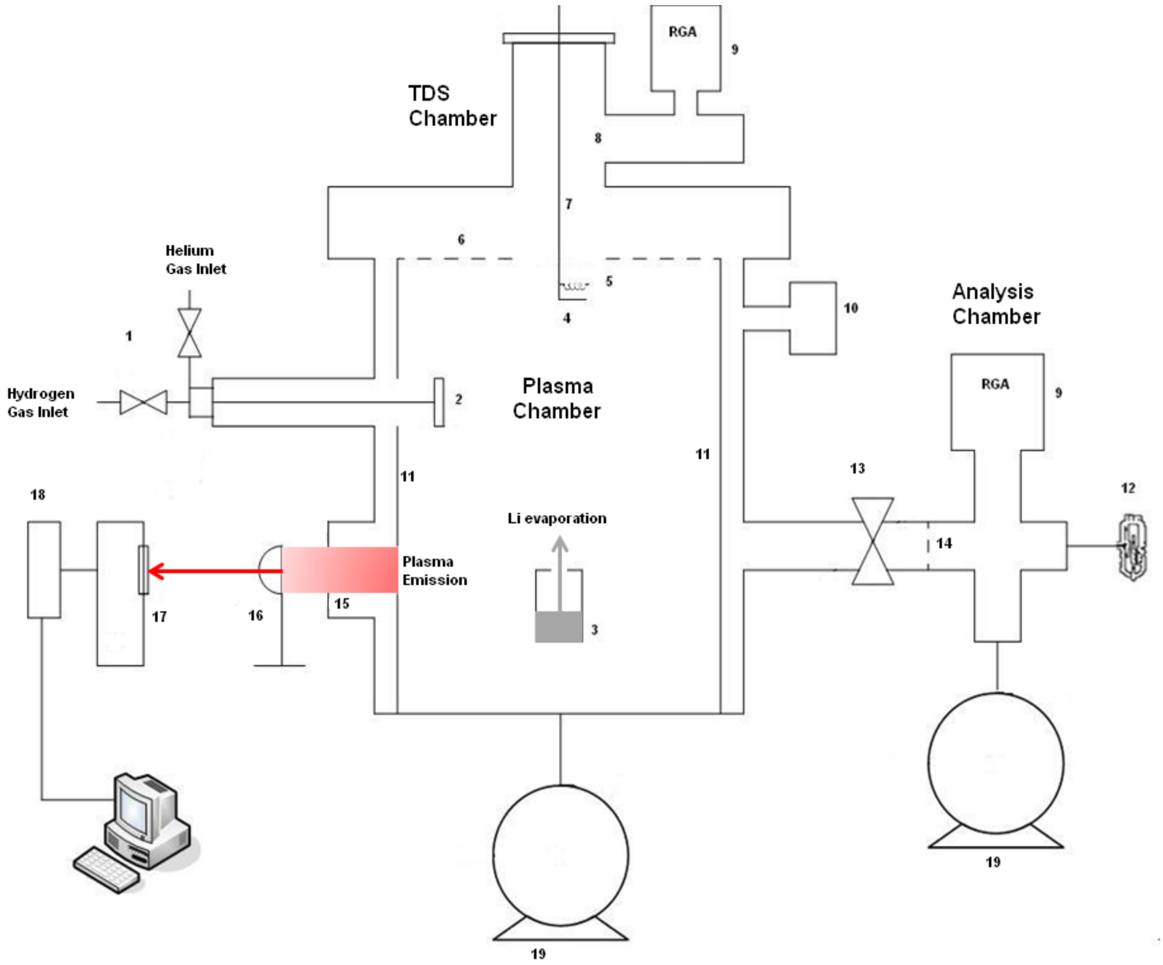

Figure 3.1. General view of the setup: 1. Mass-Flow controllers (gas inlet), 2. Anode, 3. Lithium oven, 4. Sample holder, 5. Heating filament, 6. Isolation grid, 7. Manipulator, 8. Sample position during TDS, 9. Mass spectrometers, 10. Capacitance manometer, 11. W wall (plasma chamber), 12. Ionization Gauge, 13. Gate valve, 14. Collimator (differential pumping), 15. Optical window, 16. Focusing Lens, 17 Monochromator, 18. Photomultiplier, 19. Pumping units.

The primary vessel consists on a cylindrical stainless steel vacuum chamber that acts as the grounded cathode where the irradiation with the H_2 GD plasmas is carried out. The plasma chamber (V= 5.4 L) has its inner wall totally covered with high purity cold rolled tungsten sheets (A=0.14 m^2) and is pumped by using a pumping unit that consist on a set of turbomolecular-rotary pump that decreases the base pressure until 10^{-5} Pa approximately. The pressure during the plasma operation and the lithiation process is measured with a capacitance manometer (0.1-100 Pa). Inside this chamber a cylindrical, stainless steel oven (3 cm of diameter and 6 cm of height) filled with high purity (>99%) lithium is placed to produce the evaporation of lithium for the *in situ* lithiation of the samples and the main W wall, by the effusion of the evaporated Li atoms through a circular hole (~1 cm of diameter) placed on the top of the oven. An AC power supply is used to heat up the oven, feeding an electrical resistance rolled on it. The temperature of the lithium is measured during the evaporation by a thermocouple type K that is placed inside the oven, in direct contact with the lithium. Before the lithiation process the lithium placed in the oven is outgassed by heating it until 300ºC of temperature during 30 minutes approximately inducing the hydrogen, water and impurities desorption from the lithium bulk.

On the top of the plasma chamber and open to it, a small chamber intended to harbour the in situ TDS analysis on the W-Li samples is located. To measure the H retention during the induced desorption, a residual gas analyser (SRS 200) is connected to this chamber. A manipulator that contains a holder for the W-Li samples and a pure resistive filament (fed with a 12 V direct current and 60 W of total heating power) in order to heat up the samples by radiation and induce the H desorption, is placed on the top of this TDS chamber. The temperature evolution on the sample during the TDS analysis is measured by using a type K thermocouple welded on the holder, in direct contact with the sample. The manipulator can move the samples from the plasma chamber to the TDS chamber without breaking the vacuum conditions after the H_2 GD plasma irradiation. In this way the possibility of contamination and hydrogen release from the samples before the TDS analysis can be excluded.

The samples consist on a cold rolled, high purity tungsten pieces with dimensions of 12.6±0.2 mm of width, 21.7±0.2 mm of height and 0.1 mm of thickness with a surface area exposed to the plasma of 2.7±0.1 cm^2. These samples are introduced in the holder and are outgassed by heating (up to 550ºC during 15 minutes), previously to the plasma exposure. Before the H_2 irradiation one of the samples was exposed to a previous in situ lithiation by Li evaporation at 500ºC-550ºC during 30 minutes, (Li evaporation rate of $\sim 3 \cdot 10^{18}$ atoms/$cm^2 \cdot s$ and total evaporation of 0.2 g approximately) under a H_2 flow (4 Pa of total pressure) atmosphere. Another sample was exposed directly to a H_2 GD plasma (p = 4 Pa) in a lithium evaporation environment (Li at 500ºC-550ºC during 30 minutes as in the pre-lithiated case), producing a Li-seeded H_2 GD plasma in order to study the hydrogen retention under simultaneous irradiation of Li and H on the W sample. Finally a pure W sample was also irradiated with pure H_2 GD plasma in order to compare the hydrogen retention with the two cases previously described.

Between the plasma and the TDS chamber a stainless steel grid with boron nitride insulation pieces is placed to limit the plasma in this region and assure that it does not touch any part of the TDS chamber, excluding in this way the possibility of contamination of the TDS analysis by the desorption of hydrogen from other parts non exposed in principle to the plasma. Additionally and also connected to the plasma chamber, a differentially pumped analysis chamber is placed to monitor, with a Residual Gas Analyser (RGA) Mass Spectrometer (Pfeiffer Vacuum Prisma QMS 200), the plasma operation. This analysis chamber is pumped down with another turbomolecular-rotary pump vacuum unit until a base pressure around 10^{-7} Pa, being this pressure measured with an ionization gauge sensor (Bayard Alpert). After the experiment, the lithium deposited on the main W sheets that forms the wall of the plasma chamber is removed. The sheets are cleaned by ultrasounds bath and dried in an oven at 150ºC during two hours, assuring in this way a clean and lithium free wall for the next experiment. All the experiments were carried out after a wall conditioning on the main W wall and samples that assures the reproducibility of the experiments prior to the lithiation/irradiation processes. This wall conditioning consists on pure DC-GD Helium plasma during 20 minutes in order to desorb and clean by sputtering the impurities present on the sample and main wall surfaces.

To produce the discharge, the high purity (>99.999%) gases (H_2 for the experiment and He for the wall conditioning) are introduced into the chamber by an electronic mass flow controller. The plasma characteristics of the H_2 irradiation are: ~ 4 Pa of total pressure, a discharge voltage between 100-250V, plasma current (300-350 mA) and a total hydrogen fluence up to 10^{23} m^{-2} (being the dominant plasma ions at a pressure of 4 Pa a mixture of H_2^+ and H_3^+ [120]), with a total duration of 30 minutes. During the irradiation, the main W wall and the samples were not heated up externally, but due to the plasma bombardment the surface temperature was increased until 90-100ºC approximately. To complete the measurements during the plasma operation an optical emission spectroscopy (same device explained in subchapter 2.3.2.1) diagnostic was also used to measure the intensity of the lines related with Li I (670.7 nm) and Hα (656.3 nm) transitions.

After the H_2 GD plasma irradiation the treated sample is moved to the TDS chamber with the manipulator and the hydrogen uptake on the sample is measured by TDS assisted mass spectrometry. The resistive filament that induces the heating of the sample and the hydrogen desorption is fed with a DC power supply with a nominal voltage of 12 V and a maximum current of 5 A. Finally, an absolute calibration that relates the single RGA peak at 2 amu/e signal registered by both the mass spectrometers with its associated H_2 partial pressure and fluxes was performed in order to quantify the hydrogen retention on the W samples and on the full W wall of the chamber.

3.2.1.1. Calibration works for hydrogen

Two different kinds of calibrations were performed in the experimental system, to quantify the local (samples) and global (full W wall) hydrogen retention. The calibration of the differentially pumped RGA used to measure the global retention on the W wall of the plasma chamber was performed following the same procedure explained in the previous subchapter 2.1.2.4. The calibration parameters (pumping speed, S_{H_2} and calibration constant K_{H_2}) are obtained using the same protocol that can be found in the previously referenced subchapter of the thesis. It is important to note that for the calculation of such parameters only the experimental points present in the region close to the working experimental pressure (4 Pa≡30 mTorr) are used for the linear fit determination. The previous experimental points situated at lower pressures are deviated from the linear trend visible around 4 Pa. At these lower pressure conditions the pumping efficiency of the system is higher and the experimental parameters obtained from the calibration (specially the pumping speed) are different. The corresponding calibration plot and obtained parameters are shown in figure 3.2. From it a pumping speed value of S_{H_2} = 4.6 L/s and a calibration constant, K_{H_2}=$1.6\cdot10^{-8}$ $mTorr^{-1}$ are obtained.

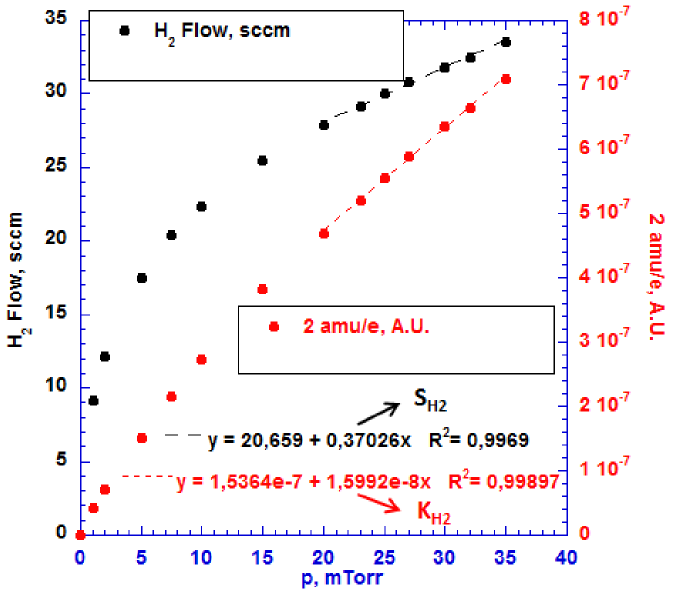

Figure 3.2. Calibration work for H_2 detected by the differentially pumped RGA

For the calibration of the RGA utilized to measure directly the hydrogen desorbed from samples a different method was used as the direct injection of gas with flowmeters is not suitable due to the overpressure and the saturation of the RGA filaments, even for flow values around 1 sccm (minimum influx available using the flowmeters). To obtain sufficiently small fluxes and not saturate the RGA, a calibrated leak method was used. It is based on the injection of small hydrogen gaseous flows and its correlation against the resultant mass to charge RGA signal measured by the mass spectrometer. To perform this calibration a small bottle with a fixed volume (0.5 L) was connected to the vacuum chamber and filled with a given pressure (10-100 Pa) of hydrogen. A capacitance manometer is connected to this reservoir to register the pressure and its evolution. The reservoir is connected to the vacuum chamber through a leak valve to regulate the gas flux input from the reservoir to the vessel. This valve is able to inject very small amounts of gas without saturating the RGA. By measuring the pressure drop (dp/dt) in the recipient with the capacitance manometer that results from the gas injection into the chamber, the input flux of the hydrogenic flux can be calculated. At low pressure the ideal gas state equation is valid:

$$pV = nRT \,. \quad (3.1)$$

In this expression p is de pressure of the gas, V the volume of the chamber, n the number of particles contained in that volume, T the absolute temperature of the gas and R the universal constant of the gases (R=8.314 J K^{-1} Kg^{-1}). At constant temperature, deriving the expression respect to the time, the equation can be expressed as:

$$\frac{d(pV)}{dt} = RT\frac{dn}{dt}, \quad (3.2)$$

the term $\frac{dn}{dt}$ corresponds to the input particle flux, (Γ, in molecules/s). For constant volume of the reservoir:

$$V\frac{dp}{dt} = \Gamma RT \rightarrow \Gamma = \frac{V}{RT}\cdot\frac{dp}{dt}. \quad (3.3)$$

The derived expression shows the linear dependence between molecular flux and the pressure changes. This parameter can be calculated from the data of the pressure evolution in the reservoir, calculating the derivative of the pressure respect to the time. Normally as the input flux is fixed by the leak valve and it is kept constant in each step of the calibration, the pressure measurement presents a linear decrease respect to the time. In this way, each section of the P-t curve can be adjusted to a linear fit. Hence, the slope of the fit (dp/dt) allows the calculation of the input molecular flux. Using the equivalence of the Loschmidt number (n_0) that gives the number of particles contained in one mbar·L ($n_0 \equiv 2.69 \cdot 10^{19}$ particles/mbar·L) the calculated slope can be converted to the corresponding flux value. This term is evaluated for the different introduced fluxes into the chamber and simultaneously, the input flux is registered by the RGA in the TDS chamber. Thus, the concomitant mass to charge ratio signal (subtracting previously the background level of the signal with no input flux into the chamber) can be correlated with the calculated flux. As the mass spectrometer is sensitive to the particle flux, the registered signal must be directly proportional to the molecular flux calculated from the derivative of the pressure. Finally by fitting the RGA mass to charge signal to the given molecular fluxes, a linear relationship between both variables is found. This expression allows converting directly the measured RGA signals during the analyses to desorbed hydrogen fluxes. Integrating these flux values over desorption time of the TDS analysis and normalizing this result to the total area of the sample, the net hydrogen retention on samples can be obtained. In figure 3.3 the result from this calibration is shown.

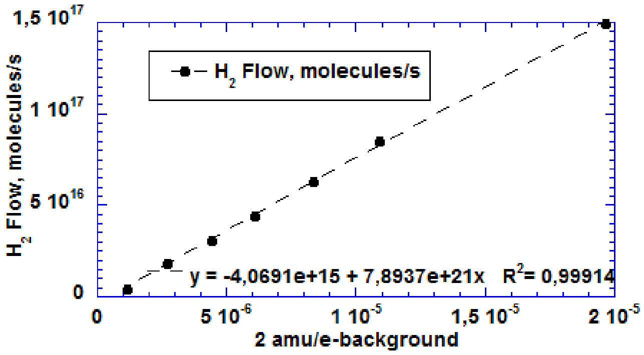

Figure 3.3. Calibration work for the H_2 quantification of the TDS measurements

3.2.2. Experimental results and discussion

3.2.2.1. Hydrogen uptake on a W sample lithiated under a H_2 atmosphere and exposed to H_2 GD plasma irradiation

In figure 3.4, the TDS analysis of the pre-lithiated sample (in a H_2 environment) and later exposed to H_2 GD plasma irradiation is presented. The heating ramp of the sample during the first part of the TDS analysis is approximately linear with a mean value of 5 K/s. A clear desorption peak is visible for the signal at 2 amu/e (directly related with hydrogen) at a sample temperature of 400ºC. The 18 amu/e signal related with water keeps approximately constant during the measurement, around a value that is at least an order of magnitude lower compared to the 2 amu/e signal. In this way the amount of hydrogen desorbed that could occur from water decomposition can be considered as negligible.

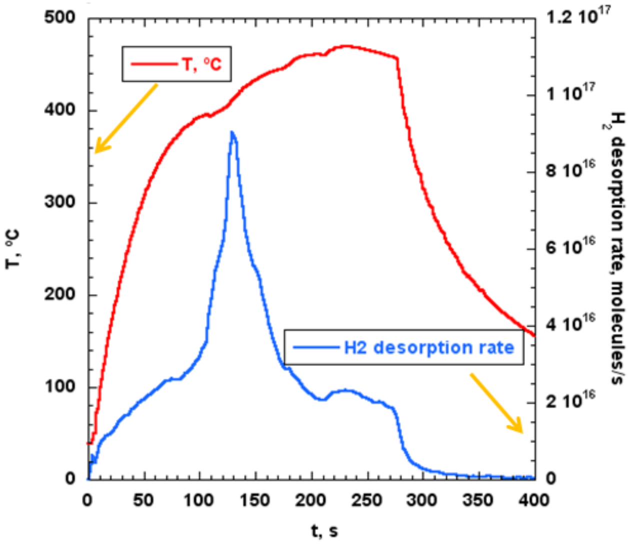

Figure 3.4. TDS measurement on a W sample irradiated with H_2 GD after its pre-lithiation under a H_2 gaseous flow environment

The figure 3.5 shows an optical emission spectroscopy measurement registered during the irradiation with H_2 GD plasma (red line). The Hα (656.3 nm) and Li I (670.7 nm) lines are clearly visible, showing the presence of lithium in the plasma as a consequence of its sputtering from the plasma chamber walls. The visual inspection of the sample during its replacement for a new one also shows the presence of lithium on the surface. Hence the interaction between the impinging hydrogen from the plasma and the W-Li surface during the irradiation process seems evident.

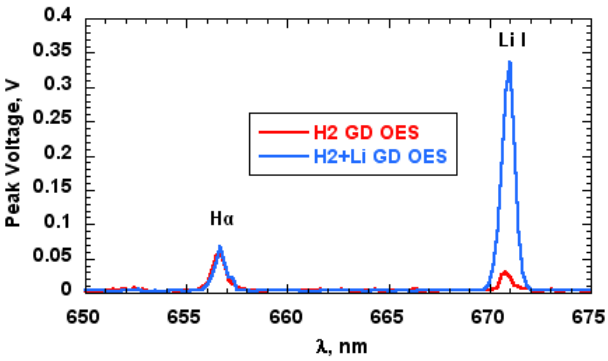

Figure 3.5. OES measurement during the H_2 irradiation of the samples previously lithiated under a H_2 flow atmosphere (red line) and exposed to H_2 GD plasma during Li evaporation (blue line)

3.2.2.2. Hydrogen uptake on a W sample exposed to H_2 GD irradiation under a Li evaporation environment

The TDS analysis of this sample is shown in figure 3.6. The heating ramp of the sample until it reaches 400ºC can be approximated as linear with a mean value around 10 K/s, (double compared to the previous case) suggesting with the lower area of the H desorbed spectrum that the amount of hydrogen present on the surface is quite lower in comparison with the previous sample. There are two main peaks in the H desorption spectrum located at 400ºC and 560ºC of sample temperature, being the second one located at a slightly higher temperature compared to hydrogen desorption peaks observed in gas exposure laboratory experiments with lithium [116, 117]. The contamination of the measured hydrogen desorption with residual hydrogen related with water decomposition, can be rejected as the water level during the TDS analysis remains at least an order of magnitude lower. The OES spectrum also shows the presence of lithium in the hydrogen plasma (figure 3.5, blue line). In this case the intensity of the Li I line is 10 times higher compared to the previous case while the intensity of Hα line remains at the same level, hence suggesting the presence of Li in the plasma as a main component not as an impurity that enters in the plasma as a result of the plasma wall interaction processes. Consequently, in this case the sample was irradiated simultaneously with mixed plasma of lithium and hydrogen due to the ionization of the evaporated atoms of lithium in the plasma. After finishing the analysis the presence of lithium layers on the sample surface was also clearly visible.

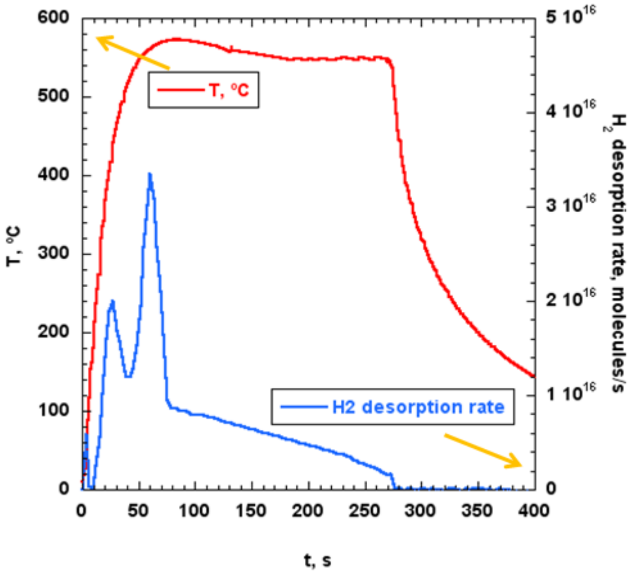

Figure 3.6. TDS analysis on the W sample exposed to Li seeded H_2 GD plasma

3.2.2.3. Hydrogen uptake on a pure W sample

The corresponding TDS spectra of a pure W sample irradiated with a H_2 GD plasma is shown in figure 6. This analysis allows the direct comparison among the Li-W hybrid layers and the pure W material in terms of hydrogen retention. The heating rate of the sample exhibits a similar behaviour during the initial step of the heating, compared to the case of the sample irradiated simultaneously with hydrogen and lithium The hydrogen desorption spectrum does not show a well-defined peak, instead of it, the spectrum presents a plateau between 400ºC and 520ºC in the sample temperature. In this range of temperatures the most of the hydrogen present on the sample is desorbed. The contribution in the desorbed hydrogen from the possible water decomposition during the measurement could also be considered as negligible as the level of the registered water signal is kept much lower that the registered signal of hydrogen.

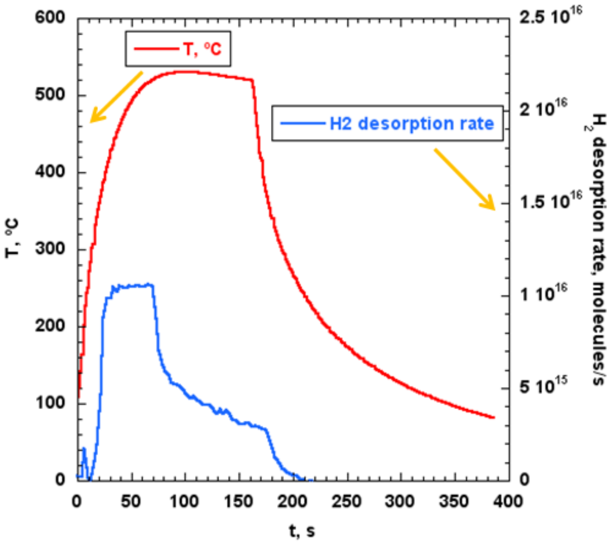

Figure 3.7. TDS analysis of a pure W sample irradiated with H_2 GD plasma

3.2.2.4. Quantification of the global and local hydrogen retention

The absolute calibration allows us the quantification of the local hydrogen retention on the samples desorbed in the TDS analyses. Furthermore by using the differentially pumped mass spectrometer to monitor the evolution of the 2 amu/e signal during the plasma operation, the global hydrogen uptake on the W wall of the plasma chamber can be estimated by particle balance calculations (using equivalent equations and mathematical treatment that was explained in subchapter 2.1.3.2) taken into account the depleted hydrogen from the gas phase during the GD plasma exposition. The associated errors in these calculations were estimated by calculating the statistic bias (least squares fit) related with the determination of the calibration parameters and the mass spectrometry measurements giving an approximated total uncertainty around 10-15%. A comparison between the local H retention measured by TDS on the samples and the concomitant global retention in the plasma chamber W wall is presented in table 3.2 for the experimental cases previously detailed.

Li-W Wall and sample state	Discharge Voltage, V	Global H retention (Wall), cm^{-2}	Local retention (Sample), cm^{-2}
Pure W irradiated with H_2 GD	250	2.10E+17	8.40E+17
pre Li W irradiated with H_2 GD	110	2.20E+18	6.10E+18
W exposed to Li-seeded H_2 GD	120	5.20E+17	1.90E+18

Table 3.2: Summary of the global (W wall) and local (W samples) hydrogen retention obtained for the different experimental cases

The calculated global H retentions for the W wall of the plasma chamber used in the experiments exhibit a clear difference among the studied cases. For the irradiation of the pure W without previous lithiation or Li evaporation during the plasma exposure a value around $2.1{\cdot}10^{17}$ cm^{-2} is obtained by particle balance for the global hydrogen retention, being in agreement with previous results [121, 122]. On the other hand for the case of the W lithiated before its H_2 GD irradiation, the global H retention obtained is $2.2{\cdot}10^{18}$ cm^{-2}, a factor 10 higher compared to pure W. Finally for the experiment with Li-seeded H_2 GD irradiation on W, the global retention calculated is $5.2{\cdot}10^{17}$ cm^{-2}, being this value approximately 4 times lower compared to the global retention calculated for the pre-lithiated W case. This difference between the both Li-W cases could be caused by the implantation of Li on W during the simultaneous irradiation in the Li-seeded H_2 plasma, assuming in this way that the H uptake by the implanted lithium atoms is much lower compared to the H uptake in just deposited Li. In this sense, previous simulations performed with the SRIM code revealed an average range implantation around 1.5 nm for Li projectiles with energy of 100 eV (very similar value compared to the case of our Li-seeded H_2 GD plasma implanted in W [123]. The local H retention on the W samples obtained by the integration of the H_2 desorption rate over the time during the TDS measurement exhibit a similar trend, being the H retention for the pre-lithiated W sample ($6.1{\cdot}10^{18}$ cm^{-2}) 3 times higher compared to the sample exposed to Li-seeded plasma ($1.9{\cdot}10^{18}$ cm^{-2}) and ~8 times higher than the retention on the pure W sample only exposed to H_2 GD plasma ($8.4{\cdot}10^{17}$ cm^{-2}). This result also points to the difference in terms of H retention between the implanted Li and the deposited Li on the samples previously commented. However the obtained values are systematically a factor 3-4 higher compared to the global retention values. This discrepancy between the global and local measurements could be caused by a non-homogeneous distribution of the plasma inside the chamber as well as spatial differences in the distribution of lithium deposition/implantation on the W surfaces.

3.2.3. Conclusions and future work

- The local hydrogen retention has been measured on W-Li samples exposed to H_2 GD plasma at a temperature of ~100ºC by TDS assisted mass spectrometry. The results show a hydrogen uptake in the case of tungsten irradiated with Li-seeded H_2 GD plasma approximately 3 times lower compared to the case of pre-lithiated W irradiated with H_2 GD plasma.
- The estimations of the global hydrogen retention on the W wall ($T_{surface}$~100ºC) of the plasma chamber, calculated by particle balance from differentially pumped mass

spectrometry measurements, also exhibit a hydrogen uptake 4 times lower for the Li-seeded H_2 GD plasma experiment, a similar factor compared to the observed for the measurements of the local H retention on the samples.

- OES measurements show the presence of Li as a main component of the plasma, indicating that the W surfaces are simultaneously bombarded by H and Li ions in the case of Li-seeded H_2 GD plasma, causing the Li implantation on the surfaces that could explain the lower H retention observed in this case.
- This scenario with simultaneous Li-H bombardment on the surface is expected in future reactor configurations that would combine W and lithium as PFM. These results represent an approximation to this topic. A further research involving hot and linear plasmas exposure is necessary to understand the behaviour of implanted Li in terms of associated fuel retention in a fusion reactor environment.

3.3. CO-DEPOSITION OF LI AND DEUTERIUM ON TUNGSTEN INFLUENCE OF SURFACE TEMPERATURE IN THE PROCESS

3.3.1. Development and performance of the LIDS technique for fuel removal and hydrogenic retention measurements on W-Li samples

Among laser methods [124], LIDS enables the *in situ* fuel removal and the measurement of the retained hydrogen isotopes in the first wall under high vacuum conditions. The desorbed hydrogen can be detected and measured using optical emission spectroscopy (ionization in a plasma bulk is in this case necessary) or mass spectrometry by means of Residual Gas Analysers [125]. The advantage of using this last option is that the absolute quantification of retained hydrogen is relatively simple as its absolute calibration requires only the use of gas injection methods to determine the correlation the absolute hydrogen desorbed flux with the mass spectrometry signals. Despite this advantage, to measure the desorption from the walls with an appropriate sampling time resolution (60-80 ms) that assures negligible data losses from the desorption peaks, the RGA diagnostic needs to be used in the leak test mode that offers the fastest time resolution (60-80 ms), but allow the detection of only one desorbed specie (one mass to charge ratio signal) during the LIDS shot. On the contrary, the optical spectroscopy detection presents a more difficult absolute calibration work, but allows the detection of all desorbed species during the laser shot. To generate the line emission spectroscopy signals, the ablation of the material (Laser Induced Ablation Spectroscopy, LIAS) that will be ionized in the plasma is mandatory. Additionally, Laser Induced Breakdown Spectroscopy, (LIBS) method allows the line ratio emission detection without the external plasma ionization. By using Q-switch laser mode operation, power density of the laser is increased and a plasma plume is generated after the interaction of the laser beam with the material. Related with these laser techniques, during February 2015, the student made a stay in the Sylvester Kaliski institute for Plasma Physics and Laser Microfusion (IFPiLM), sited in Warsaw (Poland) that is worth mentioning. In this collaboration, the student was introduced to the operation of pulsed Nd:YAG lasers utilized for LIBS applications and continuous Ytterbium fiber laser used for LIDS purposes. The valuable teaching and the skills related with laser operation acquired during this stay have been essential for the development of the LIDS experimental work related with this thesis. To perform the irradiation of the samples a solid state (Nd:YAG) laser (LITRON LPY 600) has been used. [126]. The main internal parts of the laser [127] are shown in figure 3.8.

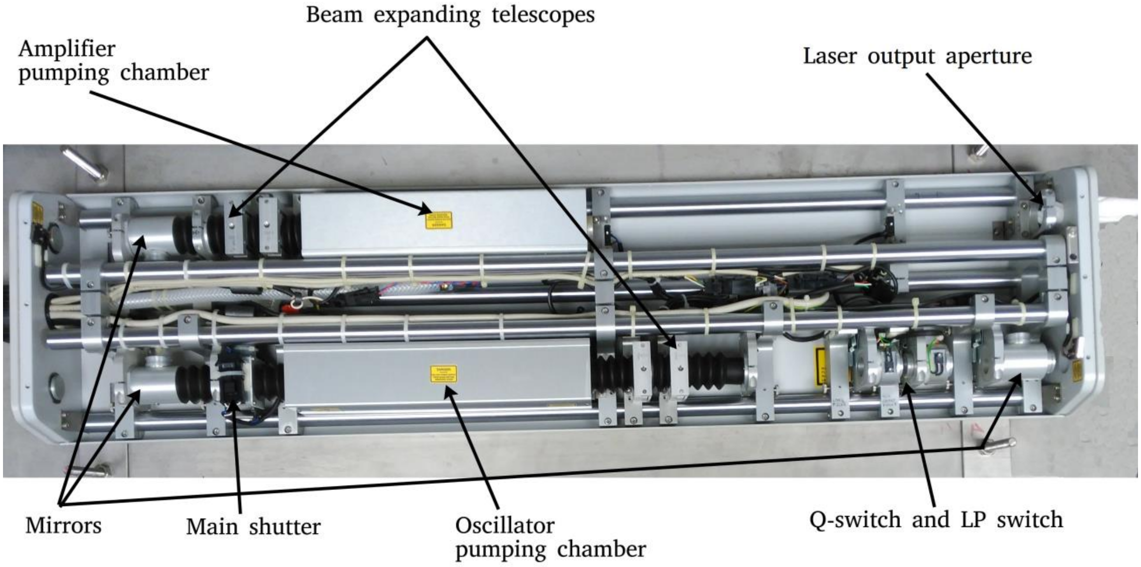

Figure 3.8. Internal components of the Nd:YAG Laser

In this laser the active medium is an yttrium aluminium garnet ($Y_3Al_5O_{12}$) solid crystal doped with neodymium ions (Nd^{3+}) that replace a part (around 1%) of the yttrium ones. These impurities are the responsible of the laser activity. A flash-lamp induces the excitation of the Nd^{3+} ions by providing the necessary radiation to the crystal. This radiation promotes the transition of the Neodymium ions to the excited level (laser pumping). After some time, the population of ions in the excited level overpasses the amount of ions in the ground level, this phenomenon is known as *population inversion***.** Excited atoms emit spontaneously photons when they decay to the ground state. In principle, the global set of emitted photons, have the same energy characteristics. On the contrary they have not any spatial coherence. However if these non-coherent photons are re-directed to the laser crystal the *stimulated emission* process takes place. This process is characterized by the emission of photons with the same frequency and phase in a high directional, spectrally pure coherent beam that forms the laser emission. Despite Nd:YAG lasers have atomic transitions around 940, 1120, 1320, and 1440 nm the main and mostly used transition operates at 1064 nm in the infrared spectral region. This transition constitutes the first harmonic of the Nd:YAG laser that can be increased in terms of frequency to second (532 nm) and higher harmonics (355 nm, 266 nm and 213 nm). Moreover, this laser can be used in two operational modes with different pulse duration: long pulse (0.25 ms) and Q-switch mode (6 ns). In these experiments, (that only need to induce the thermal desorption from samples) with moderate surface heating, the first harmonic radiation operating in long pulse mode was used in all instances. For applications that require a higher power density, for example to produce material ablation in LIAS and plasma plume formation in LIBS, operation in Q-switch mode is utilized. For both laser operation modes, the device has a maximum output of energy per pulse of 1100 mJ. Measurements of beam energy are carried out by means of a pyroelectric joulemeter (gentec-e). The spot size of the laser was measured (sensibility of 0.2 mm), presenting an approximate Gaussian distribution with a full width half maximum value (FWHM) of 6.5 mm (figure 3.9), corresponding to energy and power density values of 3.3 Jcm^{-2} and 13 kWcm^{-2} for long pulse mode.

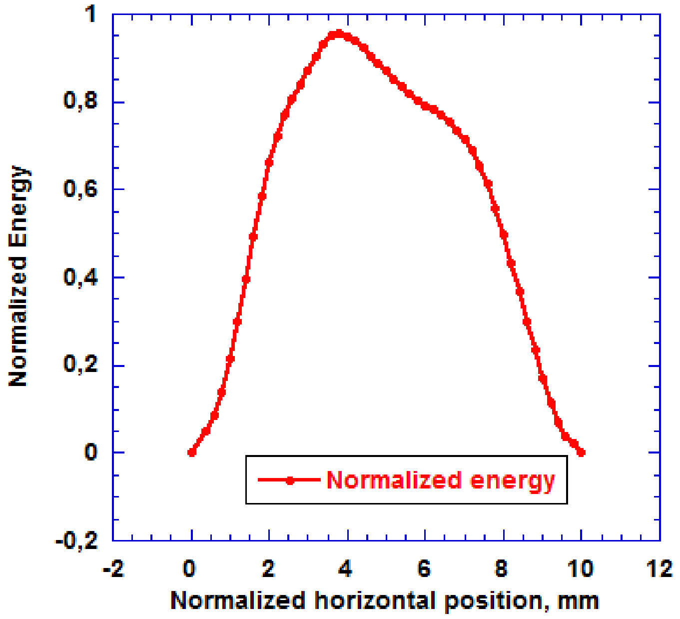

Figure 3.9. Laser spatial profile (FWHM=6.5 mm)

After focusing the laser with a converging lens (f=400 mm), a beam diameter of 0.125 mm is obtained (this diameter was measured directly from the created craters on the treated samples with profilemetry as will be shown in the subchapter 3.3.7.3). Consequently, the energetic characteristics of the laser are increased up to 90 J/cm^2 and 360 kW/cm^2. Potential Q-switch laser operation would increase the power density outputs of the system to 550 MW/cm^2 without focusing and 15 GW/cm^2 with the focused beam. The frequency of the laser can be modulated from 1 to 10 Hz. In all the experiments a repetition rate of 1 Hz was used. In order to estimate roughly the absorbed laser power, the energy losses due to reflection in the W-Li surfaces need to be taken into account. The reflectance (R) of tungsten and lithium surfaces exposed to infrared light (1064 nm) can be found in [128], being 0.60 the global value for tungsten and 0.94 for solid lithium (it is important to note that lithium melting is expected during the laser pulse and for liquid lithium the reflectance decreases). As will be explained later in the corresponding profilemetry subchapter, the non-homogeneity of the deposition process creates an irregular surface layer as the measurements show. In this situation, to use a medium value (between W and Li) for the reflectance (as well as for the thermo-physical values as thermal diffusivity [D]) seems reasonable. Furthermore, the hydrogenic and impurity content of the sample surfaces can modify the optical properties of the studied layers. The potential lithium hydride formation in samples with considerable hydrogenic content, the roughness and the surface morphology (tungsten surface is not polished) can influence in the surface characteristics of the treated materials, thus affecting the reflectance values. However, no information is available about the quantification of these effects in the reflectance experimental values. Thus, a negligible influence of these experimental conditions in the physical properties values is assumed. The rest of the thermal characteristics for tungsten [129], lithium [130] and mean values between both elements (approximation for mixed layers), are presented together with reflectance values in table 3.3.

Element	**c_p, J/Kg K**	**ρ, Kg/m^3**	**k, W/m·K**	**D, m^2/s**	**Reflectance**
Tungsten (W)	130	19250	170	6.79E-05	0.602
Lithium (Li)	3750	535	85	4.24E-05	0.941
W-Li (av. value)	1940	9918	128	5.51E-05	0.772

Table 3.3. Physical and optical properties for W, Li and average values

To achieve the maximum energy per pulse, the optimization of the laser is necessary. This optimization was carried out by lining up the internal mirrors, regulating them with accessory screws present inside the laser head and adjusting their position while the energy pulse is measured by the joulemeter until reaching the maximum output energy configuration. With this procedure, an energy of 1067±50 mJ was obtained, very close to the maximum value that the manufacturer provides. Once the laser energy output is maximized, the device is ready for operation. Normally, Laser Induced Desorption uses a relatively long pulse (around ms of duration) laser beam to induce thermal release of hydrogen and volatile compounds present on the surface layers and deposited films. Minimum power densities in the range of 50-150 kW/cm^2 are necessary to rise the temperature of the surfaces in the treated spots up to values that assure the total desorption of hydrogenic species without producing sudden ablation or disintegration in the material. On the contrary, melting and evaporation of volatile layers (in this case Li due to its low melting point) can be induced. In general, on lithium layers, the total desorption of hydrogen and deuterium content in the Li-W-D film is obtained at temperatures of 600ºC as was previously referenced. However for W and Be, using flash heating, higher temperatures up to 1000ºC or beyond are necessary to desorb completely the hydrogenic content present specially on trapping sites in the bulk microstructure. In the case of beryllium co-deposits, there are serious concerns about the requirement of melting to produce the total desorption of hydrogen isotope species using laser-based techniques. It would require temperature peaks around 1300ºC (melting point of beryllium is 1287ºC). The heat transfer and temperature changes induced by the laser will be analysed in the subchapter 3.3.4. An extensive analysis of the heat conduction equations will be applied in order to evaluate the spatial (depth profile) and temporal evolution of the temperature changes expected on the laser heated spots.

3.3.2. Mass spectrometry measurements and calibration work for the hydrogen isotopes

The detection and quantification of the hydrogenic desorbed species (H_2, HD and D_2) was carried out by using a residual gas analyser (RGA) operating in high vacuum conditions. Specifically, a SRS 100 mass spectrometer working in the leak test mode was used. By calibrating absolutely the mass spectrometer using the same method explained in subchapter 3.2.2.1, the signals associated to the hydrogenic molecules (2 amu/e for H_2, 3 amu/e for HD and 4 amu/e for D_2) can be absolutely quantified. This calibration work relates the single RGA peaks to absolute flux values (molecules/s) allowing the absolute quantification of the desorbed products. Finally by integrating the peaks registered by the RGA during the sample irradiation with the laser, the amount of hydrogen isotopes desorbed from the Li-W films can be absolutely quantified. This calibration procedure was performed separately for hydrogen (calibration respect to 2 amu/e) and deuterium (respect to 4 amu/e) as the RGA has, in principle, different sensitivity for each molecule. For the mixed specie HD, as pure HD gas is not available at laboratory, this absolute calibration was not possible. Consequently for HD, an intermediate value between the calibration constants for hydrogen and deuterium was used in the quantification. The following figures show the results of both absolute calibrations for D_2 and H_2.

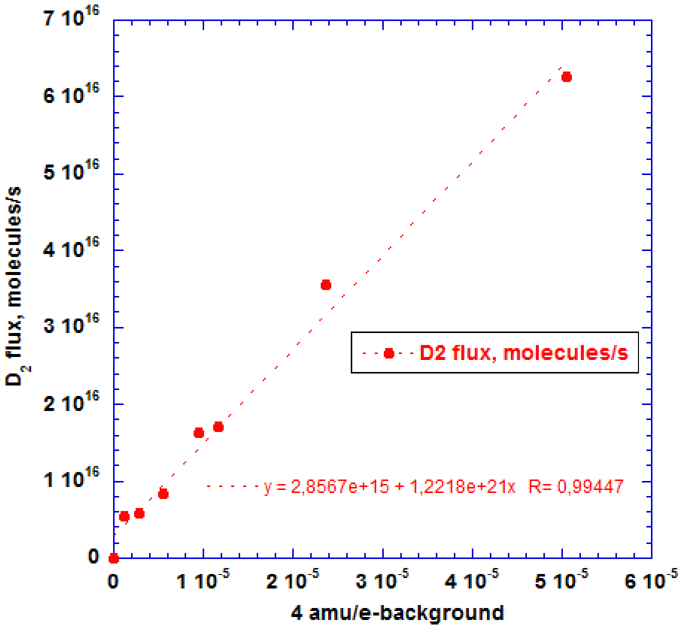

Figure 3.10. Absolute calibration work for D_2 in the LIDS chamber

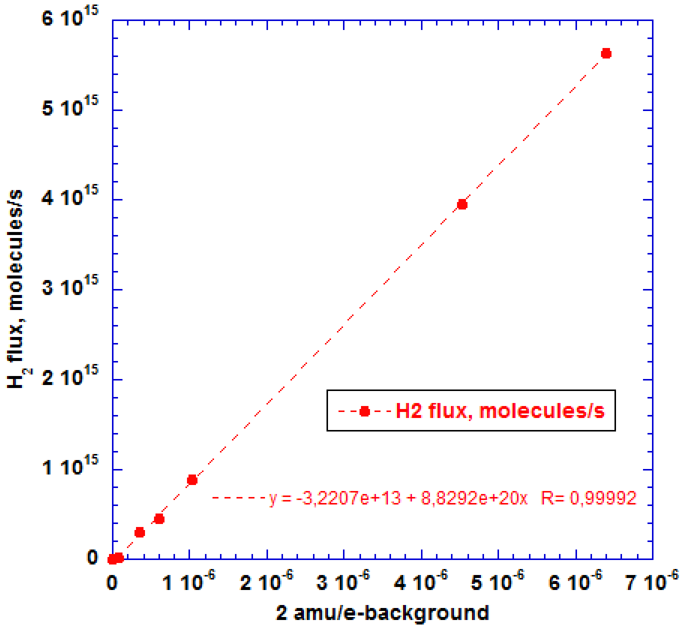

Figure 3.11. Absolute calibration work for H_2 in the LIDS chamber

As is shown in both figures the RGA signals (2 amu/e and 4 amu/e) are adjusted to the inlet fluxes in a linear fit. The slope of the fit gives the calibration constant (K_x) for the gaseous specie, whose values are presented in table 3.4.

Gaseous specie	**Calibration constant, [a.u.]**
Hydrogen	$K_{H_2}= 8.83\cdot10^{20}$
HD	$K_{HD}= 1.05\cdot10^{21}$
Deuterium	$K_{D_2}= 1.22\cdot10^{21}$

Table 3.4. Calibration constants for H_2, HD and D_2 in the LIDS chamber

3.3.2.1. Consistency of the RGA measurements during the laser pulses.

During the LIDS analysis, the hydrogenic desorption on samples is visualized after the laser shots in the mass spectrometer software as peaks in the mass to charge ratio signal. The height and area of the registered peak depends on the hydrogenic content of the heated spot. As has been explained previously, the leak test mode was used for the measurements due to its high time resolution, registering only one mass to charge ratio signal in each measurement. To guarantee that data from the desorption peaks are not missed during the measurement due to insufficient sampling resolution, a test was performed in order to compare the peaks obtained with the RGA to the absolute pressure peaks detected by the ionization gauge pressure sensor. Connecting this device to an oscilloscope the registered pressure signal can be sampled up to a fast time resolution of 5 ms. In figure 3.12 the comparison of both RGA and pressure signals is presented, for a resolution of 60-70 ms in the RGA data acquisition. It demonstrates that the correlation between both signals is optimal. In this way the data losses during the RGA measurement can be considered as negligible. Consequently, the employment of the leak test mode with time resolution (sampling) between 60-70 ms is suitable for RGA measurements of hydrogenic desorption during LIDS pulses.

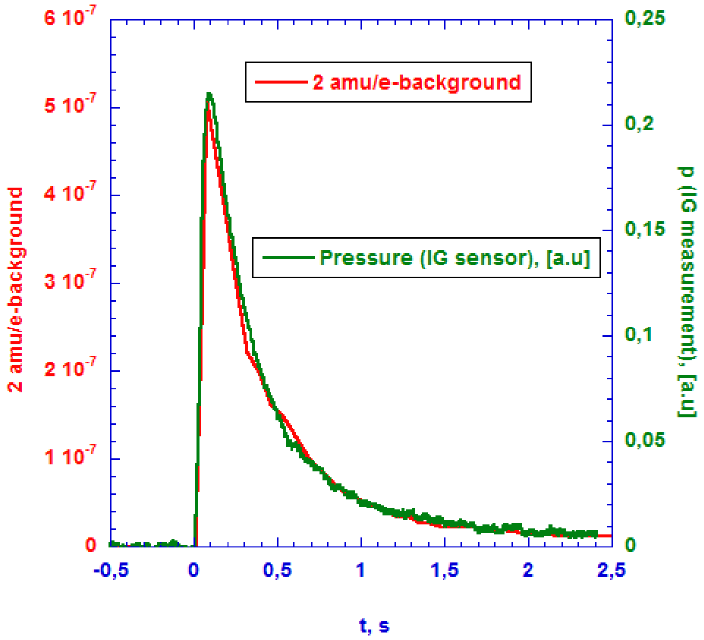

Figure 3.12. Comparison between RGA and pressure signals during LIDS pulse

3.3.3. Pulsed heat transfer between laser beams and solid surfaces

The hydrogenic release from samples is induced by the temperature rise achieved in the surface spot as a result of its interaction with the impinging laser beam. The amount of hydrogen isotope desorbed from the hot spot will depend on the maximum temperature achieved on the surface during laser irradiation. Thus, the understanding and the analytical evaluation of the heat transfer and the concomitant surface heating of the sample is essential for the estimation of the laser induced temperature changes on the surface that determines the hydrogenic desorption. The deposited heat load on the surface will be propagated through the material bulk following the Fourier's law of heat conduction:

$$\frac{dQ}{dt} = -k\nabla T \,, \quad (3.4)$$

where Q is the heat propagated, k is the thermal conductivity of the material and ∇T is the temperature gradient. Before continuing with the analytical study, several simplifications are assumed in order to clarify and simplify the equations and the evaluation of the temperature profiles in the exposed material [131].

- For pulse durations longer than 1 nanosecond, thermal transport following the Fourier law can be assumed. In this way the energy of the lattice will follow the laser pulse. With this assumption, the contribution of electrons or photons that can transfer energy to the lattice (in the time scale of picoseconds) can be neglected. Our laser operation in long pulse mode (duration of τ =0.25 ms) agrees with this general simplification.

- Geometrical considerations about the laser beam are also important. The intensity of the beam can vary spatially (also temporally) presenting normally a Gaussian distribution that leads to a three dimensional heat flow problem. On the other hand if the intensity of the laser is considered constant over the time and with a flat spatial distribution (known as top hat profile), the problem is simplified from the mathematical point of view as the heat transfer is not supposed to happen in lateral directions. In this way the heat transfer is transformed into one dimensional heat flow conduction problem (vertical heat propagation in z axis, being the energy adsorbed in a small depth compared to the spot surface dimensions). In principle our laser spot profile can be approximated to this particularity.
- The absorbed optical radiation is propagated in the vertical (z) direction normal to the surface. This source term in the heat conduction equation can be calculated as:

$$I_T = I_0 \cdot (1 - R), \quad (3.5)$$

I_0 is the intensity of the laser beam in Wm^{-2} and R is the reflectivity coefficient for the solid material calculated from optical parameters [128]. This intensity is optically attenuated following an exponential decay inside the target:

$$I(z) = I_T \cdot \exp(-\alpha \cdot z), \quad (3.6)$$

where α is the optical absorption coefficient [128] that gives an idea of the optical penetration depth of the beam. On the other hand, the energy deposited by the laser beam is distributed on the z direction as heat propagation following the heat conduction with a thermal penetration depth ($\sqrt{D\tau}$) that estimate the characteristic length for the thermal propagation. In this expression, D is the thermal diffusivity expressed in function of thermal and physical properties of the substrate ($D = \frac{k}{\rho c_p}$, being k the thermal conductivity, ρ the density of the bulk material and c_p the heat capacity) and τ is the laser pulse duration (0.25 ms). If the thermal penetration depth is much larger than the optical one, ($\sqrt{D\tau} >> \alpha^{-1}$), most of the energy is absorbed by the surface of the sample. In this way, the source term of the heat equation is independent of the z coordinate. It implies that the heat transport is dominated by the thermal transference of heat and the problem can be simplified to surface temperature absorption. In the following table the optical and thermal penetration depth values for tungsten, lithium and the mean value between both elements are presented for the case of laser heating with Nd:YAG (1064 nm) radiation.

Element	$\sqrt{D\tau}$ **, μm**	α^{-1}**, μm**
Tungsten (W)	129	0.0223
Lithium (Li)	103	0.0168
W-Li (av. value)	116	0.0196

Table 3.5. Optical and thermal penetration depth for W, Li and average values for the W-Li layer

As it is shown, thermal penetration depths in all instances are 4 orders of magnitude higher than optical penetration depths. Applying this approximation the needed mathematical treatment to get analytical solutions is much easier.

- Finally, we shall assume temperature independent thermo-physical properties such as density, heat capacity and thermal conductivity for the involved materials. In this way these properties can be considered constant during the pulsed heating.

Taking into account these simplifications and considering surface heat absorption with thermal propagation only in the z coordinate in a semi-infinite solid, the heat equation can be expressed as:

$$\frac{\partial T(z,t)}{\partial t} = D\frac{\partial^2 T(z,t)}{\partial z^2} + \frac{\alpha I_0}{\rho c_p}(1-R), \quad (3.7)$$

where the source term $S=\alpha \cdot I_T = \alpha \cdot I_0(1-R)$ is a constant term that can be evaluated from the laser energy output (E), the duration of the pulse (τ) and the spot surface area (A) of the solid-laser interaction:

$$I_0 = \frac{E}{A\tau} \rightarrow I_T = \frac{E}{A\tau} \cdot (1-R) . \quad (3.8)$$

The energy of the beam is between 1000-1100 mJ and for long pulse laser operation the duration of the pulse is 0.25 ms. The post-mortem profilemetry measurements on the treated samples show that after the beam focusing, a circular section with an approximate diameter, d≈0.125 cm can be considered for the laser spot, thus given an interaction area of around 0.0123 cm^2. With these values the power density that reaches the surface, is approximately 360 kW cm^{-2}. Supposing a lithium deposition thickness on samples around 1-2 μm (see subchapter 3.3.5.3 for the detailed lithium deposition calculations for the sample) a simple numerical estimation (taking into account the heating of lithium from room temperature to its boiling point and the latent heats of melting and vaporization) demonstrates that if the laser energy adsorbed by the heated spot (E·[1-R]) was employed to heat only the deposited lithium layer, it would be enough to heat the Li deposited atoms up to its boiling point (1342ºC), even producing the ebullition of an important part of these deposited Li atoms. Although this energy is propagated in the Z direction along the sample thickness (100 μm) and hence not all the energy is employed to heat the lithium layer, the necessary temperature rise for the total desorption of the hydrogenic content is much lover (ΔT~600ºC). Consequently, this energy loading produced by the laser shot should be enough to induce the total hydrogenic outgassing. The reached temperature on the lithium layer during the laser heating (temperature rise) will determine the hydrogen isotopes desorption and their possible total elimination.

The solution of the one dimensional differential heat equation [132] gives the evolution of the temperature (T) at a depth z and time lower or equal to the laser pulse length (τ = 0.25 ms)

$$T(z, t \le \tau) = T_0 + \frac{2I_0(1-R)}{k} \cdot \sqrt{Dt} \cdot ierfc\left(\frac{z}{2\sqrt{Dt}} \right) . \quad (3.9)$$

In this expression, ierfc is the integral of the complementary error function. It can be evaluated in terms of the error function:

$$ierfc(x) = \int_{\infty}^{x} erfc(s)ds = \frac{1}{\sqrt{\pi}} \cdot \exp(-x^2) - x\left(1 - erf(x)\right) . \quad (3.10)$$

Naming the term $\frac{z}{2\sqrt{Dt}}$ = Z and introducing the equivalence previously shown:

$$T(z,t \le \tau) = T_0 + \frac{2I_0(1-R)}{k} \cdot \sqrt{\frac{Dt}{\pi}} \cdot \left[\exp(-Z^2) - \sqrt{\pi} \cdot Z \cdot (1 - erf(Z)\right]. \ (3.11)$$

This general expression allows the evaluation of the temperature depth and time profiles. The maximum temperature rise is achieved on the surface (at z = 0→ierfc (0) = $\pi^{-1/2}$) and the equation 3.11 is reduced to:

$$T(0,t \le \tau) = T_0 + \frac{2I_0(1-R)}{k} \sqrt{\frac{Dt}{\pi}}. \ (3.12)$$

In principle, when the laser is focused using a lens into a smaller circular uniform spot (with radius r), the equation changes to:

$$T(z,t \le \tau) = T_0 + \frac{2I_0(1-R)}{k} \cdot \sqrt{Dt} \cdot \left[ierfc\left(\frac{z}{2\sqrt{Dt}}\right) - ierfc\left(\frac{\sqrt{z^2 + r^2}}{2\sqrt{Dt}}\right)\right], \ (3.13)$$

being the temperature at the surface:

$$T(z,t \le \tau) = T_0 + \frac{2I_0(1-R)}{k} \cdot \sqrt{Dt} \cdot \left[\frac{1}{\sqrt{\pi}} - ierfc\left(\frac{a}{2\sqrt{Dt}}\right)\right]. \ (3.14)$$

The term $ierfc\left(\frac{a}{2\sqrt{Dt}}\right)$ (with a=$\sqrt{z^2 + r^2}$), takes into account the losses caused by sideways diffusion [132], if this term<<1 (it implies that $\frac{a}{2\sqrt{Dt}}$ >>1) the previous expression is equivalent to 3.11. Considering r>>z this assumption will be valid if $t < \frac{a^2}{4D}$. Using a spot radius of 0.06 cm and the average value (between lithium and tungsten) for thermal diffusivity ($5.51 \cdot 10^{-5}$ m^2/s) the general solution without taking into account the focusing of the beam, can be used for t <1.6 milliseconds, a time 6.5 times longer than the laser pulse duration. For a time greater than the pulse duration ($6.5\tau > t > \tau$), the temperature profile can be evaluated introducing another term delayed in a time factor ($t-\tau$):

$$T(z, t \leq \tau) = T_0 + \frac{2 I_0 (1-R)}{k} \cdot \left[\sqrt{Dt} \cdot ierfc\left(\frac{z}{2\sqrt{Dt}} \right) - \sqrt{D(t-\tau)} \cdot ierfc\left(\frac{z}{2\sqrt{D(t-\tau)}} \right) \right], \quad (3.15)$$

3.3.3.1. Evaluation of the laser-induced temperature changes on the sample surfaces.

Depth (z) and temporal (t) temperature profile

Following the mathematical treatment previously explained, computer simulations were performed in order to evaluate the temperature changes induced during the laser operation on the W-Li targets. For the evaluation, in principle the laser beam directed to the sample will interact with the thin lithium-deuterium film. The total lithium uptake was measured by flame atomic emission spectroscopy after its dissolution on ultrapure water. These results gave a lithium thickness on the samples around 0-3 μm, being the total thickness of the W sample equal to 100 μm. In this way, after overpass of the lithium layer, the laser beam will heat the tungsten bulk. Moreover, the profilemetry measurements revealed that the deposition of lithium was very irregular, presenting zones almost without coverage and other ones that exceed the medium thickness evaluated with photometry. In this scenario with inhomogeneous and mixed surfaces, the previously commented use of intermedium (between W and Li) thermo-mechanical properties in the simulations seems reasonable. With this premise, two different simulations (shown in figures 3.13 and 3.14) were performed:

- Temporal profiles to evaluate the temperature rise during the laser irradiation and the subsequent cooling ($0<t<6\tau$) for a given z position ($0<z<100$ μm)
- Vertical (z) profiles to evaluate the temperature at different z positions ($0<z<100$ μm) at a given time ($0<t<\tau$).

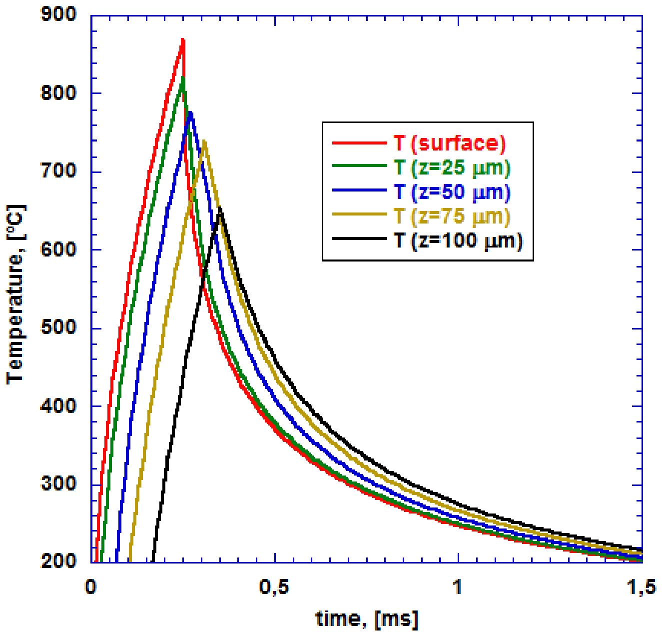

Figure 3.13. Simulations for the temperature temporal profile on the W-Li samples at various vertical (z) positions

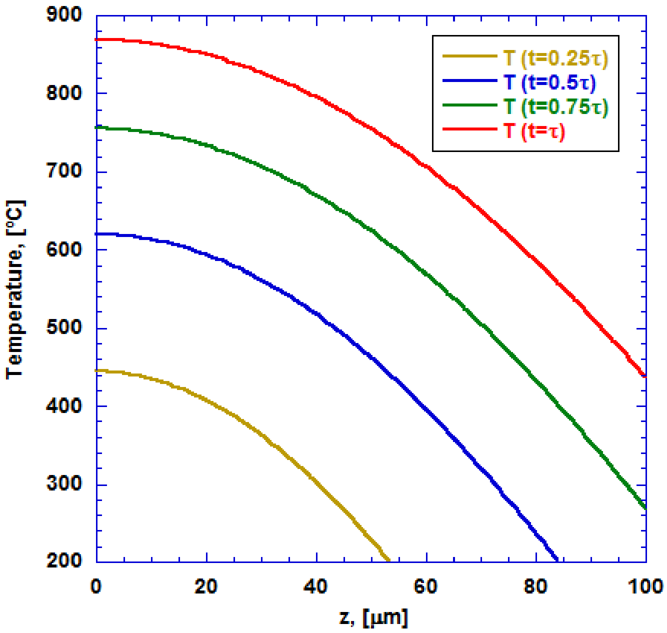

Figure 3.14. Simulations for the temperature vertical (z) profile at different times

In the case of the temporal profiles, the simulations show maximum temperatures between 900ºC-600ºC achieved on the sample. Even for the deepest point (100 μm) situated at the farthest distance from the laser beam incidence, the temperature rises beyond 600ºC. Several experimental results show that the hydrogenic desorption from lithium layers must be completed at this temperature [97, 115-117]. The figure 3.13 presents coherent curves, with the maximum situated close to the pulse duration time (0.25 ms) being them more delayed from this instant when the analysed layer is deeper. This temperature maximum also decreases with deeper positions. The depth profile simulations (figure 3.14) exhibit curves for different heating instants. From $t=0.5\tau$, the surface temperature is higher than 600ºC, reaching this temperature a maximum value close to 900ºC, at $t=\tau$. This simulation complements the first one and shows a temperature rise $(\Delta T)\sim 600$ºC for all the sample bulk. In summary, these calculations indicate that the laser shot is able to heat the sample sufficiently to induce the total hydrogenic desorption. In any case, more diagnostics and post mortem analysis were performed to assure the complete removal of the hydrogenic content.

3.3.4. Installations, procedures and techniques utilized during the experimentation

The experimental works performed during these studies can be divided into three separated phases:

- 1) Preparation of W-Li-D samples by means of its deposition under vacuum conditions (without atmospheric contamination)
- 2) LIDS measurements after transportation of the samples in closed manipulators over-pressurized with dry argon to avoid atmospheric contamination
- 3) Application of post mortem techniques for additional characterization of the films

3.3.4.1. Preparation of W-Li-D samples

The deposition of lithium and deuterium on the tungsten rectangular (20.4 mm length, 17.5 mm width, 0.1 mm thick with an exposed area of 3.6 cm^2 and total mass, $m=0.72\pm0.04$ g) samples was carried out in a stainless steel vacuum vessel (deposition chamber illustrated in figure 3.15) with an approximated volume of 5 L, pumped out by means of a turbomolecular pump in series connection with a rough pump. This deposition chamber was specifically designed and installed in the CIEMAT plasma-surface interaction laboratory.

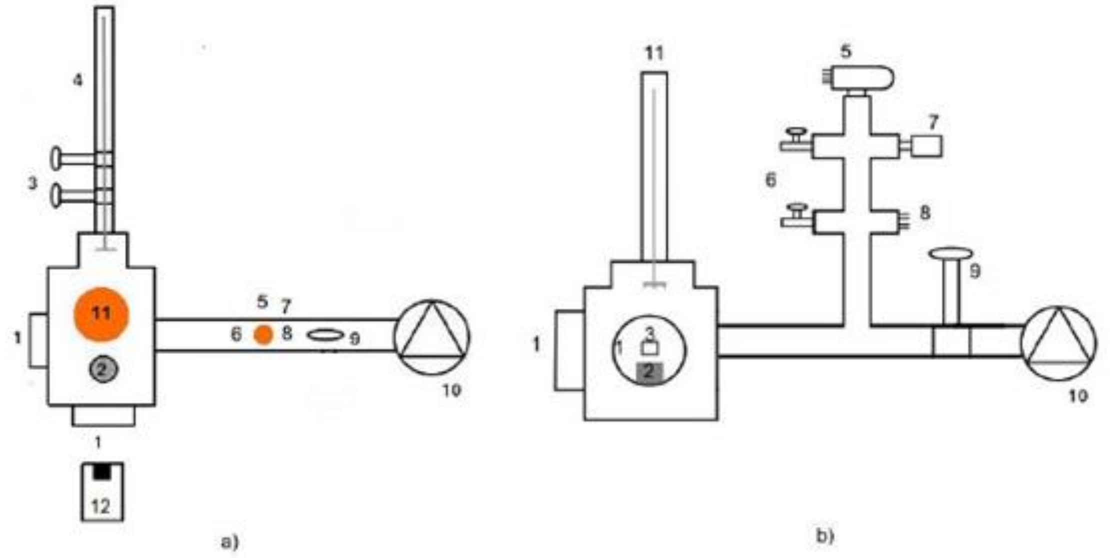

Figure 3.15. Deposition chamber sketch: a) Top view, b) Front view
1. Optical windows, 2. Lithium oven, 3. Gate valve for sample manipulator, 4. Sample manipulator, 5. Ionization gauge, 6. Gas inlet, 7. Capacitance manometer, 8. Feedthrough for Li oven and thermocouple, 9. Gate valve for turbopump, 10. Pumping unit, 11. Sample heating element (filament), 12. Pyrometer

Two different Li-D_2 interaction environments were used to prepare the samples:

- As the first objective of the experiments was to study the deuterium and lithium interaction with tungsten that can be produced in areas of a fusion reactor W first wall W, the deposition of lithium and deuterium in this case was simultaneous in a co-deposition regime at high vacuum conditions ($p_{chamber} < 1$Pa).
- To study in a broader way the deuterium uptake in W-Li films, pre-deposition of lithium on W was carried out before exposing the films to molecular deuterium at a higher pressure conditions compared to the previous case (≈133 Pa). The influence of the surface temperature in the formation of the Li-D film was studied as different samples were prepared by changing the surface temperature (200ºC, 300ºC and 400ºC) during the D_2 gas exposure.

3.3.4.1.1. Simultaneous deposition of deuterium and lithium on W. Simulation of first wall fusion reactor environment

One sample (named as wlid) was produced by evaporating lithium in a molecular D_2 (0.67 Pa) environment that tried to simulate the neutral pressure levels existent on remote areas of a fusion reactor first wall during D-T operation. Inside the deposition chamber a stainless steel oven (2.5 cm of diameter and 4 cm of height) filled with 2 grams of lithium was placed. Deposition of Li on the sample takes place after the effusion of the Li atoms through a circular hole (d=1 cm) situated on the top of the oven. The oven was heated up to 450ºC during 30 minutes during the simultaneous Li-D_2 deposition by using an electric resistance rolled around it. Temperature of lithium during the process was measured with a type K thermocouple inserted in the Li bulk. The monitoring of the temperature during the process showed a good equivalence between the measured temperature and the Li temperature as the melting of the lithium was registered around 178ºC in the thermocouple, with the nominal melting point of lithium being 180.5ºC. The tungsten samples (cold rolled and high purity commercial tungsten provided by Special Metals and Products), were washed out in an ultrasound bath followed by baking (150ºC) for their drying and a final cleaning treatment with acetone and ethanol to eliminate dust and impurities.

After this protocol the samples were placed in a 30 cm length manipulator installed in the deposition chamber through a conflat flange coupled to a gate valve. The sample was positioned at a distance of 26.5 mm, perpendicularly oriented to the oven hole, forming an angle of 25º respect the normal direction to the effusion hole surface. In this way, the sample encompasses an approximate solid angle of around 0.63 steradian when its surface is projected into the evaporation hemispherical surface of the oven hole. As a consequence of the proximity of the sample during the oven heating for the Li evaporation, the radiation increases the sample temperature up to 200-225ºC. The temperature on the tungsten surface was measured using an infrared pyrometer (OPTRIS® CT) with a measurement range between 150-1000ºC. Two optical windows were placed in chamber ports, to visualize the sample position respect the oven (lateral window) and measure its temperature (frontal window). An ionization gauge (Bayard Alpert) was used to monitor de vacuum level inside the vessel, being the residual pressure before the sample preparation normally around $6 \cdot 10^{-5}$ Pa.

Before starting the co-deposition, the sample was heated up to 550ºC during 30 minutes to produce the outgassing of residual water and hydrogen. This heating was produced with a W resistive filament placed behind the sample holder, very close but detached from it. In this way the sample is heated up by radiation. The tungsten filament is fed with an adjustable DC power supply up to a maximum power of 100 W (24 V and 4.2 A). The lithium bulk and oven were also outgassed at temperatures around 300-325ºC during 30 minutes before starting the evaporation to remove hydrogen, water and impurities and avoid their deposition together with the Li atoms on the sample surface. After these outgassing procedures the sample is ready to be exposed to the D_2/Li mixed environment. The temperature of the lithium is increased up to 450ºC. When it reaches this value, a deuterium molecular gas flow is introduced in the chamber through a leak valve up to a total pressure of 0.67 Pa (measured with a capacitance manometer) during 30 minutes in a continuous flow regime. The temperature of the sample was monitored with the pyrometer, oscillating between 200-225ºC during all the exposure. After this time the sample is prepared for the LIDS analysis in order to quantify the hydrogenic retention.

The visual inspection through the optical window reveals the deposition of a lithium layer on the sample (the surface changes its colour from brilliant grey of tungsten to matte grey of lithium). Then the manipulator is retracted and the whole chamber is vented with Argon. At this moment the gate valve of the manipulator is closed in over-pressure conditions. After this procedure the manipulator is ready to be removed from the deposition chamber in order to carry the sample to the LIDS chamber avoiding its contamination with atmospheric gases and the concomitant chemical modification of the deposited layers. Lithium is a very reactive element prone to oxidation and carbonation when is exposed to air. The interaction of the Li-D film with N_2, O_2 and water vapour has been widely studied [133, 134]. It is demonstrated that the isotope exchange induced by the chemical interaction of the Li-D films with water molecules produces the total removal of deuterium from this film [135]. Hence, a water free environment for the W-Li-D samples during all the experimental procedure is essential to keep the D content on the film unaltered.

3.3.4.1.2. Pre-deposition of lithium on tungsten followed by high pressure D_2 gas exposition

In order to produce thicker deuterium films on the W-Li surface and test the capabilities of LIDS technique to remove hydrogenic content, a different method of samples preparation was carried out in the deposition chamber using the same experimental protocol previously explained, only changing some experimental details. In this case, pre-lithiation of the tungsten samples was performed by evaporating Li at 450ºC from the oven during 30 minutes in vacuum conditions (residual pressure around $6\cdot10^{-5}$ Pa, and surface temperature around 200-225ºC on sample). After pre-lithiation, the sample is exposed to a higher D_2 pressure environment (133 Pa) for 1 hour (changing the wall temperature from 200ºC to 400ºC, thus producing different samples). The gate valve that connects the turbopump with the deposition chamber is closed to maintain this deuterium pressure without external puffing in static conditions (no pumping).

This procedure was repeated several times to prepare different samples only changing the sample temperature that can be regulated by changing the power of the heating filament. It is important to note that the deuterium exposition must be started when the temperature of the lithium present in the oven is below its melting point to avoid its exposure to deuterium in liquid state. If deuterium is injected in the deposition chamber immediately after deposition of lithium when it is still hot (and liquid) inside the oven, the liquid surface (with several grams) acts as a sink for the D_2 molecules, being them absorbed in the oven, avoiding the interaction of deuterium with the thin W-Li layer on the sample. In our experiments the exposure of the pre-lithiated samples to deuterium was carried out with temperatures lower that 100ºC inside the oven in all instances. The temperature of the sample surface is measured with the optical pyrometer previously described.

Three different surface temperatures were studied: 200ºC (sample named as wlid6), 300ºC (wlid8) and 400ºC (wlid10), assuring in this way that pre-deposited lithium is in the liquid state in all instances. The heating of the sample during the starting of the exposure to deuterium can produce the melting of the pre-deposited lithium on the vertical surface of the sample. In these conditions the gravity force acts on the liquid vertical surface producing lithium losses (that were visible during the experiment development) due to its dripping from the sample. After the complete preparation of the pre-lithiated samples, the same procedure (overpressure with argon and transportation in a sealed manipulator without air leaks) to transfer the samples to the LIDS chamber was carried out in order to assure the conservation of the chemical nature of the W-Li-D layers. Additionally, for the case with highest lithium and deuterium content, (pre-lithiation + D_2 exposure at 200ºC), another two samples (named as wlid11 and wlid13) were prepared and their D content was measured by LIDS in order to check the reproducibility of the technique and the consistency of the results.

3.3.4.1.3. Preparation of a tungsten blank sample

Finally a blank tungsten sample (wlid12) was prepared in order to compare the retention values of the W-Li layers with the uptake of the lithium-free tungsten surface. It was prepared by outgassing it with the accessory filament, as was previously explained, and exposing it later to D_2 gaseous environment (p=133 Pa during 1 hour of exposure).

3.3.4.2. Lithium evaporation estimations

As lithium is a very active chemical element compared to tungsten, the layer containing the evaporated and deposited atoms will present the most of the hydrogenic content. In order to have a previous estimation of the potential lithium (and the associated deuterium) uptake on the samples, calculations involving the temperature dependence of the lithium evaporation and its spatial distribution were performed. The dependence of the vapour pressure of lithium with temperature is exponential:

$$P_{vap}^{Li} = 133 \cdot \exp(18.4 - \frac{18759}{T}). \text{ (3.16)}$$

Inside the oven, the evaporation takes place following an effusion process through the small orifice present on the upper part of the oven. This evaporation volume is called *Knudsen cell* or effusion cell. Inside it, the area of the orifice is considered as an evaporation source of the same area. The pressure vapour value is related with the maximum evaporative flux of lithium atoms in the direction normal to the oven orifice:

$$\Gamma_{Li}^{\max} = \frac{dN_{Li}}{dAdt} = (2\pi m k_B T)^{-1/2} \cdot (P_{vap}^{Li} - P). \text{ (3.17)}$$

In this expression, m is the mass of lithium atoms, k_b is the Boltzmann constant, A is the area of the oven orifice, T is the absolute temperature of the lithium bulk and P is the surrounding pressure inside the oven during the evaporation. As the deposition of lithium was carried out in high vacuum conditions or low pressure (5 mTorr) D_2/He environments, the difference $P_{vap}^{Li} - P$ can be approximated to P_{vap}^{Li} giving the maximum evaporation rate. Integrating this previous expression over time and orifice area (A_T), the total number of evaporated lithium atoms (N_{Li}^{Tot}) can be calculated:

$$N_{Li}^{Tot} = A_T \cdot \int_0^t (2\pi m k_B T)^{-1/2} \cdot (P_{vap}^{Li}) dt. \text{ (3.18)}$$

To evaluate this expression we consider as negligible the evaporative flux of lithium at temperatures lower than 350ºC. In this expression, t=0, is the instant when the oven overpasses the temperature of 350ºC during its progressive heating up to 450ºC. This expression is integrated over all the time that the oven is maintained at 450ºC, including also the posterior time of cooling down until 350ºC. The following plot (figure 3.16) shows this integration time (almost 3000 s of total time, instead only 1800 s corresponding to the evaporation time at 450ºC) in a clearer way. The evaluation of this integral gives a total number of evaporated lithium atoms around $4.3\cdot10^{20}$ using the formula 3.18.

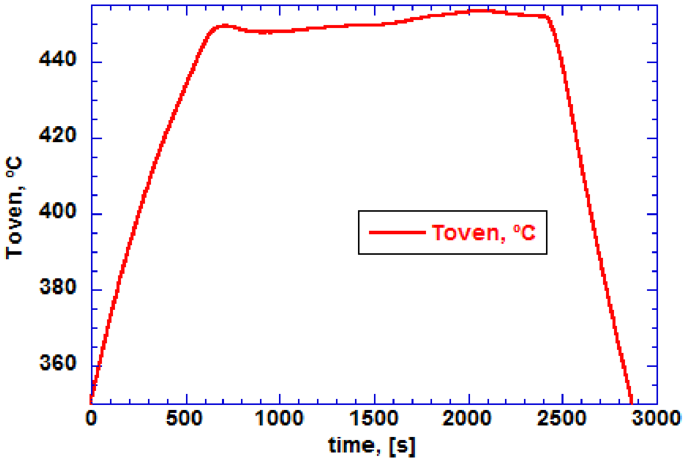

Figure 3.16. Temporal evolution of T_{oven} during Li deposition and integration time (T_{oven} $\geq$ 350ºC) for the evaporative flux

In addition, the ideal Knudsen cell exhibits an angular distribution of the evaporated particles with solid angle (ω) and exit angle (φ) through the orifice, in a cosine law distribution. As it is shown in figure 3.17 the exit angle (φ) is measured respect to the normal direction to the orifice surface. The sample is situated respect to the oven at a medium distance of 26.5 mm, being between exit angles of φ_1=12º and φ_2=35º. This configuration gives a medium exit angle of 23º and projects a solid angle (ω, represented in red in the figure 10) of 0.6 sr.

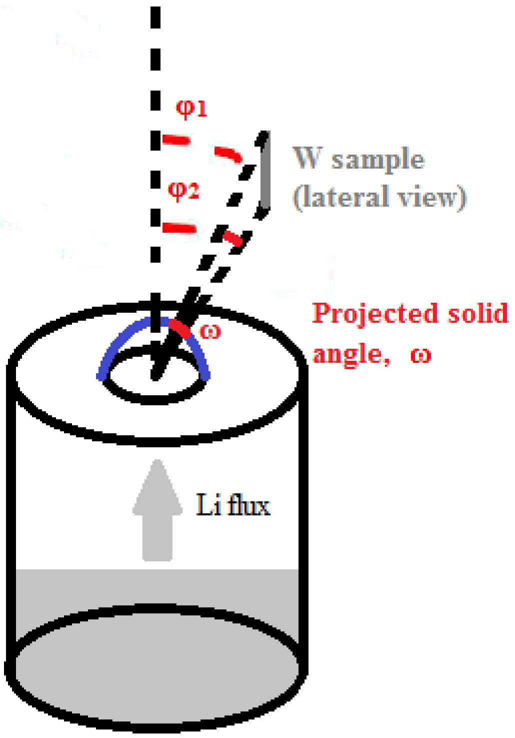

Figure 3.17. Angular dependence for the Li effusion through the oven orifice

Introducing the angular dependence previously explained for the lithium flux:

$$\frac{dN_{Li}}{d\omega} = N_{Li}^{Tot} \cdot \cos\varphi \cdot \frac{\omega}{2\pi}. \quad (3.19)$$

By integrating the expression over the angular characteristics of the sample with respect to the effusion cell, normalizing the result to the global cos φ limits (-π/2, π/2) and the whole solid angle of the semi-spherical evaporation surface of the orifice (2π sr) the total number of lithium atoms evaporated that reach the sample (N_{Li}) can be calculated:

$$N_{Li} = N_{Li}^{Tot} \cdot \frac{\omega}{2\pi} \cdot \frac{\int_{\varphi 1}^{\varphi 2} \cos\varphi \cdot d\varphi}{\int_{-\pi/2}^{\pi/2} \cos\varphi \cdot d\varphi}. \quad (3.20)$$

Evaluating the cos φ integral, the resulting mathematical expression is:

$$N_{Li} = N_{Li}^{Tot} \cdot \frac{\omega}{2\pi} \cdot \frac{\sin\varphi\big|_{\varphi1}^{\varphi2}}{2} = \qquad (3.21)$$

By using our experimental values the estimation of the total number of lithium atoms reaching the sample surface gives a value around 10^{19} that implies a medium lithium film thickness of approximately 1 μm.

3.3.4.3. Irradiation of W-Li-D samples with Nd:YAG laser beam

Once the samples are prepared and transported without atmospheric contamination to the LIDS laboratory, the manipulator is connected to the LIDS chamber (represented in figure 3.18) by using the conflat flange of the gate valve that seals the manipulator. An intermediate small port connects the manipulator valve with the main valve of the LIDS chamber. This port has a pumping hole to produce previous vacuum with a mobile pumping unit before opening the manipulator valve, avoiding in this way any contact of the sample with air. Before introducing the sample in the LIDS chamber, it is necessary a pre-pumping period (2-3 hours) in the manipulator with the mobile pumping unit to adequate its pressure to the very high vacuum conditions of the LIDS chamber ($\approx 0.8\text{-}1 \cdot 10^{-5}$ Pa). After introducing the sample in the LIDS chamber, the setup is pumped out during one night to reach the previous vacuum level before connecting the sample manipulator. This procedure allow to assure optimal vacuum levels inside the LIDS chamber, that are necessary for a good analysis avoiding in this way the increase in the residual contents of deuterium, hydrogen, HD, water and another H-D containing molecules inside the chamber. Too high residual levels of these molecules would produce a concomitant increase in the background of the related RGA mass/charge signals that can alter the mass spectrometry quantification. The LIDS chamber consists on another stainless steel vacuum vessel where the sample is introduced with the manipulator. It is pumped out by means of a turbomolecular-rough pump set. The laser beam is introduced in the chamber and directed to the sample through an optical window after being focused by a converging (focal length of 400 mm) lens. The Ionization gauge measures the residual pressure in the chamber and the mass spectrometer (SRS 100) RGA is placed to measure the hydrogenic desorption from the samples induced by the laser heating of the W-Li-D surfaces.

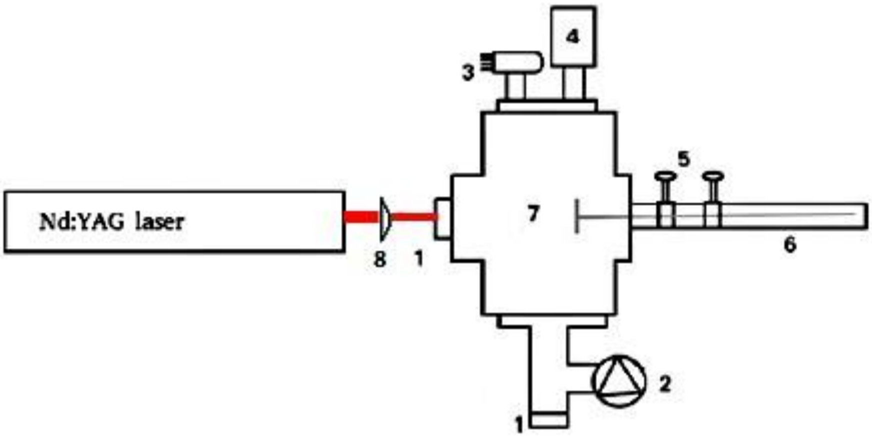

Figure 3.18. Lateral view of the LIDS chamber and Nd:YAG laser: 1. Optical windows, 2. Pumping unit, 3. Ionization gauge, 4. Residual gas analyser, 5. Gate valves for main chamber and sample manipulator, 6. Sample manipulator, 7. Vacuum chamber, 8. Focusing lens

To irradiate the W-Li-D layers with the laser, the alignment of the beam respect to the sample needs to be performed. This procedure was performed by marking the laser spot on photographic paper that is placed covering totally the optical window used for the beam entrance to the LIDS chamber. Using an auxiliary He/Ne laser pointer, the exit of the Nd:YAG laser is aligned with the laser spot marked on the photographic paper. In this way, the auxiliary laser pointer gives the position of the beam inside the chamber. By rotating/moving the converging lens that focuses the laser beam the position of the laser on the sample can be adjusted. Hence, different parts of the sample can be analysed in different laser shots very easily. All the laser analyses were performed placing the lens at a distance of approximately 375 mm respect to the position of the sample inside the LIDS chamber. Previous trials showed that focusing of the laser spot was limited by the divergence of the beam and optic characteristics of the lens. These trials consisted on the incidence of the laser on the photographic paper changing the distance between it and the focusing lens. In this way for distances between lens and sample larger than 375 mm no additional focusing was achieved.

The energy of the laser beam was measured with the joulemeter before starting the LIDS analyses and after finishing them. Different laser shots were performed on the sample, changing the position of the beam spot and the gaseous specie that is measured (D_2, H_2, HD). As was explained previously, with the RGA measurements using the leak test mode only one chemical species can be measured in each measurement. Consequently it was no possible to measure the content of more than one molecule at the same point of the sample. In this way the determination of the different hydrogenic species must be carried out in different points of the samples. Differences on the Li/hydrogenic content depending on the position of the samples are expected as a result of the non-homogeneous co-deposition of lithium and hydrogenic molecules. Several measurements for each hydrogenic molecule were performed to average the results. To perform the analysis the laser shutter is switched on manually and one shot enters to the chamber until its impact with the sample. Then, the RGA registers the hydrogenic desorption peak associated with only one laser shot. This procedure is repeated several times until the residual peaks obtained by the RGA are smaller than the 5% of the first peak. At this moment, it is considered that the total desorption (that depends on the laser power density and its thermal transfer to the sample) on the spot has taken place. Normally it happens after 2-3 laser shots on the sample spot. The small residual peaks, obtained after this, are attributed to lateral propagation of the laser radiation that induces desorption from adjacent points to the laser spot. An example of the LIDS analyses is presented in figure 3.19.

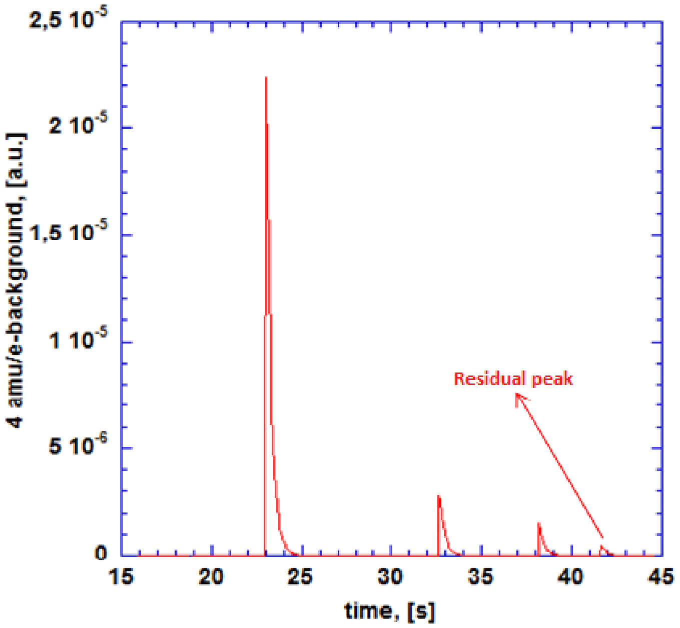

Figure 3.19. Example of LIDS analysis for D_2 uptake determination

3.3.5. Hydrogenic retention results on the prepared samples

The data obtained with the RGA during the LIDS analyses together with the absolute calibration work allows for the quantification of the hydrogenic content of the irradiated sample spots.

The desorption peaks integration over the time gives the total molecules desorbed from the laser spot:

$$H_2^{des} = K_{H2} \cdot \sum_{i=1}^{n} \int (2Amu/e - background) \cdot dt, \text{ (3.22)}$$

$$HD^{des} = K_{HD} \cdot \sum_{i=1}^{n} \int (3Amu/e - background) \cdot dt, \text{ (3.23)}$$

$$D_2^{des} = K_{D2} \cdot \sum_{i=1}^{n} \int (4Amu/e - background) \cdot dt, \text{ (3.24)}$$

To obtain the hydrogen and deuterium areal density (H_{ret} and D_{ret}) on the samples, we only need to sum the H and D atoms from their containing molecules and normalize the result dividing by the spot area (A_{spot}):

$$D_{ret} = \frac{2 \cdot D_2^{des} + HD^{des}}{A_{spot}}, \text{ (3.25)}$$

$$H_{ret} = \frac{2 \cdot H_2^{des} + HD^{des}}{A_{spot}}, \text{ (3.26)}$$

Profilemetry measurements gave a mean spot diameter of 0.125 cm. Considering it as approximately circular, the desorption area is A_{spot} ≈0.0123 cm. To obtain the retention values for hydrogen and deuterium (H_{ret} and D_{ret}) several sample points were analysed with the laser beam. Normally four or five zones were irradiated looking for the signal 4 amu/e in order to measure the D_2 desorption with the RGA and see the changes in the D uptake by the W-Li layer depending on the sample position. Another two points were used to measure the HD release and another two for the H_2 release. The number of D_2, HD and H_2 desorbed molecules was calculated using the equations 3.22-3.24. These results were averaged and finally the hydrogen and deuterium retention values were calculated with the equations 3.25 and 3.26. This procedure was repeated for the samples wlid, wlid6, wli8, wlid10, wlid11 and wlid13.

3.3.5.1. Hydrogenic retention values on sample wlid

As was explained previously, this sample was prepared in an environment with simultaneous exposition to (low pressure) molecular deuterium and evaporated lithium. The spatial distribution of the analysed laser spots is presented in figure 3.20 whose dimensions represent the real size of the sample.

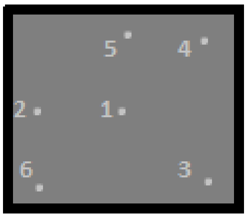

Figure 3.20. Position of the laser spots on the wild sample

Additionally, table 3.6 presents the details of the different LIDS analyses: the analysed molecule, the spot position and the number of desorbed molecules.

LIDS point	Analysed molecule	Spot position	Desorbed molecules
1	D_2 (4 amu/e)	Centre	-
2	D_2 (4 amu/e)	Left Centre	-
3	D_2 (4 amu/e)	Right lower corner	-
4	HD (3 amu/e)	Right upper centre	-
5	H_2 (2 amu/e)	Upper Centre	1.38E+14
6	H_2 (2 amu/e)	Left lower corner	1.87E+14

Table 3.6. LIDS analyses on wlid sample

The LIDS results do not show any measurable deuterium content as the analyses did not present any desorption peak related with D_2 (4 amu/e) or HD (3 amu/e). Consequently the deuterium uptake by the W-Li layers is below the limit of detection of the technique. Thus the deuterium retention on W-Li layers in this co-deposition regime (exposition time of 30 minutes) performed as an approximation to the conditions of a fusion reactor first wall can be considered as negligible. This result would imply a good perspective for the use of W-Li solutions in terms of tritium retention issues associated with co-deposition in the challenging PFCs selection for future fusion reactors. Anyway, it is necessary to take into account that the exposition times expected in the pulsed or continuous operation of a fusion reactor could be quite different compared to our experimental conditions. On the contrary the hydrogen content could be detected and the two final analyses registered peaks associated with H_2 desorption (2 amu/e). By using these results and the formula 3.26 the hydrogen retention on the wild sample can be estimated, resulting in a value:

H_{ret}= 2.6±0.6·10^{16} cm^{-2}

As the sample was not exposed directly to any hydrogen exposition, this content should be related with the presence of hydrogenic impurities in the deposited lithium layer.

3.3.5.2. Hydrogenic retention values on sample wlid6

This sample was pre-lithiated and later exposed to high pressure D_2 gas with a surface temperature of 200ºC on the sample. After the LIDS experiments this sample was also analysed with SIMS after its transportation without air contamination. In figure 3.21 the sample points irradiated with the laser are represented and table 3.7 completes the details of the analyses.

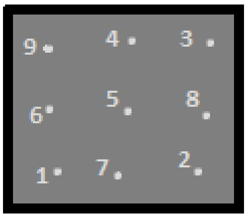

Figure 3.21. Position of the laser spots on the wlid6 sample

LIDS point	Analysed molecule	Spot position	Desorbed molecules
1	D_2 (4 amu/e)	Left lower corner	1.70E+16
2	D_2 (4 amu/e)	Right lower corner	9.82E+15
3	D_2 (4 amu/e)	Right upper corner	6.33E+15
4	D_2 (4 amu/e)	Upper centre	1.18E+16
5	D_2 (4 amu/e)	Centre	9.76E+15
6	HD (3 amu/e)	Left centre	2.12E+15
7	HD (3 amu/e)	Lower centre	1.58E+15
8	H_2 (2 amu/e)	Right centre	4.98E+14
9	H_2 (2 amu/e)	Left upper corner	6.96E+14

Table 3.7. LIDS analyses on wlid6 sample

The table shows dispersion on the desorption measurements depending on the position of the analysed spot. In general the lower-left, and the centre parts of the sample present higher contents of hydrogen isotopes, probably due to the proximity of these parts to the effusive lithium cloud output of the oven and the concomitant increase in the deposition of lithium on these zones. Effusive fluxes decrease with the square of the distance from the effusion orifice, so upper parts should show a lower content of lithium that would determine a smaller hydrogenic uptake. However, centre and upper centre parts also present higher contents compared to right-upper zones of the sample that are shadowed by the fastening screw that maintain the sample connected to the manipulator holder. Averaging the content of the different analysed points for each studied molecule, and applying the previous expressions the following results are obtained for the hydrogenic retention on the wlid6 sample:

D_{ret}= 1.9±0.7·10^{18} cm^{-2}

H_{ret}= 2.4±0.8·10^{17} cm^{-2}

3.3.5.3. Hydrogenic retention values on sample wlid8

This sample was prepared following the same protocol of the wlid6 sample, only changing the surface temperature during the D_2 exposition. In this case the temperature of the sample was 300ºC. It was also analysed with SIMS after the LIDS procedure. As for the previous sample, figure 3.22 and table 3.8 presents the different positions of the analysed sample spots, the details of the analyses and the desorption results.

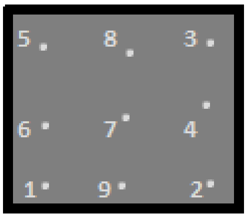

Figure 3.22. Position of the laser spots on the wlid8 sample

LIDS point	Analysed molecule	Spot position	Desorbed molecules
1	D_2 (4 amu/e)	Left lower corner	6.95E+12
2	D_2 (4 amu/e)	Right lower corner	6.08E+12
3	D_2 (4 amu/e)	Right upper corner	5.53E+12
4	D_2 (4 amu/e)	Right centre	8.44E+12
5	D_2 (4 amu/e)	Left upper corner	6.92E+12
6	HD (3 amu/e)	Left centre	4.37E+12
7	HD (3 amu/e)	Centre	5.32E+12
8	H_2 (2 amu/e)	Upper centre	2.07E+13
9	H_2 (2 amu/e)	Lower centre	2.81E+13

Table 3.8. LIDS analyses on wlid8 sample

The left and lower parts of the sample present again higher contents of hydrogenic molecules, resulting the average values for the hydrogenic retention:

D_{ret}= 1.5±0.3·10^{15} cm^{-2}

H_{ret}= 4.4±0.9·10^{15} cm^{-2}

These results show a retention decreased by three orders of magnitude compared with the wlid6 sample. It is important to note that to expose this sample to D_2 at 300ºC of surface temperature after the pre-lithiation, it was necessary to heat again the sample with the auxiliary filament. During this heating as the position of the sample was vertical, the deposited lithium layer was melted. This lithium layer slid off the sample surface being a part eliminated from the surface by dripping. Deuterium content on the sample is lower than hydrogen content, pointing to hydrogen uptake associated directly with the lithium deposition due to the impurities present in the lithium bulk.

3.3.5.4. Hydrogenic retention values on sample wlid10

This case is about a pre-lithiated sample with surface temperature of 400ºC during the D_2 exposition. The posterior analysis with SIMS was not possible for this sample. The figure 3.23 and table 3.9 show the experimental details and preliminary results of the LIDS analyses.

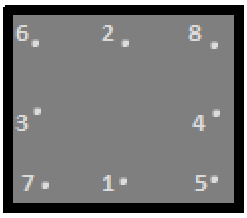

Figure 3.23. Position of the laser spots on the wlid10 sample

LIDS point	Analysed molecule	Spot position	Desorbed molecules
1	D_2 (4 amu/e)	Lower centre	-
2	D_2 (4 amu/e)	Upper centre	-
3	D_2 (4 amu/e)	Left centre	-
4	D_2 (4 amu/e)	Right centre	-
5	HD (3 amu/e)	Right lower corner	5.23E+11
6	HD (3 amu/e)	Left upper corner	4.62E+11
7	H_2 (2 amu/e)	Left lower corner	9.30E+12
8	H_2 (2 amu/e)	Right upper corner	5.90E+12

Table 3.9. LIDS analyses on wlid10 sample

For this sample no D_2 desorption was found in the LIDS analyses, no peak in the 4 amu/e RGA signal was visible during the laser shots. The D_{ret} estimations are obtained only with the contribution of the HD desorption measurements.

D_{ret}= 4.3±0.4·10^{13} cm^{-2}

H_{ret}= 1.3±0.4·10^{15} cm^{-2}

The average values for D_{ret} show a tiny retention, even lower compared to the previous case (factor 35). For H_{ret} the values are in the same order compared to wlid8 but still lower (factor 3). Comparing the deuterium and hydrogen retention the first one is a factor 30 lower. In this sample the slip and dripping of lithium was also visible during the starting of the sample heating for the D_2 exposition.

3.3.5.5. Hydrogenic retention values on sample wlid11 and wlid13

Both samples were pre-lithiated and later exposed to molecular D_2 at 200°C of surface temperature as in the case of the sample wlid6. As the wlid6 sample was the only one presenting important values of D_{ret}, this sample was prepared in order to compare these results and check the reproducibility of the technique. Finally to corroborate the deuterium retention measurements after the application of LIDS, with another reference technique, the sample were analysed with Thermal Desorption Spectroscopy (TDS). For the case of wlid11, figure 3.24 and table 3.10 present the irradiated spot and the hydrogenic desorption values.

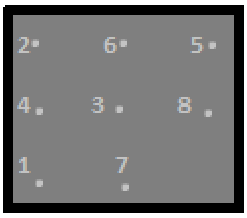

Figure 3.24. Position of the laser spots on the wlid11 sample

LIDS point	Analysed molecule	Spot position	Desorbed molecules
1	D_2 (4 amu/e)	Left lower corner	Failed shot
2	D_2 (4 amu/e)	Left upper corner	9.09E+15
3	D_2 (4 amu/e)	Centre	1.05E+16
4	D_2 (4 amu/e)	Left centre	8.40E+15
5	HD (3 amu/e)	Right upper corner	3.53E+15
6	HD (3 amu/e)	Upper centre	2.39E+15
7	H_2 (2 amu/e)	Lower Centre	6.13E+14
8	H_2 (2 amu/e)	Right Centre	7.21E+14

Table 3.10. LIDS analyses on wlid11 sample

The analysis of these results gives the following values for global deuterium and hydrogen retention:

D_{ret}= 2.0±0.3·10^{18} cm^{-2}

H_{ret}= 5.9±1.4·10^{17} cm^{-2}

The D_{ret} values are very similar compared to the sample wlid6 while the H_{ret} values are approximately two times bigger for the wlid11 sample. As in principle the sample was not exposed to hydrogen, the hydrogen uptake must be related with impurities present on the deposited lithium or present on the sample. This discrepancy may be due to differences in impurity removal from the samples or from the lithium present in the oven prior to its deposition.

For the sample wlid13 figure 3.25 and table 3.11 present the obtained LIDS results.

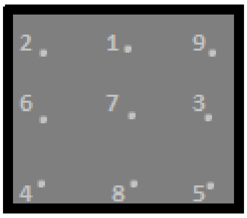

Figure 3.25. Position of the laser spots on the wlid13 sample

LIDS point	Analysed molecule	Spot position	Desorbed molecules
1	D_2 (4 amu/e)	Upper centre	1.26E+16
2	D_2 (4 amu/e)	Left upper corner	1.08E+16
3	D_2 (4 amu/e)	Right centre	1.64E+16
4	D_2 (4 amu/e)	Left lower corner	1.09E+16
5	D_2 (4 amu/e)	Right lower corner	6.10E+15
6	HD (3 amu/e)	Left centre	2.49E+15
7	HD (3 amu/e)	Centre	1.87E+15
8	H_2 (2 amu/e)	Lower Centre	6.63E+14
9	H_2 (2 amu/e)	Right upper corner	5.45E+14

Table 3.11. LIDS analyses on wlid13 sample

The global deuterium and hydrogen retention values for this sample are the following ones:

$D_{ret}= 2.0\pm0.6\cdot10^{18}$ cm^{-2}

$H_{ret}= 2.8\pm0.5\cdot10^{17}$ cm^{-2}

Both values are very similar compared to the results obtained for the wlid6 sample, thus corroborating deuterium retention values around $2\cdot10^{18}$ cm^{-2} for the case of samples at 200°C exposed to pre-lithiation followed by high pressure molecular D_2 exposure.

3.3.5.6. Hydrogenic retention values on sample wlid12

Several LIDS shots were performed in order to measure the retention in the tungsten blank sample. Different analyses were carried out looking for the D_2, HD and H_2 content, thus measuring different values of the mass to charge ratio signal during the LIDS shots. However no peak was obtained related with 4 amu/e (D_2), 3 amu/e (HD) and 2 amu/e (H_2). Therefore, the hydrogenic content of this sample is below the limit of detection of the LIDS method, being considered as negligible. For the case of the D_2 and HD values this result is completely logical as the sample was not exposed to any interaction with D_2. In the case of H_2 retention no measurable values were also obtained. However for the samples exposed to lithium evaporation, even though they were not exposed to direct H_2 exposure, the hydrogen uptake was measurable. This experimental result points directly to hydrogen uptake related with the lithium deposition. As the blank sample was not exposed to lithium, it does not present any measurable hydrogen retention. On the contrary the analyses of the samples exposed to lithium (co-deposition with D_2 or pre-lithiation) reflected this hydrogen uptake that can be attributed to the impurities (present in the lithium during its evaporation) that were deposited on the sample together with Li atoms.

3.3.5.7. Summary of the hydrogenic retention results for all the samples

A compendium of the previous LIDS results is presented in table 3.11 for the analysed samples depending on the D_2-Li exposure on the sample, and its surface temperature.

Sample	**D_2-Li exposure**	**$T_{surface}$, ºC**	**H_{ret}, cm^{-2}**	**D_{ret}, cm^{-2}**
wlid	Li-D_2 co-deposition	225	**$2.6 \pm 0.6 \cdot 10^{16}$**	-
wlid6	pre-Li+D_2	200	**$2.4 \pm 0.8 \cdot 10^{17}$**	**$1.9 \pm 0.7 \cdot 10^{18}$**
wlid8	pre-Li+D_2	300	**$4.4 \pm 0.9 \cdot 10^{15}$**	**$1.5 \pm 0.3 \cdot 10^{15}$**
wlid10	pre-Li+D_2	400	**$1.3 \pm 0.4 \cdot 10^{15}$**	**$4.3 \pm 0.4 \cdot 10^{13}$**
wlid11	pre-Li+D_2	200	**$5.9 \pm 1.4 \cdot 10^{17}$**	**$2.0 \pm 0.3 \cdot 10^{18}$**
wlid13	pre-Li+D_2	200	**$2.8 \pm 0.5 \cdot 10^{17}$**	**$2.0 \pm 0.6 \cdot 10^{18}$**
wlid12	no Li-W blank	200	-	-

Table 3.12. Hydrogenic retention results for the samples analysed with LIDS

Summarising the experimental results:

- For the case of the pre-lithiation + D_2 exposure preparation regime the three values obtained for the deuterium retention at 200ºC are very reproducible ($\approx 2.0 \cdot 10^{18}$ cm^{-2}).
- In this regime, the D retention exhibits a strong dependence with the surface temperature on sample. At 300ºC the D retention is reduced in a factor 1300, while at higher temperatures (400ºC) the amount of D atoms retained on the W-Li layer is decreased by a factor 50000 compared to the case of $T_{surface}$=200ºC. The influence of the lower lithium uptake by the sample (dripping and slipping of Li atoms induced by its melting) at higher temperatures in the net D retention seems clear, although the drastic drop observed in the retention with increasing temperature suggests perhaps a more complex phenomenon. To investigate the role of the reduced Li film at increasing temperatures, the deposited lithium on samples was determined by FAES, being this consideration analysed in subchapter 3.3.7.4. Additionally, the Li-D interaction (and the concomitant net D uptake by the Li created film) could be diminished at higher temperatures in the liquid film formed, thus reducing the retention values up to the drastically lower retention results obtained by LIDS. This possible effect will be analysed in subchapter 3.3.10.
- In the case of W surfaces exposed to simultaneous Li-D_2 exposition (co-deposition regime) the deuterium retention values are below the limit of detection as in the case of the pure tungsten sample exposed to molecular deuterium. Retention of W-Li layers exposed to this co-deposition regime would be at the same level compared to pure tungsten.

3.3.6. Post mortem analysis for W-Li-D layers characterization

3.3.6.1. Thermal Desorption Spectroscopy for cross checking the hydrogenic retention results

In order to compare the retention values obtained by LIDS with another absolute quantification technique, thermal desorption spectroscopy analyses (TDS) assisted with mass spectrometry (RGA measurements) were implemented on the samples wlid11 and wlid13 after its LIDS irradiation. The samples were transported to the deposition chamber from the LIDS chamber following the sample protocol previously detailed to avoid their contamination and the hydrogenic loss or exchange. Inside the deposition chamber the samples were heated up by using the tungsten filament placed behind the sample. The surface temperature of the sample was measured with the optical pyrometer. The desorption process was followed by registering the changes on the chamber pressure with an ionization gauge. Additionally, a SRS mass spectrometer (RGA), identical to the previous one used in the LIDS measurements, was installed in the deposition chamber trying to follow the evolution of the hydrogenic mass to charge ratio signals during the sample heating. However due to the induced desorption, the pressure on the chamber rose up beyond the limit of the RGA filament and consequently the mass spectrometry measurements failed. Before starting the TDS measurement, the W filament used for the sample heating was outgassed by feeding it with the maximum power during 30 minutes in order to eliminate water, hydrogenic molecules or another volatile species that could disturb the changes in the pressure measured during the analysis. This outgassing was performed with the sample situated in a completely retracted position along the manipulator to maintain it at room temperature and not produce any desorption from it due to residual heating induced by the filament. In this way, an approximation considering that the increase in the pressure is produced mostly due to the deuterium desorption (majority volatile component of these samples) can be done. Although this procedure is not the best and more realistic for the quantitative determination of the hydrogenic content by TDS (because water and impurity levels present during the analysis are not differentiated from the total pressure), at least this measurement can proportionate an approximate indication that allow the cross checking of the LIDS results. By correlating the absolute pressure signal in the chamber with known values of deuterium flux introduced in the chamber in an absolute calibration work (equivalent to the explained in subchapter 3.3.3) the total number of desorbed deuterium atoms can be calculated by integrating the TDS pressure spectrum over the time. The result of this calibration is shown in figure 3.26.

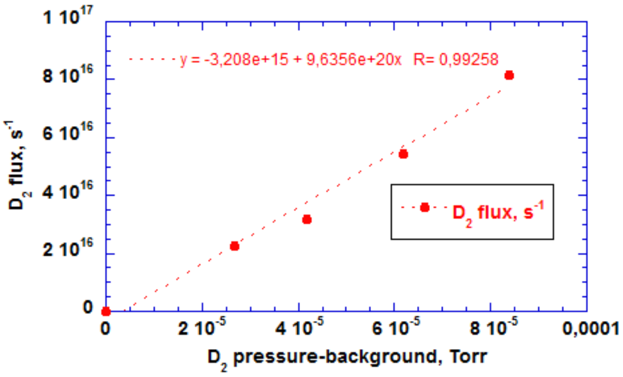

Figure 3.26. Absolute calibration for D_2 in the deposition chamber

Finally, considering an exposed area of 3.6 cm^2 for the sample and normalizing the desorbed value to this area, the deuterium retention value is obtained. Figure 3.27 shows the result of the TDS analysis performed on the sample wlid11. The corresponding TDS analysis for the sample wlid13 was failed due to overpressure in the chamber that in this case also affected the pressure (ionization gauge) sensor.

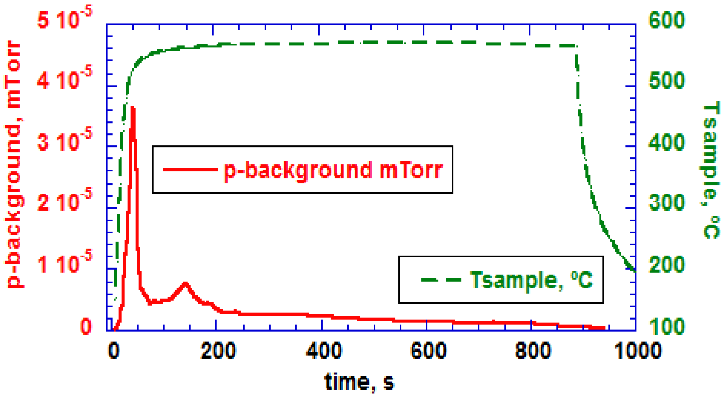

Figure 3.27. TDS spectrum for the wlid11 sample

The heating rate during the first instants of the analysis was around 11 K/s. A maximum temperature of 570°C was reached on the sample surface. Two clear peaks are visible in the TDS spectrum, the first and bigger one at 500°C of surface temperature and the second one (smaller) is at 550°C, being these results in agreement with previous findings in W-Li TDS experiments [97, 116, 117]. The TDS spectrum and the peaks shape are quite clean and defined thus suggesting that the contamination from water and impurities should not be too important. Assuming that water, hydrogen and another impurity contributions are negligible (assumption that perhaps is too optimistic), the TDS analysis gives a total deuterium retention of $1.3 \cdot 10^{18}$ cm^{-2}, that agrees reasonably with the LIDS results ($2.0 \cdot 10^{18}$ cm^{-2}), being their values comparable. Theoretically, the total decomposition of pure lithium hydride (mostly LiD in this case) takes place at temperatures close to 700°C. For LiD-Li mixtures the decomposition temperature for the hydride depends on the external pressure. Under high vacuum conditions (very low D pressure) the LiD molecules can be decomposed at lower temperatures [117].

Nevertheless as the maximum temperature achieved by the sample during the TDS is 570°C, some lithium deuteride particles could remain on the surface after the TDS, thus explaining the lower deuterium retention values obtained by TDS compared to the obtained by LIDS. However, another results showed total D release at similar temperature to the reached during a similar TDS analysis [97]. In any case, although this TDS global value is smaller, it is necessary to take into account that deposition of lithium and the concomitant D uptake on the W-Li films are not homogeneous. Moreover, the LIDS technique could induce desorption from adjacent parts of the treated spot, thus including a bigger desorption area and producing an overestimation of the obtained deuterium retention. To investigate the possible presence of deuterium (in the form of LiD) after the TDS, the sample wlid11 was transported again to the LIDS chamber in order to corroborate the total hydrogenic removal on the sample by the TDS technique. Several LIDS shots were implemented on the outgassed surface to measure desorption of the different hydrogenic species. While no desorption of D_2 and HD related peaks was visible, tiny H_2 related peaks were obtained resulting on values of $H_{ret}=3\cdot10^{14}$ cm^{-2}. These results imply:

- Total deuterium removal and no LiD remaining on sample after TDS
- 99.9% of hydrogen removal on the sample with a maximum surface temperature of 570ºC induced by TDS
- Differences between global (TDS) and local (LIDS) deuterium retention values that could be explained by the limited accuracy related with the TDS measurements, the inhomogeneity of the films, the overestimation of the LIDS desorption area or another experimental uncertainties

3.3.6.2. SIMS analysis

To study the elemental surface and chemical composition as well as to characterize the Li-D films on the W samples, Secondary Ion Mass Spectrometry (SIMS) analyses were performed after the LIDS measurements. Three samples were analysed: the wlid6 sample (corresponding to pre-lithiated sample exposed to molecular deuterium at 200ºC), the wlid8 sample (corresponding to pre-lithiated sample exposed to D_2 at 300ºC) and the wlid12 sample (pure tungsten sample without Li deposition, exposed to molecular D_2 at 200ºC). Transportation of the samples from LIDS to SIMS vacuum chambers was carried out by using the same procedure previously explained for the LIDS analyses with the used manipulator over-pressurized with dry Argon.

3.3.6.2.1. Theoretical basis of the SIMS technique

Secondary Ion Mass Spectrometry (SIMS) is a material characterization technique based on the interaction of an ion beam with the surface under study. It shows the mass spectra of the ionized particles emitted as a result of the bombardment of the studied material with energetic primary ions produced by an ion gun [136]. The impinging primary ions induce the sputtering of surface particles (normally neutral atoms or molecules although ions and neutral/ionic aggregates or clusters can be ejected). The basic process that determines the emission of the sputtered particles is known as *collision cascade* [137]. When the high energy primary ions collide with the solid surface, the energy of the projectile is transferred from the primary particle to the atoms of the material. Although a low proportion of primary ions can be back scattered, most of them will transfer their kinetic energy to the lattice through the collision sequence being implanted into the target depending on their energy, mass and impact angle. Depending on the energy of the ions and the threshold displacement energy of the material the collisions can displace surface particles, produce defects in the material or eject it out of the surface layer. Normally the threshold displacement energy of materials is in the order of tens or hundreds of eV, being the used primary ion energy around several keV. With this energetic configuration of the beam, the sputtering is induced and ejection of sample particles (atoms, ions, molecules and clusters) is achieved. However, only a low proportion of emitted particles are secondary ions detectable by the mass spectrometer sensor. The fraction of sputtered atoms that become ionized is known as the SIMS ionization yield that is related with the ionization potential in the case of positive ions and with the electron affinity in the case of negative ions. Thus the sensitivity of the technique respect to the different surface species depends on their capability to be ionized when they are bombarded. The relative sensitivity factor (RSF) measures this experimental factor and also depends on the utilized primary ion beam and the composition of the sample matrix. In general, low values for the RSF factor determines high sensitivity of the technique for the studied species. Furthermore, this relative sensitivity leads to an extremely challenging quantification.

On the contrary the technique enables to high accuracy elemental qualitative (especially for light elements as Li and D) characterization and the comparison between different obtained signals for a given element in different samples can be used for relative semi-quantification. Normally, oxygen (O_2^+) primary ion beams are employed for the analysis of metals as they increase the yield of positive ions. A concomitant effect of this ion beam is the oxidation of the surface layer of the samples. For non-metallic elements and some metals (ruthenium, rhodium and copper groups), caesium (Cs^+) ion beams are frequently used. The necessary equipment for the SIMS application consists on the following elements: a vacuum chamber (pumped out by means of a turbomolecular pump assisted by a rough pump) where the samples are introduced (through sealed manipulators), the primary ion beam (O_2^+ or Cs^+ depending on the analysed elements), the mass analyser (different kind of analysers that are used in different SIMS operation modes will be explained in this subchapter) that separates the secondary sputtered ions depending on the mass and the ion detector (Faraday cup) that determines the intensity of the signal associated to each detected ion. Additionally an electron beam (flood gun) is used for charge compensation on the treated surfaces. Figure 3.28 [138] shows a general view of these main elements. Two different operation modes can be used with the SIMS analytic method.

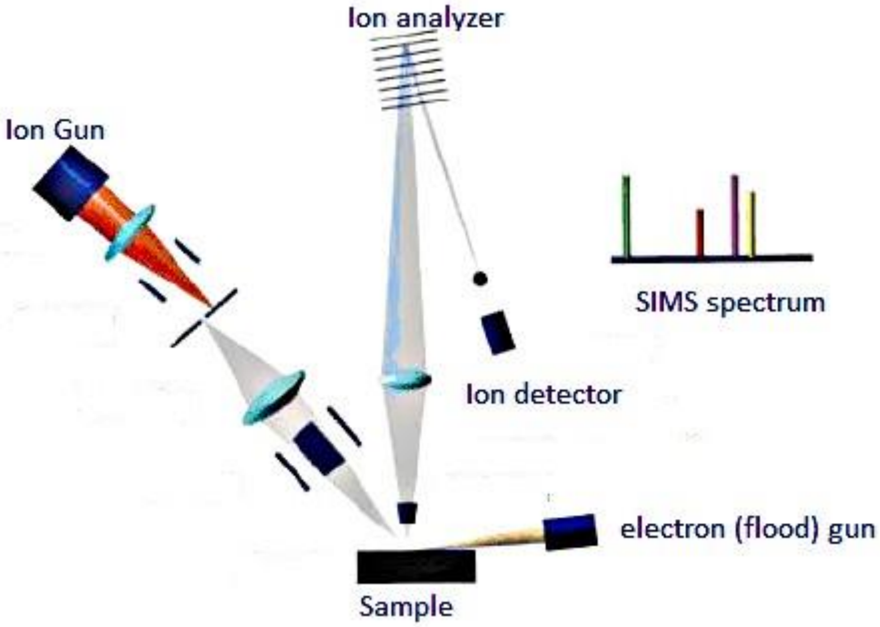

Figure 3.28. Basic scheme of the SIMS setup with the main elements

The static SIMS is used for surface (primary top layer) analysis. It employs a low primary ion dose (<10^{13} ions/cm^2) in a pulsed beam operation in an energy range of 5-25 keV. It allows a fast determination of the elemental chemical analysis on the surface. In this mode the ion analyser detection is generally based on time of flight (ToF) method.

The dynamic SIMS operation enables the depth profile analysis of the samples. Continuous beam operation (primary energy between 5-25 keV) with higher ion doses (>10^{15} ions/cm^2) are required in this case. For the secondary ions analysis, electrostatic quadrupoles (equivalent to the residual gas analysers used in conventional mass spectrometry) or improved analysers equipped with complementary magnetic sectors, are used. The use of magnetic sectors leads to an improved detection that also allows to the energy filtering of the secondary ions. In our experiments both static and dynamic (with simple electrostatic quadrupole detection) SIMS analyses with the O_2^+ primary ion beam were performed. A general view of the setup (Hiden SIMS Workstation) is shown in figure 3.29 [138]. The residual vacuum showed a pressure around

$5{\cdot}10^{-5}$ Pa inside the chamber, while the characteristics of the primary ion beam were a nominal emission current of 500 nA and a beam energy of 5 keV.

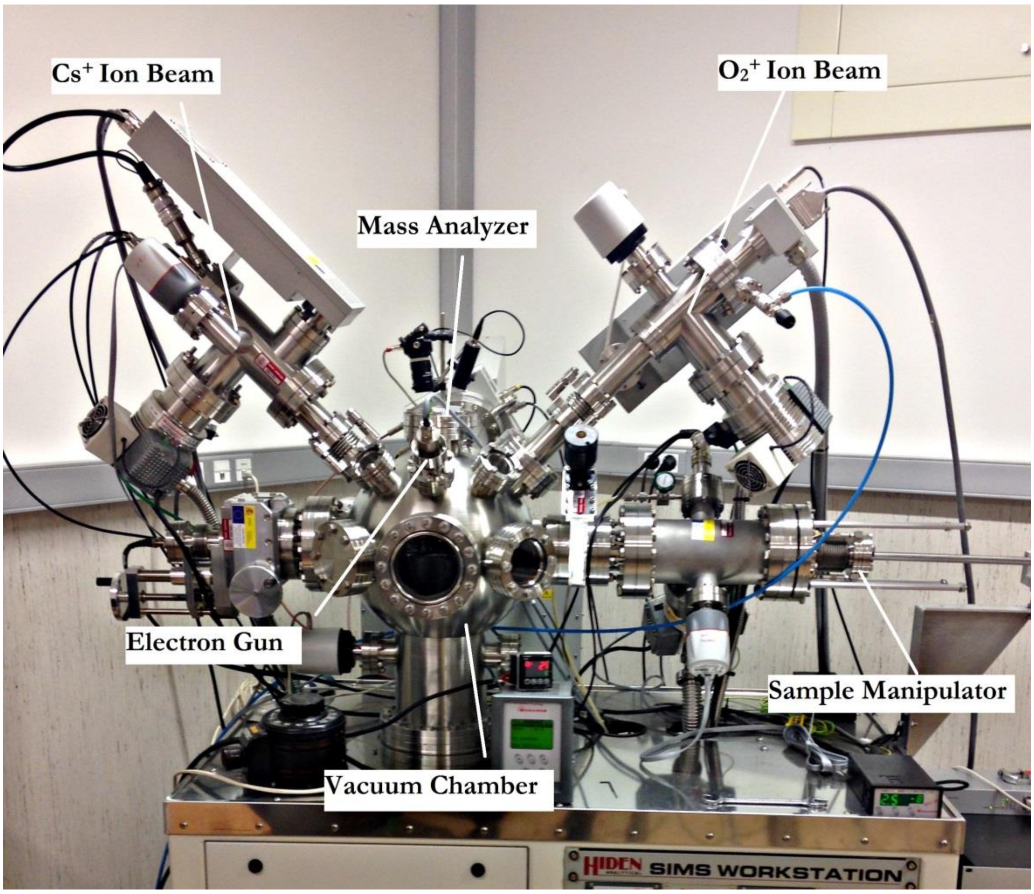

Figure 3.29. Hiden SIMS Workstation experimental unit

3.3.6.2.2. Experimental results

To identify the elements and compounds present on the surface layer of the sample a static SIMS analysis (mass to charge ratio scan) was performed as the first step of the analytical procedure. Two different mass scans were performed. The first one measured the mass to charge ratio signal in the range from 0 to 80 amu/e, in order to identify hydrogenic species (H_2 at 2 amu/e, HD at 3 amu/e and D_2 at 4 amu/e) Li isotopes (^{6}Li and ^{7}Li) oxygen from the ion beam, residual water molecules (amu/e 18-20) and the presence of Li impurities due to the atmospheric contamination: lithium oxides (amu/e 28-30 and LiO clusters from oxide cracking at amu/e 22-23), lithium hydroxides (amu/e 23-25) and lithium carbonates (amu/e 72-74). In figure 3.30, this mass scan performed for the sample with highest Li/D content (wlid6) is represented.

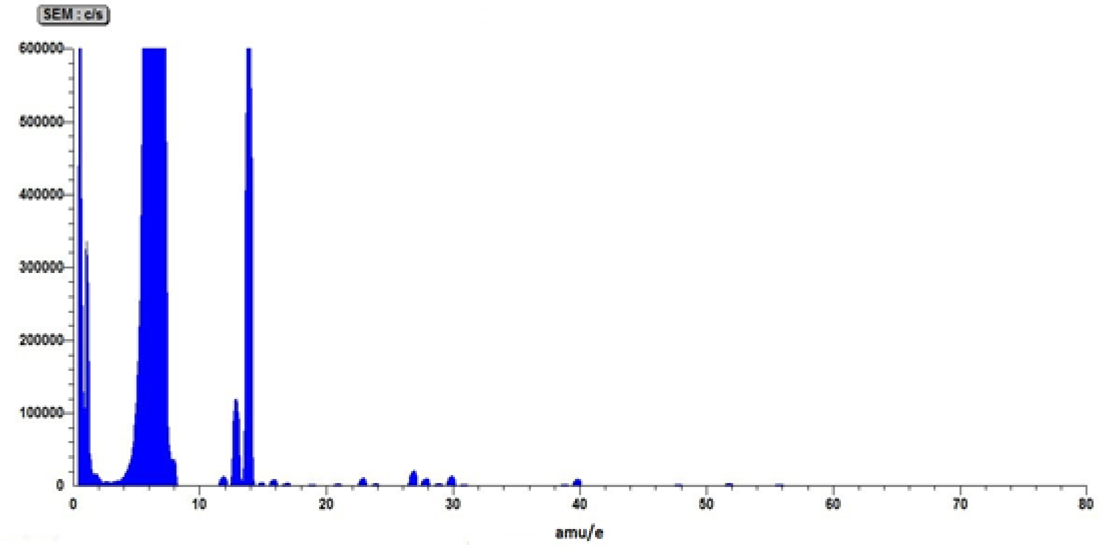

Figure 3.30. Static SIMS on wlid6 sample: mass scan from 0 to 80 amu/e

The figure shows the presence of hydrogenic molecules and Li isotopes in high intensity peaks that even saturate due to the high content on the sample and the high sensitivity of the SIMS detector for these species. Another big peaks present at 12-14 amu/e can correspond to the detection of Li_2 clusters formed on the beam plume. The presence of Li oxides is minority as the associated peaks (amu/e 28-30) are very small. It is important to note that Li oxide formation will be also induced by the interaction of the primary ion beam (O_2^+) with the Li layers. In any case the detection of Li oxides or derivative fragments does not assure their presence on the material surface as they could be formed (on surface or on the associated beam plume) as a result of the interaction of Li atoms present on the Li-W matrix with the impinging oxygen ion beam. There is no presence of lithium hydroxides and carbonates peaks. It demonstrates that the conservation and transportation of the samples during all the experimental procedure was adequate, avoiding the contamination of the Li-D layers. The second mass scan covers the m/q range from 180 to 220 in order to recognize the W isotopes (amu/e between 182-186) and the possible associated oxides (amu/e 198-202) and lithium combinations (amu/e 188-193). This mass scan is illustrated in the figure 3.31.

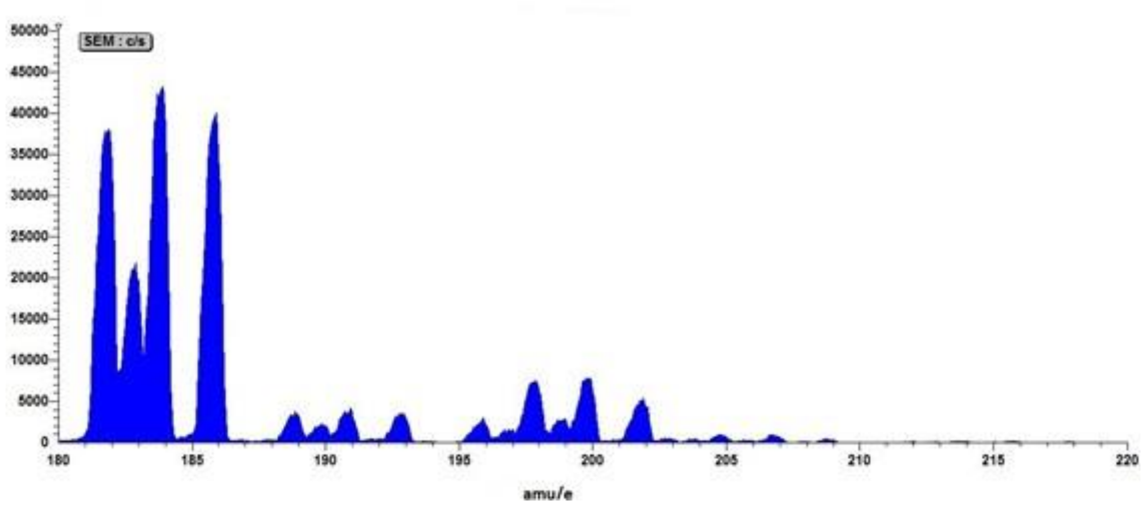

Figure 3.31. Static SIMS on wlid6 sample: mass scan from 180 to 200 amu/e

In this scan four W isotopes (182, 183, 184 and 186) are visible, corresponding the highest peak signal to ^{184}W. Small peaks associated to the combination of lithium isotopes with tungsten (amu/e 189-191 and 193) and tungsten oxides (amu/e 196-200 and 202 are also visible. These clusters can be produced due to the interaction of sputtered W and Li atoms with the oxygen ions in the beam plume. Equivalent static SIMS analyses were performed for the samples wlid8 and wlid12. Their results are exposed in figures 3.32-3.35.

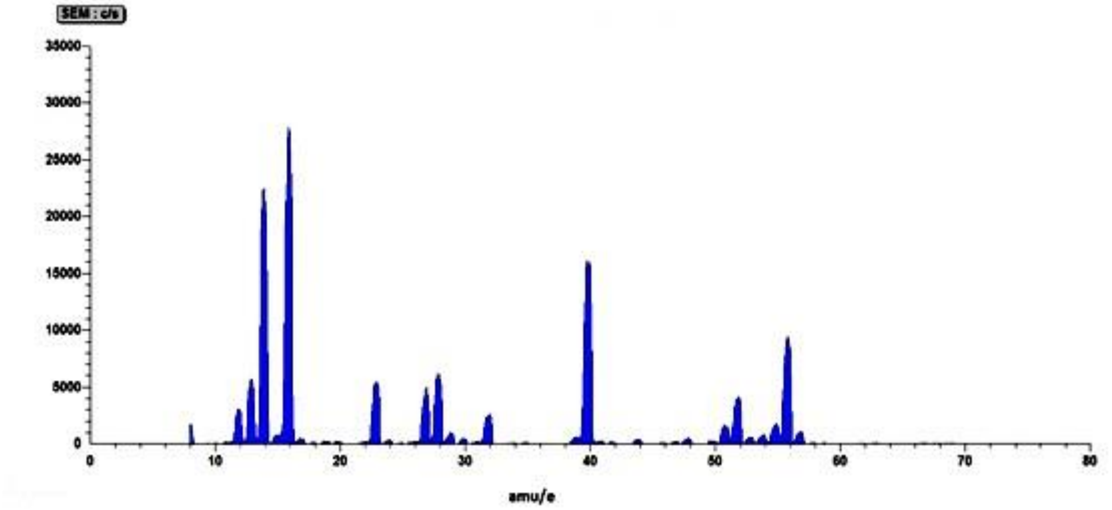

Figure 3.32. Static SIMS on wlid8 sample: mass scan from 0 to 80 amu/e

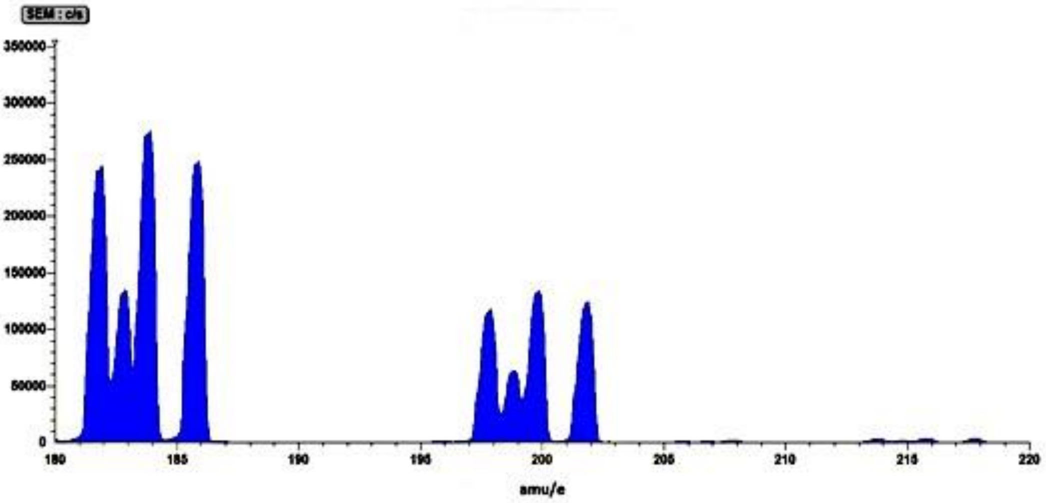

Figure 3.33. Static SIMS on wlid8 sample: mass scan from 180 to 200 amu/e

For the sample wlid8 (exposed to Li and D_2 at 300ºC), the mass scan (0-80 amu/e) does not show the peaks associated directly with Li isotopes. This anomalous result is probably due to a failure in the ion detector of the SIMS device. Dynamic SIMS registered clearly the presence of lithium on the sample. On the other hand, peaks related with lithium contamination are not significant (Li oxides and hydroxides) or non-existent. Peaks around 55-60 reveals the presence of ferritic impurities. The corresponding mass scan from 180-220 amu/e also presents the peaks associated to W isotopes and their oxides but not the W-Li cluster peaks. It could be related with the smaller lithium concentration on sample (experimental fact corroborated by the dynamic SIMS results that is shown in the following pages).

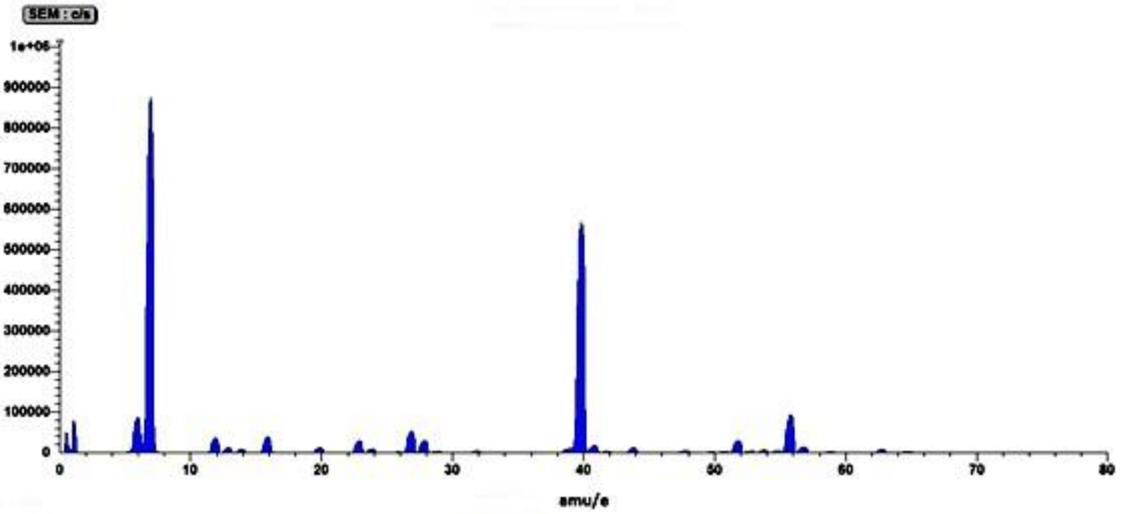

Figure 3.34. Static SIMS on wlid12 sample: mass scan from 0 to 80 amu/e

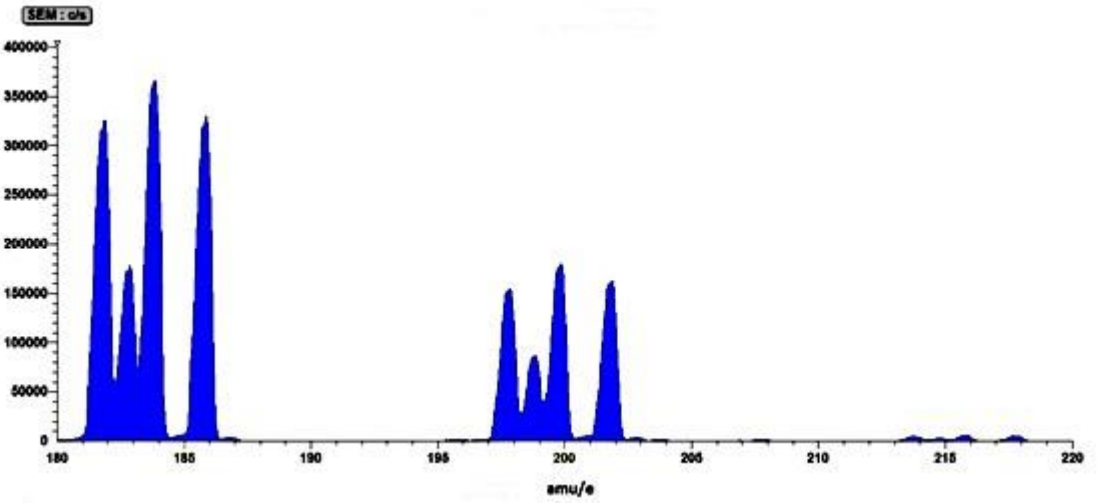

Figure 3.35. Static SIMS on wlid12 sample: mass scan from 180 to 200 amu/e

For the blank W sample, some peaks show the presence of lithium. However, no deposition of lithium was performed during the sample preparation. Probably this high detection is produced due to contamination of the chamber (in addition to our lithiated samples, the experimental SIMS setup is frequently used to analyse lithium containing samples studied for the development of Li breeder blanket research). The level of lithium contaminated compounds (oxides, hydroxides…) is also negligible. In the second static SIMS on this sample the W peaks and their oxides dominate the spectrum while associated lithium is no detected, thus pointing to the formation of WLi clusters in the beam plume after the sputtering of these species induced by the impinging beam. As the blank sample does not present any Li content on surface, these WLi clusters cannot be formed and consequently they do not appear in the static SIMS spectrum.

After the identification of the main elements and compounds, dynamic SIMS analyses were performed in order to study the depth profiles of the more interesting constituents. Several mass to charge signals were measured during these dynamic measurements: 2-4 amu/e for hydrogenic species (H_2, HD and D_2), 6 and 7 amu/e for lithium isotopes, 8 and 9 amu/e for lithium hydrides and deuterides, 16 amu/e as the blank reference for the primary ion beam evolution, 22, 23 and 25 amu/e for lithium oxides and hydroxides, 40 amu/e for argon, and 184 amu/e for the most representative tungsten isotope. Among these signals four of them were particularly interesting due to the lack of overlapping with another isotopologue species: 4 amu/e that is directly related with D_2, 6 amu/e (^{6}Li), 9 amu/e (^{7}LiD) and 184 amu/e (^{184}W). The evolution and intensity of these signals concentrated the SIMS data analysis of the treated samples.

The figure 3.36 presents the comparative dynamic SIMS results for the non-overlapping signals on the sample wlid6, wlid8 and the W reference sample (wlid12). In this plot the signals are normalized to the signal at 16 amu/e (oxygen primary ion beam for the analysis) in order to detect differences in the ion beam fluency that could affect to the extracted results.

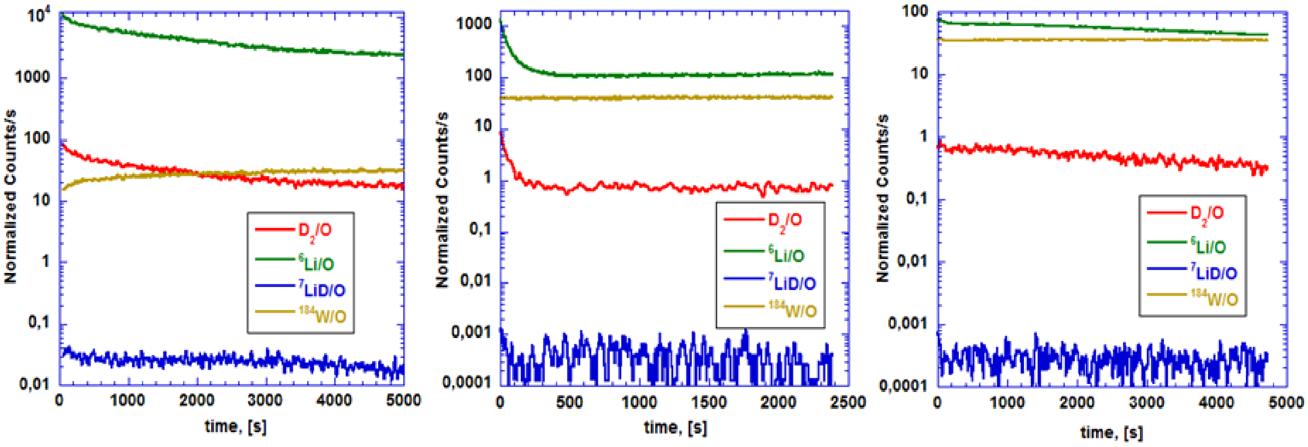

wlid6 **wlid8** **wlid12**

Figure 3.36. Comparative dynamic SIMS analyses on wlid6, wlid8 and wlid12

The highest content in Li and D for the wlid6 sample is clearly visible. Comparing both pre-lithiated samples the intensity of the Li and D_2 signals is one order of magnitude higher in wlid6. Moreover, the temporal evolution suggests that the Li-D thickness of the wlid6 sample is at least 10 times larger compared to the wlid8 sample as the analysis time necessary for the saturation of the involved signals is a factor 20 bigger. Respect to the signal related with lithium deuteride (Li^7D at 9 amu/e) it presents a significant intensity for the wlid6 sample being this signal much bigger compared to wlid8. Consequently the presence of LiD in the W-Li film seems evident. For wlid8 the signal is at the same level as the W blank (noise level), thus suggesting the absence of lithium deuteride.

In figure 3.37 the normalized profiles of D_2 and Li for samples wlid6 and wlid8 are presented in order to correlate Li and D_2 depth profiles on the sample and study the chemical interaction and association of both elements.

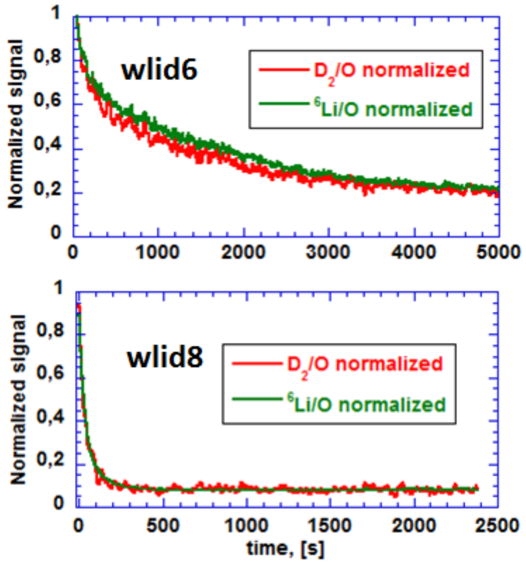

Figure 3.37. Normalized Li and D_2 profiles on wlid6 and wlid8 samples

The figure shows completely coincident profiles for Li and D_2 in both samples. It demonstrates that the deuterium retention on samples is associated to the lithium layer present on the surface. Finally although the SIMS technique does not allow a direct absolute quantification of the components (absolute calibration of this method is extremely challenging and requires specialized standards), the dynamic results shown in the previous figures were normalized to the W^{184} profile obtained for the wlid12 (W blank) sample. This procedure allows to an approximate relative semi-quantification of the D content by the comparison of the profiles for wlid6 and wlid8. The results of this analysis are represented in figure 3.38.

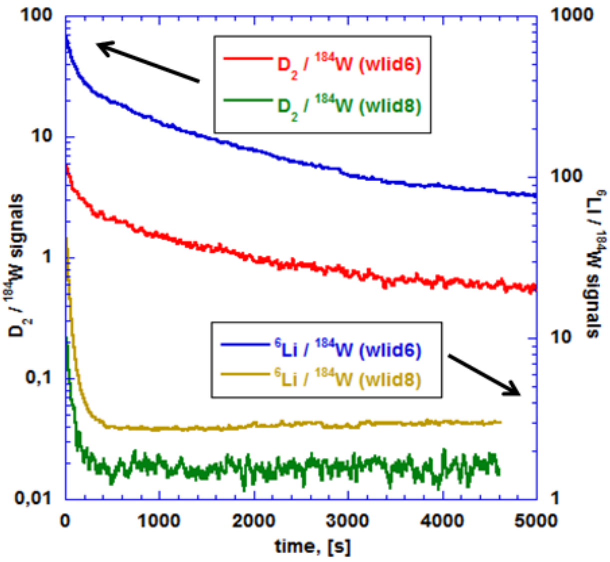

Figure 3.38. Li and D_2 profiles normalized to W^{184} profile (blank sample)

The comparison of the normalized D_2 profiles for wlid6 and wlid8 reveals values of the D_2 signal normalized to W that are a factor 20-100 times higher for the case of wlid6 sample. Furthermore, the necessary time for the saturation of the D_2 related signal is larger (factor 25) for wlid6 sample. These results would indicate a significantly lower (by several orders of magnitude) accumulated deuterium content in the case of wlid8 sample, that could be roughly estimated as a difference in a factor 500-2500 according to the comparison of such normalized profiles (figure 3.38). The LIDS results indicated absolute D content (1300 lower) in wlid8 sample. Consequently, the SIMS analyses corroborate the absolute quantification of the LIDS technique. As well as, they indicate important results about the composition of the W-Li layers as they show the presence of lithium deuteride in the sample wlid6, the absence of contamination in samples and the association of deuterium with lithium in the studied films.

3.3.6.3. Profilemetry measurements

After the SIMS measurements, the surface topology of the treated samples was investigated using profilemetry. In particular, this technique was used to estimate the size of the LIDS craters and analyse the morphology of the Li films on the W matrix. These measurements allowed to estimate the diameter of the LIDS craters and to visualize the thickness of the lithium layer deposited on the tungsten. It is necessary to take into account that these measurements were carried out in atmospheric conditions without protecting the lithium layers from contamination. No chance of performing them on a vacuum environment was possible. Under such conditions, lithium layers are chemically attacked by oxygen, carbon dioxide and water molecules present in the air, transforming the lithium atoms and hydride molecules present on the sample substrate into lithium carbonate (Li_2CO_3) molecules following the chemical reaction scheme:

$$4Li + O_2 \rightarrow 2Li_2O \quad (3.27)$$

$$2Li + 2H_2O \rightarrow 2LiOH + H_2 \quad (3.28)$$

$$LiD + H_2O \rightarrow LiOH + HD \quad (3.29)$$

$$Li_2O + CO_2 \rightarrow Li_2CO_3 \quad (3.30)$$

The formation of lithium carbonate layers on the sample surfaces was clearly visible as the grey colour of the Li layer deposited on tungsten changed to white after a few minutes corresponding with the natural colour of the Li_2CO_3. Lithium carbonate films are affected by swelling effects induced by its high hygroscopic activity, thus altering the thickness of the Li films, craters and surrounding areas. Hence, the morphology of the surface is changing during the development of the profilemeter measurements, affecting in this way the obtained results. Nonetheless, the LIDS craters created on the Li surface were perfectly visible. Although they are affected (together with the rest of the sample surface) by the atmospheric contamination, the swelling of the Li surfaces does not significantly affect the measurement of the crater diameter. However the Li surface exhibited an extremely irregular surface, presenting zones with very different deposition thickness and high roughness induced by the inhomogeneous deposition of lithium and its carbonation and swelling. Accordingly, the estimation of the real lithium film thickness produced during the sample preparation is not possible.

The profilemetry technique is widely used for surface characterization in thin film research. It allows the determination of important morphology parameters such as the roughness, the flatness or the curvature of thin films. In addition small details (craters, irregular borders or surface fractures) can be visualized and measured. Basically, profilemeters consist of at least two parts: a detector and a sample stage [139]. The detector determines where the points on the sample are and the sample stage holds the sample. In some systems, the sample stage moves to allow the measurement, in others the detector moves and in some both move. In all devices, the detector (whose aspect is similar to the needle of a vinyl record-player or the tip of a pen) scans the selected material area determining the details of its surface. Different technologies are used in profilemetry. In general, they can be divided in contact profilemeters (stylus) and non-contact (optical) ones. Stylus profilemeters use a probe (frequently constructed with diamond) in contact with the sample to determine the surface variations depending on the sample position, physically moving the probe along the surface in order to acquire the surface height. The changes in the Z (vertical) position (associated with the surface height and morphology) of the probe can then be used to reconstruct the surface. Stylus perfilometry requires force feedback and physically touching the surface, so while it is extremely sensitive and provides high Z resolution, it is sensitive to soft surfaces and the probe can become contaminated by the surface. This technique can also be destructive to some (soft) surfaces. The height range that they can measure is normally between 10 nm to 1 mm. A schematic view of a stylus profilemeter is illustrated in figure 3.39.

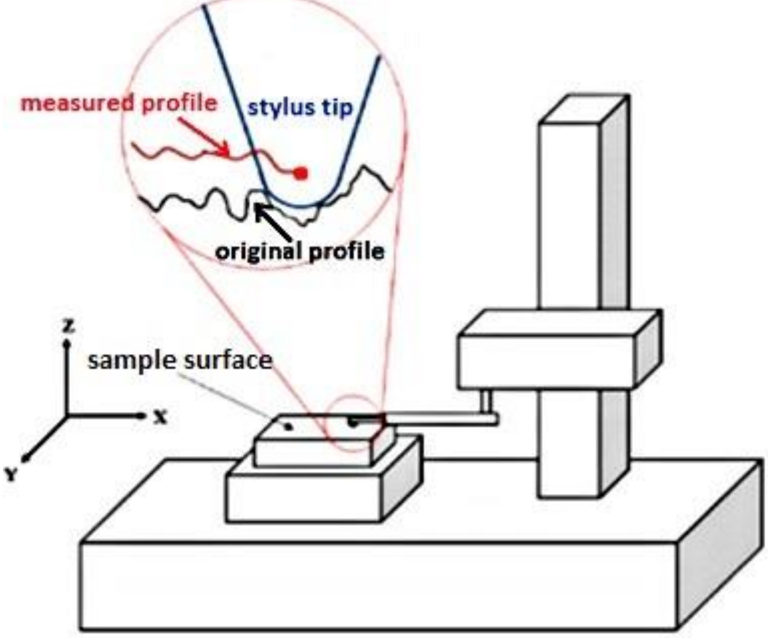

Figure 3.39. Schematic view of a stylus profilemeter

On the contrary, the optical profilemetry uses light instead of a physical probe. The key component to this technique is directing the light in a way that it can detect the surface in 3D. For the detection and processing of light reflected from the surface, there are many different techniques which are currently being employed, such as laser triangulation (triangulation sensor), confocal microscopy (used for profiling of very small objects), low coherence interferometry and digital holography. For the measurements, a 2-D stylus profilemeter (Bruker DektakXT) with a vertical resolution of 1 nm was used. It is presented in figure 3.40.

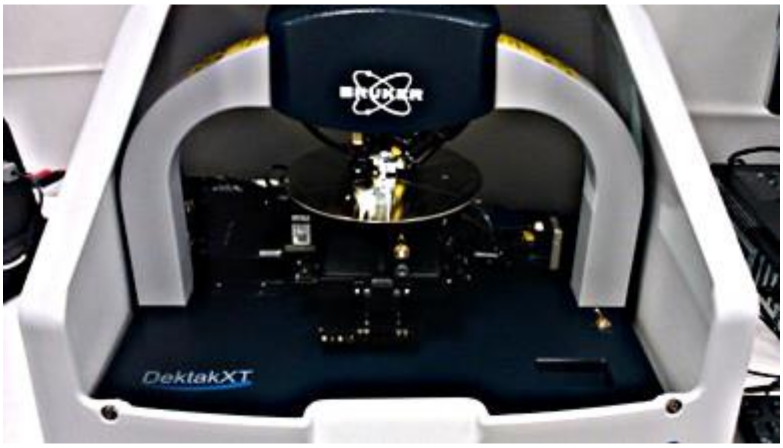

Figure 3.40. Bruker DektakXT stylus profilemeter used for the experiments

A picture of a LIDS crater present on the W-Li surface of the sample is represented in figure 3.41.

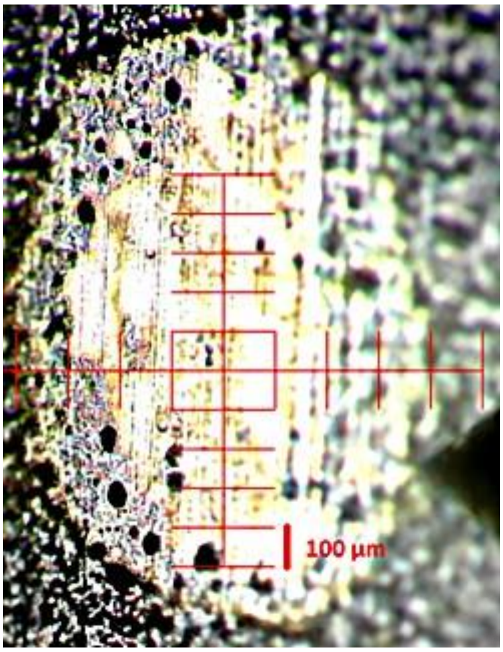

Figure 3.41. LIDS crater present on wlid6 sample

Although in the figure the geometrical shape of the crater seems ellipsoidal due to the picture deformation induced by the perspective of the profilemeter camera lens, specific measurements of the diameter in both X and Y axis shown that the crater is approximately circular. Almost all the produced craters in the analysed spots were measured by profilemetry. It is important to note that the laser beam irradiation was able to produce craters on the Li surface of the samples, but not on the original W surface where lithium was not deposited. In addition, the deep of the crater depended strongly on the thickness of the deposited lithium film deposited on the tungsten matrix. As the thermal simulations show the induced temperature rise on the irradiated surfaces (maximum temperature achieved should be around 900°C) is sufficient to melt the lithium and due to the dependence of the lithium vapour pressure with temperature the evaporation of these atoms will produce the crater. However, for the case of the samples free of lithium (only W matrix), this induced heating is not able to produce significant damage or melting on the surface. This experimental fact was observed in the case of the blank tungsten sample (wlid12). Two examples of the profilemetry measurements (taken in different craters of the sample wlid6) are shown in figure 3.42.

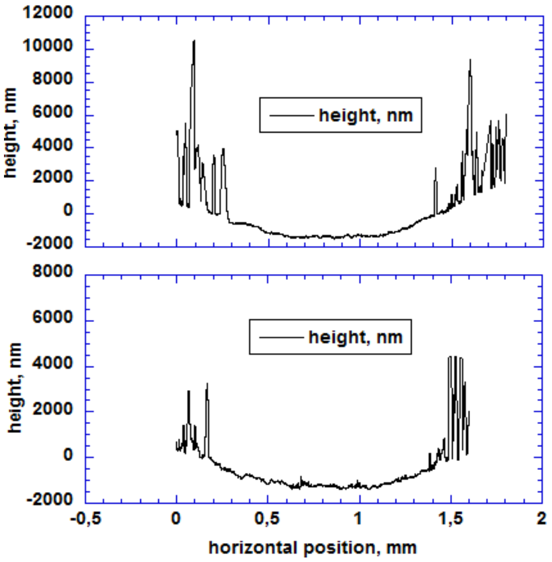

Figure 3.42. Profilemetry measurements on wlid6 sample

Both the craters present a depth around 2 μm with an approximate diameter of 1-1.25 mm. Otherwise, in the lateral part of the craters, the lithium film (being its thickness affected by carbonation and swelling) is visible in the form of high and irregular spikes that show the inhomogeneity of the deposited layer. As can be visualized in the figure the thickness of this lithium coverage oscillates between 4-10 μm for the first crater and between 2-5 μm for the second one. Both measurements belong to the same sample, thus these different thickness results attest for the irregular and contaminated lithium layer that is present on the sample surface after its preparation, laser irradiation and atmospheric exposure during profilemetry. Due to the previously commented swelling effect of the lithium carbonate layers, these measurements overestimate the lithium thickness present originally on the samples. In order to estimate the real values, the total amount of lithium deposited on samples was determined using flame atomic emission spectrometry (FAES) as will be explained in the next subchapter. Averaging the profilemetry results for all the measured craters in the treated samples, a nominal value for laser spot diameter, that is used for the calculation of the hydrogenic retention calculations, laser power density estimations and the thermal simulations, is obtained: $\mathbf{d_{spot}=0.125\pm0.008}$ **cm.**

3.3.6.4. Flame atomic emission spectrometry for quantification of the deposited lithium. Estimations of lithium film thickness

Once the previous techniques were applied to the sample characterization, the last experimental action was the measurement of the total lithium content present on the samples. As was previously commented, the Li atoms are prone to react with the atmospheric gases transforming the Li film in a Li_2CO_3 layer. This high chemical activity of lithium can be also approached to solve the lithium compounds present on samples into aqueous dissolutions. Other lithium impurities, that can be present on the sample surface, also react with water producing lithium hydroxide (LiOH) [115]. Consequently, the Li atoms present in the form of several compounds are transformed in free Li^+ ions present on aqueous aliquots suitable for Li determination by means of flame atomic emission spectrometry. This classic method of chemical analysis uses the intensity of light emitted from a flame at a particular wavelength to determine the quantity of an element in a sample [140]. The wavelength of the atomic spectral line gives the identity of the element while the intensity of the emitted light is proportional to the number of atoms of the element. It is widely used in inorganic chemical analysis to determine the concentration of certain metal ions such as alkaline (Li, Na, K…) and alkaline earth metals (Mg, Ca…). In this technique, a sample of material (in the form of diluted aqueous solution) is directed to the flame. The solvent is evaporated and the analysed atoms are excited into metastable electronic states that subsequently emit light when they return to the ground electronic state. The specific elemental emission occurs at a characteristic wavelength, (671 nm for the case of Li) which is dispersed by a grating or prism (monochromator) and detected in the spectrometer (detector) that quantifies the line intensity emitted by the sample. Absolute calibration works with specific standards, that relate the line emission intensity with known concentrations on sample, are normally applied to each element for its absolute quantification. A schematic view of the FAES technique and basic equipment [141] is illustrated in figure 3.43.

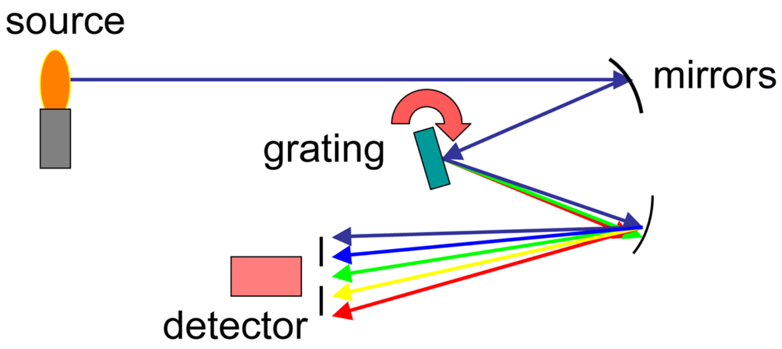

Figure 3.43 Schematic view of the FAES technique

The diluted Li specimens were prepared by immersing the W-Li samples in 50 mL of hot ultrapure (Milli-$Q^®$) water. The volume of the water was measured with a high precision graduated cylinder widely used in chemistry laboratories. After a brief time inside the water, the lithium layer present on sample is solved and the colour of the sample surface turns from white-grey (contaminated lithium) to the characteristic metallic dark grey of the tungsten. At this moment, an aliquot part of the dissolution is transferred to a small (20 mL) reservoir and sent to the chemistry laboratory that apply the FAES technique and determine the total lithium content (in mg/L of solution).

This procedure was performed for the pre-lithiated (in a high vacuum environment) samples and the wlid (exposed to simultaneous Li evaporation and D_2 atmosphere, p=0.67 Pa). Furthermore, another lithiated samples were prepared for FAES determination in order to compare the formation of the lithium film on the W surfaces depending on the deposition conditions (gas presence or absence, surrounding pressure and surface temperature). Two different sets of additional samples were prepared:

- Samples exposed to lithium evaporation in high vacuum conditions ($p \approx 6 \cdot 10^{-5}$ Pa). The evaporation of lithium took place at the same temperature compared to the samples previously studied (450ºC). Different samples were prepared varying the surface temperature during the Li evaporation (200ºC, 300ºC and 400ºC). These samples were not later exposed to any D_2 exposure, thus avoiding the concomitant and additional surface heating that eliminates a part of the lithium film due to its melting and sliding. In this way the removal of lithium due to these effects can be directly evaluated by comparing the lithium thickness in this group of samples with the obtained for the pre-lithiated samples. Additionally these samples were also analysed by LIDS to determine the hydrogen residual retention associated to the impurities present on the evaporated Li that were together deposited on the sample. The results shown an appreciable hydrogen retention that decreases clearly with higher temperature. The obtained values were:
    - $H_{ret} \approx 5.0 \cdot 10^{16}$ cm^{-2} at 200ºC on the sample during the Li deposition
    - $H_{ret} = 8.0 \cdot 10^{15}$ cm^{-2} at 300ºC of surface temperature
    - $H_{ret} = 3.0 \cdot 10^{15}$ cm^{-2} for $T_{surface} = 400$ºC
    - These results corroborate the previous considerations about the origin of this residual hydrogen content on the samples that were not exposed to hydrogen. It seems evident that lithium coverage leads to an associated H uptake on samples. This hydrogen content depends on the surface temperature that influences the H-Li interaction and the magnitude of the lithium deposition.

- Samples exposed to lithium deposition under a helium atmosphere at p=0.67 Pa. Evaporation of lithium was carried out under the identical conditions employed for the preparation of the wlid sample but changing the D_2 atmosphere by a helium one, in order to compare the influence of the presence of an inert gas instead of D_2 that in principle can interact with the lithium atoms. Different samples were prepared at surface temperatures of 200ºC, 300ºC, 400ºC and 500ºC.

The results of the Li thickness determination for all these samples are represented in table 3.13.

$T_{surface}$, ºC	**Vacuum conditions (no D_2)**	**Vacuum conditions (+ D_2)**	**He atmosphere**	**D_2 atmosphere**
200	0.94	0.89	-	-
225	-	-	0.44	1.95
300	0.47	0.06	0.03	-
400	0.06	0.11	0.03	-
500	-	-	0.04	-

Table 3.13. Li film thickness deposited on samples

The conversion of the FAES determinations (lithium concentration in mg/L) to lithium thickness originally present on sample is performed taking into account the volume of the prepared lithium dissolution (50 cm^3), the area of the sample (A=3.6 cm^2) and the density (ρ=0.534 g/cm^3) of lithium:

$$\delta_{Li} = \frac{c \cdot V}{A \cdot \rho}. \quad (3.31)$$

In principle, the incident lithium flux to the deposition areas from evaporative sources depends on the surrounding pressure that changes the mean free path (λ) of Li atoms. This parameter is influenced by the collisions of the Li atoms with the gas particles present in the chamber during the evaporation and can be considered as inversely proportional to the pressure. A detailed calculation taking into account these effects can be found in [142]. However, an exhaustive analysis of the lithiation environment dependency on the Li deposition thickness is out of the scope of this work. The second factor that influences the Li uptake by the tungsten sample is the surface temperature. Melting point of lithium is situated a 180ºC. Beyond this temperature, the lithium atoms will be in liquid state and the vertical configuration of the sample can induce the slipping and dropping of lithium that decreases the net uptake. Moreover, at temperatures higher than 350ºC the evaporation of lithium from the sample surface begin to affect to the deposition, as the remaining Li atoms can be evaporated in a significant fraction that will increase exponentially with the surface temperature. At these temperatures a competition regime between the deposition of Li atoms from the oven and the evaporation of Li on the hot sample surface would be achieved. Comparing the results of the FAES analysis for different $T_{surface}$ (at the same deposition conditions), a clear trend is visible for all the samples independently of the deposition type. The Li deposited thickness decreases at higher temperatures, being the obtained values an order of magnitude lower for temperatures of 400ºC compared to the case of 200-225ºC. At this point, the global quantification of the evaporation, dropping and slipping effects with surface temperature and the direct comparison between different samples seems difficult to evaluate. Nonetheless, the found effect of the surface temperature in the Li film formation is clear and has great importance, as a $T_{surface}$ = 400ºC determines very thin lithium films (≤0.1 μm) on the tungsten substrate for all the studied experimental conditions, thus precluding the potential formation of thick Li co-deposits on the W surfaces that could be problematic in a fusion reactor combining lithium and tungsten as PFMs.

3.3.7. Summary of the experimental findings about the influence of the surface temperature in the deuterium retention in lithium films deposited on tungsten

To relate and visualize in a simple way all the experimental implications of the temperature influence on the lithium film formation and the consequent hydrogenic retention on the W-Li layers prepared under lithium-deuterium varying Li-D_2 environments, the different results previously described separately are shown together in table 3.14.

Sample	$T_{surface}$, °C (Li-D_2 exposure)	Li film g/m^2 (µm)	D_{ret} cm^{-2}	D_{ret} mg/m^2	H_{ret}[***] cm^{-2}	H_{ret} mg/m^2	D/Li ($A_{D:Li}$)	H/Li ($A_{H:Li}$)
wlid	225 (co-deposition)	1.0 (1.95)	[**]	-	$2.6{\cdot}10^{16}$	0.43	-	0.003
wlid6	200 (pre-Li+D_2)	0.46 (0.89)	$1.9{\cdot}10^{18}$	63	$2.4{\cdot}10^{17}$	4.0	0.46	0.060
wlid8	300 (pre-Li+D_2)	0.032 (0.06)	$1.5{\cdot}10^{15}$	0.050	$4.4{\cdot}10^{15}$	0.073	0.0050	0.016
wlid10	400 (pre-Li+D_2)	0.058 (0.11)	$4.3{\cdot}10^{13}$	0.0014	$1.3{\cdot}10^{15}$	0.022	$8{\cdot}10^{-5}$	0.0026
wlid11	200 (pre-Li+D_2)	0.029[*] (0.057)	$2.0{\cdot}10^{18}$	66	$5.9{\cdot}10^{17}$	9.8	-	-
wlid13	200 (pre-Li+D_2)	-	$2.0{\cdot}10^{18}$	66	$2.8{\cdot}10^{17}$	4.6	-	-
wlid12	200 (no Li, W blank)	-	[**]	-	[**]	-	-	-

[*] Value that does not correspond to the original Li film content. Remaining Li after the TDS

[**] Below limit of detection of the LIDS technique

[***]Hydrogen uptake associated to impurities present on the deposited Li. Samples were not exposed to H_2

Table 3.14. Global summary of the D, H (obtained by LIDS measurements) and Li (FAES determination) contents for the studied samples

3.3.8. Overview and conclusions obtained from the experimental works

After the global discussion and data analysis of the experiments, the following conclusions about the hydrogenic retention in mixed W-Li layers can be extracted as a general overview:

- The LIDS technique has been developed for fuel removal and retention measurements in W-Li layers exposed to molecular deuterium
- D uptake on W (at 225°C) exposed simultaneously to Li and D_2 in a co-deposition regime is below the limit of detection of the LIDS technique (being the global D interaction for a Li film with 2 µm similar compared to pure W)

- The pre-lithiated samples exposed to molecular D_2 exhibit a retention that decreases drastically with surface temperature (non-linear effect). The Li-D interaction in liquid thin films deposited on W is substantially reduced for $T_{surface} \geq 300$ºC.
- The deuterium content is also related with lithium coverage. $T_{surface} > 200$ºC produces the melting and dropping of Li (that could be recovered in situ and directed to the liquid Li divertor in a reactor scenario) that determines the formation of a thinner lithium film being the concomitant retention lower.
- The thickness of the liquid lithium film formed on W also depends on the experimental conditions (surrounding pressure, flow regime, presence of different gas species and surface temperature)
- The hydrogen uptake on samples is associated to the presence of hydrogenated impurities in the evaporated lithium that are co-deposited together with the Li atoms.
- LIDS assure the total removal of the hydrogenic species ($T_{rise} > 600$ K for the whole W-Li layer are obtained from simulations).
- The relative semi-quantification of the W-Li-D layers performed with SIMS analyses corroborates the LIDS retention results in terms of D retention. The characterization of the surfaces shows that the deuterium uptake is associated to the lithium layer present on the W surface.
- TDS ($T_{max} = 570$ºC) also allows the total removal of deuterium and hydrogen from samples, being the absolute retention results comparable to the values obtained by LIDS.

3.3.9. Global discussion about the influence of the surface temperature in the deuterium retention on W-Li thin films

The characterization and analysis of the W-Li-D films performed in this study reveals a strong, non-linear effect of the increasing surface temperature on the D uptake in co-deposited layers on a tungsten substrate at temperatures beyond 300ºC. The global results presented in table 3.13 allow analysing the role of lithium coverage and surface temperature on the global D uptake for the samples prepared with a pre-lithiation followed by D_2 exposure regime. Comparing the Li content in the samples wlid6 and wlid8, a decrease by a factor 15 is found for the case of surface temperature of 300ºC compared to the case of 200ºC. The additional heating necessary for the subsequent D_2 exposure after the pre-lithiation can lead to the Li removal by dripping and slipping of the liquid layer. The Li content on the sample wlid10 ($T_{surface} = 400$ºC) is a bit higher compared to the sample wlid8 ($T_{surface}$ = 300ºC). In principle the lithium losses due to the effects of increasing temperatures will be larger at higher temperatures. However, once the Li layer overpasses the temperature of 300ºC it seems that the quantification of the global effects of the temperature (evaporation, dripping and slipping) in the Li losses are not evident, as another experimental factors (as presence of cold parts on surface, formation of lithium aggregates due to surface tension and forces) and uncertainties can have an influence. In any case it is clearly visible that even for the case of a $T_{surface}$ = 300ºC (sample wlid8) the decrease in the lithium content (factor 15) on sample is not proportional to the reduction in the D retention (factor 1300) thus suggesting that the interaction of Li deposited atoms with thermal deuterium molecules is affected and reduced with increasing surface temperatures. This assumption is corroborated by the results obtained for the wlid10 sample ($T_{surface}$=400ºC). As was explained previously, the lithium uptake at this temperature is not reduced compared to the pre-lithiated sample exposed to D_2 at 300ºC (wlid8). However the D uptake is a factor 35 lower. This extremely reduced D uptake at higher surface temperature on the W-Li film cannot be explained by the reduction of the Li sample coverage.

Hence the changes induced by increasing the surface temperature in the Li-D surface chemistry (that determines the adsorption, solution into Li and bonding of the deuterium atoms to the Li film that causes the global retention) seems to be the most important factor that determines the drastically lower retention values obtained at elevated temperatures. In this way the D uptake dependence with $T_{surface}$ by the Li layers deposited on tungsten is influenced by two factors: a lower Li deposition and a reduced D uptake by the lithium atoms at higher temperatures, that results in a synergistic combined effect that could explain the extremely lower retention values measured by LIDS at 400ºC. In figure 3.44 an Arrhenius-type plot of the D/Li ratio depending on temperature is shown for the three pre-lithiated samples (wlid6, wlid8 and wlid10).

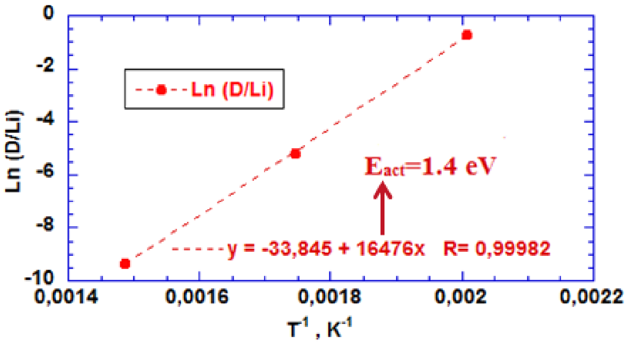

Figure 3.44. Arrhenius plot for the D/Li ratio obtained for samples wlid6, wlid8 and wlid10

Assuming that the release of deuterium from the film can be characterized by a specific activation energy, a value of $E_a = 1.4$ eV is obtained for the process. This value is smaller than the activation energy for lithium hydride decomposition (2.0 eV, [143]), and 7 times higher than the heat of solution deduced from the temperature dependence of the H solubility [144], perhaps suggesting an intrinsic dependence of the D/Li ratio on the film thickness itself. However it must be noted that this result is limited to only three experimental cases. Additional experiments (at different temperatures) would be necessary to complete the analysis and confirm this observation. Comparing the retention rate (D/Li atomic ratio) observed in these samples with the solubility data for deuterium in lithium bulk [145], the obtained result at 400ºC after one hour of exposure to D_2 is much lower (more than two orders of magnitude) compared to the equilibrium concentrations. For the sample exposed at 200ºC the retention measured is higher that the equilibrium value, thus corroborating the formation of LiD after overpassing the saturation in the hydrogen solution. Finally, the sample exposed at 300ºC presented a retention value in the order of the solubility equilibrium. According to these results, the thermodynamic behaviour of liquid lithium thin films deposited on W in terms of hydrogenic absorption seems to be different compared to the case of bulk absorption thus resulting in a reduced hydrogenic uptake at temperatures higher than 300ºC.

Nevertheless, this scenario is not the most realistic compared to the operation in a fusion reactor, as in this case the W first wall surface will be affected by simultaneous Li and D incident flux. For this co-deposition regime the obtained results at low (225ºC) wall temperature indicated a negligible D retention on the liquid Li film ($\delta_{Li} \approx 2$ μm) comparable to the case of pure W. Taking into account the previously inferred results about the temperature effect in the D retention on the W-Li pre-deposited layers, it seems logical to think that at high temperatures, ($T_{surface} \geq 400$ºC (that constitutes a realistic scenario for DEMO operation with hot W first wall) the co-deposition of deuterium in the Li films deposited on tungsten will be reduced by a very important factor. In a reactor scenario operating in these conditions, this experimental result would imply high recycling conditions for the W first walls.

At these temperatures previous experiments [146] performed on nickel substrates indicated unstable hydride (LiH) layers that decomposed when the surface temperature is increased up to 340ºC. This behaviour was found in ultrathin (<3 nm) LiH films with several (5-10) deposited monolayers. In addition, Capece et al. [147] studied the temperature effect on the D retention in ultrathin lithium films deposited on molybdenum (TZM) alloy confirming the decomposition of lithium deuteride at temperatures below 400ºC. Although our studied films at $T_{surface} \geq 300$ºC exhibited a larger thickness (60-100 nm), this LiD decomposition was also inferred as the SIMS analysis shown the absence of this molecule on these samples while LiD was present at samples exposed to D_2 at 200ºC. Hence this instability of thin lithium hydrides films at increasing temperatures seems to be behind the observed results. It must be recalled that the stability of liquid Li films under the MHD activity (which could eventually lead to liquid ejection/splashing via thermoelectric induced currents and JxB effects) would be assured for films thinner than 10 μm even for the case of the biggest thermoelectric current densities that exceed the values measured up to date [148].

Another factor to have into account in this hypothetic fusion reactor operation is the material erosion that can alter the state and composition of the Li-D films present on the W first wall elements. The effect of the temperature in the liquid lithium sputtering yield was firstly studied by Allain et al. [149]. Furthermore, this topic was also investigated in the NTSX spherical tokamak [150] on liquid lithium deposited on graphite and molybdenum substrates. They found increasing yields for higher temperatures in Li-D and Li-Li self-sputtering [151]. The same effect was also observed in NTSX [151] with increasing Li sputtering yields up to 0.2 at temperatures between 400ºC-500ºC that supposed an enhancement in a factor 2 compared to the results obtained with liquid lithium surfaces at 200ºC. Moreover, preferential sputtering of D atoms present in Li-D layers was found [152]. This enhanced erosion of the hydrogenic atoms respect to the Li ones would reduce even more the fuel retention in co-deposited layers during the operation of the fusion reactor. Despite this temperature enhanced sputtering that, in principle, would increase the input wall flux of Li impurities to the plasma, the experiments shown [151] that in liquid lithium approximately the 65% of the total Li-Li self-sputtering was in the form of Li^+ ions. This high ion fraction can prevent the penetration (and concomitant contamination) of excessive Li impurity levels in the plasma core, as the ions would be screened by the plasma sheath. Computer simulations [153], taking into account this particularity, have shown a low lithium core plasma contamination. In the divertor region where the most of the ionic flux is expected, the 95% of the sputtered lithium would be re-deposited on the divertor and only a very low fraction (0.2%) could overpass this region and reach the first wall, decreasing in this way the Li-D co-deposition on the W first wall and assuring low plasma contamination in the core due to physical sputtering.

More severe seems the restrictions related with the evaporative lithium flux resulting from the increasing vapour pressure of lithium with temperature. At reactor relevant fluxes, the evaporation input will dominate the physical sputtering contribution above 450ºC as the dominant mechanism related with erosion and impurity influx to the plasma from the first W wall. Conservative estimates based on a maximum lithium content in the plasma core around 1% establish the upper limit for lithium surfaces temperature to values around 450-500ºC [154]. However, recent modelling work has shown that higher temperatures for the evaporative liquid lithium layer could be allowed since the concomitant higher Li core pollution would be still compatible with the associated loss confinement and fusion power rate (10% of decrease for a Li core concentration around 2% [155]) that would assure an appropriated reactor performance. Recently, Goldston et al. [156] have determined that a Li evaporative temperature of 580ºC would be sufficient to dissipate the divertor power exhaust (200 MW) of a relevant fusion power plant. This study was carried out developing a power balance and a lithium vapour induced detachment model in a lithium vapour box divertor concept [25]. In any case, further research is needed to elucidate the adequate operational window for the Li surface temperature, its evaporative flux and the concomitant plasma core contamination that can be compatible with and adequate confinement in a DEMO-relevant device.

3.3.10. Implications for a fusion reactor design with integrated PFM solutions combining tungsten first wall and liquid lithium divertor concepts

For the integration of this PFCs solution for a fusion reactor, at this point, it is worth to assess the implications of the present results in the operation of a DEMO prototype operating under a liquid lithium target divertor/hot W first wall scenario. The conservative European design option for a future demonstration reactor (named as DEMO1) envisages the construction of a pulsed device operating in H-mode based on the ITER operation [2] with a pulse duration of two hours [157] or larger [158]. Another advanced configuration (DEMO2) [159, 160] is being considered for delivering as next step demonstration devices. This DEMO2 concept would explore the possibility of steady state plasma operation. Nonetheless, its construction would be contingent to the development of significant advances in the underlying physics and technology through the relevant knowledge learnt from ITER operation and experience. Both DEMO1 and DEMO2 are based in the tokamak configuration. For these designs, tungsten is planned to be used as PFC's for the first wall. The dimensional parameters [159-162] of these reactor concepts are shown in table 3.15.

Reactor prototype	**Pulse duration, h**	**Inner area, m^2**	**Inner volume, m^3**	**Major radius (R), m**	**Aspect ratio (A)**
DEMO1	2	1428	2502	9	3.1
DEMO2	≥2	1253	2217	7.5	2.6

Table 3.15. Preliminary size parameters for DEMO1 and DEMO2 designs

Given these primary characteristics for the fusion reactor prototypes, the important aspects to evaluate and compare our experimental results and conditions are related with the fuel neutral pressure and flux values onto the in-vessel W components. Consequently, the scaling of the pressure and fluxes levels to the expected ones in this reactor environment, as well as the extrapolation to long pulse or continuous operation is of paramount importance. Exploring the predictions about the distribution of neutral pressure levels expected in the sub-divertor region and adjacent parts of DEMO1 [161, 162], the D_2 pressure value used in our co-deposition regime experiments (0.67 Pa) is comparable to the expected pressures in zones close to the separatrix and SOL region. However, in the surrounding sub-divertor areas around this region (inner and outer divertor arm gaps and slots, as well as the divertor below dome) the neutral pressure decreases strongly (pressures around 0.01 Pa) [161]. For the hypothetical hot W first wall areas (situated at a larger distance from the divertor region), the neutral pressure is expected to be even more reduced, ultimately given by the recycling properties of the material. These much lower values for the neutral and molecular D_2 pressures on the hot first wall zones (that are in principle exposed to co-deposition) would imply a significant reduction in the Li-D_2 interaction and the subsequent fuel uptake. On the contrary it is important to note that energies expected for a fraction of the thermalized molecular D_2 and neutrals will overpass the level of the gas molecules (at room temperature) utilized in our experiments, thus increasing the potential interaction between tritiated species and Li layers present on the W walls. In addition, fluxes of Li and hydrogenic ions accelerated in the plasma sheath can bombard the tungsten components. It could produce implantation of Li and fuel species that will affect to the co-deposition and the tritium inventory.

About this issue, promising results have been obtained in terms of fuel retention and Li film formation, for W samples exposed to Li-seeded deuterium linear plasmas in the PISCES-A divertor simulator [163]. In this work, while a Li layer with approximate 28 μm of thickness was found in a W sample exposed to plasma at 130°C, a strongly reduced deposition rate was found for W samples exposed at temperatures between 400°C-600°C, confirming the strong reduction in the Li deposition with surface temperature experimentally found in our experiments. About the concomitant D retention in such Li-W layers, these experiments quantified the deuterium retentions by TDS and Nuclear Reaction Analysis (NRA). The retention analysis presented very low values in the order of $7{\cdot}10^{13}$- 10^{16} cm^{-2}. The temperature dependence of these results seems to produce a D uptake significantly lower for increasing surface temperatures, thus pointing to the effect found in our experiments, that leads to a reduced interaction of D with the Li films deposited on W at higher temperatures. Furthermore, another previous findings in experiments with cold W samples exposed to Li-seeded H_2 Glow Discharge (GD) plasmas (results explained in the chapter 3.2) and [97]) found a hydrogen retention lower (factor 3-4) compared to pre-lithiated W after being exposed to H_2 Glow Discharge plasma, suggesting the role of implanted Li atoms on W in the reduction of the hydrogen uptake. Following this assumption, the retention of hydrogenic species in W areas exposed to Li ionic bombardment (from a liquid Li divertor concept) would not be as problematic as the fuel co-deposition in zones exposed mostly to neutral Li fluxes as studied in this work.

Doubtlessly, the extrapolation of the temperature dependence of D co-deposition in mixed W-Li PFC's for fusion reactor environment would need the evaluation of scaling pressure effects for the larger exposure time. It is important to take into account that our experimental exposure duration for Li-D_2 co-deposition was 30 minutes instead the two hours of minimum pulse duration expected for DEMO1 or even the hypothetic steady state operation of next step devices. Although the time and the longer fluency effects are in principle supposed to be extrapolated linearly, the combination of this effect together with lower (compared to our experiments) hydrogenic neutral pressure levels expected in a reactor, is difficult to predict. In this respect, it is worth noting that the pressure of D_2 used in our experiments is far larger than that expected near the first wall of a reactor. Thus, for 400ºC, the equilibrium pressure (corresponding to the onset of hydride formation) is $\sim 10^{-2}$ Pa and still, even with P=133 Pa, a value of D/Li more than two orders of magnitude lower than the saturated solubility limit of ~1%, was recorded at this temperature. Furthermore, it is not expected that even for a lowest temperature case (with temperature around 200ºC for the first wall areas exposed to co-deposition), the Li film could grow indefinitely. Although other saturation mechanisms might exist, at least the effect of the gravity force in the liquid layer deposited on the vertical zones of the walls produces the slipping and dropping of the liquid lithium (effect that can be used to direct it to the divertor) as has been observed in the experiments. Moreover as has been discussed previously, the pressure levels existing in the divertor region will produce the inelastic collision of the evaporated atoms with the SOL species that would decrease the mean free path of Li atoms thus being deposited in adjacent parts situated closer to the divertor liquid surfaces. These experimental conditions will result in lower co-deposition of Li on the first wall zones situated far away from the divertor region as is explained in [142].

Although a scenario with a reactor first wall at temperatures as low as 200ºC is not realistic, (general studies for fusion reactors requires much higher temperatures that favour the conversion of the fusion power to electricity), it is worth to consider it under the scope of presently running devices on which limited heating capabilities of the full vessel exist. If full co-deposition of the evaporated atoms in all the first wall area takes place, assuming liquid Li divertor working at temperatures similar to our evaporator oven (450ºC), and taking into account the measured Li thickness for the sample exposed at 225ºC, the results from Li-D_2 co-deposition regime (in 30 minutes a film of 1 g/m^2 of Li, i.e. 1.95 μm equivalent to $7.4 \cdot 10^{22}$ Li atoms/m^2 is created) a lithium deposition rate of 3.9 μm/h (equivalent to $1.5 \cdot 10^{23}$ atoms/$m^2 \cdot h$) is obtained, assuming that the lithium film growing is proportional to time, as has been experimentally verified. Unfortunately, no quantification of the D uptake was possible in the co-deposition regime, most likely due to the low D_2 gas pressure and relatively low exposure time used in these experiments, so that retention values similar to those seen in pure W can be tentatively assumed.

For the reactor scheme here inferred, a first wall hotter that the divertor (i.e. at 500ºC or even at 600-700ºC) is considered, thus assuming this value as the nominal wall temperature for DEMO [164]. Consequently, if any film is formed, liquid Li slipping on the W elements will re-direct directly a considerable amount of the lithium to the coldest part of the inner vessel (divertor) that would act as a particle sink for Li, D-T isotopes and impurities. Then, the liquid lithium with fuel content can be directed out the divertor to eliminate the tritium, dust and impurity content and finally recirculate the clean Li to the divertor and the tritium for the plasma fuelling in a closed liquid lithium loop [165] or the removal could be in situ by baking at T≤600ºC [97, 115, 116, 117]. In this scheme, the recovery of evaporated lithium on the divertor by means of specific geometries and/or channels designed to conduct the liquid lithium films from the first wall surfaces to the divertor plates could be carried out if required.

In the present work, the simultaneous Li-D_2 co-deposition was not studied at higher temperatures than 225ºC. The negligible retention results (below the LIDS limit of detection) at this temperature make the expected D uptake at higher temperatures even lower and impossible to detect. Notwithstanding, the created Li film was measured in a similar co-deposition regime (Li-He environment) at same neutral pressure and higher sample temperature. Beyond 300ºC, a strongly reduced Li thickness film (factor 15 of reduction) is found. Assuming the same reduction in Li deposition with temperature for the Li-D_2 co-deposition environment, the net Li deposition rate by a hot W wall (500ºC) would be around 0.26 μm/h (or 10^{22} atoms/m^2h). For the DEMO1 more conservative concept (pulses with duration of 2 h), it would give a total Li deposition of $2\cdot10^{22}$ atoms/m^2 with a film thickness of 0.5 μm per pulse. From our experiments a direct extrapolation of the fuel co-deposition in these W-Li layers cannot be directly performed as no experimental data are available. But assuming in the worst case for the low pressure (0.67 Pa) Li-D_2 co-deposition a retention comparable (conservative extrapolation) with the experimental values for the pre-lithiated W samples exposed at 400ºC to much higher D_2 pressure (133 Pa, that yielded a D/Li atomic ratio lower than 10^{-4}), a simple calculation gives a D retention of $1.6\cdot10^{18}$ m^{-2} for a pulsed operation with plasma shots of two hours of duration. Considering as a simple, rough and conservative approximation that this average Li-D_2 co-deposition is extended homogeneously around the whole inner vessel area of the DEMO1 prototype and using an estimation [158, 159] for this area (≈1365 m^2 as mean value) the global fuel co-deposition at high temperature (400ºC) in the reactor W-Li surfaces will be around $2.2\cdot10^{21}$ atoms. As the D-T fuelling is in principle equimolar, this result would suppose net tritium retention of 5-6 mg per pulse. With a tritium inventory limited to ITER values (700 grams, [108]) a reactor design based on liquid lithium divertor (with evaporative Li fluxes at temperatures around 450ºC) combined with a hotter W first wall could be a potential solution for the problematic related with fuel co-deposition on the first wall that dominates the fuel retention in present fusion devices. At this point the global comprehension of the hydrogenic saturation characteristics of co-deposited thin liquid lithium films at high temperatures ($T_{surface}$≥450ºC) seems crucial. These results points to the possible saturation with very low deuterium uptake reached at high temperatures on thin (thickness lower than microns) liquid lithium films. The promising experimental findings must be confirmed in experimental conditions with longer and higher Li/D fluxes to determine if this low D saturation regime found in the W-Li layers can be achieved in a reactor-like regime thus maintaining a low tritium retention in the W first wall affected by lithium material migration and co-deposition. Preliminary and promising results in this line have been already obtained in PISCES A [163]. Furthermore, the possibility of exposing tungsten to Li-D_2 co-deposition environments (as the approached in this thesis) in the recently upgraded Magnum-PSI linear device, equipped with a superconducting magnet that enables an extremely large plasma fluence (up to one-tenth of that expected in the ITER divertor), appears as very attractive for this purpose.

Although another aspects related with the presence of high evaporative lithium fluxes, as the tolerable limits for Li contamination for an acceptable plasma performance (avoiding critical impurity accumulation in the plasma core or excessive dilution) or the material compatibility (possible associated corrosion problems) between Li and W must be addressed, these results represent a first approximation to this liquid metal solution for fusion reactors. The definition of realistic reactor scenarios with reliable estimations of the relevant parameters (neutral pressure and density, recombination fuel fluxes to the first wall...) and further efforts in the research under experimental conditions closer to reactor relevant regimes are mandatory to fully characterize the underlying physics that determines the Li-D co-deposition on W at high temperatures and their implications for fusion reactors PFCs design.

4. SUMMARY

This thesis has been dedicated to the study of the possible implantation of tungsten and lithium as plasma facing materials in fusion reactors. During the two first years of the thesis, the experimental studies were focused on important issues related with the impurity (ammonia) formation and accumulation in W and other materials as SS and Al. The last two years were employed to study the hydrogenic (associated tritium) retention on W-Li mixed materials.

The experimental work has approached the problematic of ammonia formation expected in ITER if nitrogen is finally seeded as radiative cooler in the divertor region. Gaseous impurity seeding is probably the best method to achieve the plasma detachment state in the divertor region. This operational regime will be mandatory in ITER and future reactors as DEMO as the power loading to the material components needs to be reduced to sufficiently low levels that assure an adequate lifetime for these components. This research has mainly utilized glow discharge plasmas to simulate the divertor environment during the N_2 seeded discharges. Additionally the accumulation of ammonia due to sticking on PFMs was also investigated with gas exposure experiments performed on AISI 304 L stainless steel surfaces.

Power exhaust handling will be a critical issue in next step fusion devices. For the viability of a reactor, the capacity of extracting the generated fusion power avoiding the progressive deterioration and finally the destruction of the employed components is of prime importance. Liquid lithium emerges as an alternative element to conform such components as its use for the heat flux handling can be advantageous. The mutual interaction of Li, W and hydrogen isotopes has been approached by studying the hydrogenic retention characteristics of W-Li layers exposed to glow discharge hydrogen plasmas and W surfaces exposed to Li-D_2 (gaseous) co-deposition.

During these experimental actions a Glow Discharge Plasma technique and a Laser Induced Desorption Spectroscopy diagnostic were tuned up to produce the irradiation of the materials and the measurement of the hydrogenic retention. The main results of these investigations are summarized in the following pages, emphasizing the consequences for the design and operation of the future ITER and DEMO devices.

4.1. FORMATION AND ACCUMULATION OF AMMONIA DURING N_2 SEEDED DISCHARGES

The generation of ammonia in a tokamak environment is a very complex process. It involves several steps with plasma phase processes as the dissociation/ionization of the precursors (N_2 and hydrogen isotopes) and surface chemical reactions (N-H recombination). The operation with D-T fuel in ITER will produce a net retention of tritium in the form of ammonia molecules. For a proper and safe operation the amount of generated ammonia has to be controlled and eliminated, thus assuring tritium content in the reactor below the safety inventory limits.

About this problematic, the previsions for ITER are not very optimistic. As these results have showed, the experimental parameters as increasing surface temperature (up to 350ºC) of the PFCs and the low nitrogen content in the plasma does not minimize the dangerous generation of ammonia. In fact, according to the experimental results, the effect of the temperature in the process is deleterious as its increase enhances the ammonia formation. For low N_2 contents in the plasma, the efficiency of the nitrogen molecule cracking is increased and consequently more nitrogen can be adsorbed on the surfaces producing higher ammonia formation yields.

The developed studies aimed to investigate the mechanism of the ammonia formation have revealed a strong correlation between the nitrogen content of the wall materials (nitrogen legacy) and the produced ammonia. In particular, no ammonia is produced if the nitrogen is not present on the wall in the form of dissociated atoms. The possible saturation of the active centres of the surface (that catalyse the reactions) with inert species as helium was proposed as a possible strategy for the inhibition or minimization of this ammonia formation. It is important to note that the presence of helium will be unavoidable as it will be generated in the D-T reactions. The found effects of the helium presence in the ammonia generation were not satisfactory, as it increased the formation yields. Although similar experiments in different experimental conditions (linear plasma devices) have shown different results (plasma flux and density regime can change completely the induced effects), it is not clear that this strategy could solve the problematic in a real reactor scenario.

The accumulation of ammonia molecules on the PFMs surfaces originated mostly by electrostatic adsorption (sticking) will also contribute to the associated tritium retention issues. For the first time the ammonia sticking process under high vacuum conditions has been quantified on stainless steel surfaces. Furthermore, the influence of the surface temperature in the process has been determined and an extrapolation method to estimate the surface saturation characteristics in higher flux devices (as processing plants and pumping lines) is included in this work. The corrosion associated problems also appear very important as the vacuum and pumping system can be seriously damaged due to their long exposure to ammonia. Nevertheless, the critical point related with this issue is the capacity of the cryo-pumping system that will collect the produced ammonia. As a consequence of the ammonia formation, the cryopumps must be regenerated at shorter periods of time, thus limiting the operational cycle of the machine and increasing the associated maintenance cost.

If the ammonia generation level determines an excessively frequent regeneration for the cryopump modules that leads to an unacceptable expensive operation, the use of nitrogen as radiative cooler in the ITER divertor will be rejected, being neon (Ne) the alternative candidate. The beneficial effects of nitrogen in the confinement improvement along the edge and pedestal region are not reproduced by using neon. Consequently, if nitrogen is substituted by neon, the associated confinement losses during the ITER operation would need to be taken into account. The possible implantation of thermal methods to decompose (at least partially) the ammonia is being investigated. They could consist in a simple set of hot ($T \geq 700$ºC) metallic filaments located along the way from the divertor to the cryopumping system. The balance between the associated cost of such engineering solutions together with the critical regeneration of the gas exhaust system and the profitable and perhaps necessary effects of nitrogen in terms of confinement and plasma performance will have the final say about this important ITER-issue.

4.2. TRITIUM RETENTION ISSUES IN MIXED W-LI LAYERS

The conventional divertor scheme based on ITER (X-point designs) supposes the baseline configuration considered for the future DEMO reactor. Moreover, tungsten remains as the first PFM candidate to construct it. The limited resistance of the solid tungsten elements against the extremely high power and particle exhaust fluxes constitutes a serious concern about the satisfactory application at reactor scale. Nowadays there are reasonable doubts about the performance of such design and its useful life before its destruction and mandatory replacement. The last considerations establish that even assuming a very optimistic scenario with maximum limits around 5 MW/m^2 for the power flux incident to PFCs and absence of type I ELMs, the erosion and accumulative damage will determine a maximum operational period of two years for such tungsten divertor. The real situation could be even worse as the considered operational conditions seem extremely difficult to be carried out.

Partial or perhaps complete detachment operation will be essential to mitigate the power exhaust until the previous tolerable maximum limit. To achieve this regime, very high divertor edge and plasma core radiation will be necessary (inducing the radiation of the 90-95% of the total power). In DEMO, the use of nitrogen for this purpose is not contemplated as the radiative characteristics of this molecule are not the most appropriated with the expected pedestal and plasma edge structures, being argon the considered candidate for the impurity seeding. Hence the problems related with the deleterious ammonia formation will be avoided. However, the required high level of impurity seeding and the associated plasma detachment can occasion the global confinement degradation with associated MARFE events that can complicate the reactor performance, thus threatening the achieving of the plasma ignition conditions mandatory for a self-sustained nuclear operation with D-T reactions. Up to date, it is quite doubtful (if not impossible) that a conventional tungsten divertor can work efficient and continuously (minimum pulses of two hours) under such operational conditions.

For next step reactors or power plants (that probably will propose stationary operation) the problem will be aggravated and it is clear that a more advanced and technologically developed configuration will be necessary to resolve the power exhaust critical issue. The use of liquid metal surfaces in the divertor could be the alternative for this objective being lithium the most highlighted option to be applied in future fusion facilities. Among the main issues and challenges associated to the development of this emergent technology, a special care needs to be taken into account with the hydrogenic retention characteristics of lithium components. The pioneer experimental work here exposed has tried to study the problematic of the tritium retention associated to W-Li mixed layers formed due to the material migration and mixing effects expected in fusion reactors with tungsten and liquid lithium PFCs, focusing in the behaviour of implanted and co-deposited Li layers and the temperature effects in the associated hydrogenic retention of such hybrid layers.

The experimental results obtained in this thesis have shown a decreased retention of implanted lithium at a relatively low temperature in the W-Li surface (~100º C) compared to lithium simply deposited on the tungsten substrate. Although the effect of the increasing temperature in this phenomenon has not been studied, recent works in PISCES-A linear plasma device have also approached the topic and have shown very promising results presenting a very low associated retention for samples exposed to Li seeded D_2 plasmas at T ≥400ºC.

This temperature effect has been widely studied for the case of lithium-deuterium co-deposition on tungsten. The research has shown that a surface temperature of 400ºC determines the formation of a thin (≤0.1 μm) lithium film as a result of the competition between deposition and evaporation of lithium, together with possible losses induced by the melting and concomitant dropping and slipping. Among the several obtained results, perhaps the most important has been the non-linear reduction in the deuterium retention for increasing surface temperatures that leads to extremely reduced values comparable to the case of pure tungsten elements. Different previous investigations has demonstrated that hydrogenic retention on liquid lithium starts ceasing at T=400ºC, and although this co-deposition phenomenology found in the experiments must be confirmed in experiments involving facilities closer to a real reactor environment, the observed effects allow to be optimistic about this co-deposition phenomenon that appears as a key problem within the tritium inventory limitation issues.

Furthermore, in a power plant this high temperature for the first wall areas necessary to inhibit a possible harmful co-deposition and associated tritium retention would not be problematic as a high temperature will be required in the blanket modules for a highly efficient conversion of the fusion power into electricity.

For the general application of these liquid metal solutions an exhaustive effort and significant advances in terms of technology and engineering are completely necessary for the global integration of such concepts. In this sense, a diverse set of technical and scientific issues must be assessed. One of the most critical points will be undoubtedly related with the tritium inventory on the liquid lithium elements present on the divertor, where larger quantities of liquid metal will be present. Temperatures of 400-450ºC in these elements will favour a low hydrogenic uptake but the problematic must be investigated and the CPS or free flowing concepts proposed for this purpose needs to be widely tested in experimental conditions similar to a real fusion reactor. From the engineering point of view, many issues, as for example: problems related with associated corrosion, compatibility between W and Li (and associated temperature effects), tritium and lithium recovery and their integration in liquid loops schemes that allow the adequate replenishment of the liquid surfaces and the recuperation of tritium for fuelling needs to be studied, evaluated and the necessary engineering and technology must to be developed for their successful application in advanced fusion power plants. Although an important part of these technologies have not studied or developed yet, the general concerns existent about the use of solid materials compatible with sufficiently long operational life under the required conditions, encourage to a worldwide research in this direction in order to develop liquid metals solutions as a promising and reasonable alternative. Doubtlessly, considering only the scientific arguments and the accumulated research experience, the liquid metals investigation for its application in the magnetic fusion development merits at least an opportunity.

GLOSSARY

- ***Breeding blanket:*** Modules destined to generate the necessary tritium for the reactor fueling by lithium transmutation (bombardment with the previously produced fusion neutrons), also extracting the fusion power transported by the neutrons. They will be located covering the vacuum vessel area, behind the first wall.
- ***CPS:*** Acronym of Capillary Porous System. Structure utilized as PFC that contains a porous mesh aimed to sustain liquid metal exposed to plasma. The working principle is based on the compensation of the Lorentz forces induced by the plasma currents on the free liquid surface with the surface tension forces originated at the micrometric scale of the surface porous
- ***DEMO:*** (DEMOnstration power plant). Next generation fusion device projected beyond ITER. Its objective is produce net electricity from D-T self-sustained fusion reactions, generating its own tritium fuel in the breeding blanket modules
- ***Disruption:*** Dramatic collapse of the plasma in a fusion device originated by the accumulation of instabilities primary generated by the existence of high toroidal currents. During them, the stored plasma energy is suddenly deposited into the PFCs, thus causing dramatic damage on them. It is specific of tokamaks
- ***Divertor:*** Configuration for the plasma shaping and power/particle exhaust purposes. It is characterized by the use of an extra set of coils that forms open field lines for the particles at the bottom of the toroidal chamber. In this way the power load is spread under bigger areas (compared to the limiter configuration) and the pumping of neutral particle and impurities is more efficient. More details in chapter 1.3.1
- ***ELMs:*** Transient events originated by magnetohydrodynamic instabilities present in the plasma edge during the H-mode. They lead to periodic ejections of plasma and energy that causes damage in the PFCs
- ***FAES:*** Acronym of Flame Atomic Emission Spectroscopy. Quantitative technique for material analysis specially employed for the absolute detection of alkaline and alkaline-earth elements. It is based on the detection of emission spectral lines absolutely calibrated for quantification purposes. The radiative emission (excitation) of the atoms is produced by means of flame

- ***First wall:*** Element that constitutes the first barrier in contact with the plasma. It is situated covering all the inner surface of the vacuum vessel, excepting the divertor
- ***Glow Discharge:*** Plasma generated by a continuous electric current circulating through a low pressure ionized gas. It is built up by providing a voltage between two electrodes (anode and cathode), inducing previously the presence of a small population of free electrons that initiate the discharge
- ***H-Mode:*** Confinement regime characterized by the formation of transport barriers in the plasma edge. Its main characteristics are an increased energy confinement time (~factor 2) and enhanced core density and temperature. More details in chapter 1.4.2
- ***ITER:*** Acronym of "International Thermonuclear Experimental Reactor". Tokamak under construction in Cadarache (France) designed to produce more fusion energy that the necessary to ignite the plasma (Q~5-10). It will be a pulsed device (duration~8 minutes) with a peak fusion power around 500 MW but no generation of electricity. In its construction participate, the EU, China, India, Japan, Russia, South Korea and the USA
- ***Knudsen cell:*** Evaporative source working under vacuum conditions that utilizes the molecular effusion through small holes to produce highly localized depositions. It is widely employed in thin film deposition and molecular beam epitaxy
- ***LIDS:*** Acronym of Laser Induced Desorption Spectroscopy. Material analysis technique based on the thermal outgassing of localized surface spots irradiated with a laser beam
- ***Limiter:*** Element situated between the first wall and the plasma boundary. Its function is to enclose the plasma shape and control the plasma-surface interaction. More details in chapter 1.3.1
- ***Mass spectrometry:*** Analytical technique that measures the composition of a residual gas. The detection of its constituents is carried out by their previous ionization and posterior separation by using quadrupole magnetic fields. In this way, they are detected depending on their mass to charge ratio (m/q)
- ***Pedestal:*** Narrow region present in the plasma edge during the H-mode characterized by abrupt changes in the density and temperature radial profiles
- ***PFCs:*** Plasma Facing Components. Elements present inside the toroidal vacuum vessel. They are in direct contact with the plasma that escapes from the magnetic trap

- ***Plasma detachment:*** Plasma edge configuration with reduced particle and thermal loading to the PFCs. Its utilization is crucial to avoid the excessive damage and destruction of such components. More details in chapter 1.4.1
- ***Profilemetry:*** Experimental technique destined to characterize the surface profile of a sample, measuring details about its topology and morphology
- ***Recycling coefficient:*** Fraction of the surface reaching particle flux from plasma that come backs to it. It is represented by the symbol R, and is specially employed to characterize the hydrogenic trapping efficiency of the material surfaces
- ***Rotational transform:*** Number of poloidal transits per single toroidal transit of a field line on a toroidal flux surface. It generates the twisting of the magnetic field lines necessary to achieve the effective magnetic confinement of the plasma particles
- ***Separatrix:*** Boundary between closed and open field line regions in diverted fusion devices. It limits the confined region from the zone where the field lines intersect the divertor tiles
- ***SIMS:*** Acronym of Secondary Ion Mass Spectrometry. Surface characterization technique based on the analysis of the sputtered material from sample induced by ionic bombardment. Detection of components is carried out by conventional mass spectrometry
- ***SOL:*** Acronym of Scrappe Off Layer. Plasma region situated beyond the separatrix where the magnetic field lines are open to transport the power and particle exhaust to the divertor plates. Consequently, its role in these issues is absolutely crucial
- ***Stellarator:*** Magnetic fusion device that does not have axisymmetry. Its magnetic trap is completely created by means of external coils. This difference in the poloidal field generation compared to tokamaks leads to a 3D magnetic structure. Unlike tokamaks they are theoretically free of disruptions but present a more complicated design of the magnetic coils, being their global construction significantly more complex
- ***Stimulated emission:*** Process in which an impinging photon interacts with an atom producing the emission of another photon with identical phase and energetic characteristics. This quantic phenomenon is the basis for the emission of energetic and spatially coherent laser radiation

- ***TDS:*** Material analysis technique based on the thermal outgassing of the whole surface of the component. Detection of the sample components is frequently carried out by using mass spectrometry
- ***Tokamak:*** Axisymmetric (2D) magnetic fusion device. The necessary toroidal magnetic field is created by external coils, instead the poloidal magnetic field that is created by a circulating current around the toroidal plasma. Nowadays, they are the most investigated fusion devices due to their easier construction compared to stellarators.

BIBLIOGRAPHY

[1] International Energy Agency (2015), "Key World Energy Statistics"

[2] United Nations Economical and Social affairs report (2004), "World population to 2300"

[3] N.L. Madureira, "Key Concepts in Energy", (2014). London: Springer International Publishing, ISBN 978-3-319-04977-9

[4] S. Sorrell et al. Energy Policy. 38 (9) (2010) 4990-5003

[5] J. Ongena and G. Van Oost, "Energy for future Centuries. Prospects for fusion power as a future energy source" (2013). Proceedings of the 11th Carolus Magnus Summer School on plasma and fusion energy physics, Bad Honnef (Germany)

[6] I. Cook et al. "Safety and environmental Impact of Fusion", (2011). EFDA-S-RE-1 Report, EUR (01) CCE-FU/FTC 8/5

[7] P. Helander et al. Plasma Phys. Control. Fusion 54 (2012) 124009

[8] I.E. Tamm and A.D. Sakharov, "Theory of the magnetic thermonuclear reactor: Plasma Physics and the Problem of Controlled Thermonuclear Reactions" Vol. 1. (1958), AN SSSR Press, Moscow

[9] L. Jr. Spitzer, Project Matterhorn Report PM-S-1 NYO-993, Princeton University

[10] "Physical processes of the interaction of fusion plasmas with solids" (1996), edited by W. O. Hofer and J. Roth, Academic Press, Inc, San Diego, California

[11] U. Samm, "Plasma-wall interactions in magnetically confined fusion plasmas" (2013). Proceedings of the 11th Carolus Magnus Summer School on plasma and fusion energy physics, Bad Honnef (Germany)

[12] A. Loarte et al. Nucl. Fusion 47 (2007) S203

[13] H. Zohm et al. Nucl. Fusion 53 (2013) 073019

[14] A. Kallenbach et al. Plasma Phys. Control. Fusion 55 (2013) 124041

[15] G.F. Matthews, J. Nucl. Mater. 220-222 (1995) 104-116

[16] T. Eich et al Phys. Rev. Lett. 107 (2011) 215001

[17] M. Makowski et al. Phys. Plasmas 19 (2012) 056122

[18] ITER Phys. Exp. Group, Nucl. Fusion 47 (2007) S203

[19] M. Kotschenreuter et al. Phys. Plasmas 14 (2007) 072502

[20] D. Ryutov, Phys. Plasmas 15 (2008) 069901

[21] M. Turnyanskiy et al. Fusion Eng. Des. 96–97 (2015) 361–364

[22] R.J. Goldston et al. Phys. Scr. T167 (2016) 014017

[23] M.L. Watkins and P.H. Rebut, 19th EPS Conf. 1992 (Innsbruck) vol 2 p 731

[24] G.C. Vlases, Plasma Phys. Control. Fusion (1993) 35 B67–80

[25] R.J. Goldston et al. Plasma Phys. Control. Fusion 59 (2017) 055015

[26] A. Kallenbach et al. Nucl. Fusion 55 (2015) 053026

[27] B. B. Lipschultz et al. Nucl. Fusion 24 (1984) 8

[28] F. Reimold et al. Nucl. Fusion 55 (2015) 033004

[29] M. N. A. Beurskens et al. Plasma Phys. Control. Fusion 55 (2013) 124043

[30] C. Giroud, G.P. Maddison, S. Jachmich, et al., Nucl. Fusion 53 (2013), 113025.

[31] F. Wagner et al. Phys. Rev. Lett. 49 (1982) 19 1408-1412

[32] P. B. Snyder et al. Nucl. Fusion 44 (2004) 320-328

[33] R. Maingi et al. Phys. Rev. Lett. 103 (2009) 075001

[34] D.C. Whyte et al. Nucl. Fusion 50 (2010) 105005

[35] W.L. Zhong et al. Nucl. Fusion 53 (2013) 083030

[36] D.K. Mansfield et al. Nucl. Fusion 53 (2013) 113023

[37] P.T. Lang et al. Nucl. Fusion 44 (2004)

[38] A. Kirschner, “Erosion and deposition mechanisms in fusion plasmas” (2013). Proceedings of the 11th Carolus Magnus Summer School on plasma and fusion energy physics, Bad Honnef (Germany)

[39] J. Linke, “High heat flux performance of plasma facing materials and components under service conditions in future fusion reactors”, (2013). Proceedings of the 11th Carolus Magnus Summer School on plasma and fusion energy physics, Bad Honnef (Germany)

[40] M. Rubel, “Structure materials in fusion reactors: issues related to tritium, radioactivity and radiation-induced effects” (2013). Proceedings of the 11th Carolus Magnus Summer School on plasma and fusion energy physics, Bad Honnef (Germany)

[41] C.H. Skinner et al. Fusion Sci. Technol. 54 (2008)

[42] R. E. Nygren and F.L. Tabarés, Nucl. Mater and Energy, 9 (2016) 6-21

[43] J.Roth et al. J. Nucl. Mater. 390-391 (2009) 1

[44] S. Brezinsek, J. Nucl. Mater. 463 (2015) 11-21

[45] R. Behrisch, J. Roth et al. Nucl. Instr. Meth. Phys. Res. B18 (1987) 629-638

[46] A. Kallenbach, M. Balden, R. Dux et al. J. Nucl. Mater. 415, (2011) S19

[47] D. Neuwirth, V. Rohde et al. Plasma Phys. Controlled Fusion 54 (2012) 085008

[48] M. Oberkofler, D. Douai, S. Brezinsek et al. J. Nucl. Mater. 438 (2013) S258-S261

[49] A. Drenik, M. Oberkofler, D. Alegre et al. J. Nucl. Mater. 463 (2015) 684-687

[50] M. Oberkofler, D. Alegre, F. Aumayr et al. Fus. Eng. Des. (2015)

[51] G. De Temmerman and R. A. Pitts, Joint WPJET 2 and WPPFC EUROfusion Annual Meeting (2015), Culham, UK

[52] G. De Temmerman, R. A. Pitts et al., 21st ITPA SOL and Divertor TG Meeting (2015), Princeton, USA

[53] A. de Castro et al. J. Nucl. Mater. 463 (2015) 676-679

[54] A. de Castro et al. Nucl. Mater. Energy (2017) https://doi.org/10.1016/j.nme.2017.02.12

[55] A. de Castro et al. Nucl. Mater. Energy 9 (2016) 1-5

[56] E. Wilhelm, R. Battino and R. J. Wilcock, Chem. Rev. 77 (2) (1977) 219–262

[57] J.M. Hales and D.R. Drewes, Atmos. Environ. 13 I6 (1979) 1133-1147

[58] C.H. Kunsman, J. Am. Chem. Soc. 50 (8), (1928) 2100–2113

[59] V. Rohde and M. Oberkofler, J. Nucl. Mater. 463 (2015) 672-675

[60] A. B. Martin-Rojo, M. González and F.L. Tabarés, "Glow Discharge Emission Spectroscopy", Informe Técnico CIEMAT 1273 (2013), Madrid, España

[61] D. Alegre, J.A. Ferreira and F.L. Tabarés, J. Mass Spectrom. 49 (2014) 342

[62] I. Langmuir and H. Mott-Smith, "The theory of collectors in gaseous discharges," Phys. Rev. 28, (1926) 727–763

[63] R. L. Merlino, Am. J. Phys. 75 (2007) 12

[64] E. Carrasco et al. Phys. Chem. Chem. Phys. 13 (2011) 19561–19572

[65] H. Kiyooka and O. Matsumoto, Plasma Chem. Plasma Process. V16 (1996) 4

[66] B. Gordiets, C.M. Ferreira et al. Plasma Sources Sci. Technol. 7 (1998) 379-388

[67] E. Carrasco et al. Plasma Phys. Control. Fusion 54 (2012) 124019

[68] J. Bohdansky, Nucl. Instrum. Methods B 2, (1984) 587

[69] W. Eckstein et al. IPP Report 9/82 (1993), Max-Planck Institut für Plasmaphysik-Garching, Germany

[70] J.F. Ziegler, et al. Nucl. Instrum. Methods Phys. Res. Sect. B. V268 (2010) I11-12

[71] K. Schmid, A. Manhard, Ch. Linsmeier et al. Nucl. Fusion 50 (2010) 025006

[72] L.Gao, W. Jacob, P. Wang, U. von Toussaint et al. Phys. Scr. T159 (2014) 014023

[73] M. Oberkofler and Ch. Linsmeier, Nucl. Fusion 50 (2010) 125001

[74] L. Marot, Ch. Linsmeier et al. Fusion Eng. Des. 88 (2013) 1728-1731

[75] W.Eckstein, IPP Report 17/20 (2010) Max-Planck Institut für Plasmaphysik-Garching, Germany

[76] J.A. Ferreira and F.L. Tabarés, J. Vac. Sci. Technol. A 25 (2007) 2

[77] K. Sawada and M. Goto, "Revision of collisional-radiative models and neutral transport code for hydrogen and helium species", IAEA Atomic and Molecular Data Report (2013), Vienna, Austria

[78] W. L. Wiese and J. R. Fuhr, J. Phys. Chem. Ref. Data 38 (2009) 3

[79] T. Dittmar et al. P1.8. Poster Contribution in 22nd International conference on Plasma Surface Interactions in controlled fusion devices (2016), Rome, Italy

[80] L. Laguardia et al. O 28, Oral Contribution in 22nd International conference on Plasma Surface Interactions in controlled fusion devices (2016), Rome, Italy

[81] O. Vaittinen, M. Metsälä et al. Appl. Phys. B 115 (2) (2013)

[82] A. de Castro, D. Alegre and F.L. Tabarés, P-91, Poster Contribution in 15th International Conference on Plasma-Facing Materials and Components for Fusion Applications (2015), Aix-en-Provence, France

[83] J.M. Lafferty, "Foundations of vacuum science and technology", Wiley-Interscience Publication (1998)

[84] J.L. Gland, B.A. Sexton and G.E. Mitchell, Surf. Sci. 115 (1982) 623-632

[85] S. Chapman and T.G. Cowling, "The mathematical theory of non-uniform gases", Cambridge University Press (1939)

[86] A. Drenik et al. "Evaluation of the plasma hydrogen isotope content by residual gas analysis at JET and AUG", (2017), submitted to Phys. Scripta

[87] A. Drenik et al. "Detection of ammonia by residual gas analysis in AUG and JET". Fusion Engineering and Design (2017). Accepted, article in press

[88] V. Philipps, J. Roth, A. Loarte, Plasma Phys. Control. Fusion 45 (2003) A17–A30

[89] R.P. Wenninger, M. Bernert, T. Eich, et al., Nucl. Fusion 54 (2014) 114003

[90] A. Loarte et al. Nucl. Fusion 47 (2007) S203-S263

[91] A. Herrmann. Plasma Phys. Control. Fusion 44 (2002) 883

[92] H. Takenaga et al. Fusion Sci. Technol. 42 (2002) 327

[93] A.S. Kukushkin, H.D Pacher and R.A. Pitts, J. Nucl. Mater. 463 (2015) 586-590

[94] A.S. Kukushkin et al. Fusion Eng. Des. 65 (2003) 355

[95] M. Bernert et al. Nuclear Materials and Energy 1 (2017) 1–8

[96] F.L. Tabarés et al. Nucl. Fusion 57 (2017) 016029

[97] A. de Castro et al. Fus. Eng. Des. 117 (2017) 212-216

[98] A. de Castro el al. "Temperature dependence of lithium film formation and deuterium retention on hot W samples by LIDS. Implications for future fusion reactors", Nucl. Fusion (2017) Submitted

[99] A. L. Neff, J. P. Allain et al., J. Nucl. Mater. 463 (2015) 1147-1151

[100] C. Li, X. Wu, C. Zhang et al., Fusion. Eng. Des. 89 (2014) 949

[101] J.S. Hu et al. Fus. Eng. Des. 89 (2014) 2875–2885

[102] G. Federici et al. J. Nucl. Mater. 14 (1999) 266–269

[103] V. Phillips et al. Nucl. Fusion 53 (2013) 093002

[104] F.L. Tabarés, Plasma Phys. Control. Fusion 58 (2016) 014014

[105] V.A. Evtikhin et al. Plasma Phys. Control. Fusion 44 (2002) 955

[106] S. V. Mirnov et al. Plasma Phys. Control. Fusion 48 (2006) 821

[107] F. L. Tabarés et al. J. Nucl. Mater. 463 (2015) 1142-1146

[108] G. Mazzitelli et al. J. Nucl. Mater. 463 (2015) 1152–1155

[109] J.Ren et al. Fus. Eng. Des. 102 (2016) 36–43

[110] D.N. Ruzic, et al., Nucl. Fusion 51 (2011) 102002

[111] M. Shimada, Y. Hirooka, Nucl. Fusion 54 (2014)

[112] D. Keroack, B. Terreault , J. Nucl. Mater. 212-215 (1994) 1443

[113] J.H. Yu, et al., J. Nucl. Mater. 438 (2013) S1150

[114] G. De Temmerman et al. Nuclear Materials and Energy 0 0 0 (2016) 1–6

[115] S.V. Mirnov et al. Nucl. Fusion 51 (2011) 073044

[116] A.B. Martin-Rojo, et al., Fusion Eng. Des. 89 (2014) 2915

[117] E. Oyarzabal, A.B. Martin-Rojo, et al. J. Nucl. Mater. 463 (2015) 1173–1176

[118] M. Ono et al. Nucl. Fusion 53 (2013) 113030

[119] M. Ono et al. Fus. Eng. Des. 89 (2014) 2838–2844

[120] M. Jiménez-Redondo et al. Phys. Chem. Chem. Phys. 13 (2011) 9655-9666

[121] T. Tanabe, Phys. Scr. T159 (2014) 014044

[122] M. Miyamoto, D. Nishijima, Y. Ueda et al., Nucl. Fusion 49 (2009) 065035

[123] P. Valson, "Deuterium retention studies on Lithiated Tungsten under varying lithiation environments", Master Thesis, Univesidad Carlos III de Madrid, 2015

[124] B. Schweer et al. Phys. Scr. T138 (2009) 014008

[125] M. Zlobinski et al. J. Nucl. Mater. 483 (2013) 1155

[126] LPY600 LITRON Laser Series Operators Handbook, 20055

[127] A. Sepetys. “Studies of hydrogen retention on lithiated targets by laser induced desorption”, Master Thesis, Universidad Carlos III de Madrid, 2016

[128] https://refractiveindex.info

[129] https://www.webelements.com

[130] D.W. Jeppson et al. Lithium literature review: Lithium’s properties and interactions (1978), Handford Engineering Development Laboratory

[131] D. Sands, Pulsed Laser Heating and Melting, Heat Transfer - Engineering Applications, (2011) Prof.Vyacheslav Vikhrenko (Ed.), ISBN: 978-953-307-361-3

[132] H. S. Carslaw and J. C. Jaeger, Conduction of Heat in Solids, (1959) 2nd ed. (Oxford V. P., London).

[133] S. Krat el al. Vacuum 105 (2014) 111-114

[134] Yu. M. Gasparyan et al. Fus. Eng. Des. (2016)

[135] A. S. Popkov et al. Phys. Procedia 71 (2015) 88 – 92

[136] D.S. McPhail, J. Mater. Sci. 41 (2006) 873

[137] Brown, W. (1985). Collision Cascades, Ionization, Spikes and Energy Transfer. MRS Online Proceedings 51, doi:10.1557/PROC-51-53

[138] M. González, Master course in Materials Engineering: Structural characterization of materials II: Spectroscopy. Universidad Politécnica de Madrid, 2015

[139] http://www.nanoscience.com

[140] W. Jackson and T.M. Mahmood, Anal. Chem. 66 (12) (1994) 252R–279R

[141] http://chemistry.tutorvista.com

[142] C.H. Skinner et al. J. Nucl. Mater. 390–391 (2009) 1005–1008

[143] E. Veleckis. J. Nucl. Mater. 79 (1979) 20

[144] H. Katsuta et al. Nucl. Technol. 32 (1977) 297

[145] P. Hubberstey et al. Journal of the Less-Common Metals, 49 (1976) 253-269

[146] J. Engbaek et al. Surf. Sci. 600 (2006) 1468-1474

[147] A.M. Capece et al. J. Nucl. Mater. 463 (2015) 1177-1180

[148] M. A. Jaworski et al. J. Nucl. Mater. 415 (2011) S985-S988

[149] J.P. Allain, “Kinematic and Thermodynamic effects on liquid lithium sputtering” PhD. thesis, University of Illinois, May 2000

[150] F. Scotti et al. J. Nucl. Mater. 463 (2015) 1165-1168

[151] J.P. Allain et al. J. Nucl. Mater. 290-293 (2001) 180-184

[152] J.P. Allain et al. J. Nucl. Mater. 313-316 (2003) 641-645

[153] J.N. Brooks et al. J. Nucl. Mater. 290-293 (2001) 185-190

[154] R. Bastasz and W. Eckstein, J. Nucl. Mater. 290-293, (2001) 19-24

[155] G. Pelka et al. Contrib. Plasma Phys. 56 (2016) 6-8, 802–807

[156] R.J. Goldston et al. Nuclear Materials Energy (2017) http://dx.doi.org/10.1016/j.nme.2017.03.020

[157] C. Bachmann et al. Fus. Eng. Des. (2015)

[158] G. Federici et al. Fus. Eng. Des. 89 (2014) 882–889

[159] A.J.H. Donné, G. Federici and PPPT Team "Overview of Design and R&D Activities towards a European DEMO", IEA-FPCC Meeting, Paris 27-28/01/2016

[160] Yu. Igitkhanov et al. Nuclear Materials and Energy 9 (2016) 560–564

[161] Chr. Day et al. Fus. Eng. Des. 89 (2014) 1505-1509

[162] C. Gleason-González et al. Fus. Eng. Des. 89 (2014) 1042–1047

[163] F.L. Tabarés et al. Plasma Phys. Control. Fusion 59 (2017) 044006

[164] S. Brezinsek et al. "Preparation of PFCs for the Efficient use in ITER and DEMO Plasma-Wall Interaction Studies within the EUROfusion Consortium", Nuclear Fusion (2017). Accepted, article in press.

[165] M. Ono et al. Fus. Eng. Des. 117 (2017) 124–129

PUBLICATIONS

MAIN PUBLICATIONS RELATED WITH THIS THESIS

1. "Ammonia formation in N_2-H_2 plasmas on ITER-relevant plasma facing materials: Surface temperature and N_2 plasma content effects". Journal of Nuclear Materials 463 (2015) 676-679
2. "Physisorption of ammonia on AISI 304 L stainless steel at different surface temperature under high vacuum conditions". Nuclear Materials and Energy 9 (2016)" 1-5
3. "Hydrogen retention studies on lithiated tungsten exposed to glow discharge plasmas under varying lithiation environments using Thermal Desorption Spectroscopy and Mass Spectrometry". Fusion Engineering and Design 117 (2017) 212-216
4. "Influence of residence time and helium addition in the ammonia formation on tungsten walls in N_2-H_2 glow discharge plasmas". Nuclear Materials and Energy (2017). Accepted, article in press
5. "Temperature dependence of liquid lithium film formation and deuterium retention on hot W samples by LIDS. Implications for future fusion reactors". Nuclear Fusion (submitted)

OTHER PUBLICATIONS

1. "First liquid lithium limiter biasing experiments in the TJ-II stellarator". Journal of Nuclear Materials 463 (2015) 1142-1146
2. "Transport, stability and plasma control studies in the TJ-II stellarator" Nuclear Fusion 55 (2015) 104014
3. "Experimental tests of LiSn alloys as potential liquid metal for the divertor target in a fusion reactor". Nuclear Materials and Energy (2016). Accepted, article in press

4. “Reactor plasma facing component designs based on liquid metal concepts supported in porous systems”. Nuclear Fusion 57 (2017) 016029
5. “Detection of ammonia by residual gas analysis in AUG and JET”. Fusion Engineering and Design (2017). Accepted, article in press
6. “3D effects on transport and plasma control in the TJ-II stellarator”. Nuclear Fusion 57 (2017) 102022
7. “Evaluation of the plasma hydrogen isotope content by residual gas analysis at JET and AUG”. Physica Scripta (2017). Accepted, article in press

LIST OF FIGURES

LIST OF TABLES